10th Anniversary

PROCEEDINGS

of the

Tenth
International Tissue Elasticity Conference™

Arlington, Texas, USA
October 12 – 15, 2011

PROCEEDINGS

of the

Tenth International Tissue Elasticity Conference™

Arlington, Texas, USA
October 12–15, 2011

Table of Contents

2011 SPONSORS

The Conference Organizers wish to express appreciation
to the following companies
for providing support of this year's Conference:

Gold Level
($10,000 or more)

UTHealth
The University of Texas
Health Science Center at Houston
THE UNIVERSITY OF TEXAS MEDICAL SCHOOL AT HOUSTON
Diagnostic & Interventional Imaging

Silver Level
($5,000 or more)

ULTRASONIX

Ultrasonix Medical Corporation
for sponsoring
the Awards for Best Student Oral Presentation and Morning Coffee Breaks

General Level
(up to $1,999)

CIRS
Tissue Simulation & Phantom Technology

CIRS, Inc.
for providing
a Model 058 Breast Elastography Phantom for a 2011 ITEC door prize

RCBU

Rochester Center for Biomedical Ultrasound
The University of Rochester

FOREWORD

Dear Conference Delegate:

Welcome! This year we celebrate the 10th Anniversary of the annual International Tissue Elasticity Conference™. In the 1990s we saw a remarkable development of technologies and approaches for imaging various elastic properties of tissues. The 2000's have seen a continuation of innovative approaches, with the addition of a major step. That important step was the creation of specialized scanners for conducting clinical research on thousands of patients in some of the most highly respected medical centers around the world. In retrospect, the evolution of the field is a superb case study of translational research, developing from "bench to bedside." This conference series has, by design, served as the place where researchers, clinicians, industry leaders, and students from around the world could trade ideas and discuss the latest advances, while creating an archival record of their progress. The international participation in the Conference now includes virtually all global entities engaged in research, development, commercialization and practice in the field.

Last year's Conference feedback was again unanimous in the desire for continuation of the tutorial series. We are pleased that Drs. Jeffrey Bamber (UK) and Mark Palmeri (US) have agreed to present this year's exciting tutorials on the technical and clinical progress over the last 10 years as well as potential for the future. We are also continuing last year's popular format of the formal Poster Session, where each presenter has the opportunity to give a brief oral summary of his/her poster, and we thank Drs. Salavat Aglyamov (US) and Hani Eskandari (CA) for their enthusiastic leadership in conducting this event.

This year we continue to attract a rapidly growing number of clinical papers. Following on last year, we continue to have three clinical sessions and two cardiovascular sessions.

Last year's Student Best Paper Presentations and Awards session was a resounding success. Due to the generous ongoing Silver sponsorship that we received from Ultrasonix Medical Corporation, the Conference will again deliver Student Best Paper certificates and cash awards to the authors of papers that have been judged as most meritorious through independent review cycles. On Wednesday afternoon, we will have a special session in which the eight finalists will present their abstracts. The final awardees will be announced during the Conference dinner on Thursday evening.

We also thank The University of Texas Medical School at Houston, Diagnostic & Interventional Imaging Department (US) as a Gold sponsor of the Conference this year.

This year we welcome back Supersonic Imagine, Inc. (US) as exhibitors and welcome CIRS (US) as first time exhibitors at the Conference.

We would like to thank all the new and returning delegates, reviewers and session chairs for their continuing support of the Conference. Special thanks are in order to our enthusiastic support staff that has worked above and beyond. Ms. Charlene Waldron volunteered with correspondence and financial aspects of the Conference; Ms. Karen Ophir volunteered to design the Conference's artwork, publications and web site, negotiate the hotel contract, organize the scientific program and edit all abstracts and compile the Conference Proceedings; Ms. Sonja van de Ven helped with the Registration Desk and on–site organization; and Drs. Reza Zahiri Azar and Vladimir Egorov as our official Conference photographer and videographer, respectively, again this year.

The Conference is conducted under the joint auspices of the University of Rochester Center for Biomedical Ultrasound and the Ultrasonics and Elastographics Laboratory in the Department of Diagnostic and Interventional Imaging at the University of Texas Health Science Center at Houston. Most direct funding for the Conference is derived from registration fees, and, with your continued support in abstract submissions and attendance, we are committed to improve and expand the Conference in the years to come. We appreciate your written and oral feedback that always helps us in planning for future Conferences.

We hope that you will enjoy this year's scientific and social programs as well as the Dallas/Fort Worth and Texas hospitality. We hope to see you again at the 11th ITEC next year!

J. Ophir and K.J. Parker, Conference Organizers

Arlington, Texas, USA, October 12th 2011

Go to Page 123 for the BackWord

CONFERENCE–AT–A–GLANCE

Tenth International Tissue Elasticity Conference™

The Sheraton Arlington Hotel – Arlington, Texas, USA October 12–15, 2011

Wednesday, October 12		**9:00A – 8:00P**	
9:00A – 12:00P	**Set Up:**	Oral Presenters load presentations (CD or jump drive)	Ballroom I
		Poster Presenters set up presentations	Champions Ballroom III
		Exhibitors set up exhibits	Champions Ballroom III
9:00A – 8:00P		Registration Desk Open	Champions Ballroom Foyer
11:00A – 8:00P	**Session EEX:**	Equipment Exhibit *(during breaks & Reception)*	Ch Ballroom III
12:00P – 2:00P	**Session SAS:**	**Oral Presentations of Finalists for Student Awards Session**	
		Sponsored by Ultrasonix Medical Corporation	Champions Ballroom I
2:00P – 2:30P		*Coffee Break*	Champions Ballroom Foyer
2:30P – 4:30P	**Session TUT:**	**Tutorials: Keynote Presentations**	Champions Ballroom I
4:30P – 5:00P		*Recess*	
5:00P – 6:00P	**Session POS:**	**Poster Session – Live Oral Summaries**	Champions Ballroom III
6:00P – 8:00P		*Opening Dinner Reception*	Champions Ballrooms II & III
Thursday, October 13		**7:00A – 10:30P**	
7:00A – 8:00A		*Group Breakfast*	Champions Ballroom Foyer
7:00A – 5:45P		Registration Desk Open	Champions Ballroom Foyer
8:00A – 5:45P	**Session POS:**	Posters	Champions Ballrooms III
8:00A – 5:45P	**Session EEX:**	Equipment Exhibit	Champions Ballrooms III
7:45A – 8:00A		Opening Remarks	Champions Ballroom I
8:00A – 10:15A	**Session CVE–1:**	**Cardiovascular Elasticity – I**	Champions Ballroom I
9:00A – 9:30A		*Tourist Information*	Champions Ballroom Foyer
10:15A – 10:45A		*Coffee Break*	Champions Ballroom III
10:45A – 12:00P	**Session FIP:**	**Forward and Inverse Problems**	Champions Ballroom I
12:00P – 1:30P		*Group Lunch*	Champions Ballroom Foyer
1:30P – 3:00P	**Session MIP–1:**	**Methods for Imaging Elastic Tissue Properties – I**	Ch Ballroom I
3:00P – 3:30P		*Coffee Break*	Champions Ballroom III
3:30P – 5:45P	**Session CAA-1:**	**Clinical and Animal Applications – I**	Champions Ballroom I
7:30P – 10:30P		*10th Anniversary Conference Dinner featuring JB Clark, singer*	Plaza on the Hill
Friday, October 14		**7:00A – 6:45P**	
7:00A – 8:00A		*Group Breakfast*	Champions Ballroom Foyer
7:00A – 5:30P		Registration Desk Open	Champions Ballroom Foyer
8:00A – 5:30P	**Session POS:**	Posters	Champions Ballroom III
8:00A – 5:30P	**Session EEX:**	Equipment Exhibit	Champions Ballroom III
8:00A – 9:45A	**Session SIP:**	**Signal and Image Processing**	Champions Ballroom I
9:45A – 10:15A		*Coffee Break*	Champions Ballroom III
10:15A – 12:00P	**Session MPT:**	**Mechanical Properties of Tissues**	Champions Ballroom I
12:00P – 1:30P		*Group Lunch*	Champions Ballroom Foyer
1:30P – 2:45P	**Session MIP–2:**	**Methods for Imaging Elastic Tissue Properties – II**	Ch Ballroom I
2:45P – 3:15P		*Coffee Break*	Champions Ballroom III
3:15P – 4:15P	**Session CAA–2:**	**Clinical and Animal Applications – II**	Champions Ballroom I
4:15P – 5:45P	**Session MMT:**	**Mechanical Measurement Techniques for Tissues**	Ch Ballroom I
5:45P – 6:45P		*Group Photo*	TBA
Saturday, October 15		**7:00A – 10:00P**	
7:00A – 8:00A		*Group Breakfast*	Champions Ballroom Foyer
7:00A – 4:00P		Registration Desk Open	Champions Ballroom Foyer
8:00A – 4:00P	**Session POS:**	Posters	Champions Ballroom III
8:00A – 4:00P	**Session EEX:**	Equipment Exhibit	Champions Ballroom III
8:00A – 10:00A	**Session BTM:**	**Biomechanical Tissue Modeling**	Champions Ballroom I
10:00A – 10:30A		*Coffee Break*	Champions Ballroom III
10:30A – 11:45A	**Session CAA–3:**	**Clinical and Animal Applications – III**	Champions Ballroom I
11:45A – 1:15P		*Group Lunch*	Champions Ballroom Foyer
1:15P – 3:00P	**Session CVE–2:**	**Cardiovascular Elasticity – II**	Champions Ballroom I
3:00P – 3:30P		*Coffee Break*	Champions Ballroom III
3:30P – 5:00P	**Session MIP–3:**	**Methods for Imaging Elastic Tissue Properties – III**	Ch Ballroom I
5:00P – 5:30P	**Session CMM:**	**Complementary & Multi Modality Elasticity Imaging Techniques**	CB I
7:00P – 10:00P		*Closing Pizza Party (Proceedings Book Signing)*	The Poolside Pavilion

PROGRAM

Tenth International Tissue Elasticity Conference™

Arlington, Texas, USA
October 12 – 15, 2011

Wednesday, October 12 9:00A – 8:00P

9:00A – 12:00P Presentation & Exhibit Set Up

All Oral Presenters load presentations onto Conference computers — Champions Ballroom I
Poster Presenters set up presentations — Champions Ballroom III
Exhibitors set up exhibits — Champions Ballroom III

9:00A – 8:00P

Registration Desk Open — Champions Ballroom Foyer

11:00A – 12:00P 2:00P – 2:30P 4:30P – 5:00P 6:00P – 8:00P
Session EEX: Equipment Exhibit — Champions Ballroom III

Wednesday 12:00P – 2:00P

Session SAS: Oral Presentations of Finalists for Student Awards Session

Sponsored by Ultrasonix Medical Corporation, Vancouver, BC, Canada

Chair: SE Salcudean, Canada *Co-Chair: C Sumi, Japan* Champions Ballroom I

Page No.

12:00P – 12:15P

020 *IN VIVO* ASSESSMENT OF CORNEAL SHEAR ANISOTROPY USING SUPERSONIC SHEAR IMAGING. 24

T–M Nguyen[1], J–F Aubry[1], D Touboul[2], J Bercoff[3], M Tanter[1].*

[1]Institut Langevin Ondes et Images, ESPCI ParisTech, Paris, FRANCE; [2]Centre Hospitalo–Universitaire de Bordeaux, Bordeaux, FRANCE; [3]SuperSonic Imagine, Aix en Provence, FRANCE.

12:15P – 12:30P

044 *IN VIVO* NONINVASIVE MULTI–ANGLE STRAIN IMAGING OF SEVERELY STENOTIC ARTERIES. 25

HHG Hansen[1], GJ de Borst[2], G Pasterkamp[2], CL de Korte[1].*

[1]Radboud University Nijmegen Medical Centre, Nijmegen, THE NETHERLANDS; [2]University Medical Centre Utrecht, Utrecht, THE NETHERLANDS.

12:30P – 12:45P

046 HUMAN SCLERA STRAINS UNDER PHYSIOLOGICAL LOADINGS USING ULTRASONIC SPECKLE TRACKING. 26

J Tang[1], J Liu[1].*

[1]Ohio State University, Columbus, OH, USA.

12:45P – 1:00P

054 PULSE WAVE IMAGING FOR ARTERIAL STIFFNESS MEASUREMENT IN NORMAL AND PATHOLOGICAL HUMAN ARTERIES *IN VIVO*. 27

RX Li[1], J Luo[1], SK Balaram[2], FA Chaudhry[2], JC Lantis[2], EE Konofagou[1].*

[1]Columbia University, New York, NY, USA; [2]St. Luke's–Roosevelt Hospital Center, New York, NY, USA.

(Session SAS continues on next page)

1:00P – 1:15P

058 ANALYSIS OF PLAQUE CHARACTERISTICS USING ULTRASOUND, STRAIN AND PHOTOACOUSTIC IMAGING. 28

AA Satari[1], IM Graf[1], SY Emelianov[1].*
[1]University of Texas at Austin, Austin, TX, USA.

1:15P – 1:30P

061 MULTIMODALITY IMAGE REGISTRATION OF PROSTATE ARFI IMAGES TO MR AND HISTOLOGY DATA. 29

C Hsu[1], M Davenport[2], R Gupta[2], T Polascik[2], R Varley[2], E Kulbacki[2], J Madden[2], ML Palmeri[1], KR Nightingale[1].*
[1]Duke University, Durham, NC, USA; [2]Duke University Medical Center, Durham, NC, USA.

1:30P – 1:45P

065 INVESTIGATING THE INFLUENCE OF IMAGING PARAMETERS AND TISSUE HETEROGENEITIES ON STIFFNESS RECONSTRUCTION FOR ENDORECTAL MRE. 30

A Arani[1,2], DB Plewes[1,2], R Chopra[1,2].*
[1]Sunnybrook Research Institute, Toronto, Ontario, CANADA; [2]University of Toronto, Toronto, Ontario, CANADA.

1:45P – 2:00P

071 CORRELATION OF MECHANICAL BRAIN PROPERTIES ASSESSED WITH MAGNETIC RESONANCE ELASTOGRAPHY WITH HISTOPATHOLOGY IN A MOUSE MODEL OF MULTIPLE SCLEROSIS. 31

K Schregel[1,2], E Wuerfel[1], P Garteiser[2], D Petersen[1], J Wuerfel[1], R Sinkus[2].*
[1]University Luebeck, Luebeck, GERMANY; [2]INSERM UMR 773, Centre de Recherches Biomédicales Bichat–Beaujon, Paris, FRANCE.

2:00P – 2:30P

COFFEE BREAK Champions Ballroom III

Wednesday 2:30P – 4:30P

Session TUT: Keynote Tutorials:

10th Anniversary ITEC – Progress and Prospects

Chair: R Sinkus, France *Co-Chair: AK Thittai, USA* Champions Ballroom I

2:30P – 3:15P

101 WHEN PUSH COMES TO SHOVE (OR SHEAR), WHERE ARE WE AFTER TEN YEARS OF FURTHER DEVELOPMENT? 32

JC Bamber[1].*
[1]Institute of Cancer Research and Royal Marsden NHS Foundation Trust, Sutton, Surrey, England, UK.

3:15P – 3:30P Discussion

3:30P – 4:15P

094 BIOLOGICAL FOUNDATIONS AND CLINICAL APPLICATIONS OF SOFT TISSUE ELASTICITY IMAGING. 33

ML Palmeri[1,2].*
[1]Duke University, Durham, NC, USA; [2]Duke University Medical Center, Durham, NC, USA.

4:15P – 4:30P Discussion

4:30P – 5:00P

Recess

Wednesday 5:00P – 6:00P

(Posters will be available for viewing and Coffee Break Discussion through the afternoon Coffee Break, Saturday, October 15)

Session POS: Poster Session – Live Oral Summaries

Chair: SR Aglyamov, USA *Co-Chair: H Eskandari, Canada* Champions Ballroom III

(Session POS continues on next page)

(Session POS continued from previous page)

5:16P – 5:18P

070 A FINITE ELEMENT MODEL OF CERVICAL ARFI IMAGING. 42
A Homyk[1], TJ Hall[2], H Feltovich[2,3], ML Palmeri[1].*
[1]Duke University, Durham, NC, USA; [2]University of Wisconsin–Madison, Madison, WI, USA; [3]Maternal Fetal Medicine, Intermountain Healthcare, Park City, UT, USA.

5:18P – 5:20P

075 SMALL BREAST LESION CLASSIFICATION PERFORMANCE USING THE NORMALIZED AXIAL–SHEAR STRAIN AREA FEATURE. 43
AK Thittai[1], JM Yamal[2], J Ophir[1].*
[1]The University of Texas Medical School, Houston, TX, USA; [2]The University of Texas School of Public Health, Houston, TX, USA.

5:20P – 6:00P **Discussion**

Wednesday 6:00P – 8:00P
Opening Dinner Reception *Proceedings Book Signing* Champions Ballrooms

Thursday, October 13 7:00A – 10:30P

7:00A – 8:00A
GROUP BREAKFAST Champions Ballroom Foyer

7:00A – 5:30P
Registration Desk Open Champions Ballroom Foyer

8:00A – 5:30P **Session POS: Posters** Champions Ballroom III
Session EEX: Equipment Exhibit Champions Ballroom III

9:00A – 9:30A
Tourist Information Champions Ballroom Foyer

Thursday 7:45A – 8:00A
OPENING REMARKS
KJ Parker, J Ophir Champions Ballroom I

Thursday 8:00A – 10:15A
Session CVE–1: Cardiovascular Elasticity – I
Chair: EE Konofagou, USA *Co-Chair: RGP Lopata, The Netherlands* Champions Ballroom I

8:00A – 8:30A **Invited Presentation**

099 MYOCARDIAL ELASTOGRAPHY AND ELECTROMECHANICAL WAVE IMAGING – FROM THEORY TO CLINICAL APPLICATIONS. 44
EE Konofagou[1], WN Lee[1], S Okrasinski[1], J Provost[1].*
[1]Columbia University, New York, NY, USA.

8:30A – 8:45A

045 ASSESSMENT OF MYOCARDIAL ELASTOGRAPHY PERFORMANCE IN NORMAL AND ISCHEMIC PHANTOMS UNDER PHYSIOLOGIC MOTION CONFIGURATIONS WITH PRELIMINARY *IN VIVO* VALIDATION. 45
SJ Okrasinski[1], EE Konofagou[1].*
[1]Columbia University, New York, NY, USA.

8:45A – 9:00A

031 DIRECT *IN VIVO* MYOCARDIAL INFARCT VISUALIZATION USING 3D ULTRASOUND AND PASSIVE STRAIN CONTRAST. 46
BC Byram[1], DP Bradway[1], D Hyun[1], DM Gianantonio[1], M Jakolvjevic[1], AL Crowley[2], HW Kim[2], M Parker[2], R Kim[2], R Judd[2], GE Trahey[1].*
[1]Duke University, Durham, NC, USA; [2]Duke University Medical Center, Durham, NC, USA.

Page No.

9:00A – 9:15A

032 CARDIAC ABLATION LESION VISUALIZATION – ARFI AND STRAIN COMPARISON. 47
BC Byram[1], DM Dumont[1], SJ Hsu[1], PD Wolf[1], GE Trahey[1].*
[1]Duke University, Durham, NC, USA.

9:15A – 9:30A

049 SINGLE–HEARTBEAT ELECTROMECHANICAL WAVE IMAGING WITH OPTIMAL STRAIN ESTIMATION USING TEMPORALLY–UNEQUISPACED ACQUISITION SEQUENCES. 48
J Provost[1], S Thiébaut[1], J Luo[1], EE Konofagou[1].*
[1]Columbia University, New York, NY, USA.

9:30A – 9:45A

040 SHEAR STRAIN ENDOVASCULAR ELASTOGRAPHY: VALIDATION WITH *IN VITRO* DATA. 49
Y Majdouline[1], S Le Floc'h[2], D Garcia[1,3], M–H Roy Cardinal[1], J Ohayon[2,4], G Cloutier[1].*
[1]University of Montréal Hospital Research Center (CRCHUM), Montréal, Québec, CANADA; [2]UJF–Grenoble 1, CNRS, Grenoble, FRANCE; [3]University of Montréal Hospital Research Center (CRCHUM), Montréal, Québec, CANADA; [4]University of Savoie, Polytech Savoie, Le Bourget du Lac, FRANCE.

9:45A – 10:00A

010 *IN VIVO* 3D (+t) STRAIN IMAGING AND ELASTOGRAPHY OF THE HUMAN AORTA. 50
RGP Lopata[1,2], HHG Hansen[3], EMH Bosboom[2], GJLM Jongen[1], CL de Korte[3], FN van de Vosse[1,2].*
[1]Eindhoven University of Technology, Eindhoven, THE NETHERLANDS; [2]Maastricht University Medical Center, Maastricht, THE NETHERLANDS; [3]Radboud University Nijmegen Medical Centre, Nijmegen, THE NETHERLANDS.

10:00A – 10:15A

090 COMPARISON OF MECHANICAL PROPERTIES OF AORTIC ANEURYSMS ASSESSED WITH MRI AND ULTRASOUND ELASTOGRAPHY. 51
RGP Lopata[1,2], MFJ Peters[1], VI Nyugen[2], CL de Korte[3], FN van de Vosse[1,2], EMH Bosboom[2].*
[1]Eindhoven University of Technology, Eindhoven, THE NETHERLANDS; [2]Maastricht University Medical Center, Maastricht, THE NETHERLANDS; [3]Radboud University Nijmegen Medical Centre, Nijmegen, THE NETHERLANDS.

10:15A – 10:45A

COFFEE BREAK Champions Ballroom III

Thursday 10:45A – 12:00P
Session FIP: Forward and Inverse Problems

Chair: PE Barbone, USA *Co-Chair: MD Alenezy, Saudi Arabia* Champions Ballroom I

Page No.

10:45A – 11:15A Invited Presentation

092 A MODEL–BASED APPROACH TO QUASI–STATIC, HARMONIC AND TRANSIENT ELASTOGRAPHY. 52
MM Doyley[1].*
[1]University of Rochester, Rochester, NY, USA.

11:15A – 11:30A

060 A DIRECT VARIATIONAL ALGORITHM FOR SOLUTION OF THE TIME–HARMONIC VISCOELASTIC INVERSE PROBLEM. 53
Y Zhang[1], AA Oberai[1], PE Barbone[2], I Harari[3].*
[1]Rensselaer Polytechnic Institute, Troy, NY, USA; [2]Boston University, Boston, MA, USA; [3]Tel Aviv University, Ramat Aviv, ISRAEL.

11:30A – 11:45A

067 SPARSITY REGULARIZATION IN DYNAMIC ELASTOGRAPHY. 54
M Honarvar[1], R Rohling[1], SE Salcudean[1].*
[1]University of British Columbia, Vancouver, BC, CANADA.

(Session FIP continues on next page)

(Session FIP continued from previous page) Page No.

11:45A – 12:00P

089 DATA REQUIREMENTS FOR LINEAR AND NONLINEAR ELASTIC MODULUS RECONSTRUCTION IN TWO AND THREE DIMENSIONS. 55

E Rodrigues Ferreira[1,2], U Albocher[3], I Harari[3], A Oberai[1], PE Barbone[4].*

[1]Rensselaer Polytechnic Institute, Troy, NY, USA; [2]Université Libre de Bruxelles, Bruxelles, BELGIUM; [3]Tel Aviv University, Ramat Aviv, ISRAEL; [4]Boston University, Boston, MA, USA.

12:00P – 1:30P

GROUP LUNCH Champions Ballroom Foyer

Thursday 1:30P – 3:00P

Session MIP–1: Methods for Imaging Elastic Tissue Properties – I

Chair: JC Bamber, UK *Co-Chair: E Mazza, Switzerland* Champions Ballroom I

Page No.

1:30P – 1:45P

009 COLON TUMOR GROWTH AND ANTIVASCULAR TREATMENT IN MICE: COMPLEMENTARY ASSESSMENT WITH MR ELASTOGRAPHY AND DIFFUSION–WEIGHTED MR IMAGING. 56

L Jugé[1], BT Doan[2], J Seguin[2], M Albuquerque[1], B Larrat[3], N Mignet[2], GG Chabot[2], D Scherman[2], V Paradis[1,4], V Vilgrain[1,4], BE Van Beers[1,4], R Sinkus[1].*

[1]Université Paris Diderot, Paris, FRANCE; [2]UPCGI/Chimie–ParisTech, Paris, FRANCE; [3]ESPCI–ParisTech, Paris, FRANCE; [4]Hôpital Beaujon, Assistance Publique–Hôpitaux de Paris, Clichy, FRANCE.

1:45P – 2:00P

014 ON THE ACOUSTIC RADIATION FORCE GENERATED BY MODULATED ULTRASOUND IN TISSUE–LIKE SOLIDS. 57

EV Dontsov[1], BB Guzina[1].*

[1]University of Minnesota, Minneapolis, MN, USA.

2:00P – 2:15P

015 USING CRAWLING WAVE SONOELASTOGRAPHY FOR THE MEASUREMENT OF INTRAHEPATIC FAT CONTENT. 58

BN Mills[1], CT Barry[2], Z Hah[1], DJ Rubens[2], KJ Parker[1].*

[1]University of Rochester, Rochester, NY, USA; [2]University of Rochester Medical Center, Rochester, NY, USA.

2:15P – 2:30P

016 VAGINAL TACTILE IMAGER FOR DIRECT MODULUS ESTIMATION. 59

V Egorov[1], M Patel[1], AP Sarvazyan[1].*

[1]Artann Laboratories, Trenton, NJ, USA.

2:30P – 2:45P

018 A HAND–HELD SYSTEM FOR QUANTITATIVE MAPPING OF ELASTIC PROPERTIES WITHIN A BIOMATERIAL FROM CRAWLING WAVES GENERATED ON THE SURFACE. 60

A Partin[1], Z Hah[1], BN Mills[1], DJ Rubens[2], KJ Parker[1].*

[1]University of Rochester, Rochester, NY, USA; [2]University of Rochester Medical Center, Rochester, NY, USA.

2:45P – 3:00P

026 PASSIVE ELASTOGRAPHY FROM COMPLEX SHEAR WAVE FIELD IN SOFT SOLIDS. 61

S Catheline[1], T Gallot[1], P Roux[1], J Brum[1], C Negreira[2].*

[1]Grenoble University & CNRS, LGIT, Grenoble, FRANCE; [2]Science University, LAU, Montevideo, URUGUAY.

3:00P – 3:30P

COFFEE BREAK Champions Ballroom III

* *indicates Presenter*

Thursday 3:30P – 5:45P

Session CAA–1: Clinical and Animal Applications – I

Chair: BS Garra, USA *Co-Chair: J Triano, USA* Champions Ballroom I

Thursday 7:30P – 10:30P

10th Anniversary Conference Dinner Plaza on the Hill

Proceedings Book Signing *Announcement of Student Best Paper Award Recipients*

Musical Event: *Selections performed by JB Clark*

Friday, October 14 7:00A – 6:45P

7:00A – 8:00A

GROUP BREAKFAST Champions Ballroom Foyer

7:00A – 5:30P

Registration Desk Open Champions Ballroom Foyer

8:00A – 5:30P **Session POS: Posters** Champions Ballroom III

Session EEX: Equipment Exhibit Champions Ballroom III

Friday 8:00A – 9:45A

Session SIP: Signal and Image Processing

Chair: E Brusseau, France *Co-Chair: R Zahiri Azar, Canada* Champions Ballroom I

Page No.

8:00A – 8:30A **Invited Presentation**

100 MAINSTREAM SIGNAL PROCESSING METHODS FOR STRAIN IMAGING. 70

RGP Lopata[1,2].*

[1]Eindhoven University of Technology, Eindhoven, THE NETHERLANDS; [2]Maastricht University Medical Center, Maastricht, THE NETHERLANDS.

8:30A – 8:45A

021 RETAINING AXIAL–LATERAL ORTHOGONALITY IN STEERED ULTRASOUND DATA FOR IMPROVED IMAGE QUALITY IN RECONSTRUCTED LATERAL DISPLACEMENT DATA. 71

L Garcia[1], J Fromageau[1], RJ Housden[2], GM Treece[2], C Uff[1], JC Bamber[1].*

[1]Institute of Cancer Research, Sutton, Surrey, England, UK; [2]University of Cambridge, Cambridge, England, UK.

8:45A – 9:00A

053 PHYSICAL BOUNDARY RECONSTRUCTION: A NOVEL METHOD TO DETERMINE VISCOELASTIC PARAMETERS FROM MAGNETIC RESONANCE ELASTOGRAPHY DATA. 72

P Garteiser[1], S Doblas[1], V Vilgrain[2], B Van Beers[1,2], R Sinkus[1].*

[1]INSERM UMR773, Bichat–Beaujon Biomedical Research Center, Clichy, FRANCE; [2]Beaujon Hospital, Clichy, FRANCE.

9:00A – 9:15A

064 LATERAL MODULATION IMAGING USING SIMPLE NON–STEERING BEAMFORMING. 73

C Sumi[1], Y Takanashi[1], Y Ishii[1], N Yamazaki[1].*

[1]Sophia University, Chiyoda–ku, Tokyo, JAPAN.

** indicates Presenter*

9:15A – 9:30A

9:30A – 9:45A

9:45A – 10:15A

COFFEE BREAK Champions Ballroom III

Friday 10:15A – 12:00P
Session MPT: Mechanical Properties of Tissues

Chair: A Sarvazyan, USA *Co-Chair: BB Guzina, USA* Champions Ballroom I

10:15A – 10:45A Invited Presentation

10:45A – 11:00A

11:00A – 11:15A

11:15A – 11:30A

11:30A – 11:45A

11:45A – 12:00P

12:00P – 1:30P
GROUP LUNCH — Champions Ballroom Foyer

Friday 1:30P – 2:45P
Session MIP–2: Methods for Imaging Elastic Tissue Properties – II
Chair: YP Zheng, China *Co-Chair: S Catheline, France* Champions Ballroom I

2:45P – 3:15P
COFFEE BREAK — Champions Ballroom III

Friday 3:15P – 4:15P
Session CAA–2: Clinical and Animal Applications – II
Chair: JM Rubin, USA *Co-Chair: JR Grajo, USA* Champions Ballroom I

* *indicates Presenter*

Page No.

3:45P – 4:00P

003 SHEAR WAVE ELASTOGRAPHY MAY OUTPERFORM STRAIN ELASTOGRAPHY AND MAY ADD A NEW DIMENSTION TO THYROID ULTRASOUND. 89

RZ Slapa[1], WS Jakubowski[1], J Slowinska–Srzednicka[2], A Piwowonski[3], J Bierca[4], KT Szopinski[1].*

[1]Medical University of Warsaw, Warsaw, POLAND; [2]Center for Postgraduate Medical Education, Warsaw, POLAND; [3]Diagnostic and Research Medical Centre, Walbrzych, POLAND; [4]Solec Hospital, Warsaw; POLAND.

4:00P – 4:15P

082 DIAGNOSTIC PERFORMANCE OF STRAIN ELASTOSONOGRAPHY IN MULTINODULAR THYROID GOITER IS UNSATISFACTORY. 90

RZ Slapa[1], WS Jakubowski[1], J Bierca[2], B Migda[1], J Slowinska–Srzednicka[3].*

[1]Medical University of Warsaw, Warsaw, POLAND; [2]Solec Hospital, Warsaw; POLAND; [3]Center for Postgraduate Medical Education, Warsaw, POLAND.

Friday 4:15P – 5:45P

Session MMT: Mechanical Measurement Techniques for Tissues

Chair: G Cloutier, Canada *Co-Chair: T Shiina, Japan* Champions Ballroom I

Page No.

4:15P – 4:45P Invited Presentation

097 MEASUREMENT METHODS FOR THE MECHANICAL CHARACTERIZATION OF SOFT BIOLOGICAL TISSUE. 91

E Mazza[1].*

[1]Swiss Federal Institute of Technology, Zurich, SWITZERLAND.

4:45P – 5:00P

079 MULTI-PUSH (MP) ARF ASSESSMENT OF VISCOELASTIC PROPERTIES IN A TISSUE MIMICKING PHANTOM. 92

MR Scola[1], CM Gallippi[1].*

[1]The University of North Carolina at Chapel Hill, Chapel Hill, NC, USA.

5:00P – 5:15P

083 DEVELOPMENT OF A MINIATURIZED WATER JET ULTRASOUND INDENTATION PROBE FOR DETECTION OF ARTICULAR CARTILAGE DEGENERATION. 93

YP Huang[1], YP Zheng[1].*

[1]Hong Kong Polytechnic University, Hong Kong, CHINA.

5:15P – 5:30P

084 A MINIATURIZED AIR JET INDENTATION PROBE BASED ON OPTICAL COHERENCE TOMOGRAPHY (OCT) FOR MECHANICAL ASSESSMENT OF SOFT TISSUE. 94

LK Wang[1], YP Huang[1], YP Zheng[1].*

[1]Hong Kong Polytechnic University, Hong Kong, CHINA.

5:30P - 5:45P

086 DEVELOPMENT OF A VIBRO–ULTRASOUND METHOD FOR SKELETAL MUSCLE STIFFNESS ASSESSMENT UNDER HIGH LEVELS OF ISOMETRIC CONTRACTION. 95

CZ Wang[1], YP Zheng[1].*

[1]The Hong Kong Polytechnic University, Hong Kong, CHINA.

Friday 5:45P – 6:45P

Group Photo TBA

After 6:45P *No Conference Activities*

Saturday, October 15 7:00A – 10:00P

7:00A – 8:00A
GROUP BREAKFAST — Champions Ballroom Foyer

7:00A – 4:15P
Registration Desk Open — Champions Ballroom Foyer

8:00A – 4:15P **Session POS: Posters** — Champions Ballroom III
Session EEX: Equipment Exhibit — Champions Ballroom III

Saturday 8:00A – 10:00A
Session BTM: Biomechanical Tissue Modeling

Chair: ML Palmeri, USA *Co-Chair: KJ Parker, USA* Champions Ballroom I

Page No.

8:00A – 8:30A Invited Presentation

093 BIOMECHANICAL IMAGING: ELASTOGRAPHY BEYOND YOUNG'S MODULUS. 96
PE Barbone[1].*
[1]Boston University, Boston, MA, USA.

8:30A – 8:45A

004 A NOVEL FRACTIONAL ORDER VISCOELASTIC MATERIAL MODEL FOR SOFT BIOLOGICAL TISSUES AND ITS FINITE ELEMENT APPLICATION. 97
N Demirci[1], E Tönük[1].*
[1]Middle East Technical University, Ankara, TURKEY.

8:45A – 9:00A

036 DISPERSION AND DISTORTION OF SHEAR WAVE PULSES. 98
KJ Parker[1], Z Hah[1].*
[1]University of Rochester, Rochester, NY, USA.

9:00A – 9:15A

041 SHEAR WAVE SPEED BASED ASSESSMENT OF NONLINEAR MATERIAL PROPERTIES. 99
VM Rotemberg[1], ML Palmeri[1,2], KR Nightingale[1].*
[1]Duke University, Durham, NC, USA; [2]Duke Medical Center, Durham, NC, USA.

9:15A – 9:30A

062 DEVELOPMENT OF A NEW MICROSTRUCTURE–BASED CONSTITUTIVE MODEL FOR HEALTHY AND CANCEROUS TISSUE. 100
E Rodrigues Ferreira[1,2], S Goenezen[1], PE Barbone[3], AA Oberai[1].*
[1]Rensselaer Polytechnic Institute, Troy, NY, USA; [2]Université Libre de Bruxelles, Bruxelles, BELGIUM; [3]Boston University, Boston, MA, USA.

9:30A – 9:45A

066 MECHANICAL MODEL ANALYSIS FOR QUANTITATIVE EVALUATION OF LIVER FIBROSIS BASED ON REAL–TIME TISSUE ELASTOGRAPHY. 101
T Shiina[1], M Yamakawa[1], M Kudo[2], A Tonomura[4], T Mitake[4].*
[1]Kyoto University, Kyoto, JAPAN; [2]Kinki University School of Medicine, Osaka–Sayama, JAPAN; [4]Hitachi–Aloka Medical, Ltd., Chiba, JAPAN.

9:45A – 10:00A

073 *IN VIVO* MR RHEOLOGY OF LIVER AT MULTIPLE FREQUENCIES IN 3D: EFFECT OF DISPLACEMENT DATA DIMENSIONALITY ON SHEAR MODULUS. 102
RS Sahebjavaher[1,2], P Garteiser[2], BE Van Beers[2], SE Salcudean[1], R Sinkus[2].*
[1]University of British Columbia, Vancouver, BC, CANADA; [2]Centre de Recherche Biomedicale Bichat–Beaujon, Paris, FRANCE.

* *indicates Presenter*

10:00A – 10:30A
COFFEE BREAK — Champions Ballroom III

Saturday 10:30A – 11:45A
Session CAA–3: Clinical and Animal Applications – III

Chair: W Weitzel, USA *Co-Chair: H Feltovich, USA* Champions Ballroom I

Page No.

10:30A – 10:45A

011 RENAL ALLOGRAFT ELASTICITY ASSESSED BY SUPERSONIC AIXPLORER™ AND BY MAGNETIC RESONANCE ELASTOGRAPHY – PRELIMINARY RESULTS. 103
R Souchon[1], S Lounis[2], G Pagnoux[3], JM Ménager[2], E Morelon[3], O Rouvière[3].*
[1]INSERM, Lyon, FRANCE; [2]SCM IRM Lyon–Villeurbanne, Lyon, FRANCE, [3]Hospices Civils de Lyon, Lyon, FRANCE.

10:45A – 11:00A

012 A NOVEL NONLINEAR ANALYSIS IN ULTRASOUND ELASTICITY IMAGING OF EDEMA AND FIBROSIS IN CROHN'S DISEASE. 104
JM Rubin[1], J Xu[2], S Tripathy[2], RW Stidham[1], LA Johnson[1], PD Higgins[1], K Kim[2].*
[1]University of Michigan, Ann Arbor, MI, USA; [2]University of Pittsburgh, Pittsburgh, PA, USA.

11:00A – 11:15A

052 APPLICATION OF THE MEASUREMENT OF VISCOSITY BY MAGNETIC RESONANCE ELASTOGRAPHY TO THE CHARACTERIZATION OF HEPATIC TUMORS. 105
P Garteiser[1], S Doblas[1], J–L Daire[1,2], M Wagner[1], H Leitao[3], V Vilgrain[2], B Van Beers[1,2], R Sinkus[1].*
[1]INSERM UMR773, Bichat–Beaujon Biomedical Research Center, Clichy, FRANCE, [2]Beaujon Hospital, Clichy, FRANCE; [3]Hospitais de Universidade de Coimbra, Coimbra, PORTUGAL.

11:15A – 11:30A

027 NONINVASIVE EVALUATION OF HEPATIC FIBROSIS USING ACOUSTIC RADIATION FORCE– BASED SHEAR STIFFNESS IN PATIENTS WITH NONALCOHOLIC FATTY LIVER DISEASE. 106
ML Palmeri[1], MH Wang[1], NC Rouze[1], MF Abdelmalek[2], CD Guy[2], B Moser[2], AM Diehl[2], KR Nightingale[1].*
[1]Duke University, Durham, NC, USA; [2]Duke University Medical Center, Durham, NC, USA.

11:30A – 11:45A

077 DIFFERENTIAL TISSUE STRAIN ESTIMATION ACROSS STRATA OF LUMBAR TISSUES UNDER INTRINSIC MOTION. 107
J Triano[1], HM Langevin[2], EE Konofagou[3].*
[1]Canadian Memorial Chiropractic College, Toronto, Ontario, CANADA; [2]University of Vermont, Burlington, VT, USA; [3]Columbia University, New York, NY, USA.

11:45A – 1:15P
GROUP LUNCH — Champions Ballroom Foyer

Saturday 1:15P – 3:15P
Session CVE–2: Cardiovascular Elasticity – II

Chair: CL de Korte, The Netherlands *Co-Chair: K Kim, USA* Champions Ballroom I

Page No.

1:15P – 1:45P Invited Presentation

096 REVIEW ON STRAIN BASED CARDIOVASCULAR FUNCTIONAL IMAGING. 108
CL de Korte[1].*
[1]Radboud University Nijmegen Medical Centre, Nijmegen, THE NETHERLANDS.

(Session CVE–2 continues on next page)

(Session CVE–2 continued from previous page) Page No.

1:45P – 2:00P

007 NON–INVASIVE MECHANICAL CHARACTERIZATION OF CAROTID ATHEROSCLEROTIC PLAQUES WITH ULTRASOUND ELASTOGRAPHY AND CORRELATION WITH HIGH RESOLUTION MAGNETIC RESONANCE IMAGING: A CLINICAL REPORT. 109

C Naim[1], G Cloutier[1,2], E Mercure[1], F Destrempes[1], MF Giroux[2,3], G Soulez[2,3].*

[1]University of Montréal Hospital Research Center (CRCHUM), Montréal, Québec, CANADA; [2]University of Montréal, Montréal, Québec, CANADA; [3]University of Montréal Hospital (CHUM), Montréal, Québec, CANADA.

2:00P – 2:15P

008 REDUCING ARTIFACTS IN NON–INVASIVE VASCULAR ELASTOGRAPHY OF CAROTID ARTERIES. 110

E Mercure[1], F Destrempes[1], Y Majdouline[1], J Ohayon[2,3], G Soulez[4,5], G Cloutier[1,5].*

[1]University of Montréal Hospital Research Center (CRCHUM), Montréal, Québec, CANADA; [2]CNRS, Laboratory TIMC–IMAG, Grenoble, FRANCE; [3]University of Savoie, Le Bourget du Lac, FRANCE; [4]University of Montréal Hospital (CHUM), Montréal, Québec, CANADA; [5]Institute of Biomedical Engineering, Montréal, Québec, CANADA.

2:15P – 2:30P

005 PERFORMANCE OF NEW MECHANICAL CRITERIA USED TO EXTRACT *IN VIVO* VALID MODULOGRAMS FROM A CARDIAC CYCLE CORONARY IVUS STRAIN SEQUENCE. 111

G Cloutier[1], S Le Floc'h[2], Y Saijo[3], G Finet[4], P Tracqui[2], RI Pettigrew[5], J Ohayon[2,6].*

[1]University of Montréal Hospital Research Center, Montréal, Québec, CANADA; [2]CNRS, Laboratory TIMC–IMAG, Grenoble, FRANCE; [3]Tohoku University, Sendai, JAPAN; [4]INSERM Unit 886, Lyon, FRANCE; [5]NIH, Bethesda, MD, USA. [6]University of Savoie, Le Bourget du Lac, FRANCE.

2:30P – 2:45P

059 SIMULATED PULSE WAVE IMAGING FOR LOCAL STIFFNESS ESTIMATION IN PATIENT–SPECIFIC AORTAS WITH PHANTOM VALIDATION. 112

D Shahmirzadi[1], RX Li[1], J Luo[1], EE Konofagou[1].*

[1]Columbia University, New York, NY, USA.

2:45P – 3:00P

088 MINIMALLY CONSTRAINED RECONSTRUCTIONS IN INTRAVASCULAR ULTRASOUND ELASTOGRAPHY: INITIAL CLINICAL INVESTIGATION. 113

MS Richards[1], MM Doyley[1].*

[1]University of Rochester, Rochester, NY, USA.

3:00P – 3:30P

COFFEE BREAK Champions Ballroom III

Saturday 3:30P – 5:00P

Session MIP–3: Methods for Imaging Elastic Tissue Properties – III

Chair: TJ Hall, USA *Co-Chair: MS Richards, USA* Champions Ballroom I

Page No.

3:30P – 3:45P

072 NUMERICAL EVALUATION OF ARTERIAL PRESSURE EQUALIZATION TECHNIQUES FOR ENHANCED VASCULAR STRAIN IMAGING. 114

D Dutta[1], P Gottschalk[2], J Hamilton[2], K Kim[1].*

[1]University of Pittsburgh, Pittsburgh, PA, USA; [2]Epsilon Imaging, Inc., Ann Arbor, MI, USA.

3:45P – 4:00P

042 3D VECTOR FIELD MAGNETIC RESONANCE ELASTOGRAPHY FOR DETECTING TISSUE PRESSURE CHANGES IN HUMAN BRAIN. 115

D Klatt[1], S Hirsch[1], J Braun[1], FB Freimann[1], I Sack[1].*

[1]Charité–University Medicine Berlin, GERMANY.

* *indicates Presenter*

Page No.

4:00P – 4:15P

043 LOCAL SHEAR SPEED ESTIMATION OF *EX–VIVO* PROSTATE USING ACOUSTIC CRAWLING WAVES (ARC) GENERATED FROM RADIATION FORCES. 116
Z Hah[1], C Hazard[2], BN Mills[1], DJ Rubens[3], KJ Parker[1].*
[1]University of Rochester, Rochester, NY, USA; [2]GE Global Research, Niskayuna, NY, USA; [3]University of Rochester, Rochester, NY, USA.

4:15P – 4:30P

048 REAL–TIME TRANSIENT ELASTOGRAPHY ON STANDARD ULTRASOUND USING MECHANICALLY INDUCED VIBRATION. 117
R Zahiri Azar[1], K Dickie[1], BE Kerby[1], S Bernardo[1], C Cheung[1], L Pelissier[1].*
[1]Ultrasonix Medical Corporation, Richmond, BC, CANADA.

4:30P – 4:45P

050 MULTI–PARAMETRIC MONITORING OF THERMAL LESIONS USING HARMONIC MOTION IMAGING FOR FOCUSED ULTRASOUND (HMIFU). 118
GY Hou[1], F Marquet[1], J Luo[1], EE Konofagou[1].*
[1]Columbia University, New York, NY, USA.

4:45P – 5:00P

051 FEASIBILITY OF ACQUIRING VOLUMETRIC B–MODE/ARFI/DOPPLER DATA BY SWEEPING. 119
DM Dumont[1], JR Doherty[1], SY Lee[1], GE Trahey[1].*
[1]Duke University, Durham, NC, USA.

Saturday 5:00P – 5:30P
Session CMM: Complementary and Multi Modality Elasticity Imaging Techniques

Chair: V Egorov, USA *Co-Chair: R Souchon, France* Champions Ballroom I

Page No.

5:00P – 5:15P

033 COMPARISON OF ULTRASONIC MEASUREMENTS OF UNRIPENED AND RIPENED CERVICES. 120
L Reusch[1], L Carlson[1], ML Palmeri[2], JJ Dahl[2], H Feltovich[1,3], TJ Hall[1].*
[1]University of Wisconsin–Madison, Madison, WI, USA; [2]Duke University, Durham, NC, USA; [3]Maternal Fetal Medicine, Intermountain Healthcare, Park City, UT, USA.

5:15P – 5:30P

056 THE APPLICATION OF FREE–HAND TISSUE DEFORMATION AND SPATIO–TEMPORALLY REGULARISED SPECKLE TRACKING TO PHOTOACOUSTIC IMAGE CLUTTER REDUCTION: A FIRST CLINICAL DEMONSTRATION. 121
M Jaeger[1], D Birtill[1], A Gertsch[1], E O'Flynn[1,2], JC Bamber[1].*
[1]Institute of Cancer Research and Royal Marsden NHS Foundation Trust, Sutton, Surrey, England, UK; [2]Royal Marsden NHS Foundation Trust, Sutton, Surrey, England, UK.

5:30P – 7:00P *No Conference Activities*

Saturday 7:00P – 10:00P
Closing Pizza Party

Proceedings Book Signing The Poolside Pavilion

** indicates Presenter*

SuperSonic Imagine, Inc.
Bothell, WA, USA.

CIRS – Tissue Simulation and Phantom Technology.
Norfolk, VA, USA.

www.jbclark.com

JB Clark

Folk – Rock singer, songwriter, guitarist.

Born in Salem, Oregon in 1954 and living in Texas since 1991, JB Clark was raised in Southern California until the age of 11 when his mother passed and the family moved to St. Louis, Missouri, where he lived until joining the Air Force when he was 17. His dad gave him his first guitar for his 14th birthday, and he has been playing the guitar and singing ever since.

His first paying gig was with a friend in Minnesota in 1975 while in the service then on to Alaska and Italy. The first song he learned to play was, "Blowing in The Wind", by Bob Dylan. His first tunes were mostly folk songs and tunes by Paul Simon. He calls his favorite kind of music Folk-Rock Baby Boomer Music, and some of his favorite artists are: Paul Simon, Gordon Lightfoot, Harry Chapin, John Denver and Crosby, Stills, Nash & Young, some of which you will hear at the 10th Anniversary ITEC Dinner.

He wanted to be a full time musician after the service, but marriage and a family allowed him to travel the world in the field of radio communications. He landed in Texas in 1991, got his pilot's license in 1994 (his other dream) and in November 2002, he started performing again! He was so hooked on performing and enjoyed the people so much that he hasn't missed a performance since!

JB has performed at some very special events including the Terlingua International Festival (Terlingua, TX), Vietnam Security Police Association (San Antonio, TX) and the 6th Annual Fruit of the Vine Gala Benefitting Kids Matter International 2010 (Dallas, TX)

We hope you will enjoy the Folk-Rock style of this exceptional vocalist who accompanies himself on acoustic guitar and harmonica.

A detailed program will be available at the Conference Dinner.
Thursday, October 13th, 2011
Performance will start at 9:00 pm

AUTHOR INDEX

AUTHOR INDEX

ABSTRACTS

Tenth International Tissue Elasticity Conference™

Arlington, Texas, USA October 12 – 15, 2011

Session SAS: Oral Presentations of Finalists for Student Awards Session

Wednesday, October 12 12:00P – 2:00P

Sponsored by Ultrasonix Medical Corporation, Vancouver, BC, Canada

020 ***IN VIVO* ASSESSMENT OF CORNEAL SHEAR ANISOTROPY USING SUPERSONIC SHEAR IMAGING.**

Thu–Mai Nguyen[1], Jean–François Aubry[1], David Touboul[2], Jeremy Bercoff[3], Mickaël Tanter[1]*

[1]Institut Langevin Ondes et Images, ESPCI ParisTech, CNRS UMR 7587, Inserm ERL U979, Paris, FRANCE; [2]Centre Hospitalo–Universitaire de Bordeaux, Bordeaux, FRANCE; [3]SuperSonic Imagine, Aix en Provence, FRANCE.

Background: The elastic behavior of soft tissues is known to be linked to their microstructure. The cornea is mainly composed of collagen fibers whose organization determines its biomechanical properties. Understanding these properties has become a crucial issue in ophthalmology to predict the cornea response to refractive surgery procedures and to avoid post–treatment complications.

Aims: The aim of this study is to adapt the Supersonic Shear Imaging (SSI) elastography technique to assess the corneal shear anisotropy. 3D elastic maps of the cornea were obtained by rotating the imaging plane above the corneal surface.

Methods: The SSI method consists of inducing a shear wave by ultrasonic radiation force using a linear ultrasonic array. The resulting propagation direction is transverse to the ultrasound beam. The probe is then switched to an ultrafast imaging mode (30kHz) to follow the shear wave propagation. Its local speed is then evaluated to retrieve the shear modulus of the medium. We implemented the SSI technique with specially designed high frequency rotating arrays (15MHz, 128 elements) to estimate the tissue elastic anisotropy. 3D scans were performed on human eyes (*ex vivo*) and porcine eyes (*ex vivo* and *in vivo*). Differences in the local shear wave speed for different propagation directions were highlighted.

Results: Elasticity maps of the cornea surface were obtained both *ex vivo* and *in vivo* with good repeatability (standard deviation <6% of the shear modulus). On both human and porcine corneas, the peripheral part turned out to be 70±10% softer than the central part. Human corneas did not exhibit any strong anisotropy whereas porcine corneas were stiffer within a 50±5° sector around the horizontal meridian (16±2kPa) than in the diagonal and vertical directions (7.8±0.5kPa).

Conclusions: It is known from X–ray diffraction measurements [1] that the fibers are mainly oriented along the horizontal meridian in the porcine cornea, while there are two preferential directions in the human cornea (horizontal and vertical). In both cases, the fibers are more likely to be circumferential at the limbus. The elasticity maps obtained here are consistent with pioneering *ex vivo* findings [1], proving the sensitivity of SSI to tissue fibers orientation in both *ex vivo* and *in vivo* conditions.

References:

[1] S. Hayes et al: Comparative Study of Fibrillar Collagen Arrangement in the Corneas of Primates and Other Mammals. The Anat. Rec., 290, pp. 1542–1550, 2007.

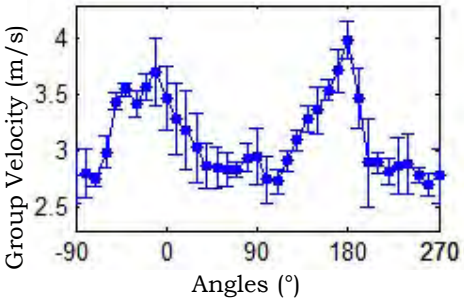

Figure1: Shear wave speed as a function of the propagation direction for an *in vivo* porcine cornea. The standard deviation corresponds to the spatial heterogeneity. (0° corresponds to the horizontal meridian, along the ear–nose direction).

* *indicates Presenter*

044 ***IN VIVO* NONINVASIVE MULTI–ANGLE STRAIN IMAGING OF SEVERELY STENOTIC ARTERIES.**

HHG Hansen[1], GJ de Borst[2], G Pasterkamp[2], CL de Korte[1].*
[1]Radboud University Nijmegen Medical Centre, Nijmegen, THE NETHERLANDS; [2]University Medical Centre Utrecht, Utrecht, THE NETHERLANDS.

Background: Atherosclerotic carotid plaque rupture is one of the main causes of stroke. The rupture proneness of a plaque is related to its composition and geometry. Geometry can be assessed using B–mode ultrasound images. Plaque composition might be determined using strain imaging techniques, because of the different elastic properties of the various plaque components: thrombus, lipids and fibrotic tissue. Recently, a noninvasive technique was developed that combined radiofrequency (RF) ultrasound data acquired at three beam steering angles to determine the radial strains for full transverse cross–sections of carotid arteries [1]. In this study, the method was applied *in vivo* to severely stenotic carotid arteries in symptomatic patients. The strain results were compared with photographs of the same carotid cross–section taken after endarterectomy (surgical excision of the plaque and inner vessel wall).

Aims: To investigate if multi–angle strain imaging allows identification of different plaque components.

Methods: RF data of 5 carotid arteries were recorded at the site of largest stenosis for 3 seconds using a Medison Accuvix V10 system equipped with an L5–13 linear array transducer. RF data were recorded for beam steering angles of 0°, +θ and -θ (20°≤θ≤30°) at a frame rate of 129Hz. The steering angle was changed sequentially in between frames. 2D displacements were estimated for each steering angle using a coarse–to–fine 2D cross–correlation based algorithm. Projection of the angular axial displacement fields resulted in the radial displacements. Least squares strain estimation yielded the radial strains. Cumulative radial strain images were calculated from begining systole until end systole. The strain results obtained by the three–angle method were compared to strain images obtained with conventional single angle strain imaging in which axial and lateral components are combined to derive the radial strains [2].

Results: In all 5 arteries, the strain images correlated with plaque morphology as depicted from the photographs of the excised specimen. Images of two interesting cases are shown in Figure 1. On the left is (a) a strain image of a plaque with low strains. The photograph (b) reveals that this plaque is fibrotic and calcified which explains the low levels of strain. On the right is (c) a strain image of a plaque with a region of radial expansion during the systolic phase. This unexpected expansion might be explained by a rupture of the plaque; this rupture resulted in an open connection between the lumen and the core of the plaque which had been filled with fatty material and thrombus ((d), bottom left). The pressure of the blood acting on this core during the systolic phase leads to the observed radial expansion. The other three specimens had a heterogeneous composition. The corresponding strain images showed a heterogeneous pattern of low and high strain. The specimens are currently being processed for histology allowing confirmation of these findings. In all cases, the three–angle method outperformed conventional strain imaging, especially at 3 and 9 o'clock where the lateral component is aligned with the radial component.

Figure 1:

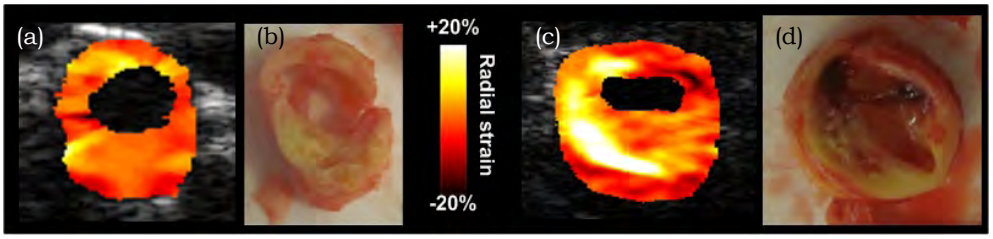

Conclusions: These preliminary results illustrate that strain values measured *in vivo* with the noninvasive three–angle method seem to provide relevant information on plaque composition and might eventually be suitable for the detection of vulnerable plaques.

Acknowledgements: The support of the Dutch Technology Foundation (STW) is acknowledged, and the authors would like to thank Medison for the development of the automatic multi–angle scanning sequence.

References:

[1] H.H.G. Hansen, R.G.P. Lopata and C.L. de Korte: Full 2D Displacement Vector and Strain Tensor Estimation for Superficial Tissue using Beam Steered Ultrasound Imaging. Phys. Med. Biol., (55), pp. 3201–3218, 2010.
[2] H. Ribbers, R. G. Lopata, S. Holewijn, G. Pasterkamp, J. D. Blankensteijn and C. L. de Korte: Noninvasive Two–Dimensional Strain Imaging of Arteries: Validation in Phantoms and Preliminary Experience in Carotid Arteries *In Vivo*. Ultrasound Med. Biol., Vol. 33, No. 4, pp. 530–540, 2007.

046 **HUMAN SCLERA STRAINS UNDER PHYSIOLOGICAL LOADINGS USING ULTRASONIC SPECKLE TRACKING.**

Junhua Tang[1], Jun Liu[1,2].*
[1]Biomedical Engineering and [2]Ophthalmology Departments, Ohio State University, Columbus, OH, USA.

Background: Glaucomatous vision loss can occur at both normal and elevated levels of intraocular pressure (IOP), and the optic nerve head (ONH) is the principle site of damage. Previous computational models have shown that scleral mechanical properties play an important role in affecting the mechanical environment of the ONH [1]. It is thus important to characterize the mechanical behavior of sclera under physiological loadings, such as elevated IOP.

Aims: The purpose of this study is to monitor scleral tensile and through–thickness strains under physiological loadings by using a cross–correlation based ultrasonic speckle tracking algorithm [2].

Methods: Three human globes were obtained within 72 hours postmortem. The intact posterior sclera shell was dissected and mounted onto a custom built pressurization chamber. A saline column with a reservoir was connected to the chamber to control the IOP, and the IOP was confirmed by a pressure sensor (Omega Px154, Omega Engineering Inc., Stamford, CT, USA). Each scleral shell was preconditioned by 5 cycles of pressurization from 5–45mmHg in 60 seconds and allowed to recover for 360 seconds at 5mmHg. An ultrasound imaging system (Vevo660, VisualSonics Inc. Toronto, Canada) with a 55MHz transducer was employed to acquire radiofrequency (RF) signals and scan a cross–section of the sclera at the posterior pole along the circumferential direction. The RF signals were sampled and recorded by using a digitizer (500MHz/8–bit, DP105, Acqiris, Monroe, NY, USA). IOP was first maintained at 5mmHg and gradually increased to 45mmHg at steps of 5mmHg. A 2–D cross–correlation based ultrasound speckle tracking algorithm was utilized to compute the displacement of ultrasound speckles at each level of IOP elevation. Both through–thickness compressive strain and circumferential tensile strain were calculated from the speckle displacement.

Results: The average through–thickness compressive strain at the posterior pole of the human sclera was 1.8%, 3.1%, 4.4% and 6.1% at pressure of 15mmHg, 25mmHg, 35mmHg and 45mmHg, respectively. The corresponding circumferential tensile strain was 0.45%, 0.62%, 0.67% and 0.67% (Figure 1).

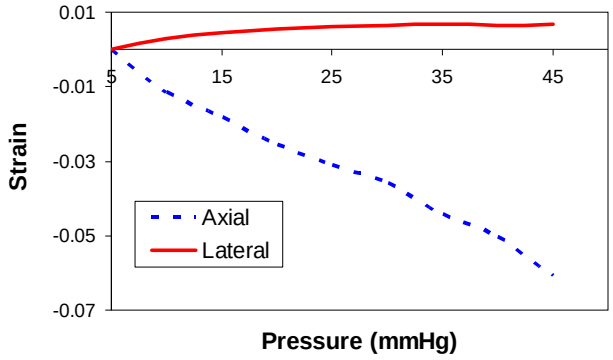

Figure 1: Through–thickness (axial) and circumferential tensile (lateral) strain at different pressures (n=3).

Conclusions: The ultrasound speckle tracking method provides an inexpensive high resolution method to assess scleral deformation through its full thickness under physiological IOP loadings. Our preliminary results showed that the compressive strains were larger than the tensile strains in the sclera under IOP elevation. Future work will validate this result in a larger sample size and investigate the use of the ultrasound method to examine regional viscoelastic properties of human sclera.

Acknowledgements: Donor globes were obtained from the Ohio Lions Eye Bank. Dr. Cynthia J. Roberts kindly assisted with the acquisition of the experimental samples.

References:

[1] Sigal IA, Flanagan JG, Ethier CR: Factors Influencing Optic Nerve Head Biomechanics. Investigative Ophthalmology & Visual Science, 46, pp. 4189–4199, 2005.
[2] Cohn NA, Emelianov SY, Lubinski MA, O'Donnell M: An Elasticity Microscope .1. Methods. IEEE Trans. on Ultras. Ferro. and Freq. Cntrl, 44, pp. 1304–1319, 1997.

* *indicates Presenter*

054 **PULSE WAVE IMAGING FOR ARTERIAL STIFFNESS MEASUREMENT IN NORMAL AND PATHOLOGICAL HUMAN ARTERIES *IN VIVO*.**

Ronny X. Li[1], Jianwen Luo[1], Sandhya K. Balaram[2], Farooq A. Chaudhry[2], John C. Lantis[2], Elisa E. Konofagou[1].*

[1]Columbia University, New York, NY, USA; [2]St. Luke's–Roosevelt Hospital Center, New York, NY, USA.

Background: Arterial stiffening has been identified as an independent predictor of numerous cardiovascular risk conditions [1] such as hypertension, abdominal aortic aneurysm (AAA) and atherosclerosis. The Pulse Wave Velocity (PWV) has been recognized as a significant and independent index for quantification of arterial stiffness [2]. In addition to its velocity, the pulse wave's nature of propagation (duration, uniformity, reflections, etc.) may also reveal valuable mechanical properties of the arterial wall. Pulse Wave Imaging (PWI) has previously been developed by our group [3] as a reliable, accurate and noninvasive ultrasound imaging–based method to measure the regional velocity of the pulse wave and map its spatial–temporal propagation over the imaged segment.

Aims: The primary aim of this study was to compare the PWI results in the aortas of healthy subjects, hypertensive patients and patients with AAAs. A secondary aim of this study was to evaluate the feasibility of PWI in the carotid arteries of healthy subjects.

Methods: The descending abdominal aortas of 20 healthy volunteers, 20 hypertensive patients and 9 AAA patients were scanned with a Sonix RP (Ultrasonix, Burnaby, Canada) using a 3.3MHz curved linear array transducer. Some patients were excluded from the study due to poor echographic imaging. In addition, the common carotid arteries of 5 healthy volunteers were scanned with a SonixTOUCH (Ultrasonix, Burnaby, Canada) using a 10MHz linear array transducer. In all acquisitions, the RF signals were sampled at 20MHz. For processing, a fast normalized cross–correlation technique [4] was used to compute axial inter–frame velocities in the arterial walls. The anterior wall velocities were plotted over time to generate spatio–temporal profiles of pulse wave propagation. From these profiles, the PWV was estimated through linear regression of the position vs. time relationship of the foot of the pulse wave.

Results: The PWVs in the aortas of healthy volunteers were found to vary between 4.5–7m/s, lower than in most hypertensive subjects (5–12m/s). However, the linear fit correlations in hypertensive subjects were much lower than those in healthy volunteers suggesting non–uniform mechanical properties in hypertensive cases. The highly non–uniform nature of the pulse wave in AAA patients rendered it difficult to confidently estimate a single PWV value. However, the AAA spatio–temporal profiles revealed that in the saccular region of the aneurysm, wall velocities decreased (indicating elevated stiffness), and the pulse wave duration decreased significantly. The average PWVs in the carotid arteries of healthy, young human subjects were found to be on the order of 4–5m/s with very high correlation of the linear regression.

Conclusions: PWI provides a noninvasive means to accurately and reliably quantify stiffness in human aortas and carotid arteries *in vivo* using a clinical system which may have a widespread impact on the detection and diagnosis of cardiovascular disease. A trade–off between high spatial resolution (required to accurately segment the anterior wall) and high frame rate (required to confidently estimate PWV) was identified. Future work will focus on the development and implementation of methods to optimize PWI.

Acknowledgements: The authors would like to thank Debbie Kim and Danny Pudpud (St. Luke's–Roosevelt Hospital Center) for their help in scanning patients. This work was supported in part by NIH Grant R01HL098830.

References:

[1] Mitchell, G. F.: Arterial Stiffness and Wave Reflection: Biomarkers of Cardiovascular Risk. Artery Research, 3(2), pp. 56–64, 2009.

[2] Mookerjee, A., Al–Jumaily, A.M., and Lowe, A.: Arterial Pulse Wave Velocity Measurement: Different Techniques, Similar Results–Implications for Medical Devices. Biomechanics and Modeling in Mechanobiology, 9(6), pp. 773–81, 2010.

[3] Fujikura, K., Luo, J., Gamarnik, V., Pernot, M., Fukumoto, R., Tilson, M.D., et al.: A Novel Noninvasive Technique for Pulse–Wave Imaging and Characterization of Clinically–Significant Vascular Mechanical Properties *In Vivo*. Ultrasonic Imaging, 29(3), pp. 137–54, 2007.

[4] Luo, J., and Konofagou, E.: A Fast Normalized Cross–Correlation Calculation Method for Motion Estimation. IEEE Transactions on Ultrasonics, Ferroelectrics and Frequency Control, 57(6), pp. 1347–57, 2010.

058 **ANALYSIS OF PLAQUE CHARACTERISTICS USING ULTRASOUND, STRAIN AND PHOTOACOUSTIC IMAGING.**

Arman A. Satari[1], Iulia M. Graf[1], Stanislav Y. Emelianov[1].*
[1]Biomedical Engineering Department, University of Texas at Austin, 107 W. Dean Keeton Street, Austin, TX, 78712, USA.

Background: Plaque vulnerability is dependent on morphology, variation in strain rate and tissue composition [1].

Aims: An integrated system of non–invasive imaging combining ultrasound (US) with strain rate (SR) and spectroscopic photoacoustic (SPA) imaging modalities can more accurately assess cardiovascular risk by analyzing multiple arterial properties correlated to the severity of atherosclerosis.

Methods: A system integrating US, SR and SPA imaging was studied *ex vivo* on freshly excised human coronary atherosclerotic arteries. A 20MHz linear array transducer combined with a Vevo 2100 (Visualsonics, Toronto, Canada) US system was used for all imaging modalities. US images were acquired at 50Hz frame rate, covering a volume of 21mm axial, 23mm lateral, 20mm longitudinal, with 0.09mm and 0.15mm lateral and longitudinal resolution, respectively. To derive SR, blood flow of 50cm/s from a fluid pump induced an arterial pulsation of 2Hz. The radio frequency (RF) data was acquired at 210Hz frame rate, covering a volume of 21mm axial, 11mm lateral, 20mm longitudinal, with 0.09mm and 1mm lateral and longitudinal resolution, respectively. SPA imaging was performed by irradiating the artery with a laser beam in the wavelength ranges of 750–850nm and 1210–1230nm (fluence of 15mJ/cm^2 and a 5ns pulse length). SPA images were acquired at 2Hz frame rate and the scanned volume and image resolutions were equal to the US acquisition settings.
Following image acquisition, the RF data sets were imported and processed in Matlab (The MathWorks, Inc., MA, USA). US images were used for volume segmentation and characterization of arterial morphology (Figure 1a). SR rate was derived from RF data by using cross–correlation method (0.10mm×0.24mm×10ms kernel sizes) for both cross–sectional and longitudinal data sets. For SPA imaging analysis, multi–wavelength algorithms were used to assess lipid concentration of the artery in the spectroscopic range of 1210–1230nm where the maximum optical absorption of lipids exists (Figure 1c). US, SR and SPA images were compiled in Amira (Visage Imaging, Inc., CA, USA) to form 3–D renderings of a 20mm longitudinal section of the artery (Figure 1).

Results: US images reflect the morphological changes, assisting identification of plaque formation (i.e., degree of stenosis) (Figure 1a). SR images show variation in arterial stiffness with regions of low distensibility being associated with advanced atherosclerosis (Figure 1b) [2]. The imaged sample presents an average SR of 3.1±0.2%/s and a maximum SR value of 9.5%/s. SPA images indicate the tissue composition (Figure 1c). In the illustrated sample the lipid accumulation within the arterial wall was 12%.

Conclusions: The study demonstrates the feasibility of a non–invasive imaging system for the simultaneous assessment of 3–D arterial morphology, variation in elasticity, and lipid concentration for future vascular studies.

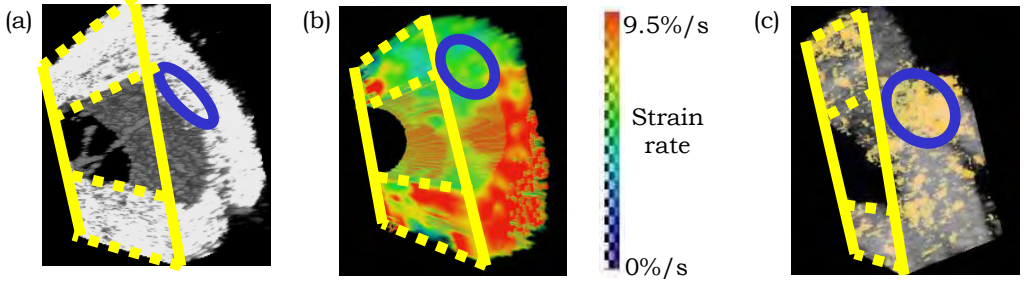

Figure 1: Imaging of atherosclerotic coronary artery: (a) US 3–D image (fibrotic region encircled); (b) SR 3–D image (region with lowest strain rate encircled); (c) SPA 3–D image (lipid dense region encircled).

Acknowledgements: Funding provided by a University of Texas Undergraduate Research Fellowship

References:

[1] I.M. Graf, et al.: Staging Atherosclerosis using Ultrasound, Strain and Photoacoustic Imaging. Proc. IEEE Ultrasonics Symposium, San Diego, 2010.
[2] P.J. Brands, et al.: A Radio Frequency Domain Complex Cross–Correlation Model to Estimate Blood Flow Velocity and Tissue Motion by Means of Ultrasound. Medicine & Biology, Vol. 23, pp. 911–920, February 17, 1997.

* *indicates Presenter*

061 **MULTIMODALITY IMAGE REGISTRATION OF PROSTATE ARFI IMAGES TO MR AND HISTOLOGY DATA.**

Christina Hsu[1], Matthew Davenport[2], Rajan Gupta[2], Thomas Polascik[3], Rebecca Varley[4], Evan Kulbacki[4], John Madden[4], Mark L. Palmeri[1], Kathryn R. Nightingale[1].*

[1]Biomedical Engineering Department, Duke University, Durham, NC, USA; [2]Radiology Department, [3]Urology Division, Surgery Department, [4]Pathology Department, Duke University Medical Center, Durham, NC, USA.

Background: Acoustic Radiation Force Impulse (ARFI) imaging [1–4] is undergoing evaluation to determine its utility in guiding needle biopsy and focal therapy of prostate cancer (PCa). In our previous *ex vivo* studies, we have demonstrated correlation of structures and regions of pathology between ARFI images and histology. In our previously reported *in vivo* feasibility study, challenges were identified in determining the correlation between the *in vivo* ARFI images and the *ex vivo* histology slides due to poor sampling and alignment challenges.

Aims: This study's goal is to correlate *in vivo* ARFI, conventional B–mode ultrasound and MR images with *ex vivo* whole mount histology data. The co–localization of pathology across modalities will facilitate ARFI image interpretation and the evaluation of its utility for guiding prostate needle biopsy and focal therapy.

Methods: Currently, ARFI data from ten patients have been acquired under an ongoing IRB–approved study. Preoperative, dedicated prostate MR images were acquired using standard T1– and T2–weighted sequences in combination with newer DCE and DWI techniques. *In vivo* 3D ARFI and B–mode ultrasound images were obtained immediately preceding radical prostatectomy. Following surgery, the excised specimens were fixed in formalin for 48 hours, whole mount sectioned and processed and then digitized.

Image manipulation was required to register the data from the different modalities due to dissimilar acquisition protocols (position, resolution, etc.). Images from all modalities were segmented into different components (e.g., prostate volume, verumontanum, rectal wall, etc.) using ITK–SNAP (Philadelphia, PA) [5]. The segmented images were used to form a 3D mesh model of the prostate using Hypermesh (Altair Engineering, Troy, MI). The node and element information generated in the segmented 3D model was next extrapolated into a 3D image matrix of equivalent size for all modalities using MATLAB (Mathworks 2010a, Natick, MA). The subsequent non–rigid registration of the different 3D models was performed using the ANTs (Advanced Normalization Tools, Philadelphia, PA) package implemented with a cross–correlation metric [6]. The registered images were then evaluated for co–localization of pathology in all modalities.

Results: The registration methodology was able to successfully align the images from the different modalities and localize the confirmed pathology in the ultrasound B–mode and ARFI images as well as the MR datasets. The 3D models of the prostate demonstrate tissue deformation and dissimilar orientation between the multimodality acquisitions due to changes in patient orientation and different forms of prostate compression. The registration between histology and ARFI enables more precise localization of confirmed pathology in the ARFI data. Further, the registration between histology and MR images confirm radiologist identified pathology in the MR data.

Conclusions: The registration of the multimodality data simplified image comparison and analysis and suggested that ARFI holds promise for providing targeted image guidance of prostate focal therapy and needle biopsy. In the future, it will be necessary to improve both the field of view and ARFI penetration depth to fully capture the prostate volume with this imaging method.

Acknowledgements: The authors would like to thank Alexandra Badea, Liang Zhai and Stephen Rosenzweig for their help with this project. This work is supported by NIH R01CA142824.

References:

[1] K. Nightingale, M.S. Soo, R. Nightingale, et al.: Ultrasound in Medicine and Biology, 28, pp. 227–235, 2002.
[2] B. Fahey, K. Nightingale, D. Stutz, et al.: Ultrasound in Medicine and Biology, 30 (3), pp. 321–328, 2004.
[3] L. Zhai, J. Madden, W.C. Foo, et al.: Ultrasound Med. Biol., 36 (4), pp. 576–588, 2010.
[4] L. Zhai, J. Madden, W.C. Foo, et al.: Ultrasonic Imaging, in press.
[5] P.A. Yushkevich, J. Piven, H. Hazlett, et al.: Neuroimage, 31(3), pp. 1116–28, Jul 1, 2006.
[6] http://www.picsl.upenn.edu/ANTS.

065 **INVESTIGATING THE INFLUENCE OF IMAGING PARAMETERS AND TISSUE HETEROGENEITIES ON STIFFNESS RECONSTRUCTION FOR ENDORECTAL MRE.**

A Arani[1,2], DB Plewes[1,2], R Chopra[1,2].*

[1]Imaging Research, Sunnybrook Research Institute, Toronto, Ontario, CANADA; [2]Medical Biophysics Department, University of Toronto, Toronto, Ontario, CANADA.

Background: The feasibility of dynamic intracavitary magnetic resonance elastography (MRE) to produce stiffness maps of the prostate gland has previously been investigated using both endorectal and transurethral approaches [1,2]. The unique cylindrical shear wave geometry produced with intracavitary approaches is something that needs investigation in order to optimize this technique for practice.

Aims: To simulate the propagation of shear waves produced in endorectal MRE (eMRE) and to investigate the impact that the Signal–to–Noise Ratio (SNR) and tissue heterogeneity have on identifying prostate tumors.

Methods: A coupled harmonic oscillator (CHO) model, first described by Braun et al. [3], was implemented and customized to simulate shear waves generated with an endorectal actuator and travelling through the prostate gland (Figure 1B). The simulated phantom consisted of an endorectal coil surrounded by a rectal wall (6mm thick), a uniform prostate region, a 5mm diameter inclusion and a surrounding of muscular tissue (Figure 1A). The stiffness values of the muscle, rectal wall, prostate and inclusion were set to 12.2kPa [4], 2.9kPa, 3.3kPa [5] and 6.9kPa, respectively. Wave images were simulated using a matrix size of 128x128, a field of view of 14cm, an oscillation frequency of 200Hz and a circular 2.5cm diameter driving force mimicking a vibrating endorectal actuator or MR receiver coil. Shear wave amplitudes were attenuated at 0.34 $Np \cdot cm^{-1}$ to match *in vivo* canine results obtained at the same frequency [4]. Gaussian distributed noise was added to the wave images to give SNR values ranging from 1–40. The SNR was defined as the maximum displacement amplitude (actuator surface) divided by standard deviation of the noise floor. Stiffness maps were produced from the wave images using a previously described local frequency estimation (LFE) inversion algorithm [5] (Figure 1C). Regions of interest were drawn within the prostate region of the phantom and the inclusion, and the mean and standard deviation of the stiffness estimates were calculated for each SNR value.

Results: The shear modulus measurements in the prostate and inclusion regions were calculated as a function of SNR and plotted in Figure 1D. With SNR values ≥15, simulations showed that a 5mm inclusion could be distinguished from the background. Considering shear wave attenuation, the SNR within the inclusion was approximately 1.5. These results suggest that a displacement uncertainty of 1μm would require shear wave amplitudes ≥1.5μm in the region of interest to identify a 5mm inclusion. For the eMRE geometry a displacement of ≥15μm at the rectal wall, which is experimental feasible, would be required to achieve these results.

Conclusions: A working mechanical model producing wave patterns commonly observed experimentally with eMRE was successfully implemented. Simulations suggest that 5mm inclusions can be resolved with eMRE while using experimentally feasible parameters, which motivates further research in this area.

Acknowledgements: Arvin Arani was supported by the Natural Sciences and Engineering Research Council of Canada (NSERC), and this study was funded by the Canadian Institutes of Health Research (CIHR).

References:

[1] Arani A, Plewes D, Krieger A, Chopra R.: Magn Reson Med., In Press, 2011.
[2] Chopra R, Arani A, Huang Y, et al.: Magn Reson Med., 62, pp. 665–671, 2009.
[3] Braun J, Buntkowsky G, Bernarding J, Tolxdorff T, Sack I.: Magn Reson Imaging, 19, pp. 703–713, 2001.
[4] Ringleb S, Bensamoun S, Chen Q, Manduca A, An K, Ehman R.: J. Magn. Reson. Imaging, 25, pp. 301–309, 2007.
[5] Kemper J, Sinkus R, Lorenzen J, Nolte-Ernsting C, Stork A, Adam G.: Rofo., 176(8), pp. 1094–1099, 2004.
[6] Arani A, Plewes D, Chopra R.: Magn Reson Med, 65, pp. 340–349, 2011.
[7] Zhao F, Arani A, Plewes DB, Chopra R: ISMRM, 2010.

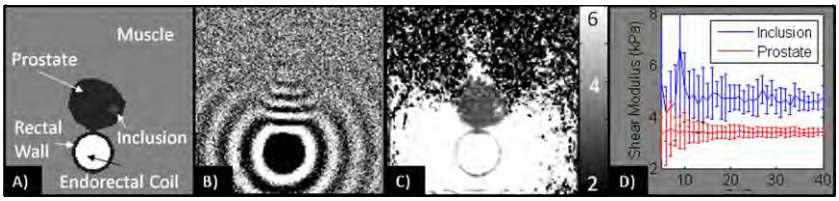

Figure 1: A) Simulated stiffness matrix of eMRE. B) Simulated wave image from CHO method, with an SNR of 15. C) Corresponding stiffness map produced by LFE algorithm. D) Mean shear modulus measurements of the prostate and inclusion regions of the phantom, where the errorbars are the standard deviation of the mean.

* *indicates Presenter*

071 **CORRELATION OF MECHANICAL BRAIN PROPERTIES ASSESSED WITH MAGNETIC RESONANCE ELASTOGRAPHY WITH HISTOPATHOLOGY IN A MOUSE MODEL OF MULTIPLE SCLEROSIS.**

K. Schregel[1,3], E. Wuerfel[2], P. Garteiser[3], D. Petersen[1], J. Wuerfel[1] and R. Sinkus[3].*
[1]Institute of Neuroradiology, [2]Pediatrics Department, University Luebeck, Luebeck, GERMANY; [3]INSERM UMR 773, CRB3, Centre de Recherches Biomédicales Bichat–Beaujon, Paris, FRANCE.

Background: Magnetic Resonance Elastography (MRE) non–invasively visualizes and quantifies biomechanical tissue properties. Recent preliminary clinical studies, e.g., in multiple sclerosis (MS), revealed a high sensitivity of MRE in detecting occult brain parenchymal damage [1]. However, it is still unclear how these viscoelastic properties translate into cellular and molecular conditions. In a mouse model of reversible toxic demyelination, we assessed the influence of various aspects of neuroinflammation longitudinally, e.g., demyelination, cellular infiltration, astrogliosis and extra–cellular matrix alterations.

Methods: Transient demyelination was induced in two groups comprising 30 female C57BL/6 mice having a diet enriched with 0.2% Cuprizone (CPZ). After nine weeks, one group returned to normal chow allowing for remyelination; the other group continued with the CPZ diet. Both groups were compared to age– and sex–matched healthy controls. In each mouse, full 3D–MRE with an isotropic image resolution of 300µm and highly resolving T2–weighted anatomical imaging were performed every three weeks. For MRE, mechanical waves at 1000Hz were transmitted into the mouse brain [2]. Mean values and standard deviation of the complex–valued shear modulus (G*=Gd+iGl) in regions of interest (ROI) covering the corpus callosum (CC) were calculated and analyzed on reconstructed maps. After each scanning session, 2–3 mice of each cohort were sacrificed for extensive histological analysis.

Results: Viscoelasticity in the CC increased continuously during adolescence, related to ongoing brain maturation. This development was reciprocal to the age–dependent viscoelasticity reduction reported at senescence [3] (Figure A). In the CPZ cohort, this development was reversed and resulted in a significant decrease at week 12, corresponding with demyelination in myelin–stainings (Figures E,F). In T2–weighted images, the CC became increasingly isointense in CPZ mice, corresponding to developing demyelination (Figure C). Astrogliosis and accumulation of macrophages/microglia in the CC of CPZ mice started after week 3 of treatment, peaked at week 9 (Figures D,E) and declined at week 12. In conventional histological stainings (H&E, alcian blue), we detected a progressive degradation of the extracellular matrix and parenchymal spongiosis peaking at week 12 (data not shown). When returning one group to normal chow at week 9, CC remyelination occurred, accompanied by partial recovery of the viscoelasticity (Figures A,B).

Interpretation: MRE is sensitive to the degree of myelination under physiological conditions. CPZ treatment resulted in a significant decrease of viscoelasticity correlating with progressive demyelination and degradation of the extracellular matrix. The activation of macrophages/microglia and astrogliosis started early during the CPZ treatment at time points when a significant impact on viscoelasticity was not yet detectable. However, when a subgroup of animals returned to normal chow, remyelination could be closely monitored *in vivo* by a recuperation of the viscoelastic properties.

Figure A: Viscoelasticity of the CC increased during adolescence, reaching a maximum at week 9. CPZ treatment decreased viscoelasticity significantly (week 9 and 12). Mice halting CPZ diet recovered partially.

Figure B: Examplary G* maps of a treated mouse (top) and a control at week 12 (bottom).

Figure C: In T2–weighted images, CPZ diet causes isointensity of the CC (arrows) with partial recovery due to remyelination when omitting the treatment (week 12, lower right panel).

Figure D: CPZ diet induced strong astrogliosis in the CC (arrowheads) peaking at week 9 (GFAP staining).

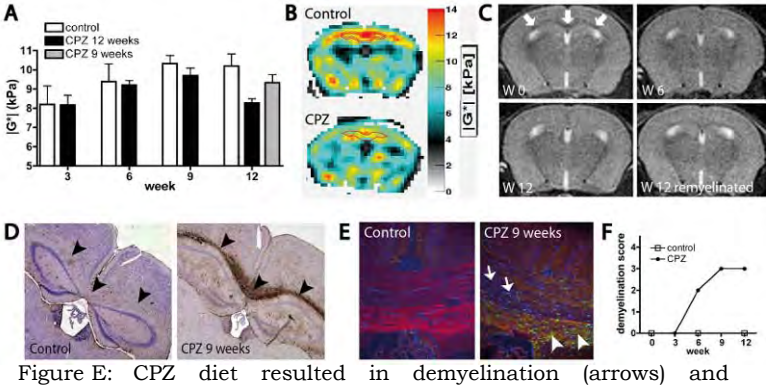

Figure E: CPZ diet resulted in demyelination (arrows) and accumulation of activated macrophages/microglia (arrowheads) in the CC (immunofluorescence: red: fluoromyelin → myelin; green: IBA-1 → macrophages/ microglia; blue: Hoechst → cell nuclei).

Figure F: Demyelination in CPZ–treated mice was initially detectable at week 6 and reached a maximum at week 9.

References:

[1] Wuerfel et al.: Neuroimage, 2010.
[2] Schregel et al.: Proc. ISMRM, 2010.
[3] Sack et al.: Neuroimage, 2009.

* *indicates Presenter*

101 **WHEN PUSH COMES TO SHOVE (OR SHEAR), WHERE ARE WE AFTER TEN YEARS OF FURTHER DEVELOPMENT?**

Jeffrey C. Bamber[1,2]*.
[1]Joint Department of Physics, Institute of Cancer Research and Royal Marsden NHS Foundation Trust, Sutton, Surrey, England, UK; [2]CRUK–EPSRC Cancer Imaging Centre, Institute of Cancer Research and Royal Marsden NHS Foundation Trust, Sutton, Surrey, England, UK.

Background: Although the beginnings of ultrasound elastography can be traced to when ultrasound itself was still in its infancy, substantial technical progress only began during the 1990s, with the development of methods such as quasistatic strain, shear wave speed and acoustic radiation force impulse and vibration imaging. Nevertheless, the techniques remained largely the province of the small number of researchers who were developing the methods and their medical colleagues. Following the first of the annual International Tissue Elasticity Conferences™ (ITEC), research effort began to accelerate, leading to an explosion of methods, medical applications, commercially available systems and biomechanical properties that may be imaged.

Aims: This tutorial aims to review the technical progress that has occurred in the field of ultrasound tissue elasticity imaging during the period 2001–2011, the ten years that ITEC is celebrating, with the intention of evaluating the status of the field, its achievements and its potential for continued technical development. The intention is to complement the accompanying tutorial in this session, in which the current and potential clinical applications of the various elastographic methods are explored.

Methods: Use was made of the ITEC Proceedings books as well as other literature, to identify both key moments of progress as well as the steady build–up of knowledge and expertise in specific areas. Attention is drawn to the complementary nature of many of the different elastographic technologies, particularly in relation to the biomechanical properties of tissues that they are each most suited to evaluate, their different physical performance properties, the artefacts with which they are associated, their limitations and the different body sites and diseases for which they are suitable.

Results: A classification scheme for the various elastographic methods was arrived at, as described in Figure 1. The four characteristics illustrated were chosen to classify the methods because they determine the final capabilities and limitations of each elastographic technique, particularly the biomechanical properties and organs and diseases that may be easily imaged.

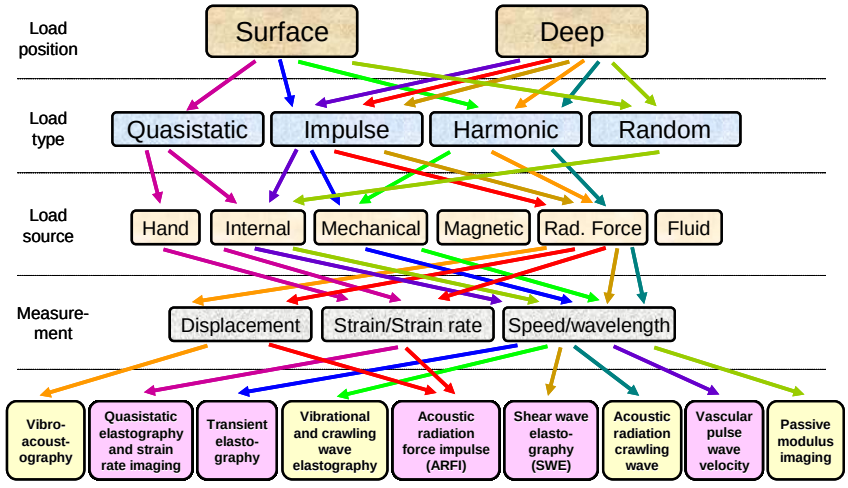

Figure 1: An approach to classifying techniques in elastography. The bottom row lists selected elastography methods according to their commonly used names, with methods that have resulted in commercial systems highlighted in pink. (Apologies are offered to those whose favorite technique is missing; there was insufficient space to include all methods or all names for similar methods.) The path to each method taken by the color–coded sequence of arrows identifies the class of elastographic technique according to four system characteristics: 1) the tissue deformation property that is measured by echo–ultrasound, 2) the source of the load, 3) the temporal nature of the load, and 4) the position of the load.

Conclusions: The choices made by system developers have resulted in elastographic methods that are often complementary in terms of biomechanical properties and clinical utility. All have substantial potential for further development, particularly for improving image quality, reduction of user dependence and other sources of variation and the measurement of a wider range of mechanical properties of normal and diseased tissues.

Acknowledgements: I should like to take this opportunity to thank to all the colleagues and friends whose effort over the years has made this field so exciting, productive and enjoyable.

094 **BIOLOGICAL FOUNDATIONS AND CLINICAL APPLICATIONS OF SOFT TISSUE ELASTICITY IMAGING.**

Mark L. Palmeri[1].*
[1]Duke University, Durham, NC, USA.

Background: Elasticity imaging has been a research interest for the past 20 years with the goal of generating novel images of soft tissues based on their material properties (i.e., stiffness and viscosity). Many soft tissues can have poor contrast in traditional imaging modalities (e.g., ultrasound and magnetic resonance imaging), but these tissues may have very different mechanical properties that can be used to clearly visualize normal anatomy and delineate diseased tissues and masses. Recently, elasticity imaging techniques have moved from the laboratory to the clinical setting, where clinicians are beginning to characterize tissue stiffness as a diagnostic metric, and commercial implementations of elasticity imaging are beginning to appear on the market.

Aims: This tutorial will provide an overview of the clinical foundations for elasticity imaging, including a description of the microanatomy of healthy and diseased tissues and the pathophysiology of disease processes associated with changes in tissue stiffness. The tissue models assumed in elasticity imaging will be outlined in the content of this microanatomy, ranging from simple linear, isotropic, elastic models to nonlinear, anisotropic, viscoelastic models. Current clinical applications of elasticity imaging will be reviewed, including applications in the breast, thyroid, heart, vasculature, brain, uterus, cervix and liver. The clinical niches for magnetic resonance and ultrasonic elasticity imaging approaches will be discussed, as will the role of both static and dynamic elasticity imaging modalities. Commercial realizations of several elasticity imaging technologies will be compared and contrasted, and the current successes, limitations and future directions of elasticity imaging in the clinical setting will also be discussed during this tutorial.

019 **OPTIMAL DAMPER DESIGN FOR STATIC ELASTOGRAPHY.**

T. Sato[1], Y. Watanabe[1] and H. Sekimoto[1].*
[1]Faculty of Engineering, Tokyo Metropolitan University, 1–1 Minami Osawa, Hachioji, Tokyo, 192–0397 JAPAN.

Background: In static elastography, an effective method of improving the nonuniformity of the stress applied by the shape of a transducer head is to insert a damper between the tissue being analyzed and the transducer head. We previously demonstrated the effectiveness of inserting a damper through computer simulations of structural and acoustic analyses [1], however, the design optimization was not investigated.

Aims: This study aims to discover the appropriate conditions for the damper thickness and the Young's modulus. It also aims to demonstrate the effectiveness of a plano–concave damper.

Methods: As Figure 1 shows, a three–dimensional convex–shaped tissue model was designed for assessing the effectiveness of inserting a damper. The shape of the transducer face was assumed to be a plane. The convex–shaped tissue, mimicking the human breast, had a curved surface with a 10cm radius and 3cm height. The convex tissue had a Young's modulus of 10kPa and a Poisson's ratio of 0.49. The transducer and the tissue had a common center axis, and a steady–state compression was executed. By assuming axial symmetry, the FEM models, using a FEM software (Ansys ED 9.0 2005), were built using quarter models, and the tissue bottom was assumed to be attached to a rigid bone. The dampers were given a fixed thickness of 3mm and various Young's moduli of from 1kPa to 10^{11}kPa. To assess the effects of damper thickness, the dampers were given a fixed Young's modulus of 10kPa and thicknesses of from 1 to 10mm. The plano–concave damper which has a concave face that has been designed to perfectly fit the convex curve of the tissue surface, and a plane face that is fitted to the plane transducer is designed. It had a Young's modulus of 10, 100 and 1000kPa and a common thickness (3mm directly above the tissue top, 33mm directly above the tissue edge). The Poisson's ratio of 0.49 was used for all damper conditions. A "flatness" index, which is the ratio of the axial strain directly under the edge of the transducer to the strain directly under the center of the transducer at the same depth, was defined in this study.

Results: The results of the FEM simulations are shown in Figures 2–4. As an approximate trend, the softer and the thicker the damper, the higher the flatness value (Figures 2 and 3). The simulation results for the plano–concave damper are shown in Figure 4. The higher the Young's modulus, the better the flatness value. The flatness curve for 1000kPa in particular has values close to 1, thus, the differences to the value of 1 are minimum throughout the depth range. This is regarded as the best result among all the flatness curves discussed in this study.

Conclusions: The improvements of the strain flatness in this study would help to simplify the tissue elasticity reconstructions in static elastography.

Reference:

[1] T. Sato, S. Sato, Y. Watanabe, S. Goka, H. Sekimoto: Development of an Estimation Method for Damper Design in Static Elastography. Japan. J. Appl. Phys., Vol. 49, 07HF30, 2010.

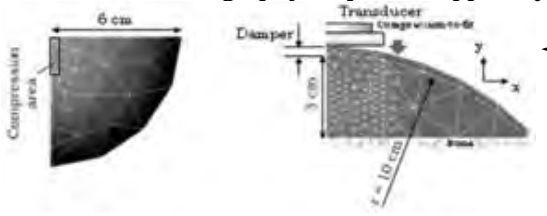

(a) Top View (b) Side View

Figure 1: Simulation model of convex tissue (quarter model).

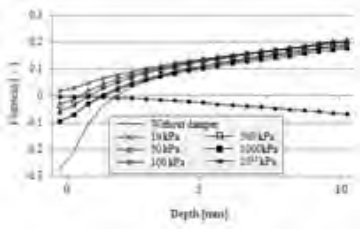

Figure 2: Flatness distribution in convex tissue. (Parameter: Young's modulus, Thickness=3mm constant)

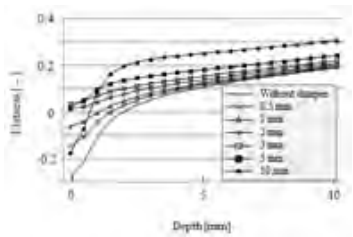

Figure 3: Flatness distribution in convex tissue. (Parameter: Thickness, Young's modulus=10kPa constant)

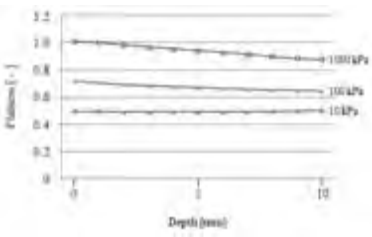

Figure 4: Flatness distribution with plano–concave damper.

* *indicates Presenter*

002 **SHEAR WAVE ELASTOGRAPHY APPLIED TO ABDOMINAL AND RETROPERITONEAL ULTRASOUND EXAMINATION – INITIAL EXPERIENCE.**

RZ Slapa[1], WS Jakubowski[1], AA Kasperlik–Zaluska[2], A Piwowonski[3], RK Mlosek[1], KT Szopinski[1].*
[1]Diagnostic Imaging Department, Medical University of Warsaw, Warsaw, POLAND; [2]Endocrinology Department, Center for Postgraduate Medical Education, Warsaw, POLAND; [3]Diagnostic and Research Medical Centre, Walbrzych, POLAND.

Background: The new generation of elasticity imaging called supersonic shear wave elastography (SSWE) has already been introduced to imaging of superficial organs as breast and thyroid with high frequency linear probes [1–3]. This type of elastography does not require the compression of the tissues during the elasticity examination and may be applied with lower frequency convex probes for examination of deep laying organs and tissues in abdomen and retroperitoneum.

Aims: The purpose of the study was to evaluate the feasibility of assessment of elasticity of adrenal masses and liver parenchyma and masses with SSWE performed during abdominal sonographic examination.

Methods: We evaluated with ultrasound 17 consecutive patients with adrenal and/or liver masses including evaluation of liver parenchyma in 3 patients after chemotherapy. The B–mode ultrasound revealed 16 adrenal masses that were examined with SSWE quantitatively, using the Aixplorer™ (Supersonic Imagine, Inc., France) with a convex abdominal transducer. Five liver masses were similarly evaluated with shear wave elastography. SSWE included evaluation of liver parenchyma in 3 patients after chemotherapy and 4 controls. The final diagnosis was based on contrast enhanced ultrasound, CT, MRI, follow–up, biochemical studies and pathology examination.

Results: Final diagnoses of the adrenal lesions were: 1 myelolipoma, 7 hyperplastic nodules, 5 adenomas, 3 cysts. In 1 patient with a small left adrenal nodule, ultrasound did not show the lesion. Final diagnoses of the liver lesions were: 2 cases of metastases, 1 focal nodular hyperplasia, 1 haemangiomna, 1 benign lesion. All the solid adrenal lesions showed the elasticity map. The adrenal myelolipoma was stiffer than the adenomas and hyperplastic nodules. The adrenal cysts (some not obvious on B–mode imaging) did not show elasticity signal, as shear waves do not propagate through liquids. Stiffness of the liver haemangioma was medium. The breast cancer metastasis was partly very stiff and partly soft. Other liver lesions were soft. The liver parenchyma of the patients after chemotherapy was stiffer than in controls.

Conclusions: (1) This preliminary report based on small number of cases indicates that SSWE with convex ultrasound probe is a feasible technique that can be performed during ultrasound of abdominal cavity and retroperitoneal space. (2) SSWE shows some potential for differential characterization of adrenal and liver masses. (3) SSWE indicates the liquid content of adrenal cystic lesions, even those that do not present simple cyst features on B–mode ultrasound. (4) SSWE indicates the increased stiffness of liver parenchyma in patients after chemotherapy. (5) Further large–scale studies evaluating the full advantage of application of SSWE for abdominal and retroperitoneal ultrasound are warranted.

Acknowledgements: Supported by the Ministry of Science and Higher Education of Poland grant Nr N N402 481239 in years 2010–2013.

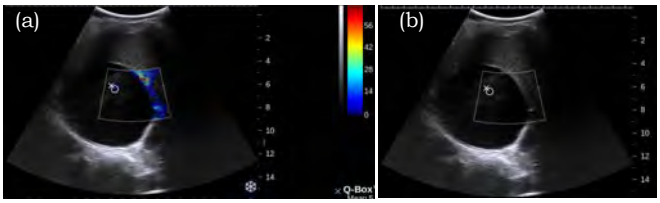

Figure 1 Large recurrent cyst of the right adrenal gland with elasticity imaging (a) and B–mode ultrasound (b). Cyst does not show elasticity signal as shear waves do not propagate through liquids. Some denser material inside the cyst shows soft elasticity signal of 5 kPa.

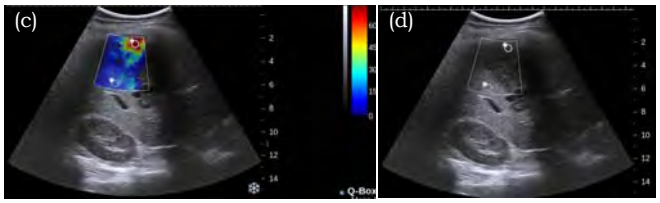

Figure 2 Hypoechoic large metastasis of invasive ductal carcinoma of the breast is visible in the liver (d). Part of the metastasis is very stiff on SWE (110kPa) with softer parts at the periphery. As breast ductal carcinomas are very stiff, the stiffness of the metastases could resemble the stiffness of primary lesion. Note the change of echo of the liver parenchyma on B–mode with slightly increased stiffness of 16kPa on SSWE in the patient after chemotherapy.

References:

[1] Bercoff J, et al.: Supersonic Shear Imaging: A New Technique for Soft Tissue Elasticity Mapping. IEEE Transactions on Ultrasonics, Ferroelectrics and Frequency Control, 51, pp. 396–409, 2004.
[2] Evans A, et al.: Quantitative Shear Wave Ultrasound Elastography: Initial Experience in Solid Breast Masses. Breast Cancer Res., 12, R104, 2010.
[3] Sebag F, et al.: Shear Wave Elastography: A New Ultrasound Imaging Mode for Differential Diagnosis of Benign and Malignant Thyroid Nodules. J Clin Endocrinol Metab, 95, pp. 5281–5288, 2010.

023 **ROTATION PARAMETERS AND THE STRAIN OF LEFT VENTRICLE WITH NEW COMPUTATIONAL MODEL USING TAGGED MAGNETIC RESONANCE IMAGING.**

Mohammed. D. Alenezy[1].*
[1]Dammam University, Dammam, SAUDI ARABIA.

Background: During systole, the apex rotates clockwise, and the base rotates counter–clockwise as viewed from the base while both of them experience the deformation. This twist motion between the apex and base results in torsion in the LV wall tissues. At the midventricle of a healthy heart, on the other hand, the rotational motion is negligible, and the cardiac motion is dominated by the deformation that causes the radial and circumferential strains in the tissue. During diastole (systole), moreover, the LV wall at the midventricle experiences its smallest (largest) thickness. Without detailed information on the material property of the tissues, it is very difficult to develop a comprehensive mathematical model to simulate such a complicated LV wall motion. To simplify the problem, we considered only the two-dimensional motion, radial deformation and rotation, on a cross–section (short axis plane) of LV that is perpendicular to the long axis of LV.

Aims: The goal of this study is to apply a new computational model to quantitatively describe the LV wall motion of the heart using tagged MRI (tMRI) data from the short axis view of rat and human hearts.

Methods: It has been shown [1] that the following model is effective in describing the deformation of LV in its midventricle, apex and base. In this study, this model is used to calculate different biomechanical parameters of LV, such as strain, strain rate, torsion and torsion velocity. From the original equation of motion for this model:

$$x'=(1-\alpha^2/r^2)(x\cos\theta - y\sin\theta).$$
$$y'=(1-\alpha^2/r^2)(x\sin\theta + y\cos\theta),\ \theta=\beta/r$$

where α and β are the deformation and the rotation parameter, respectively, that characterize the severity of the deformation and rotation, θ, the rotational angle, and $\vec{r}=(x,y)$ and $\vec{r}'=(x',y')$ be the Cartesian coordinates of a point on the LV wall in the short-axis plane without (at end diastole) and with deformation or/and rotation. The Lagrange Strain tensor can be found using the above equation, and then the strain rate can also be found by taking the derivative of the strain equation. Other biomechanical parameters' equations can easily be derived from the above original motion equation of LV wall motion $\theta(r) = \theta(r)_{apex} - \theta(r)_{base}$ is twist angle between apex and base of the LV at any given point, r. Note that the rotational angle of the apex (θ_{apex}) and of the base (θ_{base}) are defined by positive and negative angles, respectively. To test our model, we used short axis images of the apex and base of the LV from rat and human hearts during the cardiac cycle.

Results: An example of the application of our new model on the rat and human apex is shown in Figure 1; Figures 2 and 3 show the LV torsion (τ) and strain of the human and rat heart based on our provide any biomechanical parameter of LV at any given point on the LV wall using one set of tagged MRI data obtained during a full cardiac cycle.

Conclusions: Our computational model is capable of accurately describing the dynamics of deformation and rotation motion of the LV of heart. In addition, by using this model, any regional or global biomechanical parameter of the LV can be calculated by deriving the equation of this parameter using our original equation of LV wall motion. Furthermore, we found that the calculation of the twist angle based on this model is sensitive to small rotations of the apex and base at different locations of the LV wall. This model provides another dimension in the study of the twist motion of heart using tagged MRI data. Our current efforts are focused on applying this model on diseased rat and human hearts.

Reference:

[1] Alrefae T, Smirnova I.V, Cook L.T, Bilgen M: A Model–Based Time Reversal of Left Ventricular Motion Improves Cardiac Motion Analysis using Tagged MRI Data. Biomed. Eng. Online, 7:15, 2008.

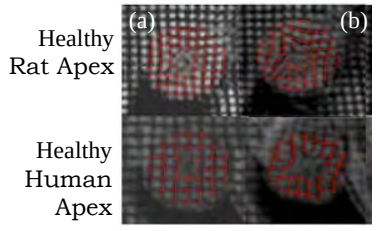

Figure 1: Application of the new computational model on the LV of rat and human at the apex at (a) end systole and (b) at end diastole

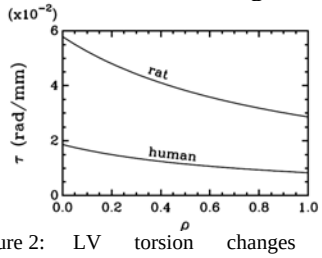

Figure 2: LV torsion changes from endocardium to epicardium of rat and human LV.

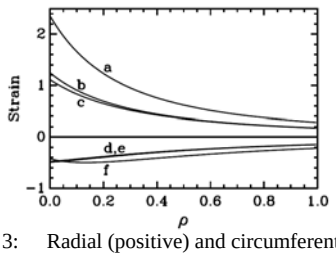

Figure 3: Radial (positive) and circumferential (negative) strain changes from endocardium to epicardium of a diabetic rat (a, f), a healthy rat (b, d) and a human (c, e) LV.

* *indicates Presenter*

025 **A METHOD FOR IMPROVING DIRECTIVITY OF ELASTIC SHEAR WAVES USING STRESS DISTRIBUTION HAVING ODD FUNCTION FORM.**

R. Tanaka[1], T. Omura[1], K. Okubo[1], N. Tagawa[1], S. Yagi[2].*
[1]Tokyo Metropolitan University, 6–6 Asahigaoka, Hino, Tokyo, JAPAN; [2]Meisei University, 2–1–1 Hodokubo, Hino, Tokyo, JAPAN.

Background: Recently, elastic shear waves have been used for various medical ultrasound imaging, e.g., the spinal cord and the heart. Especially, the latest real–time elastography systems have a tendency to use share waves, the velocity of which is measured to obtain stiffness of a tumor [1,2]. Generally, when we supply stress in tissue along a certain direction, arising shear waves spread like a cone around the stress direction [3]. This phenomenon is unfavorable for fine imaging.

Aims: In order to properly send elastic shear waves to the region of interest (ROI), we study a method for generating elastic shear waves with high forward directivity. In this study, to simplify the problem, we restrict the propagation space to be two–dimensional, and examine a one–dimensional input stress distribution. We adopt the derivative of the Gaussian function as a stress distribution because of its ease of use and its smoothness characteristics. Such an odd function causes the superposition of two arising stress patterns, which have mutually inverse phases; hence, we expect that the shear waves having high directivity can be generated.

Methods: We examined the directivity of the shear waves generated by the above–mentioned excitation method through numerical evaluations using PZFlex (Weidlinger Associates, Washington, DC), which is a standard FEM code for analysis of ultrasound propagation. In the simulations, we stretched the spatial gap g (m), which is a no stress portion and is placed on the center of the input stress distribution, and varied the time duration of the input stress pulse T (s). The propagation material was modeled as living soft tissue, and the parameters are adjusted as follows: the density is 1000kg/m^2, the velocity of a longitudinal wave is 1500m/s and the velocity of a shear wave is 1m/s. It should be noted that the particle velocity of a longitudinal wave is represented as a gradient of the scalar potential and that of a shear wave is represented as a rotation of the vector potential. Since the rotation of the gradient is zero, we can compute the quantity proportional to the strength of a shear wave by evaluating the rotation of the particle velocity obtained using PZFlex.

Results: Figure 1 indicates the quantity of the generated shear waves for various g at 90ms after the input stress is applied. From these results, as g is decreased, the directivity becomes high. Figure 2 shows the generation process for various T, and we confirmed that, as T is increased, the directivity becomes high. The top direction in these figures indicates the propagation direction of the shear wave.

Conclusions: From the above results, we know that for small g and long T, the superposition holds properly, and the high directivity is actualized. In the future, we are going to expand these two–dimensional results into the three–dimensional problem including two–dimensional excitation system.

References:

[1] M. Pernot, et al.: Dynamic and Quantitative Assessment of Myocardial Stiffness using Shear Wave Imaging. IEEE Int. Conf. Biomedical Imaging: From Nano to Macro, pp. 976–979, 2010.
[2] R. Yokoyama et al.: Experimental Evaluation of the High–Speed Motion Vector Measurement by Combining Synthetic Aperture Array Processing with Constrained Least Square Method. Jpn. J. Appl. Phys., pp. 07GJ04–1–3, 2009.
[3] S. Yagi, et al.: Analysis of Transient Shear Wave Generation for Real–Time Elastography. IEEE Ultrasonic Symp., pp. 1356–1359, 2004.

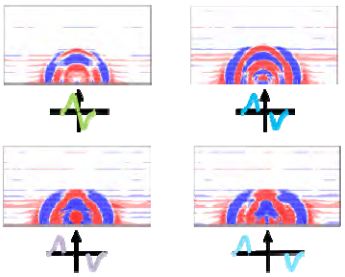

Figure 1: Generated shear wave patterns for various g.

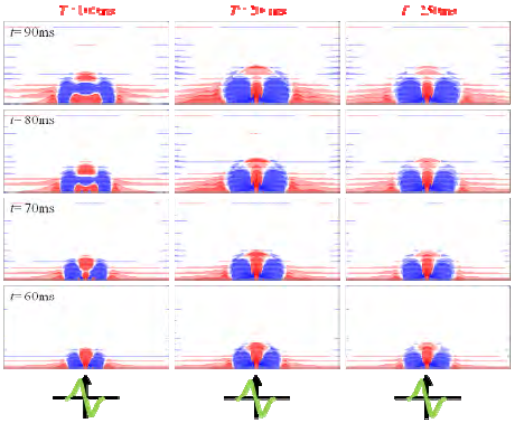

Figure 2: Generation process of shear wave for various T.

* *indicates Presenter*

035 **MEARUING CIRCUMFERENTIAL AND RADIAL COMPONENT OF DISPLACEMENT USING A NON-RIGID REGISTRATION BASED DISPLACEMENT ESTIMATOR**

Shayin Jing[1], Michael S. Richards[1], Marvin M. Doyley[1].*
[1]Electrical and Computer Engineering Department, University of Rochester, Rochester, NY, USA.

Background: Intravascular ultrasound elastography is emerging as an imaging modality that can visualize the radial strain distribution within vascular tissues — new diagnostic information that cardiologists may use to detect rupture prone atherosclerotic plaques [1]. Since plaques typically rupture in areas where the circumferential stress is high [2,3], it should prove useful to develop methods to measure both the radial and circumferential component of displacement.

Aims: To investigate the feasibility of developing elastographic methods for visualizing the circumferential strain within vascular tissue using a single–element-rotating catheter.

Methods: Elastography imaging was performed on homogeneous and heterogeneous vessel phantoms using a commercially available intravascular ultrasound scanner (ILAB™, Boston Scientific) that was equipped with a 40 MHz rotating element catheter. The phantoms were pressurized using dynamic pressurization system (peak to peak 20 mmHg, 1Hz) during elastographic imaging. We developed a non–rigid image registration based method to obtain both radial and circumferential displacements, based on which radial and circumferential strain elastograms were computed. Since we are using a single element rotating transducer, non–uniform rotation distortion (NURD) exists that will induce additional circumferential motion [4]. The magnitude of NURD is dependent on the catheter position; in this study the magnitude of the non–uniform distortion was estimated to be ±1–2° from the angular location. To make the method feasible when NURD exists, an incompressibility constraint was introduced in the image registration method procedure. Phantom studies were performed to investigate the feasibility of the method.

Results: Figure 1 shows representative examples of radial and circumferential strain images obtained from a homogeneous vessel phantom. Figure 2 shows representative examples of radial and circumferential strain images obtained from a heterogeneous phantom that contained a soft plaque.

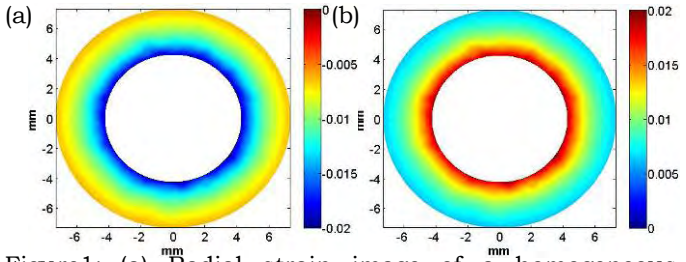

Figure1: (a) Radial strain image of a homogeneous phantom; (b) Circumferential strain of a homogeneous phantom.

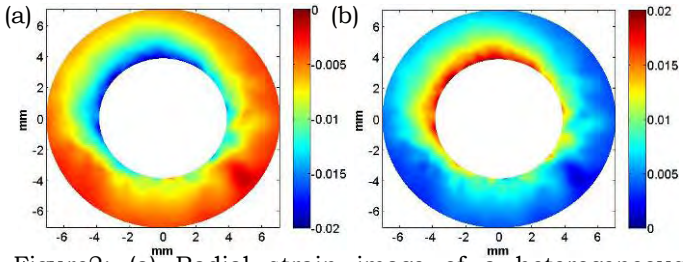

Figure2: (a) Radial strain image of a heterogeneous phantom; (b) Circumferential strain of a heterogeneous phantom.

Conclusions: The result of this preliminary investigation suggests that circumferential strain images can be computed using a registration based displacement estimator with a commercially available IVUS imaging system.

Acknowledgements: Work is funded part by the National Heart and Lungs Research grant R01 HL088523.

References:

[1] Johannes A. Schaar, Chris L. de Korte, et al.: Characterizing Vulnerable Plaque Feature with Intravascular Elastography. Circulation, 108, pp. 2636–2641, 2003.
[2] Richardson, P.D., Davies, M.J., et al.: Influence of Plaque Configuration and Stress Distribution on Fissuring of Coronary Atherosclerotic Plaques. Lancet, 2, 8669, pp. 941–944, 1989.
[3] Schroeder, A.P. and Falk E.: Vulnerable and Dangerous Coronary Plaques. Atherosclerosis, 118 Suppl., pp. S141–149, 1995.
[4] Kimura, B.J., Bhargava, V., et al.: Distortion of Intravascular Ultrasound Images Because of Nonuniform Angular Velocity of Mechanical–Type Transducers. Am Heart J, 132, 2, Pt 1, pp. 328–336, 1996.

* *indicates Presenter*

057 **TOWARDS MICRO–ELASTOGRAPHY FOR STUDYING THE INTERACTION BETWEEN MATRIX STIFFNESS AND CELL BEHAVIOUR.**

Eli Elyas[1,2], Janine Erler[3], Simon Robinson[2], Thomas Cox[3], Jeffrey Bamber[1,2].*

[1]Joint Department of Physics and [2]CRUK and EPSRC Cancer Imaging Centre, The Institute of Cancer Research and The Royal Marsden NHS Foundation Trust, Downs Road, Sutton Surrey, England, UK; [3]Cell and Molecular Biology, The Institute of Cancer Research, 237 Fulham Road, London, England, UK.

Background: The extension of elastography to the microscopic scale is expected to provide invaluable information on soft tissue mechanobiology by facilitating hitherto impossible experiments to study the relationship between local variations in extracellular matrix (ECM) stiffness and cellular behaviour. The areas of mechanobiology that motivate this work include stiffness regulation of adhesion to the ECM, resistance to apoptosis, lineage commitment, differentiation state, motility, morphology and proliferation. We are working towards the provision of a tool for *in vitro* and *in vivo* experiments, using optical coherence tomography (OCT) to create micro–elastograms with an intended resolution better than 25μm.

Aims: This presentation reports early progress towards constructing an elastic microscope.

Methods: Our proposed experimental method differs from previous OCT elastography studies [1] in that, although we continue to employ our previously used multi–focal swept–source OCT microscope (VivoSight®, Michelson Diagnostics, Orpington, UK) to generate images for optical speckle tracking [2, 3], a vibrating needle inserted into the sample [4] is used to generate shear waves that propagate laterally across the imaged field. OCT M–mode scans (line rate 10kHz) are then used to track the one–dimensional time–varying speckle motion, due to shear wave–induced displacements of optical scatterers down a single optical line of sight. Eventually, this M–mode line will be scanned to create an elastogram based on shear wave time–of–flight, although, to date, it is the amplitude of the vibrating needle–generated shear waves that has been measured in this way.

Results: At this early stage of the work, results obtained by vibrating gelatine at frequencies in the range of 0.1–1kHz confirm that vibration amplitude decreases as gel stiffness increases, a step towards imaging stiffness. Figure 1 provides an example result where the amplitude of a 500Hz propagating shear wave is shown to depend linearly on the amplitude of the sinusoidal voltage driving the electromagnetic shaker (Type 4810 Mini–shaker, Brüel & Kjær, Nærum, Denmark) used to move the needle. Shear wave amplitudes as low as 4μm were detected using only the amplitude of the OCT backscatter signal (i.e., without extracting its phase [3]). Gelatine stiffening due to water loss by evaporation while the gel sample was held at room temperature for about 15 minutes is clearly apparent.

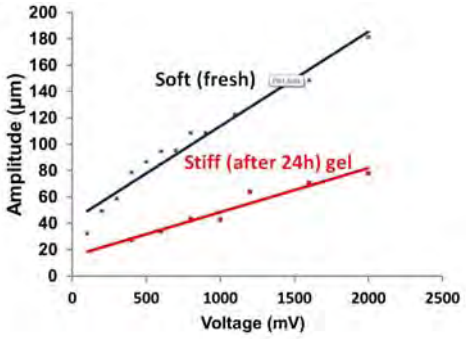

Figure 1: The OCT–measured amplitude of 500Hz shear waves (generated by an embedded vibrating needle) after propagating several millemetres in gelatine, as a function of shear–wave source drive voltage. The linearly elastic character of gelatine is apparent, as is the stiffening of the gel due to water loss by evaporation (lower curve) relative to freshly–made gel (upper curve).

Conclusions: Needle–generated shear waves were detectable, and their amplitudes reliably measurable, after several millimeters of propagation in gelatine, using OCT M–mode tracking. A next step is to image shear wave speed. This technical approach shows promise for the eventual provision of micro–elastography as a research tool in cell biology.

Acknowledgements: Support was received from the Institute of Cancer Research and the CRUK and EPSRC Cancer Imaging Centre, in association with the Department of Health.

References:

[1] Sun C, Standish B, Yang VX: Optical Coherence Elastography: Current Status and Future Applications. J Biom Optics, 16(4),043001, pp. 1–12, 2011.

[2] Grimwood A, Garcia L, Bamber J, Holmes J, Woolliams P, Tomlins P, Pankhurst QA: Elastographic Contrast Generation in Optical Coherence Tomography from a Localized Shear Stress. Phys Med Biol, 55, pp. 5515–5528, 2010.

[3] Grimwood A, Bamber JC, Holmes J, Tomlins P, Pankhurst Q: Nano–Scale Shear Wave Measurements using Optical Coherence Tomography. Proc 9th ITEC, Snowbird, Utah, p. 39, 2010.

[4] Orescanin M, Toohey KS, Insana MF: Quantitative Shear Wave Imaging of Cell Culture Gels. Proc of Int Ultrason Symp, ISBN 978–1–4244–4389–5 IEEE, pp. 483–486, 2009.

063 **INCREASE IN ACCURACY OF DISPLACEMENT MEASUREMENT BY USING SPATIAL RESOLUTION OF BEAM ANGLE: APPLICATION TO LATERAL MODULATION (LM) AND A STEERING ANGLE (ASTA).**

Chikayoshi Sumi[1], Yuuki Takanashi[1], Yousuke Ishii[1], Naoto Yamazaki[1].*
[1]Sophia University, Sophia University, 7–1, Kioicho, Chiyoda–ku, Tokyo 102–8554, JAPAN.

Background: The developments of useful tissue displacement measurement methods increase the applications of displacement/strain measurements (e.g., various blood flow, motions of the heart, liver, etc). Our previously developed combination of the multidimensional autocorrelation method (MAM) and lateral modulation (LM) methods [1,2] or a steering angle (ASTA) method [3] resulted in accurate displacement vector measurements. The lateral Doppler method was also developed for a lateral displacement measurement [3]. Alternatively, we also reported the use of multiple crossed beams (MCB) for a high accuracy displacement vector measurement using accurately measured axial displacements (e.g., [2]).

Aims: In order to increase the accuracy of the displacement vector and lateral displacement measurements using MCB and ASTA (including 0°), a spatial resolution in a beam angle generated is used (referred to as S), i.e., obtainable by calculating the arctangent of ratio of the axial and lateral instantaneous frequencies or the first moments of a local spectra [3]. The no use is referred to as NS.

Methods: The frequency division method (FDM) used in the MAM or 1–dimensional (1D) AM was used together with the multidimensional moving average [2]. For versions of FDM, the spectra is divided using the line passing through a direct current and the center of the spectra with no rotation (NR: FDM1) or rotation (R: FDM2) [3] of echo data using S or NS. The displacements measured are used to obtain the displacement in the beam direction measured or an arbitrary direction. Also, with 1D AM, the local displacement in the beam direction is measured by dividing the local instantaneous phase change by the instantaneous frequency calculated in the beam direction (i.e., R or NR with S or NS). When using S, the 1D AM with MCB but NR equals to MAM with LM. For ASTA, the same lateral Doppler can also be obtained theoretically. The same various synthetic apertures were realized on the same laterally compressed agar phantom [1,2] (a stiff cylindrical inclusion with dia=10mm; relative shear modulus, 3.29). Using FDM3 or the original lateral Doppler, the lateral displacement was also directly measured with setting the lateral coordinate in the dominant deformation direction [3] (echo rotation, 7.7°).

Results: Figure 1 shows the statistics evaluated for the displacement vector magnitude measured using two steered beams (±11.9°) with the most accurate transmission dynamic focusing. With NS, the order of accuracy was, LM>MCB with 1D AM>MCB with FDM. However, the difference in accuracy is the order of micron, and with S, almost the same accuracy as that of LM was achieved by MCB. Alternatively, for ASTA, those of lateral displacement measurements vs a steering angle (4–30°) revealed that FDM and 1D AM yielded almost the same accuracy regardless S or NS (e.g., Figure 1 for 11.9°; and a large steering angle increased all the accuracy). The original Lateral Doppler yielded erroneous measurements (omitted). However, the increment in accuracy obtained by S was significantly amplified by differentiation of the displacement data for elasticity measurements (e.g., Figure 2 for MCB with 1D AM, and ASTA and 0° cases omitted).

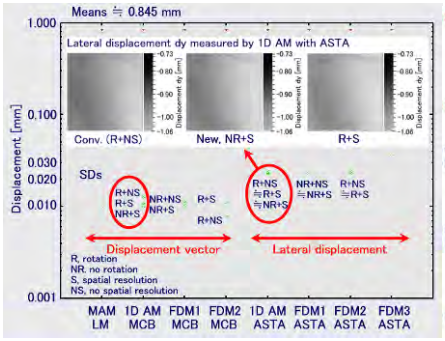

Figure 1: Measurement accuracy.

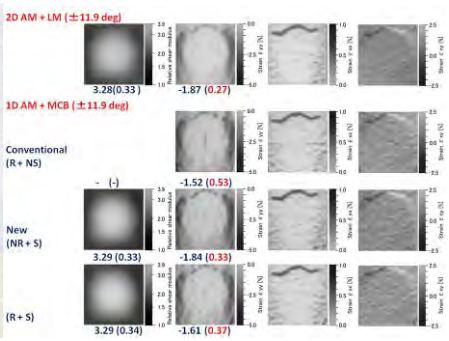

Figure 2: Strains and shear moduli.

Conclusions: The rotation of echo data led to a low accuracy, i.e., the original lateral Doppler and particularly, MCB with FDM2 using the Fourier transform of small local echo data (i.e., R+S in Figure 1). Moreover, all R+S made it impossible to accomplish the measurement in real–time. In this study, the real–time LM and NR+S yielded a high accuracy. Omitted data will also be reported in detail.

References:

[1] C. Sumi, T. Noro, A. Tanuma: IEEE Trans. on UFFC, Vol. 55, pp. 2607–2625, 2008.
[2] C. Sumi: IEEE Trans on UFFC, Vol. 55, pp. 24–43, 2008.
[3] C. Sumi: Reports in Medical Imaging, Vol. 3, pp. 61–81, 2010.

* *indicates Presenter*

069 **ACOUSTIC RADIATION FORCE–BASED NEEDLE VISUALIZATION AND INJECTION MAPPING.**

S Lipman[1], V Rotemberg[1], S Grant[2], D MacLeod[2], KR Nightingale[1], ML Palmeri[1,2].*
[1]Duke University, Durham, NC, USA; [2]Duke University Medical Center, Durham, NC, USA.

Background: Ultrasonic imaging has become increasingly popular in the guidance of regional anesthesia procedures because it provides improvements in visualizing nerves, needle orientation and surrounding anatomy [1]. Difficulties with ultrasound guidance in these areas often result from steep needle insertion angles and spatial offsets between the imaging plane and the needle. In addition, poor acoustic contrast often limits the visualization of distribution of injected anesthetic. Ultrasonic algorithms have not yet been implemented to visualize injected anesthetics and their perineural distribution for more effective and safe nerve blocks with improved pain management [2]. Direct visualization of the needle and objective confirmation of the anesthetic spread will allow regional anesthesiologists to reposition needles during injections to optimize the distribution of the anesthetic around the nerve of interest, reducing the likelihood of nerve block failure.

Aims: The work evaluates the feasibility of Acoustic Radiation Force Impulse (ARFI) imaging to improve needle visualization and the feasibility of a decorrelation metric to generate maps of the injected anesthetics from these needles.

Methods: A three–step segmentation algorithm has been developed to identify a needle in an ARFI image and overlay the needle prediction on a co–registered B–mode image. The steps are: (1) contrast enhancement by median and Laplacian operator filtration, (2) noise suppression through displacement estimate correlation coefficient thresholding and (3) smoothing by removal of outliers and best–fit line prediction [3]. This algorithm was applied to datasets from 18, 21 and 25 gauge needles offset 0–4mm offset in elevation from the transducer imaging plane. For the injection mapping studies, saline injections were performed in a 40 year old male subject at three different anatomic locations: (1) popliteal fossa, (2) supraclavicular brachial plexus and (3) interscalene brachial plexus. Ultrasonic imaging guidance was performed during the injections using a Siemens SONOLINE™ Antares scanner with a VF10–5 linear array operating at 6.7MHz with a focus at 20mm. Raw RF data were captured at a rate of 42fps before, during and after the injections. Regions of decorrelation (correlation coefficients <0.8 persisting for 20% of the elapsed imaging time) were identified and mapped in superimposed colors on the B–mode images. Data acquisition was ECG–triggered to minimize physiologic motion artifacts for nerves adjacent to arterial structures.

Results: Needle tips were visualized within 2mm of their actual position for both horizontal needle orientations up to 1.5mm offset in elevation from the transducer imaging plane and on–axis angled needles between 10°–35° above the horizontal orientation [3]. ARFI–based needle maps subjectively improved needle visualization and needle tip localization. Injection maps were successfully created in tissue–mimicking phantoms, cadaveric specimens and *in vivo* trials. Validation studies in phantoms revealed that injection maps are restricted to the region of infused fluids, except during large boluses where tissues deform to accommodate the new volume of fluid.

Conclusions: We conclude that segmented ARFI images overlaid on matched B–mode images hold promise for improved needle visualization in many clinical applications. Injection visualization using ultrasonic decorrelation algorithms has been successfully performed in several common anatomic nerve block locations. This additional information will complement traditional B–mode images, providing the regional anesthesiologists with additional tools to optimize their anesthetic injections for effective and safe nerve blocks with improved pain management for their patients.

Acknowledgements: This work was supported by NIH grants R01 CA–142824, R01 EB–002132, MSTP training grant T32 GM007171 and the Duke–Coulter Translational Partners Grant Program.

References:

[1] Marhofer P., Greher M., and Kapral L.: Ultrasound Guidance in Regional Anaesthesia., British Journal of Anaesthesia, 94, pp. 7–17, 2005.
[2] Site B.D., Neal J.M. and Chan V.: Ultrasound in Regional Anesthesia: Where Should the Focus Be Set? Regional Anesthesia and Pain Medicine, 54(6), 2009.
[3] Rotemberg et al.: Acoustic Radiation Force Impulse (ARFI) Imaging–Based Needle Visualization. Ultrasonic Imaging, 33, pp. 1–16, 2011.

070 **A FINITE ELEMENT MODEL OF CERVICAL ARFI IMAGING.**

A Homyk[1], TJ Hall[2], H Feltovich[2,3], ML Palmeri[1].*
[1]Duke University, Durham, NC, USA; [2]University of Wisconsin–Madison, Madison, WI, USA; [3]Maternal Fetal Medicine, Intermountain Healthcare, Park City, UT, USA.

Background: Every day, 1,300 children in the U.S. and an additional 34,000 children worldwide are born prematurely [1]. Although many of these children grow up to live fulfilling lives, a large percentage of them suffer from debilitating conditions such as cerebral palsy, physical deformities or, in some cases, infant mortality. A great deal of dedicated research has focused specifically on identifying individual susceptibility to preterm birth events and their prevention.

Early researchers in this field recognized that the softening of the uterine cervix is an indicator of when birth will occur. The "Hegar Sign" was first described in 1895 by Hegar and Reinl as an indicator of cervical softening [2]. This softening has been shown to be linked with micro–structural changes in the collagen orientation in the cervix [3]. As the collagen shifts within the extracellular framework of the cervix, the circumferential stiffness of the myometrium weakens, eventually allowing cervical dilation and childbirth [4]. This softening has been observed visually and qualitatively, but never quantitatively.

Aims: The goal of this research is to develop a Finite Element Method (FEM) model to optimize acoustic radiation force impulse–based (ARFI) shear wave methodology for use in the quantitative evaluation of the stiffness in pregnant women's cervixes [5]. FEM was used in conjunction with the Field II software package to simulate radial ultrasonic pulses generated within the os or central canal of the cervix [6].

Methods: LS–DYNA3D and Altair HyperMesh 10.0 were used in conjunction with Field II to create a 3D quad–symmetric, transversely isotropic, cervical structure based upon laboratory measurements of hysterectomy specimens. The cervix was simulated using three component layers: the perimetrium (25kPa), the myometrium (100kPa) and the endometrium (10kPa). ARFI excitations using a Siemens AcuNav catheter–based array were simulated using Field II at various focal depths within the cervix 3D model. These excitations were evaluated to determine an optimum focal depth for *in vivo* testing based on displacement amplitudes and uniform shear wave front propagation.

Results: Preliminary results for a 17mm radially thick cervix indicate that a focal depth between 8–10mm optimizes the displacement amplitudes and propagating shear wave front (Figure 1). This occurs despite the reduced aperture size at this shallower focal depth. Adequate displacements can be observed down to the distal boundary with a 10mm excitation focus due to the excitation depth of field in this configuration.

Conclusions: Acoustic radiation force–based shear wave imaging could prove to be a valuable quantitative tool for *in vivo* evaluation of pregnancy. These FEM models can be used to optimize the radiation force excitations and shear wave tracking algorithms for clinical studies. Future studies will include a parametric analysis of different degrees of cervical anisotropy and ultrasonic displacement tracking.

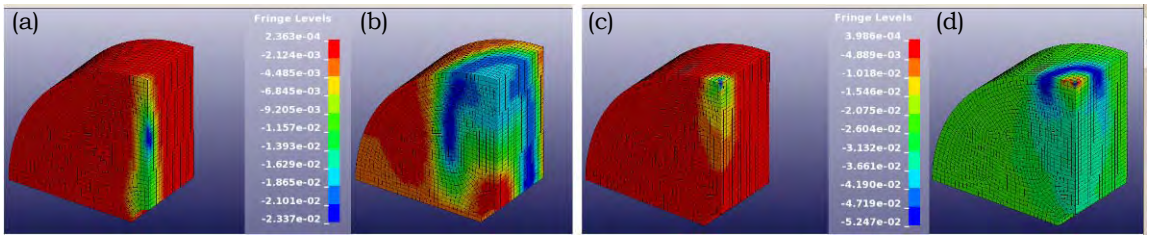

Figure1: The displacement field (mm) resulting from a radiation force excitation focused at 10mm (a) immediately after the excitation and (b) 4.0ms after the excitation in an isotopic cervix (E=10.0kPa). The same displacement fields for a radiation force focused at 17mm, the distal boundary of the cervix from the os, (c) immediately after excitation and (d) 4.0ms after excitation.

References:

[1] Beck S, et al.: The Worldwide Incidence of Preterm Birth. Bull World Health Organ, 88(1). pp. 1–80, 2010.
[2] A. Hegar: Deutsche Medizinische Wochenschrift, Berlin, 21 (35), pp. 565–567, 1895.
[3] Maul H, et al.: Cervical Ripening. Clin Obstet Gynecol, 49(3), pp. 551–563, 2006.
[4] Munoz–de–Toro M et al.: Collagen Remodeling During Cervical Ripening Is a Key Event for Successful Vaginal Delivery. Braz. J. Morphol. Sci., 20(2), pp. 75–84, 2003.
[5] M Palmeri et al.: A Finite–Element Method Model of Soft Tissue Response to Impulsive Acoustic Radiation Force. IEEE UFFC, 52(10), pp. 1699–1712, 2005.
[6] J.A. Jensen et al.: Calculation of Pressure Fields from Arbitrarily Shaped, Apodized, and Excited Ultrasound Transducers. IEEE UFFC, 39, pp. 262–267, 1992.

* *indicates Presenter*

075 **SMALL BREAST LESION CLASSIFICATION PERFORMANCE USING THE NORMALIZED AXIAL–SHEAR STRAIN AREA FEATURE.**

AK Thittai[1], JM Yamal[2], J Ophir[1].*

[1]Diagnostic and Interventional Imaging Department, The University of Texas Medical School, Houston, TX, USA; [2]Division of Biostatistics, The University of Texas School of Public Health, Houston, TX, USA.

Background: Breast cancers that are found and confirmed because they are causing symptoms tend to be larger and are more likely to have already spread beyond the breast [1]. Thus early detection and confirmation are of paramount importance. The normalized axial–shear strain area (NASSA) [3: p. 196] feature from the axial–shear strain elastogram (ASSE) has been shown as a feature that can identify the boundary bonding conditions that are indicative of the presence of cancer [2]. Recently, we investigated and reported on the potential of NASSA feature for breast lesion classification into fibroadenomas and cancers [3]. However, no analysis on the effect of lesion size on the results was performed or reported.

Aims: The aim of this work was to investigate the size distribution of the lesions that were part of the previous study and analyze classification performance specifically on small lesions (<10mm diameter).

Methods: We performed an analysis of the lesion size distribution in the data that were part of previously reported observer study [3]. Briefly, the data consisted of *in vivo* digital radiofrequency (RF) data of breast lesions that were originally acquired for evaluating standard axial elastograms. A total of 33 biopsy–proven malignant tumors and 30 fibroadenomas were included in the study that involved 3 observers blinded to the BIRADS® ultrasound scores. The observers outlined the lesions on the sonograms. The ASSE was automatically segmented and color overlaid on the sonogram, and the NASSA feature from ASSE was computed semi–automatically. The lesion size (equivalent diameter in mm) was computed from the sonographic lesion area, obtained from the lesion outlines made by the observers. Receiver operating characteristic (ROC) curves were then generated, but only for the cases involving lesion sizes <1cm (to enable comparison with previously published ROC curves in [3] that involved data from combined small and large lesion sizes). Box–plots were produced for the two different lesion size groups, small and large, from a logistic regression classifier that was built previously [3].

Results: The Histograms in Figure 1 show that size of approximately 38% and 22% of the fibroadenomas and cancers, respectively, were <1cm**.** Further, it was found that NASSA had a perfect classification of the small lesions, both in the training data and in the cross–validation. The box–plots shown in Figure 2 demonstrate that the lesions with a small (<1cm) diameter actually had better classification than the larger lesions (>1cm). In addition, we show example images of lesions <1cm (Figure 3) so that the effectiveness of ASSE used on small lesions could be better appreciated.

Conclusions: These results clearly demonstrate that the ASSE feature can work equally well even on small lesions to improve the standard BIRADS–based breast lesion classification of fibroadenoma and malignant tumors.

Acknowledgements: Data used in this study were acquired previously for projects supported by NIH Program Project grants P01–CA64597 and P01–EB02105–13. The current work was supported by NIH grant R21–CA135580. The authors would also like to thank Dr. Brian Garra and his team at University of Vermont for acquiring the original data that were used in this study.

References:

[1] http://www.cancer.org/Cancer/BreastCancer/MoreInformation/BreastCancerEarlyDetection/breast–cancer–early–detection.

[2] Thitai Kumar A, Krouskop TA, Garra BS and Ophir J: Visualization of Bonding at an Inclusion Boundary using Axial–Shear Strain Elastography: A Feasibility Study. Phys. Med and Biol., 52, pp. 2615–2633, 2007.

[3] Thittai, A.K., Yamal, J, Mobbs, L.M., et al.: Axial–Shear Strain Elastography for Breast Lesion Classification: Further *In Vivo* Results from Retrospective Data. Ultras. Med and Biol., 37 (2), pp. 189–197, 2011.

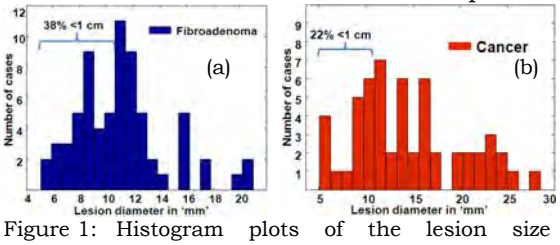

Figure 1: Histogram plots of the lesion size distributions of fibroadenomas (a) and cancers (b) that were part of the observer study reported in [2].

Figure 2: Box–plots of the predicted values from a logistic regression model using NASSA values and the BIRADS scores as predictors. Path 0 and 1 represent fibroadenomas and cancers, respectively.

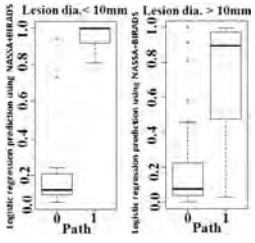

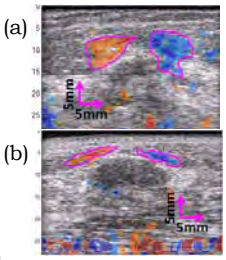

Figure 3: Examples showing the axial–shear strain regions of interest as a color–overlay on corresponding sonograms of a small–sized (a) cancer and (b) fibroadenoma.

Invited Presentation:

099 **CARDIAC ELASTICITY IMAGING – FROM THEORY TO CLINICAL APPLICATIONS.**

Elisa E. Konofagou[1], Wei–Ning Lee[1], Stan Okrasinski[1] and Jean Provost[1].*
[1]Biomedical Engineering Department, Columbia University, New York, NY, USA.

Background: Heart disease is the largest major cause of death of both men and women in the U.S. According to the latest report on Heart Disease and Stroke Statistics, nearly 2,400 Americans die of cardiovascular disease each day, i.e., two Americans per minute [1]. One of the main reasons for this high number of lives lost is the severe lack of an effective diagnostic imaging technique for early detection and localization of the abnormality upon the patient exhibiting a symptom and/or anomaly detected on the electrocardiogram (ECG). The two most widely used imaging techniques in the clinic are CT angiography and echocardiography with limitations in speed of application and reliability, respectively. At the same time, it has been established that the mechanical properties of the myocardium change dramatically as a result of heart disease, both at its onset and beyond. Therefore, ultrasound–based cardiac elasticity imaging methods, such as Doppler Myocardial Imaging [2], Strain Rate Imaging [3], Speckle Tracking [4], etc., have been under development over the past couple of decades and some of them have recently been incorporated in commercial clinical scanners. Those techniques encompass imaging of any kind of mechanical parameter that would reflect the mechanical property of the myocardium during physiologic deformation, such as displacement, strain, strain rate, velocity, shear strain, torsion, shear modulus, etc. Since assessment of the myocardial mechanical parameters has proven to be a critical step in the detection of cardiac abnormalities, cardiac elasticity imaging has the potential of making a significant impact in this field and providing complementary information on the myocardial viability.

Current Studies: Our group's efforts have focused on the methods of Myocardial Elastography [5,6] and Electromechanical Wave Imaging [7,8]. Myocardial Elastography benefits from the development of techniques that can be used for high precision 2D time–shift based strain estimation techniques and high frame rate currently available in ultrasound scanners to obtain a detailed map of the intrinsic transmural strain in normal and pathological cases over different cardiac phases and cycles. In animal studies, Myocardial Elastography has been shown to detect and localize myocardial strain abnormalities resulting from 40% or higher coronary flow reduction. In clinical studies, the strain images obtained were corroborated by MR tagging strains in both normal and pathological subjects while 60% or higher coronary flow reduction was localized and corroborated by CT angiography. Electromechanical Wave Imaging (EWI) has been shown capable of noninvasively mapping the spontaneously occurring conduction wave during propagation across all four cardiac chambers. We identified that high frame rates (>500 fps) and precise 2D imaging of the cardiac deformation is feasible so that the transient cardiac motion resulting from the fast electromechanical wave can be mapped in murine, canine and human hearts *in vivo*. Pacing origins in both sinus rhythm and induced pacing schemes can be reliably identified and high correlation with the electrical activation pattern has also been demonstrated without angle independence. Electrically altered acute ischemic regions have also been localized on EWI images in animal studies and atrial and ventricular arrhythmias have been mapped in the clinic.

Future Prospects: Given that all aforementioned techniques can be easily integrated in standard ultrasound scanners, they stand to have an important impact in the diagnosis and treatment of cardiovascular disease in the near future.

Acknowledgements: Supported in part by NIH R01EB006042, NIH R21HL096094 and the Wallace H. Coulter Foundation.

References:

[1] Lloyd–Jones et al.: Circulation, 119(3), p. e21, 2009.
[2] Sutherland et al.: J Am Soc Echo, 7, p. 441, 1994.
[3] Heimdal et al.: J Am Soc Echo, 11, p. 1013, 1998.
[4] Kaluzynski et al.: IEEE–TUFFC, 48, p. 1111, 2001.
[5] Konofagou et al.: Proc. IEEE Ultrason Symp, p. 1273, 2000.
[6] Lee et al.: IEEE–TUFFC, 54, p. 2233, 2007.
[7] Pernot and Konofagou: Proc. IEEE Ultras. Symp., p. 1091, 2005.
[8] Provost et al.: Proc. Nat. Acad. Sci., 108(21), p. 8565, 2011.

* *indicates Presenter*

045 **ASSESSMENT OF MYOCARDIAL ELASTOGRAPHY PERFORMANCE IN NORMAL AND ISCHEMIC PHANTOMS UNDER PHYSIOLOGIC MOTION CONFIGURATIONS WITH PRELIMINARY *IN VIVO* VALIDATION.**

Stanley J Okrasinski[1], Elisa E Konofagou[1,2].*
[1]Biomedical Engineering and [2]Radiology Departments, Columbia University, New York, NY 10025, USA.

Background: Myocardial Elastography (ME) is a non–invasive, ultrasound based strain imaging modality which can detect and localize early onset of abnormalities in myocardial mechanics. By acquiring radiofrequency (RF) frames at high frame rates, the 2D deformation components of the myocardium can be estimated and used to identify regions of abnormal deformation indicative of ischemia.

Aims: In this study, we pursue assessment of ME in accurately depicting rotation, torsion and combined deformation and rotation using polyacrylamide phantoms and in canines *in vivo*.

Methods: Phantoms of homogeneous stiffness (25kPa) or containing harder inclusions (50kPa) were subjected to 4 motion schemes: rotation, torsion, deformation and a combination of torsion and deformation. The phantoms were imaged using a SonixTouch system (Ultrasonix, Richmond, BC, Canada) with a 7MHz linear array and a frame rate of 187Hz. Inter–frame axial and lateral displacements were estimated using normalized cross–correlation (window size: 7mm, 90% overlap) and were accumulated during each motion scheme. The axial and lateral components were used to estimate the angular displacement, and axial and lateral Lagrangian strains were estimated using a least–squares estimator (kernel size: 14mm). The axial and lateral strains were then converted to radial and circumferential strains following a manual centroid selection. Ultrasound RF frames in the short axis view at basal and apical levels were also acquired using a phased array in an open chest canine *in vivo*. Incremental displacements were accumulated through systole and then converted to angular displacement. Torsion in the canine was estimated by subtracting basal rotation from apical rotation.

Results: In the rotational scheme, the input rotation of 30º and estimated rotation were in excellent agreement in both normal (28±4º) and ischemic (29±6º) cases. In the torsional scheme, the estimated rotation was found to be highest in the plane closest to the motor (25±8º) and lowest in the plane farthest from the motor (7±7º). Unlike the rotational and torsional schemes, in the deformation scheme, if an inclusion was not present, the estimated strain patterns accurately depicted the homogeneity; while in the opposite case, abnormalities were observed which enabled detection of the inclusion. In addition, no significant rotation was detected at the level of the inclusion. In the combined scheme, if an inclusion was not present, the estimated strain patterns accurately depicted homogeneity; while if an inclusion was present, abnormalities were observed which enabled detection of the inclusion. Also, torsion could be decoupled from the combined scheme and imaged separately and was found to be similar to the pure torsion results. In the open chest canine normal heart *in vivo*, twist of 8.4±3.8º was detected, which agrees with previous findings from literature [1].

Conclusions: This study showed feasibility of ME to distinguish between rotation, torsion and deformation in both the decoupled and combined cardiac–mimicking motion schemes. The ME rotation estimates were in excellent agreement with the imposed configurations. The ME torsion estimates were also shown to agree with the input values and were capable of distinguishing it from rotation. The "normal" and "ischemic" phantoms were successfully distinguished based on the ME strain estimates in the deformation scheme and shown to be distinct from the rotation and torsion schemes. The ME estimates of the combined motion schemes also distinguished the normal from the ischemic phantoms and provided estimates consistent with both pure torsion and deformation schemes. Finally, positive preliminary results were obtained in an *in vivo* canine model.

Acknowledgements: Funded in part by NIH–NHLBI R01EB00604 and CTSA KL2RR024157.

References:

[1] MacGowan GA et al.: Cardiovascular Research, Vol. 31, Iss. 6, pp. 917–925, 1996.

031 **DIRECT *IN VIVO* MYOCARDIAL INFARCT VISUALIZATION USING 3D ULTRASOUND AND PASSIVE STRAIN CONTRAST.**

BC Byram[1], DM Gianantonio[1], DP Bradway[1], D Hyun[1], M Jakolvjevic[1], AL Crowley[2], HW Kim[2], M Parker[2], R Kim[2], R Judd[2], GE Trahey[1].*

[1]Duke University, Durham, NC, USA; [2]Duke University Medical Center, Durham, NC, USA.

Background: Previously, methods have been developed to measure active myocardial strain during ventricular contraction [1]. Strain estimates during this period correlate to current heart function but only indirectly and approximately to the underlying efficacy of myocardial tissue. In most clinical scenarios featuring chronic myocardial infarct (MI), there is a mixture of healthy, stunned and infarcted tissue, which to date has not been differentiable using strain induced by ventricular contraction.

Aims: The purpose of this work is to develop and evaluate a method that uses passively induced strain in the ventricles to visualize myocardial infarct.

Methods: Passive strain contrast is induced in the ventricles using atrial contraction. The contraction of the atria occurs immediately prior to the onset of ventricular systole and rapidly injects a bolus of blood into the ventricles. The blood bolus results in a small, rapid increase in ventricular volume, which can be used as a contrast mechanism for ventricular strain imaging. The new approach to myocardial elastography was tested on mongrel canines with chronic MI. Three canines were scanned at volume rates between 80 and 240Hz based on the anatomical constraint of the heart's location. All canine subjects also underwent delayed enhancement contrast MR (deCMR) scans – the gold standard for MI visualization [2]. Data were also acquired on one open–chested canine with direct epicardial contact of the transducer.

Ultrasound data were acquired as 3D volumes at baseband (i.e., IQ) using a 30 receive beams–per–transmit imaging configuration, and a 2.8MHz transmit frequency with an Acuson SC2000 and a 4Z1C matrix array (Siemens Healthcare, Ultrasound Business Unit, Mountain View, CA, USA). The ultrasound data were used to estimate displacements using a new Bayesian speckle tracking algorithm coupled with a quality guidance algorithm similar to that described by Chen et al. [3]. Displacements were used to calculate axial strains, and the full axial strain magnitude was used to construct the ultrasound MI image. All processing was implemented in Matlab (The MathWorks Inc., Natick, MA, USA).

Results: Results from 3 transthoracic scans of mongrel canines are reported. An example result from the largest canine subject is shown below as side by side ultrasound/strain and deCMR images. In the images, the MI is mapped to dark pixels in the ultrasound and bright pixels in the deCMR images. The images show qualitative agreement. Additionally, an open–chested canine subject with an ablation lesion in the right ventricle (modeling an MI) was also scanned and showed contrast of 5.4dB and contrast–to–noise ratio of 7.4dB using the described methods.

Conclusions: The described approach for infarct visualization shows promise, but confidence is mitigated by a small sample population and poor registration between the ultrasound and deCMR results. Additionally, all the subjects had viable atrial contraction, which is likely not true in all damaged hearts. A larger sample size and more sophisticated methods for MR and ultrasound registration are in progress.

Acknowledgements:
NIH Grants 5T32EB001040 and 5R37HL096023.

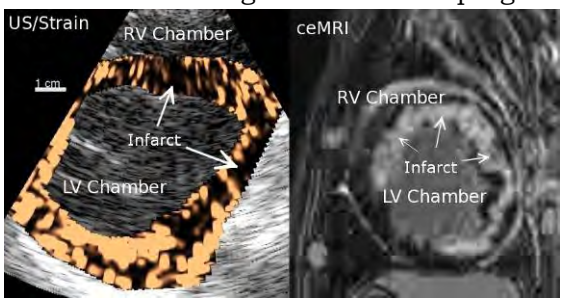

Figure 1

References:

[1] E.E. Konofagou, J. D'Hooge, J. Ophir: Myocardial Elastography – A Feasibility Study *In Vivo*. Ultrasound Med. Biol., Vol., 28, No. 4, pp. 475–482, 2002.

[2] R.J. Kim, D.S. Fieno, T.B. Parrish, K. Harris, E.L. Chen, O. Simonetti, J. Bundy, J.P. Finn, F.J. Klocke, R.M. Judd: Relationship of MRI Delayed Contrast Enhancement to Irreversible Injury Infarct Age and Contractile Function. Circ., Vol. 100, pp. 1992–2002, 1999.

[3] L. Chen, R.J. Housden, G.M. Treece, A.H. Gee, R.W. Prager: A Hybrid Displacement Estimation Method for Ultrasonic Elasticity Imaging. IEEE Trans. Ultrason. Ferroelect., Freq. Contr., Vol., 57, No. 4, pp. 866–882, 2010.

* *indicates Presenter*

032 **CARDIAC ABLATION LESION VISUALIZATION – ARFI AND STRAIN COMPARISON.**

BC Byram[1], DM Dumont[1], SJ Hsu[1], PD Wolf[1], GE Trahey[1].*
[1]Duke University, Durham, NC, USA.

Background: Radio frequency (RF) ablations are a common method for correcting a number of electrophysiological complications in the heart. One of the challenges of ablation procedures is determining the size and location of the ablated region. A solution to this challenge is particularly important when trying to determine whether an aberrant region of electrical conduction has been isolated (or destroyed). Acoustic radiation force impulse (ARFI) imaging has been validated against histology as a method for *in vivo* visualization of ablated tissue [1]. Ablated tissues are also known to exhibit contrast using strain imaging [2].

Aims: The aim of this work is to compare ARFI and strain imaging of cardiac RF ablation lesions.

Methods: ARFI contrast of ablated tissue comes from the differences in stiffness between the healthy tissue and ablated tissue and is highest during diastole. Strain contrast is created by the difference in contraction between the healthy and ablated tissue and is derived between end diastole and end systole.

In order to compare ARFI and strain images, data were acquired from ablation lesions. The ablation lesions were formed on two mongrel dogs with an open–chest preparation. Ablation lesions were formed using an 8 French SteeroCath catheter (Boston Scientific, Natick, MA, USA). When possible ablations were formed on the endocardial layer of the right ventricle, otherwise the lesions were placed epicardially. Ultrasound sequences were created with 8–15Hz ARFI frames with a 2cm lateral field of view (FOV) followed immediately by 125–160Hz B–mode frames with a 4cm lateral FOV. Data were acquired with a 6.67MHz transmit frequency and a receive F/# of 2 using a VF10–5 transducer on a Siemens SONOLINE Antares ultrasound system (Siemens Healthcare, Ultrasound Business Unit, Mountain View, CA, USA). The data were acquired with the transducer fixed against the epicardial heart surface to maintain registration between the ARFI and B–mode sequences. Displacements were estimated for both ARFI and strain data using a new Bayesian speckle tracking algorithm. The ARFI tracking kernel was 1.5λ while the strain image was made using a 3λ tracking kernel and a strain estimation kernel of 10λ by 5 lateral samples at Nyquist.

Since ARFI has been validated successfully against histology [1], it serves as an adequate demarcator of lesion boundaries for the purposes of calculating the contrast and contrast–to–noise ratio (CNR).

Results: An example result of an RF–ablation lesion on the right ventricle is shown in Figure 1. In this example, ARFI images of the ablation lesion have peak contrast during diastole around .74, and a corresponding CNR of 3.6. Strain images produce a peak contrast of 0.52 and a peak CNR of 5.9.

Conclusions: Initial results show that ARFI and strain imaging are roughly comparable in their capacity to visualize cardiac ablation lesions. The method of image formation appears to play a strong role in differences between the two methods. The filtering that occurs during strain image creation appears to smooth the image boosting CNR at the cost of contrast compared to ARFI. Without a clear improvement in image quality ARFI may be a better method of lesion visualization since it is computationally faster.

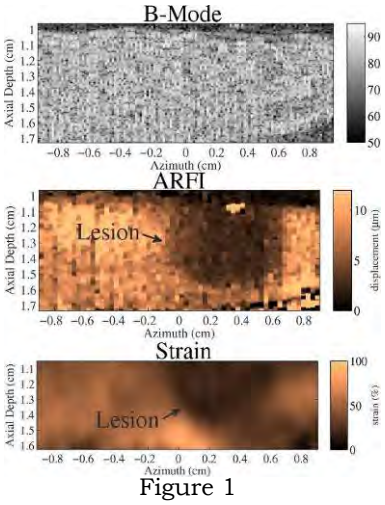

Figure 1

Acknowledgements: NIH Grants 5T32EB001040 and 5R37HL096023.

References:

[1] S.A. Eyerly, S.J. Hsu, S.H. Agashe, G.E. Trahey, Y. Li, P.D. Wolf: An *In Vitro* Assessment of Acoustic Radiation Force Impulse Imaging for Visualizing Cardiac Radiofrequency Ablation Lesions. J. Cardiovasc. Electrophysiol., Vol. 21, No. 5, pp. 557–563, 2010.

[2] T. Varghese, J. Zagzebski, F. Lee: Elastographic Imaging of Thermal Ablation Lesions in the Liver In Vivo Following Radiofrequency Ablation: Preliminary Results. Ultrasound Med. Biol., Vol. 28, pp. 1467–1473, 2002.

049 **SINGLE–HEARTBEAT ELECTROMECHANICAL WAVE IMAGING WITH OPTIMAL STRAIN ESTIMATION USING TEMPORALLY–UNEQUISPACED ACQUISITION SEQUENCES.**

Jean Provost[1], Stéphane Thiébaut[1], Jianwen Luo[1], Elisa E. Konofagou[1].*
[1]Columbia University, New York, NY, USA.

Background: Electromechanical Wave Imaging (EWI) is an entirely non–invasive, ultrasound based imaging method capable of mapping the electromechanical wave (EW) *in vivo*, i.e., the transient deformations occurring in response to the electrical activation of the heart. We have recently demonstrated the close relationship existing between the electromechanical and electrical activations in normal canines and humans [1], indicating that EWI can be used to map the transmural cardiac activation sequence in all four chambers. Achieving the optimal imaging frame rates necessary to capture the EW in a full view of the heart poses a technical challenge due to the limitations of conventional imaging sequences, in which the frame rate is low and tied to the imaging parameters. To achieve higher frame rates, EWI is typically performed in multiple small regions of interest acquired over separate heartbeats which are then combined into one view. Yet, the frame rates achieved remain sub–optimal because they are determined by the imaging parameters rather than being optimized to image the EW. More importantly, the reliance on multiple heartbeats precluded the study from application in non–periodic arrhythmias such as fibrillation.

Aims: In this presentation, we develop a temporally–unequispaced acquisition sequence (TUAS) for which a wide range of frame rates are achievable independently of the imaging parameters, while maintaining a full view of the heart at high beam density. TUAS is first used to determine the optimal frame rate for EWI in a paced canine heart *in vivo*. The feasibility of performing single–heartbeat EWI during ventricular fibrillation is then demonstrated.

Methods: One male mongrel canine was anesthetized before undergoing lateral thoracotomy. After removal of the pericardium, electrodes were sutured on the epicardium to pace the heart and trigger ventricular fibrillation. TUAS was implemented in an Ultrasonix MDP by interweaving RF beams acquired using a 3.3MHz phased array. Axial incremental displacements and strains were estimated at rates ranging from 40–2000Hz in a full view of the heart using RF cross–correlation (window size: 4.6mm, 90% overlap) and a least squares estimator (window size: 6.75mm), respectively. The elastographic signal–to–noise ratio (SNRe) was computed by averaging and calculating the standard deviation of the incremental strains within an axial window of 4.85mm for individual pixels over multiple frames, corresponding to up to 5 heart cycles, after segmenting the heart. Using these measures, the conditional probability density of the SNRe was constructed for 9 different motion–estimation rates and compared to the strain filter.

Results: The incremental strain distribution varied greatly during the heart cycle, and its center achieved a maximum during the EW. The expected value of the SNRe during the EW achieved a maximum at 160 and 350Hz during the entire heart cycle and the EW, respectively. A sharp decrease in SNRe was observed when exceeding 4% incremental strains, suggesting that the motion–estimation rate should be chosen to be sufficiently high to avoid estimating strains above this threshold value. During pacing, the localization of the pacing site and the propagation of the EW were clearly depicted using TUAS. Finally, during fibrillation, i.e., a non–periodic arrhythmia, the strains were estimated in a full view of the heart. Regions of the myocardium were oscillating rapidly from thinning to thickening and thickening to thinning over time.

Conclusions: In this study, we developed a novel temporally unequispaced acquisition sequence to perform single–heartbeat EWI at an optimal motion–estimation rate. In an open–chest setting, EWI in a paced canine heart was found to maximize the expected value of the SNRe when performed at 350Hz. TUAS was shown suitable for depicting the EW during both pacing and ventricular fibrillation, at high spatial resolution, without ECG gating, for the first time. These results indicate the feasibility of the real–time application of single–heartbeat EWI in the clinic for the depiction of both periodic and non–periodic cardiac events.

Acknowledgements: Supported in part by NIH R01EB006042 and R21HL096094.

References:

[1] Provost J., Lee W-N., et al. : Proc. Natl. Acad. Sci. U.S.A., Vol. 108, No. 21, pp. 8565–8570, 2011.

** indicates Presenter*

040 **SHEAR STRAIN ENDOVASCULAR ELASTOGRAPHY: VALIDATION WITH *IN VITRO* DATA**

Younes Majdouline[1], Simon Le Floc'h[2], Damien Garcia[3,4], Marie–Hélène Roy Cardinal[1], Jacques Ohayon[2,5], Guy Cloutier[1,4].*

[1]Laboratory of Biorheology and Medical Ultrasonics, University of Montréal Hospital Research Center (CRCHUM), Montréal, Québec, CANADA; [2]UJF–Grenoble 1, CNRS, Laboratory TIMC–IMAG UMR 5525, DyCTiM Research Team, Grenoble, F–38041, FRANCE; [3]BiomeCardio Laboratory, University of Montréal Hospital Research Center (CRCHUM), Montréal, Québec, CANADA; [4]Radiology Department, Radio–Oncology and Nuclear Medicine, and Institute of Biomedical Engineering, University of Montréal, Montréal, Québec, CANADA; [5]University of Savoie, Polytech Savoie, Le Bourget du Lac, FRANCE.

Background: Endovascular elastography (EVE) was introduced to investigate atherosclerotic coronary artery plaques and to predict their vulnerability to rupture [1]. We previously proposed the Lagrangian Speckle Model Estimator [2] (LSME) based on the optical flow approach to quantify all components of the strain tensor including the shear strain that could be involved in plaque hemorrhage, inflammation and rupture mechanisms [3]. However, the LSME performance to compute the shear strain elastogram (SSE) has never been tested nor validated with real intravascular ultrasound (IVUS) measurements.

Aims: We investigated the potential of the LSME method to quantify the shear strain based on real IVUS phantom data and a new implementation that considers the optical flow in polar coordinates.

Methods: *In vitro* polyvinyl alcohol cryogel (PVA–C) vascular phantom experiments were conducted with IVUS acquisitions to investigate the accuracy of the measured SSE. Shear strain distributions within cross–sections of PVA–C vessels containing one and two soft inclusions were computed from phantom ultrasound RF images [3]. SSE maps estimated with the new implementation of the LSME were compared to real shear strain amplitudes and distributions obtained by performing finite element (FE) simulations with the COMSOL Multiphysics software (Comsol Inc., Grenoble, France).

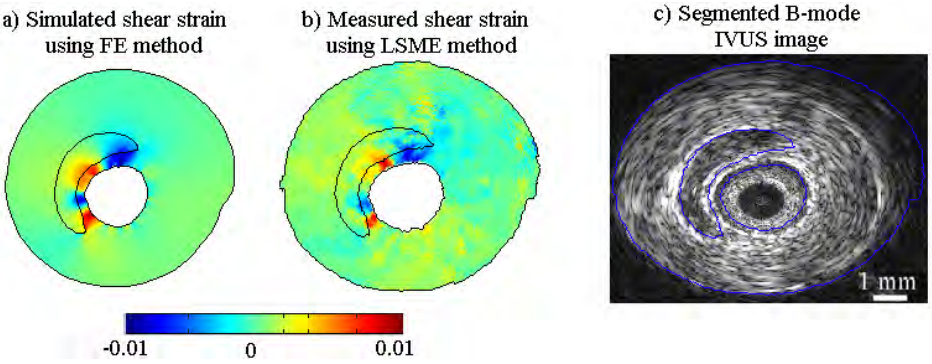

Figure1: a) Simulated (using the FE method) and b) measured (using the LSME method) shear strain elastograms. c) Corresponding segmented reconstructed B–mode IVUS image from RF data used to initiate the FE simulation with known mechanical properties and luminal pressure. The inclusion contour is displayed to make easier qualitative comparisons between the simulated and experimental elastograms, and with the B–mode IVUS frame.

Results: Both simulated and measured elastograms for both the one and two soft inclusion conditions had similar profiles and amplitudes, with high shear strain values located at the level of the mimicked thin fibrous cap (see the example of the one soft inclusion in Figure 1).

Conclusions: This study demonstrated the performance of the new LSME implementation to accurately estimate the shear strain distribution and the feasibility of SSE to highlight atherosclerotic plaque vulnerability characteristics (i.e., high shear strains close to the boundaries of the fibrous cap).

Acknowledgements: This research was supported by a strategic grant of the Natural Sciences and Engineering Research Council of Canada (STPGP–381136–09).

References:

[1] C.L. de Korte et al.: Ultrasound Med. Biol., 23, pp. 735–746, 1997.
[2] R.L. Maurice et al.: J. Acoust. Soc. Am., 116 (2), pp. 1276–1286, 2004.
[3] J.M. U.-King–Im et al.: J. Neurol., 253 (3), pp. 379–381, 2006.
[4] S. Le Floc'h et al.: Phys. Med. Biol., 55, pp. 5701–5721, 2010.

010 **IN VIVO 3D (+t) STRAIN IMAGING AND ELASTOGRAPHY OF THE HUMAN AORTA.**

R.G.P. Lopata[1,2], H.H.G. Hansen[3], E.M.H. Bosboom[2], G.J.L.M. Jongen[1], C.L. de Korte[3], F.N. van de Vosse[1,2].*

[1]Cardiovascular BioMechanics, Biomedical Engineering Department, Eindhoven University of Technology, Eindhoven, THE NETHERLANDS; [2]Biomedical Engineering Department, Maastricht University Medical Center, Maastricht, THE NETHERLANDS; [3]Clinical Physics Lab, Children's Hospital, Radboud University Nijmegen Medical Centre, Nijmegen, THE NETHERLANDS.

Background: Rupture of an abdominal aortic aneurysm (AAA) is the 13th cause of death in the Western world. Currently, only generic measures such as aneurysm size (>5.5cm) and growth rate (>1cm/year) are used to decide on treatment to prevent rupture. Surgical intervention, however, carries substantial risk. Recently, mechanical modelling was applied using finite element methods based on CT images [1]. This promising approach revealed the aneurysm wall stress for a patient–specific geometry. Unfortunately, the material properties in these models are still literature–based thus generic. A less invasive imaging modality is required to monitor aortic wall properties and growth over time. To satisfy both these requirements, 3D (+t) ultrasound is proposed.

Aims: As a first step towards patient–specific modelling, 3D strain imaging and *in vivo* elastography of the abdominal aorta was explored in healthy subjects.

Methods: Three–dimensional radiofrequency (RF) data of the abdominal aorta were acquired during one cardiac cycle using a Philips iE33 ultrasound scanner and an X7–2 matrix array probe in 11 healthy subjects (age=22–47 years). Simultaneously, blood pressure was monitored real–time using a NexFin (BMEYE, NL). Manual segmentation of the aorta was performed by drawing contours, thereby indicating the vessel axis and local radii. The RF data were processed using a 3D coarse–to–fine displacement estimation algorithm [2]. The segmented aorta was tracked over time. Next, the radial (R), circumferential (C) and longitudinal strain (L) were estimated. Furthermore, the compliance, distensibility and Young's modulus were derived from the 4D displacement data. For the Young's modulus, a thin–walled tube geometry was assumed analogous to an MRI study by Van 't Veer et al. [3].

Results: Strains over time in three orthogonal directions were obtained for the aorta within a field of view that spanned 3–6.5cm. The resulting maximum strains had a median value of R=-5.6% (inter–quartile range [IQR] =-8.0 – -4.2%), C=6.5% (IQR=4.1 – 8.4%) and L=1.8% (IQR=1.2 – 2.7%). Results revealed a median compliance per vessel length (m) of 4.5mm^2/kPa (IQR=4.0 – 4.7 mm^2/kPa) and distensibility of 22 1/MPa (IQR=20 – 33 1/MPa). The median Young's modulus was 430kPa (IQR=260–650kPa), which is in accordance with our previous 2D work. The distensibility was found to be significantly larger for the older subjects ($p<0.03$, $\alpha=5\%$), although no significant differences in Young's Modulus were found.

Conclusions: The first results on 3D time–resolved strain imaging and *in vivo* elastography of the abdominal aorta seem promising. The strains that were found and Young's moduli are within the physiological range. This study did have some limitations: the field of view of the transducer is relatively small compared to other modalities, and the brachial blood pressure measured will differ from the actual aortic blood pressure. In the future, the ultrasonic measurement of biomechanical vessel wall properties will enable patient–specific modelling of AAAs. This combination of non–invasive functional imaging and mechanical modelling will allow monitoring of AAAs and will help us to understand AAA growth and possibly prevent rupture. The next step will be to demonstrate feasibility in a patient study.

References:

[1] L. Speelman, F.A.M.V.I. Hellenthal, B. Pulinx, E.M.H. Bosboom, M. Breeuwer, M.R. van Sambeek, F.N. van de Vosse, M.J. Jacobs, WK. Wodzig, G.W.H. Schurink: The Influence of Wall Stress on AAA Growth and Biomarkers. Eur. J. Vasc. Endovasc. Surg., 39(4), pp, 410–416, 2010.

[2] R.G.P. Lopata, M.M. Nillesen, J.M. Thijssen, L. Kapusta, C.L. de Korte: Three–Dimensional Cardiac Strain Imaging in Healthy Children using RF–Data. Ultrasound Med. Biol., 2011 Conditionally accepted.

[3] M. van 't Veer, J. Buth, M.A.G. Merkx, P. Tonino, H. van den Bosch, N.H.J. Pijls, F.N. van de Vosse: Biomechanical Properties of Abdominal Aortic Aneurysms Assessed by Simultaneously Measured Pressure and Volume Changes in Humans. J. Vasc. Surg., 48(6), pp. 1401–1407, 2008.

* *indicates Presenter*

090 **COMPARISON OF MECHANICAL PROPERTIES OF AORTIC ANEURYSMS ASSESSED WITH MRI AND ULTRASOUND ELASTOGRAPHY.**

R.G.P. Lopata[1,2], M.F.J. Peters[1], V.I. Nyugen[3], C.L. de Korte[4], F.N. van de Vosse[1,2], E.M.H. Bosboom[2].*

[1]Cardiovascular BioMechanics, Biomedical Engineering Department, Eindhoven University of Technology, Eindhoven, The NETHERLANDS; [2]Biomedical Engineering Department, Maastricht University Medical Center, Maastricht, The NETHERLANDS; [3]Vascular Surgery Department, Maastricht University Medical Center, Maastricht, The NETHERLANDS; [4]Clinical Physics Laboratory, Children's Hospital, Radboud University Nijmegen Medical Centre, Nijmegen, The NETHERLANDS.

Background: An abdominal aortic aneurysm (AAA) is an asymptomatic, progressive, local dilation of the aorta. If left untreated, an AAA can eventually rupture, leading to a life threatening hemorrhage. In the decision for intervention, AAA diameter and diameter growth are currently the main determinants. However, there are indications that in rupture risk estimation, AAA wall stress has a higher sensitivity and specificity than maximum diameter [1]. Besides, AAA growth does not solely depend on AAA diameter [2]; growth is decreased for AAAs subjected to relatively low wall stresses [3].

AAA wall stress analyses are currently based on CT images, and generic values are used for the mechanical properties of the wall. A more individualized approach could be based on dynamic MRI; as with dynamic MRI, mechanical properties can be determined. Ultrasound elastography could be an economical alternative to assess the mechanical properties in follow–up and screening studies.

Aims: To compare the mechanical properties of the aortic aneurysm assessed from MRI and 2D ultrasound elastography.

Methods: Four patients with an AAA between 4 and 5.5cm were included. ECG triggered 3D BTFE scans were acquired with a 1.5T Philips MRI scanner for the aortic region between the renal and iliac bifurcations. Subsequently, ultrasound RF data of the aorta were acquired with a curved array transducer (f_c=3.5MHz) using a Esaote Mylab70 ultrasound system equipped with an RF interface. Simultaneously, blood pressure was monitored in real–time using a NexFin (BMEYE, NL).

Volumes and volume changes were extracted from the MRI images using dedicated prototype software (Hemodyn, Philips Medical, NL) on a slice to slice basis. Only slices that were in the field of view of the ultrasound acquisition were included. For the ultrasound images, first, the aorta was manually segmented. Next, the RF data were processed using a 2D coarse–to–fine displacement estimation algorithm, and the segmented aorta was tracked over time. Distensibility, *D*, and Young's modulus, *E*, were derived for both MRI and ultrasound from the volume data and the pulse pressures, assuming a thin–walled tube geometry [4].

Results: For MRI distensibility was D=0.9–1.8MPa^{-1}, while for ultrasound D=1.4–2.9MPa^{-1}. Young's modulus assessed from MRI was E=0.7–3.6MPa, while from ultrasound E=0.6–4.2MPa. Differences in Young's moduli between MRI and ultrasound for the four patients were -30%, 16%, -13% and 4%.

Conclusions: Young's moduli assessed with ultrasound elastography were comparable with Young's moduli assessed with MRI, despite assumptions made in either of the analyses. Ultrasound images were 2D, hence axisymmetry of the AAA needed to be assumed. In the analysis of the MRI images, longitudinal displacement of the aorta was not assessed. Further analysis and application in AAA wall stress analysis should reveal the clinical significance of determining individualized material properties.

References:

[1] M.F. Fillinger et al.: *In Vivo* Analysis of Mechanical Wall Stress and Abdominal Aortic Aneurysm Rupture Risk. J. Vasc. Surg., 36(3), pp. 589–597, 2002.

[2] M. Vega de Céniga et al.: Growth Rate and Associated Factors in Small Abdominal Aortic Aneurysms. Eur. J. Vasc. Endovasc. Surg., 31, pp. 231–236, 2006.

[3] L. Speelman et al.: The Influence of Wall Stress on AAA Growth and Biomarkers. Eur. J. Vasc. Endovasc. Surg., 39(4), pp. 410–416, 2010.

[4] M. van 't Veer et al.: Biomechanical Properties of Abdominal Aortic Aneurysms Assessed by Simultaneously Measured Pressure and Volume Changes in Humans. J. Vasc. Surg., 48(6), pp. 1401–1407, 2008.

Invited Presentation:

092 **A MODEL–BASED APPROACH TO QUASI–STATIC, HARMONIC AND TRANSIENT ELASTOGRAPHY.**

Marvin M. Doyley
Hajim School of Engineering and Applied Sciences, University of Rochester, Rochester NY, USA

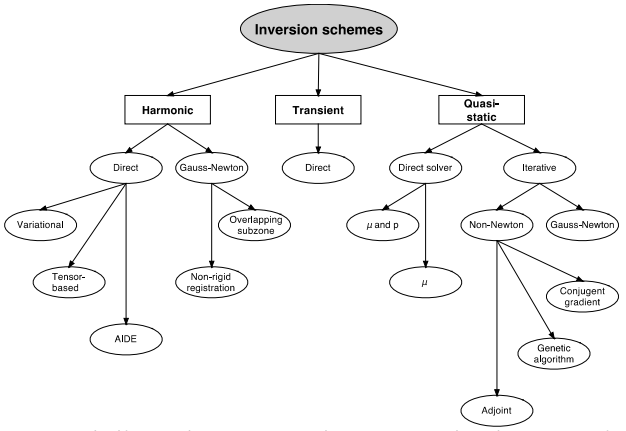

Figure 1: Diagram of proposed approaches to shear modulus estimation for harmonic, transient and quasi–static elastography

Background: Elastography is emerging as an imaging modality that can detect and characterize atherosclerotic plaques, guide minimally invasive therapeutic techniques and improve the differential diagnosis of breast and prostate cancers. Although current approaches to elastography vary considerably, the general principles of elastography can be summarized as follows:

(1) Perturb the tissue using a quasi–static, harmonic or transient mechanical source;
(2) Measure the internal tissue displacements using a suitable ultrasound, magnetic resonance or optical displacement estimation method;
and (3) Infer the mechanical properties from the measured mechanical response, using either a simplified or continuum mechanical model.

Several groups have developed approaches for obtaining approximate estimates of shear modulus with all three approaches to elastography, and, despite their limited accuracy these techniques are fast and robust – traits that make them clinically appealing. For example, Ophir et al.[1] used a simple mechanical model to compute approximate modulus elastograms, but stress concentration and target hardening artifacts compromised the diagnostic quality of the ensuing elastograms. Similarly, Parker et al. [2] computed local estimates of shear modulus from local estimates for wavelength, but the weakness of this approach is that it is difficult to obtain accurate estimates of wavelength in complex structures such as the breast and brain. To overcome these issues, several groups have proposed inversion schemes for computing the mechanical properties within soft tissues. Figure 1 summarizes the inversion schemes that have been proposed for the three different approaches to elastography.

Objective: In this presentation, we will

(a) Review a selection of the inversion schemes for all three areas – quasi–static, harmonic and transient elastography;
(b) Describe practical techniques for transforming the ill–posed problem to a well–posed one;
(c) Describe better test procedures for evaluating the performance of modulus elastograms;
(d) Report the results of pre–clinical studies conducted with simulated and physical phantoms and volunteers;
and (e) Discuss new opportunities for model–based elastography.

Acknowledgements: This work is supported by NIH National Heart and Lungs research grant R01–HL 088523. The author would like to thank Prof. Kevin Parker in the Department of Electrical and Computer Engineering at the University of Rochester for many valuable discussions and comments, and Dr. Jiang Yao in the Department of Mechanical Engineering at the University of Rochester for her useful discussions.

References:

[1] Ophir J, Cespedes I, Ponnekanti H, Yazdi Y and Li X: Elastography: A Quantitative Method for Imaging the Elasticity of Biological Tissues. Ultrason Imaging, 13, pp. 111–34, 1991.
[2] Parker KJ, Huang SR, Musulin RA and Lerner RM: Tissue-Response to Mechanical Vibrations for Sonoelasticity Imaging. Ultrasound in Med. & Biol., 16, pp. 241–6, 1990.

* *indicates Presenter*

060 **A DIRECT VARIATIONAL ALGORITHM FOR SOLUTION OF THE TIME–HARMONIC VISCOELASTIC INVERSE PROBLEM.**

Yixiao Zhang[1], Assad A. Oberai[1], Paul E. Barbone[2], Isaac Harari[3].*
[1]Rensselaer Polytechnic Institute, Troy, NY, USA; [2]Boston University, Boston, MA, USA; [3]Tel Aviv University, Ramat Aviv, ISRAEL.

Background: In dynamic elastography, the viscoelastic parameters, in particular, the complex–valued shear modulus is determined by solving an inverse problem, with the knowledge of the displacement field in the interior of tissue subject to time–harmonic excitation. Due to experimental constraints and measurement limitations several approximations are used to simplify the equations of elasto–dynamics. For example, the displacement vector may be known only in a plane, or only two components of the vector may be known. These approximations lead to simplified mathematical models that include the scalar Helmholtz equation, the anti–plane shear, the plane stress and the plane strain states. In this presentation, we will describe a unified variational approach that solves these problems directly (without iterations) for the shear modulus and makes use of measurements corresponding to multiple excitations in a straightforward manner.

Aims: The aim is to develop a direct, accurate, robust and efficient finite element based method for determining the complex shear modulus of tissue under various approximations leading up to the three–dimensional equations of viscoelasticity.

Methods: We consider the following simplified models of viscoelastic behavior: the scalar Helmholtz equation, anti–plane shear, plane stress and plane strain. In each case, we analyze the problem and determine the boundary data and/or the interior displacement data that would be required to generate a unique solution of the complex–valued shear modulus. In order to solve these problems, we propose a new variational formulation, called the Complex Adjoint Weighted Equations (CAWE) [1]. A simple finite element discretization of this formulation leads to a direct (non–iterative), efficient and robust method for determining the spatial distribution of the shear modulus. We test the performance of the CAWE algorithm for different mathematical models using synthetic and tissue–mimicking phantom data. We utilize a quadratic least-squares filter to smooth noisy measurements, and resort to multiple measurements to reduce the need for boundary data. We compare the shear modulus distributions obtained using CAWE with known distributions for synthetic data and with independent mechanical measurements for phantom data.

Results: We have successfully recovered shear modulus distributions from synthetic and tissue–mimicking phantom data using the CAWE formulation for different mathematical models. Comparison of the results for plane strain with the B–mode image shows that the location of the inclusion is recovered well. The ratio of the shear modulus of the inclusion to the background is also consistent with formulas based on gelatin concentration in the background and the inclusion.

Conclusions: We have developed and implemented an accurate, direct variational algorithm for determining the spatial distribution of the complex–valued shear modulus that is applicable to a wide range of two–dimensional mathematical models. Its extension to three–dimensional, incompressible elasticity models and time–varying displacement measurements is underway.

Acknowledgments: This work has been supported by the NIH through the grant NIH RO1 AG029804. The authors thank J. R. McLaughlin and A. M. Maniatty at Rensselaer Polytechnic Institute for helpful discussions, Kevin J. Parker's team at the University of Rochester and Christopher R. Hazard at GE Global Research for tissue–mimicking phantom data.

References:

[1] Zhang, Y., Oberai, A.A., Barbone, P.E., and Harari, I.: Solution of the Time–Harmonic Viscoelastic Inverse Problem with Interior Data in Two Dimensions. Submitted to Inverse Problems.

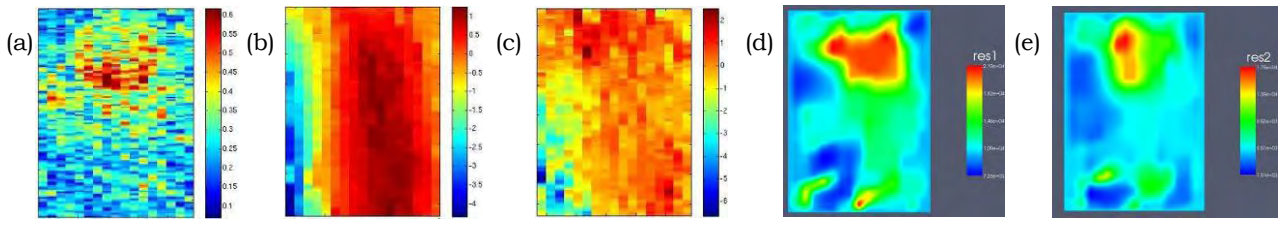

Figure 1: Reconstruction of shear modulus from tissue-mimicking phantom data using CAWE for plane strain. (a) B-mode image; (b)-(c) Real part of the vertical and lateral components of the displacement field; (d)-(e) Reconstruction of the real and imaginary part of the shear modulus.

067 **SPARSITY REGULARIZATION IN DYNAMIC ELASTOGRAPHY.**

M Honarvar[1], R Rohling[1], SE Salcudean[1].*
[1]University of British Columbia, Vancouver, BC, CANADA.

Background: The inverse elasticity problem is often ill–posed due to lack of complete 3D motion vector measurements and measurement noise. Elasticity identification is especially challenging when using a mixed formulation of finite elements for nearly incompressible materials to solve the inverse problem because both elasticity and pressure distributions need to be identified, which increases the number of unknowns [1]. Regularization is typically added to constrain the solution space. For example, Tikhonov regularization is commonly used whereby the low–order spatial derivatives of the solution are penalized, which results in smooth solutions [1]. The parameters of the Tikhonov regularization should be tuned to a given excitation and boundary conditions.

Aims: To determine through simulations whether sparsity regularization [2] can calculate similar quality elasticity maps with less dependency on parameter tuning.

Methods: The original variables are transformed into another set of variables which results in sparse representative of original variables. This provides a good approximation of the original field but with fewer unknowns. In this presentation, we use the discrete cosine transform (DCT) as the sparsifying transform. We solve the dynamic elastography problem using a mixed (displacement–pressure) finite element technique, assuming time harmonic motion and linear, isotropic, elastic behavior for the tissue. A direct FEM inversion is used to solve the inverse problem with sparsity regularization applied on both shear modulus and pressure variables. A 2D region with a plane strain assumption is used to create synthetic input measurements for the mixed FEM. The region has two Gaussian inclusions, and the density and Poisson ratio are 1000kg/m^3 and 0.4995, respectively. The inverse problem was solved for two excitation frequencies: 100Hz and 250Hz. For Tikhonov regularization, the parameters were optimized for 250Hz and kept the same when solving for 100Hz. No parameters were changed for the sparsity regularization for the two frequencies.

Results: Figure 1 shows the elastograms obtained using direct mixed FEM inversion solutions with both Tikhonov and sparsity regularization methods for two different excitation frequencies. At 250Hz, the calculated elasticity maps were similar for the two techniques. At 100Hz, the quality of the elasticity reconstruction is degraded with Tikhonov regularization but is not degraded with sparsity regularization.

Conclusions: Tikhonov regularization is dependent on excitation and boundary conditions, and the regularization parameters need to be adjusted according to those conditions. Sparsity regularization is independent of the boundary conditions, and no readjustment is needed in this method.

Acknowledgements: This research was supported by Natural Sciences and Engineering Research Council (NSERC).

References:

[1] E. Park and A.M. Maniatty: Shear Modulus Reconstruction in Dynamic Elastography: Time Harmonic Case. Phys. Med. Biol., Vol. 51, p. 3697, 2006.
[2] B. Jafarpour, V.K. Goyal, D.B. McLaughlin and W.T. Freeman: Transform–Domain Sparsity Regularization for Inverse Problems in Geosciences. Geophysics, Vol. 74, p. R69, 2009.

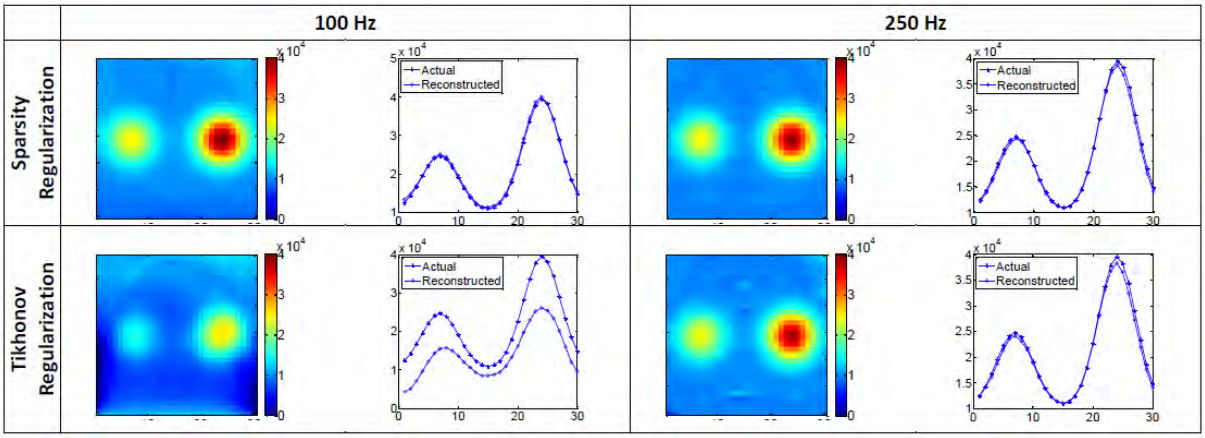

Figure 1: Comparison of Tikhonov and sparsity regularization for inverse FEM: Simulation Results.

* *indicates Presenter*

089 **DATA REQUIREMENTS FOR LINEAR AND NONLINEAR ELASTIC MODULUS RECONSTRUCTION IN TWO AND THREE DIMENSIONS.**

Elizabete Rodrigues Ferreira[1,2], Uri Albocher[3], Isaac Harari[3], Assad Oberai[1], Paul Barbone[4].*
[1]Mechanical Aerospace and Nuclear Engineering Department, Rensselaer Polytechnic Institute, Troy, NY 12180, USA; [2]Université Libre de Bruxelles, Département de Mathématique, C.P. 218/1, 1050 Bruxelles, BELGIUM; [3]Engineering Department, Tel Aviv University, 69978 Ramat Aviv, ISRAEL; [4]Mechanical Engineering, Boston University, Boston, MA 02215, USA.

Background: Our interest is the quantitative reconstruction of the spatial distribution of tissue mechanical properties from *in vivo* ultrasound measured deformation fields. Except in the simplest cases however, tissue mechanical property distributions are not completely determined by an observed deformation field. That is, under identical loading conditions, different material property distributions can give rise to the same deformation pattern. Therefore, some information in addition to an observed deformation must be used for the reconstruction of material properties. That additional information can be in the form of prior information, ad hoc assumptions or additional measurements.

Aims: The aim here is to determine and report on data sets that provide sufficient information to uniquely determine tissue mechanical properties in various cases. The cases considered are 2D plane stress deformation, 2D plane strain deformation, 3D isotropic compressible material, 3D isotropic incompressible material, 3D transversely isotropic material, 2D nonlinear models and 3D poroelastic models.

Methods: We assume we are given measured displacement fields, and that these measured displacement fields satisfy the equilibrium equations in an elastic medium. The precise form of the equilibrium equation depends upon the material model (e.g. linear elastic vs. nonlinear elastic) used, and whether the problem is 2D or 3D. With the displacement fields known, the equilibrium equations thus yield a system of partial differential equations for the material parameters. We use known results from the theory of partial differential equations to determine the data required for their solution. We further examine the extent to which that data may be obtained from known boundary conditions in the experiment. Finally, considering the possibility of measuring several displacement fields in the same body, we obtain an over–determined system of partial differential equations. This system will have only a small number of possible solutions, and our goal is to find this number of solutions.

Results: Mathematical theorems are derived and their results are presented. A typical result is that the mechanical property distribution of interest may be given as a combination of $N_{PATTERNS}$ different patterns with $N_{OBSERVATIONS}$ different observed displacement fields. For linear elastic, incompressible, isotropic materials, the results are: Plane stress, $N_{PATTERNS} = 1$ with $N_{OBSERVATIONS} = 1$; Plane strain, $N_{PATTERNS} = 4$ with $N_{OBSERVATIONS} = 2$; Three dimensions, $N_{PATTERNS} = 5$ with $N_{OBSERVATIONS} = 2$. For nonlinear elastic, incompressible, isotropic materials, the results for Neo–Hookean materials are the same as for linear elastic materials. For modified Blatz (aka Veronda–Westmann) materials, we have two material coefficients. In Plane stress, $N_{PATTERNS} = 2$ (one pattern for each coefficient) with $N_{OBSERVATIONS} = 2$, one at low strain, one at high strain; Plane strain, we have $N_{PATTERNS} = 4$ for each coefficient, with $N_{OBSERVATIONS} = 4$, two observations at low strain, and two at higher strain. For triphasic poroelastic materials modeling vascularized soft tissues, there are two material parameters beyond those characterizing the elastic response. We find that the filtration coefficient may be reconstructed (i.e. $N_{PATTERNS} = 1$) with $N_{OBSERVATIONS} = 2$ taken at two closely spaced time intervals.

Conclusions: In many practical cases of interest, the data needed to uniquely determine the material property distributions can be collected by straightforward means. This may require the measurement of several distinct deformation patterns and the identification of several calibration constants. A single strain image, or even a strain image sequence, however, is insufficient to determine the material properties except in plane stress scenarios.

Acknowledgements: Fulbright Foundation, Université Libre de Bruxelles, R21CA133488, R01CA140271.

009 **COLON TUMOR GROWTH AND ANTIVASCULAR TREATMENT IN MICE: COMPLEMENTARY ASSESSMENT WITH MR ELASTOGRAPHY AND DIFFUSION–WEIGHTED MR IMAGING.**

L. Jugé[1], BT. Doan[2], J. Seguin[2], M. Albuquerque[1], B.Larrat[3], N. Mignet[2], G.G. Chabot[2], D. Scherman[2], V. Paradis[1,4], V. Vilgrain[1,5], B.E. Van Beers[1,5], R. Sinkus[1].*
[1]Université Paris Diderot, Sorbonne Paris Cité, INSERM U773, Paris, FRANCE; [2]UPCGI/Chimie–ParisTech, UMR8151, INSERM U1022, Paris, FRANCE; [3]ESPCI–ParisTech, UMR 7587 Paris, FRANCE; [4]Département d'Anatomie Pathologique, [5]Département de Radiologie, Hôpital Beaujon, Assistance Publique–Hôpitaux de Paris, Clichy, FRANCE.

Background: A precise evaluation of tumor vascularization and cellularity is of major importance for diagnosis and treatment follow–up of cancer [1–3]. Some insight into these features can be obtained with quantitative MR imaging, including diffusion–weighted (DW) MR imaging correlated with tissue architecture, cell density and necrosis [4]. MR elastography [5] is a new quantitative MR imaging method that provides information about the micro–structure of tissue [6,7]. Our hypothesis is that alterations of the vasculature induce significant changes in the viscoelastic properties of tissue that can be probed with MR elastography. Therefore, the aim of our study was to assess the potential value of a combined MR elastography and DW MR imaging method in the detection of micro–structural changes of murine colon tumors during normal growth and anti–vascular treatment.

Aims: To investigate the potential value of MR elastography and diffusion–weighted (DW) MR imaging in the detection of micro–structural changes of murine colon tumors during growth and anti–vascular treatment.

Methods: Forty–eight Balb–C mice bearing ectopic and orthotopic colon tumors were monitored during 3 weeks with high resolution T_2–weighted MR imaging (RARE sequence, 125µm x 125µm in plane resolution), three–dimensional steady–state MR elastography with a vibration frequency of 1000Hz (250µm isotropic image resolution) and DW MR imaging (b–values: 250, 500, 750, 1000 and 2000s/mm^{-2}) in a horizontal 7T animal scanner (Bruker, Pharmascan). The same imaging protocol was performed 24h after injection of 100mg/Kg of combretastatin A4 phosphate in 12 mice on day 11. The complex shear modulus (G*) (Figure1C) and the apparent diffusion coefficient (ADC) were measured in the viable zones of tumors and compared to micro–vessel density, cellularity and micro–necrosis.

Figure 1: Ectopic tumor (red ROI): (A) T_2 weighted image depicting the anatomy (TE=14ms, TR=2454ms); (B) Unwrapped phase imaging of the MR elastography acquisition showing wave propagating at 1000Hz in the tumor; (C) |G*| (kPa) map depicting the mechanical properties.

Results: During tumor normal growth, G* increase was correlated with the micro–vessel density (MVD) (r=0.70, *P*=0.08 and r=0.78, *P*=0.002, for ectopic and orthotopic models, respectively). Moreover, the ectopic tumors displayed decreased ADC which correlated with increased cellularity (r=0.77, *P*=0.04), whereas no changes of ADC and cellularity were observed in orthotopic tumors. After combretastatin administration, G* decreased in the ectopic model (*P*<0.001), similar to the MVD evolution, whereas no significant changes of G* and MVD were observed in the orthotopic model. ADC increased in both models (*P*<0.05) in relation to increased micro–necrosis.

Conclusions: The results of this study show that mechanical properties and diffusivity provide non invasive complementary information during tumor growth and regression that are respectively linked to vascularity and the balance between tumor micro–necrosis and cellularity. If these results are confirmed in humans, viscoelastic properties could become a pertinent biomarker of vasculature in tumor growth and regression after anti–vascular treatment.

References:

[1] Degani H, Chetrit–Dadiani M, Bogin L, Furman–Haran E: Thromb Haemost, 89, pp. 25–33, 2003.
[2] Chenevert TL, Meyer CR, Moffat BA, et al.: Mol Imaging, 1, pp. 336–343, 2002.
[3] Rudin M: Eur Radiol, 17, pp. 2441–2457, 2007.
[4] Hamstra DA, Rehemtulla A, Ross BD: J Clin Oncol, 25, pp. 4104–4109, 2007.
[5] Muthupillai R, Lomas DJ, Rossman PJ, Greenleaf JF, Manduca A, Ehman RL: Science, 269, pp. 1854–1857, 1995.
[6] Sinkus R, Tanter M, Xydeas T, et al.: Magn Res Imag, 23, pp. 159–165, 2005.
[7] Huwart L, Peeters F, Sinkus R, et al.: NMR Biomed, 19, pp. 173–179, 2006.

* *indicates Presenter*

014 **ON THE ACOUSTIC RADIATION FORCE GENERATED BY MODULATED ULTRASOUND IN TISSUE–LIKE SOLIDS.**

Egor V. Dontsov[1], Bojan B. Guzina[1].*
[1]Civil Engineering Department, University of Minnesota, 500 Pillsbury Drive SE, Minneapolis, MN 55455, USA.

Background: Acoustic radiation force (ARF) is a phenomenon stemming from the nonlinear effects of finite–amplitude wave propagation. It represents the mean momentum transfer from the sound wave to the medium and allows for an effective computation of the mean motion induced by a high–intensity sound wave. The concept of the ARF bears relevance to a number of emerging biomedical applications [1], where the ultrasound beam (used to generate the ARF) is typically modulated with a low–frequency signal as a tool to facilitate the local reconstruction of the tissue's viscoelastic properties [2, 3].

Aims: To cater to biomedical applications of ARF, this study investigates the generation of ARF in homogeneous tissue–like solids in situations when the elevated intensity, focused ultrasound field is modulated by a low–frequency signal.

Methods: To expose the mechanics of ultrasound–based tissue palpation, the analysis of the nonlinear wave motion at hand is simplified by taking the ratio between the modulation and ultrasound frequencies, the Mach number, the ratio of the shear to bulk modulus and the dimensionless attenuation coefficient, each to be small and commensurate in magnitude. A scaling approach, that is driven by the geometry of the focused ultrasound beam and entails normalization of the transverse coordinates by the width of the focal zone, demonstrates that the waves are nearly planar within the region of interest (i.e., the zone of the coalescence of ultrasound waves). In this case, following the approach of the recent plane–wave study [4], the computation of ARF due to the modulated ultrasound field is facilitated by introducing the "fast" and "slow" time variables, allowing one to parse out the ultrasound rate and modulation rate variations in the solution. To study the mean motion induced by ARF, the "fast" time average, computed over the period of ultrasound vibrations, is introduced to extract the mean motion from the solution.

Results: On approximating the constitutive response of soft tissues as that of a nonlinear viscoelastic solid with heat conduction, the governing equations for the mean tissue motion, featuring the new formula for ARF, are obtained by taking the "fast" time average of the nonlinear field equations dictating the original ultrasound–scale problem. The computed radiation force has two qualitatively different terms: 1) the potential body force term, which is proportional to the gradient of the intensity and produces mostly compressional waves, and 2) the directional body force term, which acts along the transducer's axis and generates predominantly shear motion.

Conclusions: A comparison with the existing theory reveals a number of key features that are brought to light by the new formulation, including the contributions to ARF of ultrasound modulation and thermal expansion, as well as the precise role of constitutive nonlinearities in generating the sustained body force in tissue–like solids by a focused ultrasound beam.

Acknowledgements: The support provided by the endowed Shimizu Professorship during the course of this study is kindly acknowledged.

References:

[1] A.P. Sarvazyan, O.V. Rudenko and W.L. Nyborg: Biomedical Applications of Radiation Force of Ultrasound: Historical Roots and Physical Basis. Ultras. Med. Biol., 36, pp. 1379–1394, 2010.
[2] B.B Guzina, K. Tuleubekov, D. Liu and E. Ebbini: Viscoelastic Characterization of Thin Tissues using Acoustic Radiation Force and Model–Based Inversion. Phys. Med. Biol., 54, pp. 4089–4112, 2009.
[3] M. Fatemi and J. Greenleaf: Vibro–Acoustography: An Imaging Modality Based on Ultrasound–Stimulated Acoustic Emission. Proc. Natl. Acad. Sci., 96, pp. 6603–6608, 1999.
[4] E. Dontsov and B. B. Guzina: Effect of Low–Frequency Modulation on the Acoustic Radiation Force in Newtonian Fluids. SIAM J. Appl. Math., 71, pp. 356–378, 2011.

015 **USING CRAWLING WAVE SONOELASTOGRAPHY FOR THE MEASUREMENT OF INTRAHEPATIC FAT CONTENT.**

Bradley Mills[1], Christopher Barry[2], Zaegyoo Hah[1], Deborah J. Rubens[2], Kevin J. Parker[1].*
[1]University of Rochester, Rochester, NY, USA; [2]University of Rochester Medical Center, Rochester, NY, USA.

Background: Hepatic steatosis affects 31% of the U.S. population and as much as 67% of those who are obese. Non–alcoholic fatty liver disease (NAFLD) is the most common cause of chronic liver dysfunction in Western countries and can progress to end stage liver disease as a result of non–alcoholic steatohepatitis (NASH) [1]. Current understanding of the pathophysiological progression from NAFLD to NASH is incomplete [2]. The gold standard for measuring intrahepatic fat content is liver biopsy followed by histologic analysis. This procedure can increase patient risk and discomfort, be logistically cumbersome and subject to interpretive errors upon analysis [3]. The ability to effectively measure hepatic fat content is essential for both evaluating livers for transplant and diagnosing all stages of NAFLD [2].

Aims: The objective of this study is to demonstrate the correlation between hepatic steatosis and shear speed frequency dependence (dispersion) of viscoelastic liver tissue. A non–invasive technique using crawling waves (CrWs) to measure both the stiffness and fat content of liver samples is proposed.

Methods: Excised mouse and human liver specimens were examined using CrW sonoelastography. Phantoms were prepared by embedding the samples in a porcine gelatin background (8–11%). Two vibration sources were positioned at each side of the phantom with the ultrasound transducer scanning from the top. CrWs were driven at frequencies ranging from 100–300Hz by offsetting a small frequency difference between two sources. CrW data was de–noised and sinusoidal curve fitting was applied to a similar ROI in each frame to determine the relative wavelength. Wavelengths were then used to calculate respective shear velocities at each frequency for a given sample. The rate of increase in shear velocity over a frequency band was collected to reveal the dispersion of each specimen.

Results: In ob/ob genetically obese mice (n=10), the mean dispersion slope is 0.15+/-0.015cm/sec per 100Hz, compared to lean ob/- littermates (n=10) at 0.075+/-0.02cm/sec per 100Hz. Histologic analysis using H&E and oil red O staining confirms steatosis up to 65% in ob/ob animals and 0% to <5% in ob/- animals. Additionally, human liver scans from patients over a range of steatosis and fibrosis suggests that our method can discriminate degrees of steatosis (e.g., minimal <20%, moderate 20–40%, and severe >40%) as well as fibrosis.

Conclusions: CrW sonoelastography is potentially a non–invasive, cost effective and efficient technique for grading not only the stiffness but also the fat content of liver tissue. This method has promise as a safe and effective way to assess liver health in both the realm of liver transplant patients as well as the general population.

Acknowledgements: This work was supported by NIH grant 5R01AG029804.

References:

[1] Tim CMA Schreuder et al.: Nonalcoholic Fatty Liver Disease: An Overview of Current Insights in Pathogenesis, Diagnosis and Treatment. World Journal of Gastroenterology, 14(16), pp. 2474–2486, 2008.
[2] Marta I. Minervini et al.: Liver Biopsy Findings from Healthy Potential Living Liver Doners: Reasons for Disqualification, Silent Diseases and Correlation with Liver Injury Tests. Journal of Hepatology, 50(3), pp. 501–510, 2009.
[3] Christian P. Strassburg et al.: Approaches to Liver Biopsy Techniques – Revisited. Seminars in Liver Disease, 26(4), pp. 318–327, 2006.

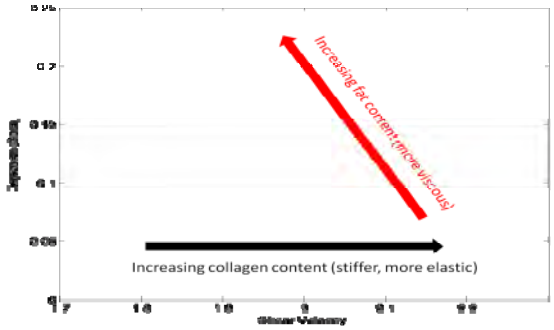

Figure 1. Two parameter hypothesis of the effect of steatosis.

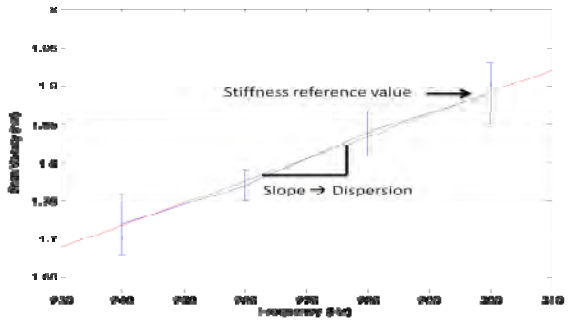

Figure 2. Estimation result of an obese mouse liver.

* *indicates Presenter*

016 **VAGINAL TACTILE IMAGER FOR DIRECT MODULUS ESTIMATION.**

Vladimir Egorov[1], Milind Patel[1], Armen P. Sarvazyan[1].*
[1]Artann Laboratories, 1459 Lower Ferry Rd, Trenton, NJ, 08619, USA.

Background: Assessment of the mechanical properties of the pelvic floor is increasingly attracting attention from gynecologists because at least 50% of women in the US are affected during their lifetimes by pelvic floor disorders such as prolapse and incontinence closely related to changes in tissue elasticity. Currently, there is no adequate solution to this important problem. Addressing this problem, we developed the Vaginal Tactile Imager (VTI) based on the Tactile Imaging (aka Mechanical Imaging or Stress Imaging) technology successfully implemented in the devices for detection and visualization of abnormalities in breast and prostate [1, 2].

Aims: To develop a method that allows quantitative measurement of tissue elasticity (Young's modulus) based on tactile imaging and to evaluate its accuracy and reproducibility in a phantom–based study.

Methods: The VTI is shown in Figure 1. The vaginal probe is comprised of a pressure sensor array and a motion tracking sensor. On average, each pressure sensor has a sensitivity of 20Pa; reproducibility is about 300Pa and operational range of 30kPa. The six–degree–of–freedom motion tracking system provides positioning accuracy better that 1mm. The data acquisition rate is 25 pressure patterns per second. Seven silicone phantoms were designed to represent geometry and elasticity of real tissue with Young's modulus in the range from 2–40 kPa. Force–elongation measurements were performed on cylindrical specimens used in the silicone phantoms; these measurements were considered as the gold standard for comparison with VTI data. The phantom examination procedure includes multiple compressions of the internal walls and allows composing a circumferential 3–D tactile image or pressure map of the phantom (Figure 2). Young's modulus of the tissue was calculated from spatial gradients in resulting 3–D pressure map with the use an empirical function derived from all collected data. To estimate VTI pressure mapping reproducibility we calculated standard deviation for the normalized convolutions of each 3–D pressure map relative to the average 3–D pressure map for the same phantom.

Results: We found that VTI provides elasticity measurements with accuracy ±15–20% and reproducibility ±5–7% for Young's modulus in the range from 2–40kPa. The pressure mapping reproducibility was in the range from 3.5% to 6%.

Figure 1: Vaginal Tactile Imager.

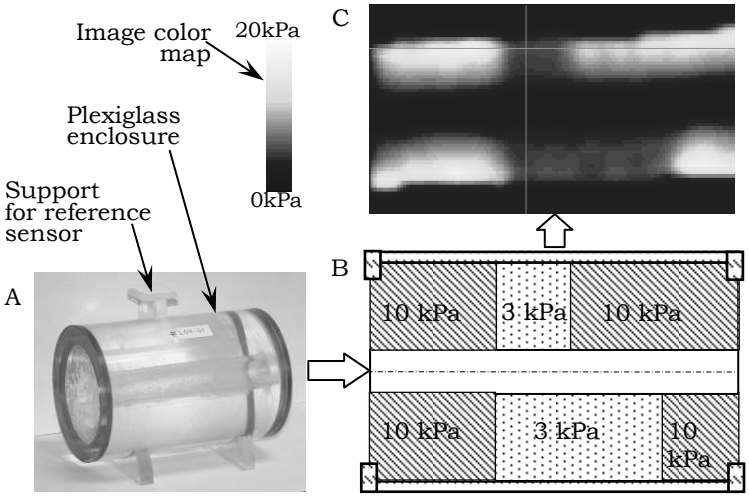

Figure 2: Vaginal phantoms with realistic soft tissue elasticity range to allow VTI verification. (A) an example of a phantom; (B) VTI pressure pattern in sagittal cross–section; (C) sagittal cross–section of 3–D pressure map obtained with VTI for the phantom.

Conclusions: Our findings suggest that VTI is suitable for 3–D elasticity imaging and quantification.

Acknowledgements: The work was supported by the National Institute on Aging, USA, grant R43 AG034714.

References:

[1] Egorov V, Sarvazyan AP: Mechanical Imaging of the Breast. IEEE Trans Med Imaging, 27, pp. 1275–87, 2008.
[2] Weiss RE, et al.: Prostate Mechanical Imaging: A New Method for Prostate Assessment. Urology, 71, pp. 425–29, 2008.

* *indicates Presenter*

018 **A HAND–HELD SYSTEM FOR QUANTITATIVE MAPPING OF ELASTIC PROPERTIES WITHIN A BIOMATERIAL FROM CRAWLING WAVES GENERATED ON THE SURFACE.**

Alexander Partin[1], Zaegyoo Hah[1], Bradley N. Mills[1], Deborah J. Rubens[2], Kevin J. Parker[1].*
[1]Electrical and Computer Engineering Department, University of Rochester, Rochester, NY, USA; [2]University of Rochester Medical Center, Rochester, NY, USA.

Background: Earlier Crawling Wave (CrW) approaches used external vibration sources to generate the wave propagation within the tested biomaterial. The CrW generation was executed using strip bars (line sources) placed at the opposite sides of the medium. In some cases, restrictions of physical shape and small size render this approach impractical. In order to overcome this problem, a pair of vibration sources can be placed on each side of the scanning transducer to generate the CrW within the medium [1,2]. Further, an estimation algorithm for mapping the elastic properties from the data collected with one of these configurations was presented [3]. However, that estimation algorithm was valid only for a ROI where the interference could be approximated to a plane wave, and the ROI was relatively small comparable to the whole scanned cross–section.

Aims: We employ circular loads adjacent to the scanning transducer for the generation of the CrW. The use of circular loads with small radius (point sources) provides more flexible applications with a smaller footprint. Also, a novel estimation algorithm is developed, based upon the shear wave solution to the interfering sources, which quantitatively maps the elastic properties of soft tissues in a much bigger ROI than the previously suggested algorithm.

Methods: CrW experiments are performed on two types of homogenous phantoms: a plain gelatin phantom and an oil–gelatin (fatty) phantom with 40% oil. Two point sources are placed on top of a phantom. Each source vibrates normally to the surface of the phantom, generating shear wave propagation within the material, as illustrated in Figure 1a. An interference pattern inside the phantom is created by the superposition of the waves originating from each of the sources. The pattern will slowly propagate across the screen when a small offset between the frequencies is applied. An ultrasound scanning probe is placed in between the vibration sources and tracks the motion. A single frame of the CrW movie and the geometry of the setup are presented in Figure 1b. The developed estimation technique requires the known parameters including the frequencies of the vibration sources, the distance between sources and the position of the ultrasound probe with respect to the vibration sources.

Results: The output result of the estimator is presented as a shear speed map. For a plain gelatin phantom, the range of the shear speed in the ROI is 4.47±0.4m/s, and, in the fatty phantom, the range is 3.2±0.3m/s. The limitations of the ROI are due to the depth of penetration. Higher frequencies and higher percentage of oil reduces the effective ROI. Otherwise, the algorithm is valid for the whole cross–section.

Conclusions: Using the suggested setup and estimation technique, elastic properties of biomaterial could be mapped within the ROI on the order of 2.8 by 4.2cm at 400Hz, as shown in Figure 1c. The estimated shear speed map shows good fit with respect to independent measures on these biomaterials.

Acknowledgements: This study was partly supported by NIH Grant 5 RO1 AG29804.

References:

[1] G.F. Miller and H. Pursey: The Field and Radiation Impedance of Mechanical Radiators on the Free Surface of a Semi–Infinite Isotropic Solid. Proc. R. Soc. Lond. A, Vol. 223, pp. 521–541, 1954.
[2] Zhe Wu et al.: Shear Wave Focusing for Three–Dimensional Sonoelastography. JASA, Vol. 111, pp. 439–446, 2002.
[3] Kenneth Hoyt et al.: Quantitative Sonoelastography for the *In Vivo* Assessment of Skeletal Muscle Viscoelasticity. Phys. Med. Biol., Vol. 53, pp. 4063–4080, 2008.

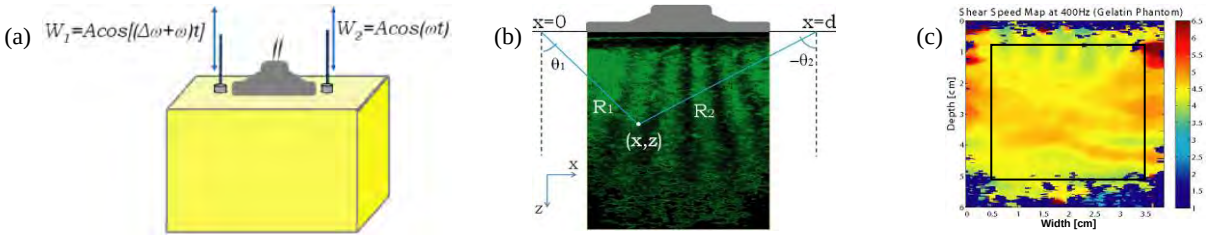

Figure 1: (a) Schematic drawing of the experimental setup. (b) A single frame of the CrW movie of a gelatin phantom. (c) Calculated shear speed map (Color bar units are m/s).

* *indicates Presenter*

026 **PASSIVE ELASTOGRAPHY FROM COMPLEX SHEAR WAVE FIELD IN SOFT SOLIDS.**

Stefan Catheline[1], Thomas Gallot[1], Philippe Roux[1], Javier Brum[1], Carlos Negreira[2].*
[1]Grenoble University & CNRS, LGIT, Grenoble, FRANCE; [2]Science University, LAU, Montevideo, URUGUAY.

Background: Time Reversal experiments allow focalization of waves in soft solids [1]. The mechanical properties of the medium can be extracted from the refocusing field. Similar techniques developed in the field of seismology were recently shown to allow tomography from multiply scattered wave fields [2]. Applied in the field of elastography, these techniques gave a passive method that does not need any controllable shear wave source [3].

Aims: In this work, passive elastography is enhanced by using a passive inverse filter.

Methods: Heartbeats, breathing and muscle activity: the human body presents natural sources of vibration creating a complex shear wave field. Indeed, the shear wave noise inside soft tissues is measured by ultrasonic techniques developed in elastography. The particle motions estimated along lines or planes inside the medium can be used as artificial stars for time reversal experiments. In other words, Green's functions can be recovered from noise correlations which result in a totally passive imaging technique. However, the assumption of an ideal isotropic diffuse field is rarely verified. The effect of a directional wave field introduces biases in the tomography reconstruction. In order to correct these biases, the use of a spatio–temporal inverse filter is described.

Results: The physiological noise is demonstrated in this work to be useful for quantitative elasticity imaging. A quantitative imaging of the shear speed in the liver region is presented in Figure 1. The biases visible on Figure1E are analysed. A spatio–temporal inverse filter approach was thus elaborated. Applied to seismic data as well as elastography data, the use of this filter is shown to improve the Green's function reconstruction and as a consequence the final tomography.

Conclusions: An i*n–vivo* experiment demonstrates the feasibility of passive elastography. The biases present in the tomography reconstruction are better understood and partly removed in the final images, thanks to a passive inverse filter.

References:

[1] S. Catheline, N. Benech, X. Brum, and C. Negreira: Time Reversal of Elastic Waves in Soft Solids. Phys.Rev.Letter, 100, p. 064301, 2008.
[2] M. Campillo and A. Paul: Long–Range Correlations in the Diffuse Seismic Coda. Science, 299, pp. 547–549, 2003.
[3] T. Gallot, S. Catheline, P. Roux, J. Brum, C. Negreira: Passive Elastography: Shear–Wave Tomography from the Physiological–Noise Correlation in Soft Tissues. IEEE UFFC, June, 2011.

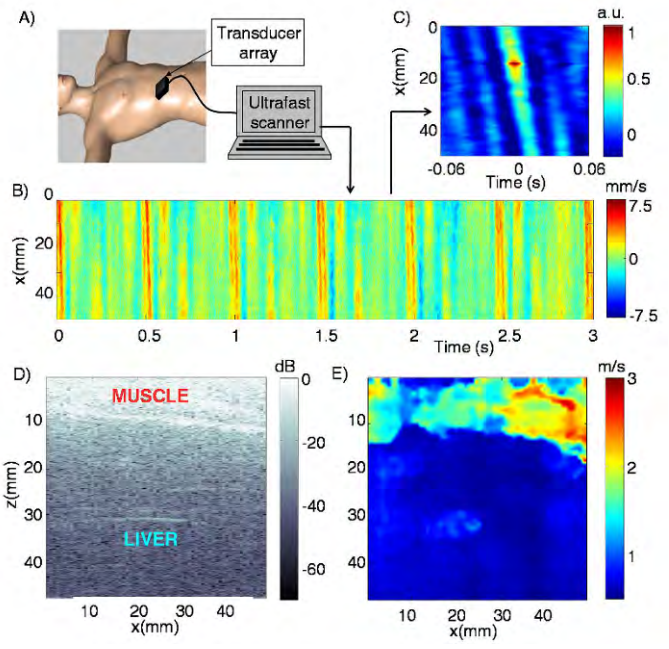

Figure 1: A) Experimental set–up for the *in–vivo* correlation-based tomography: an ultrafast scanner was used to measure the natural displacement field in the liver region.
B) The particle velocity along an acquisition line at 4cm, and parallel to the array, shows the physiological elastic field.
C) In the correlation map $C(x_0; x; t)$ with x_0 = 14mm, only one direction of propagation emerged from the refocusing field.
D) Sonogram of the liver region. The interface between the abdominal muscles and the liver is visible around z = 12mm.
E) The passive shear–wave-speed tomography from the correlation width clearly shows the two regions. The averaged shear–speed estimations are in agreement with values in the literature.

* *indicates Presenter*

Invited Presentation:

095 **VASCULAR ELASTICITY AND CARDIOVASCULAR RISK ASSESSMENT.**

William F. (Rick) Weitzel[1].*
[1]Internal Medicine Department, University of Michigan, 312 Simpson Memorial Institute, 100 Observatory Drive, Ann Arbor, MI, 48109, USA.

Background: The burden of cardiovascular (CV) disease is enormous worldwide. In the United States alone over 80 million people suffer from CV diseases with unsustainable financial burden of $500 billion/year [1]. Improvements in measurement and management of CV disease are essential to reduce this burden. While simple brachial artery blood pressure (BP) remains entrenched as a valuable measurement tool, there is growing evidence that central hemodynamics may be better predictive of outcome [2] and differently affected by antihypertensive medications.

Current Methods: New tools to measure central hemodynamics reliably and noninvasively are being developed for measuring CV risk and manifestations of organ damage [2]. Many are based on the physiology of the pressure wave generated by the left ventricle and the reflected waves generated at multiple peripheral sites; the resulting pressure waveform recorded at any site of the arterial tree is the sum of the forward traveling waveform and the backward traveling wave reflected at peripheral sites. When the large conduit arteries are healthy and compliant, the reflected wave merges with the incident in the proximal aorta during diastole augmenting the diastolic BP and aiding coronary perfusion. In contrast, when the arteries are stiff, pulse wave velocity (PWV) increases accelerating the incident and reflected waves augmenting the aortic systolic rather than diastolic pressure. Changes in pulse pressure (PP), the pulse wave velocity (PWV) and parameters derived from the central waveform such as the augmentation index (AI) are becoming recognized as predictors of vascular health and disease, as well as future clinical events [2].

A growing set of vascular experimental measurements are based on direct measurements of vascular motion and strain. For example, high frame rate ultrasound imaging with accurate tracking may allow direct measurement of PWV from the carotid, aorta or peripheral arteries. This is contrasted with conventional aortic PWV measurements obtained from the carotid to femoral time difference. These also allow direct vascular strain measurements to be obtained from arteries. Figure 1 shows an example of non–invasive measurements in the carotid artery. Figure 1a shows a B–mode frame of the inferior vessel wall of the carotid artery in a healthy volunteer. The image has a colored velocity map overlaid of motion tracked (blue/white for motion down) along the beam. Figure 1b and 1c show data derived from RF speckle tracking with regions of interest separated by approximately 3cm displaying a 15ms time lag in peak velocity resulting in a local PWV measurement of approximately 2m/s.

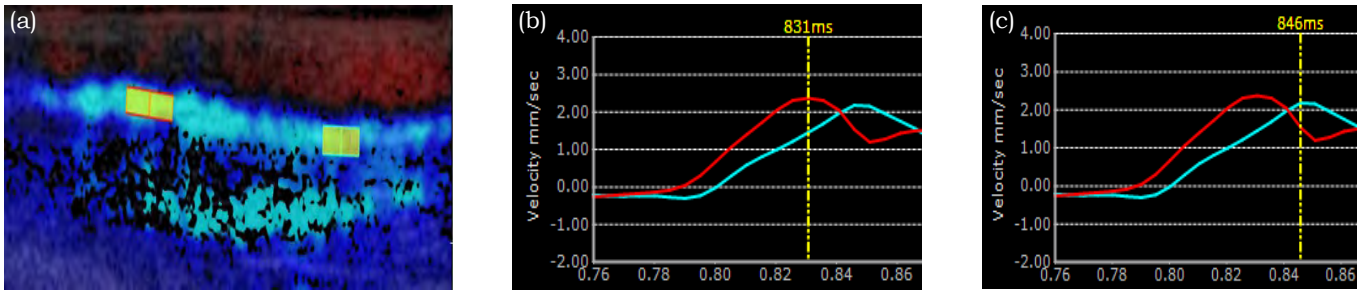

Figure 1:

Future Trends: Current efforts to advance these measurement methods have the potential advantage of direct assessment for measuring regional or local disease. In addition, these emerging tools may allow development of operator independent, simple methods to meet the growing need for CV risk assessment. These and other topics will be discussed in this presentation.

References:

[1] Bosworth H, Powers B, Oddone E: Patient Self–Management Support: Novel Strategies in Hypertension and Heart Disease. Cardiology Clinics, 28(4), pp. 655–663, 2010.
[2] E. Agabiti–Rosei, G. Mancia, M.F. O'Rourke, M.J. Roman, M.E. Safar, H. Smulyan, J–G. Wang, I.B. Wilkinson, B. Williams, C. Vlachopoulos: Central Blood Pressure Measurements and Antihypertensive Therapy: A Consensus Document. Hypertension, 50, pp. 154–160, 2007.

* *indicates Presenter*

047 **RESPONSE TO COMPRESSION OF DIFFERENT BREAST LESIONS OBSERVED *IN VIVO* WITH 2D LOCALLY REGULARIZED STRAIN ESTIMATION METHOD.**

Elisabeth Brusseau[1], Valérie Detti[1], Agnès Coulon[2], Emmanuèle Maissiat[2], Nawèle Boublay[3], Yves Berthezène[1,2], Jérémie Fromageau[4], Nigel Bush[4], Jeffrey Bamber[4].*

[1]CREATIS, CNRS UMR5220, Inserm U1044, INSA–Lyon, Université Lyon 1, 7 av. Jean Capelle, 69621 Villeurbanne, FRANCE; [2]Hospices Civils de Lyon, Service de Radiologie, Hôpital de la Croix–Rousse, 69004 Lyon, FRANCE; [3]Hospices Civils de Lyon, Pôle Information Médicale Evaluation Recherche, Université Lyon 1, EA 4129, Lyon, F–69424 FRANCE; [4]Joint Department of Physics, Institute of Cancer Research, 15 Cotswold Rd, Sutton, Surrey SM2 5NG, England, UK.

Background and Aims: We have recently reported preliminary results of *in vivo* strain images of breast lesions, fibroadenomas and malignant tumors, computed with our 2D locally regularized strain estimation method [1]. In this study, we report a more complete analysis on the tissue response to compression by including cystic cases.

Methods: Twenty clinical cases are examined: ten cysts, five fibroadenomas and five malignant tumors consisting of two invasive ductal carcinoma grade I (IDC I), one IDC II, one IDC III, as well as one suspected carcinoma. In this two–center study, data were acquired at the Hôpital de la Croix–Rousse, Lyon, France, with an Ultrasonix (Sonix RP) ultrasound scanner equipped with a L14–5W/60 linear probe and at the Royal Marsden Hospital, London, England, with an Acuson 128XP ultrasound system, working with a L7EF probe. Radio–frequency echo data were sampled at 40 MHz and processed off–line.

Results: Trends in tissue response to compression are reported here. Cysts can be subjected to significant strain under compression, leading to elastograms where a cystic lesion can be more or less visible in comparison to the surrounding tissue strain. Fibroadenomas and malignant tumors both appear stiffer than surrounding tissues. Lesion size, shape and margin in the strain images tend to be similar to those of the corresponding hypoechoic region in B–mode images for fibroadenomas, whereas for malignant tumors, the stiffer region appears in many cases to be more extended with significantly different margin aspects, in particular more irregular, (Figure1). Moreover, the normalized correlation coefficient (NCC) map provides relevant complementary information for strain image interpretation. It allows the identification of decorrelation areas, subjected to regularization by our method to locally enforce smoothness within strain images. In addition to indicating which areas of strain images require cautious interpretation, in some cases, the NCC map confirms the presence of cystic lesions.

Conclusions: The trends reported here are consistent with previously published works [2,3]. Moreover, lesion size, shape and margin in the strain images associated with the NCC values offer complementary information for lesion interpretation. This analysis will be completed and refined with future progress.

References:

[1] E. Brusseau, V. Detti et al.: A Two Dimensional Locally Regularized Strain Estimation Technique: Preliminary Clinical Results for the Assessment of Benign and Malignant Breast Lesions. Spie Medical Imaging, 2011.
[2] B.S. Garra, E.I. Cespedes et al.: Elastography of Breast Lesions: Initial Clinical Results. Radiology, 202(1), pp. 79–86, 1997.
[3] E.S Burnside, T.J. Hall et al.: Differentiating Benign from Malignant Solid Breast Masses with US Strain Imaging. Radiology, 245(2), pp. 401–410, 2007.

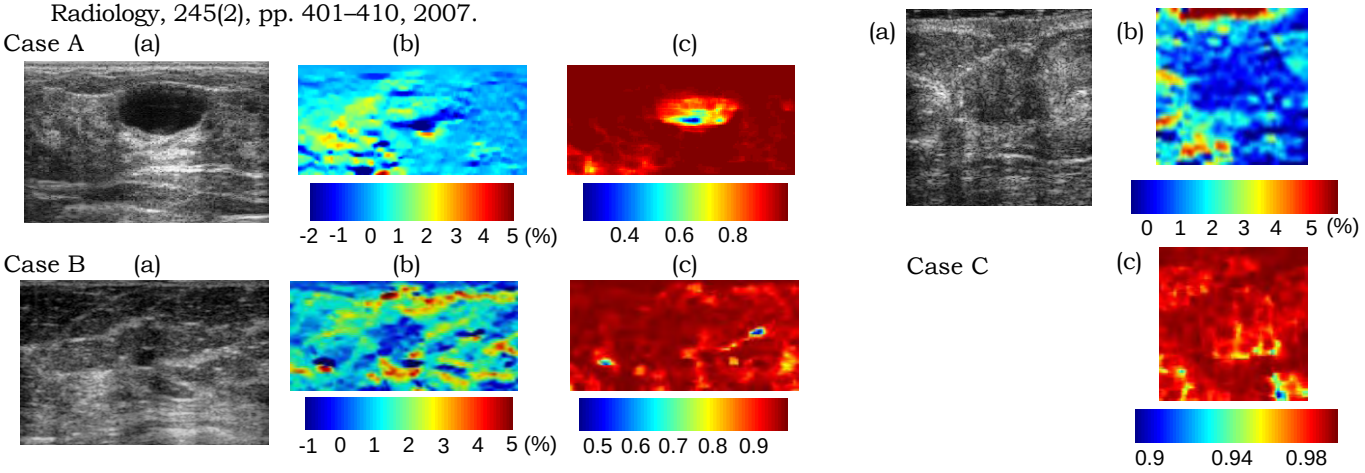

Figure 1: Examples of breast lesion deformation for a cyst (Case A), a histologically confirmed fibroadenoma (Case B) and an IDC II (Case C). For each case, (a) ultrasound image, (b) strain image and (c) NCC map are shown.

074 **SONOELASTOGRAPHY PRESENTATION OF HIGH GRADE BREAST CARCINOMAS.**

Eduardo Fleury[1].*
[1]Radiology, Santa Casa de Misericordia de São Paulo, São Paulo, BRAZIL.

Background: Sonoelastography has been implemented in clinical practice to help differentiate benign from malignant breast masses with a good performance [1,2]. However, the histological spectrum of presentation of breast carcinoma may have a large variation from low–grade insidious carcinomas to aggressive high–grade carcinomas. These are generally related with the worst prognosis due to high rate of cellular replication and anaplasia. Usually, intratumoral necrosis and inflammation are associated.

Aim: The objective of the study is to demonstrate the presentation of high–grade breast carcinomas by sonoelastography and discuss their results.

Methods: Retrospective analysis of 1200 ultrasound guided percutaneous breast biopsies was performed. It included 35 cases of histological high–grade carcinomas and undifferentiated carcinoma. The sonoelastography presentation was correlated with the histological degree of carcinoma. The sonoelastography studies were performed as previously described, where lesions scores 1, 2 and 3 were considered as soft (false negative), while score 4 was considered as hard (true positive) [3].

Results: The results showed that most lesions confirmed by histology as high grade breast carcinomas or with undifferentiated carcinomas appeared as soft on sonoelastography, i.e., 29 were classified as score 3 and 6 were classified as score 4.

Conclusion: High–grade breast carcinomas and undifferentiated carcinomas have a tendency to present as false–negative results by sonoelastography, as compared to its histological presentation.

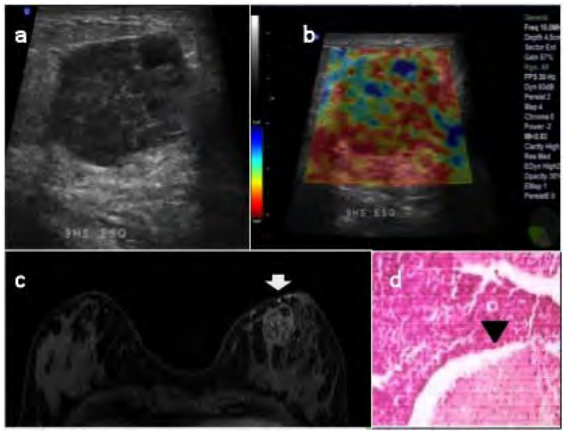

Figure 1: High grade carcinoma associated with necrosis, presented as soft on sonoelastography:
a) B-mode;
b) Sonoelastography;
c) MRI;
d) Histology.

References:

[1] Tohno E, Ueno E: Current Improvements in Breast Ultrasound, with a Special Focus on Elastography. Breast Cancer, 15(3), pp. 200–204, 2008.
[2] Scaperrotta G, Ferranti C, Costa C, Mariani L, Marchesini M, Suman L, Folini C, Bergonzi S: Role of Sonoelastography in Non-Palpable Breast Lesions. Eur Radiol, 18(11), pp. 2831–2839, 2008.
[3] Fleury EFC, Rinaldi JFR, Piato S, Fleury JCV, Roveda JRD: Features of Cystic Breast Lesions at Ultra–Sound Elastography. Radiol Bras, 41 (3), pp. 167–172, 2008.

* *indicates Presenter*

080 **VIBRO–ELASTOGRAPHY OF BREAST LESIONS: INITIAL CLINICAL STUDY.**

H Eskandari[1], PV Nasute Fauerbach[2], SE Salcudean[1], R Rohling[1], PB Gordon[2], LJ Warren[2].*
[1]Electrical and Computer Engineering Department, [2]Radiology Department, University of British Columbia, Vancouver, BC, CANADA.

Aims: To explore the characteristic viscoelastic features of breast lesions that can help classify cancers, fibroadenomas and fibrocystic lesions. The viscosity and elasticity images are obtained during real–time vibro–elastography (VE) examination of the breast.

Methods: Vibro–elastography involves applying a controlled low–amplitude multi–frequency vibration to the surface of the tissue with an external exciter and recovering the viscoelastic properties in real–time [1]. To evaluate this technique for breast lesion characterization, we attached a small actuator to an L14–38 ultrasound probe, acquired raw radiofrequency data with an ultrasound machine (Sonix Touch, Ultrasonix Medical Corp., Richmond, BC, Canada) and processed them to obtain viscosity and elasticity images of the underlying tissue [2]. We tested 12 patients with a total of 14 breast lesions, and the findings from the viscoelasticity images were compared to the biopsy results. The elasticity and viscosity images were displayed as color–intensity images superimposed on a region of interest within the B–mode image. The data were processed in real–time and displayed on the screen to the sonographer and radiologist at 1–2 frames/second depending on the sector size and line density of the images. Also, all data were recorded for offline analysis. The elasticity contrast of the lesions and the viscosity pattern around them were examined to identify distinguishing characteristics between benign and malignant breast abnormalities. Based on the core needle biopsy and fine needle aspiration results, among the 14 lesions, 5 were fibroadenoma, 4 were IDC, 2 were cysts, 2 were other types of benign masses and one was a heterogeneous malignant cell spindle.

Results: Based on the vibro–elastography images, the elasticity within fibroadenomas appeared to be between 2 to 4 times higher than the surrounding fibroglandular tissue. Invasive ductal carcinoma of the breast was between 3 to 10 times harder than the normal breast tissue, which is consistent with the results reported in the literature [3]. In addition to the higher elasticity contrast, the cancerous lesions mostly exhibited a more heterogeneous elasticity pattern than the fibroadenomas. The viscosity pattern inside malignant lesions also appeared to be more heterogeneous compared to the viscosity distribution within benign lesions, such as fibroadenomas and cysts. This can be associated with the higher vascularization or desmoplasia around cancerous tissues [4]. The two fluid–filled cysts that were examined exhibited a considerable contrast in the viscosity within their boundaries compared to the surrounding tissue.

Conclusions: The elasticity and viscosity images obtained during breast vibro–elastography were analyzed and various differentiating features were extracted in order to identify benign and malignant masses. These features include shape and contrast of the lesions in the elasticity images and the viscosity patterns of the lesions.

Acknowledgements: The authors would like to thank NSERC for supporting this work and Dr. William Svensson for his extremely useful insights in breast elastography techniques.

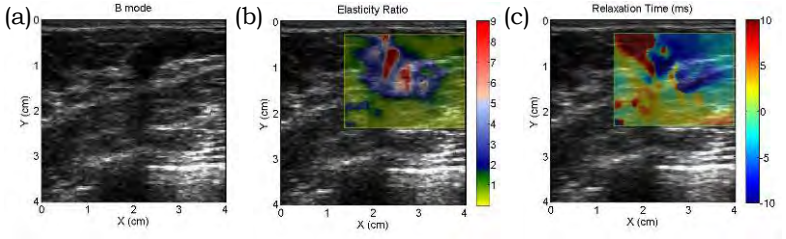

Figure 1: Vibro–elastography of an IDC lesion showing heterogeneity in the parameters. (a) B–mode image, (b) relative elastogram, and (c) relative relaxation–time images of the lesion.

References:

[1] Turgay E. et al.: Identifying Mechanical Properties of Tissue by Ultrasound. Ultras. Med. Biol., V32/N2, 2006.
[2] Eskandari H. et al.: Viscoelastic Parameter Estimation Based on Spectral Analysis. IEEE Trans. UFFC, V55/N7, 2008.
[3] Samani A. et al.: Elastic Moduli of Normal and Pathological Human Breast Tissues: An Inversion–Technique-Based Investigation of 169 Samples. Phys. Med. Biol., V52/N6, 2007.
[4] Insana M.F. et al.: Viscoelastic Imaging of Breast Tumor Microenvironment with Ultrasound. J. Mammary Gland Biol. and Neoplasia, V9/N4, 2004.

* *indicates Presenter*

017 **VAGINAL TACTILE IMAGING: CLINICAL RESULTS.**

Vladimir Egorov[1], Heather van Raalte[2], Vincent Lucente[3].*
[1]Artann Laboratories, 1459 Lower Ferry Rd, Trenton, NJ, 08619, USA; [2]Princeton Urogynecology, 601 Ewing St, Ste. B–19, Princeton, NJ, 08540, USA; [3]The Institute for Female Pelvic Medicine, 3050 Hamilton Blvd, Ste. 200, Allentown, PA, 18104, USA.

Background: Changes in the elasticity of vaginal walls, connective support tissues and muscles are thought to be significant factors in the development of pelvic organ dysfunction with age and parity. Earlier, we tested clinically the Vaginal Tactile Imager (VTI) which has allowed tissue imaging at specified locations in the vagina and assessment of tissue elasticity by means of the elasticity index [1]. VTI is based on principles similar to those of manual palpation; it is capable of visualizing tissue mechanical structure by measuring surface stress patterns under tissue deformation using a pressure sensor array [2].

Aims: The objective of this study is to assess the clinical suitability of new approach for 3–D imaging of the vagina and tissue elasticity quantification.

Methods: Thirty one women were enrolled in the study. The study subjects included 18 women with normal pelvic support and 13 women with pelvic organ prolapse (Stage I–III), average age 60±17 from 28 to 90 years old and average parity 2.5±1.3 (range 0–6). The transvaginal probe comprised of 128 pressure sensors and a 3–D motion tracking sensor covered by disposable sheath with ultrasound lubricant. The images were obtained and recorded in an office setting at the time of routine vaginal examination. Three orthogonal projections of the 3–D vaginal tactile image with VTI probe location are observed by the operator in real time. For prolapse classification, we used the Pelvic Organ Prolapse Quantification (POP–Q) system. The tissue elasticity (Young's modulus) was calculated from spatial gradients in resulting 3–D tactile images. In bench testing, we established accuracy (±15-20%) and reproducibility (±5%) of the method.

Results: All 31 enrolled women were successfully examined with the VTI. Figure 1 presents an example of the imaging data. We found substantial differences in anatomy and tissue elasticity between normal and prolapse conditions, with the age and parity. Young's modulus of vaginal tissue ranged from 1 kPa to 40 kPa. The data demonstrate the respective elasticity modulus decrease up to 320% for the apical anterior walls with Stage III prolapse relative to normals. Average values for tissue elasticity for apical anterior and posterior compartments of nulliparous women were 10.4±4.2 kPa and 7.0±3.4 kPa respectively. For women having 5–6 pregnancies the average values of elasticity modulus decreased up to 290%. The patients were asked to assess the comfort level of VTI examination relative to manual palpation: 80% reported that VTI procedure is the same or more comfortable than manual palpation. No adverse events were reported.

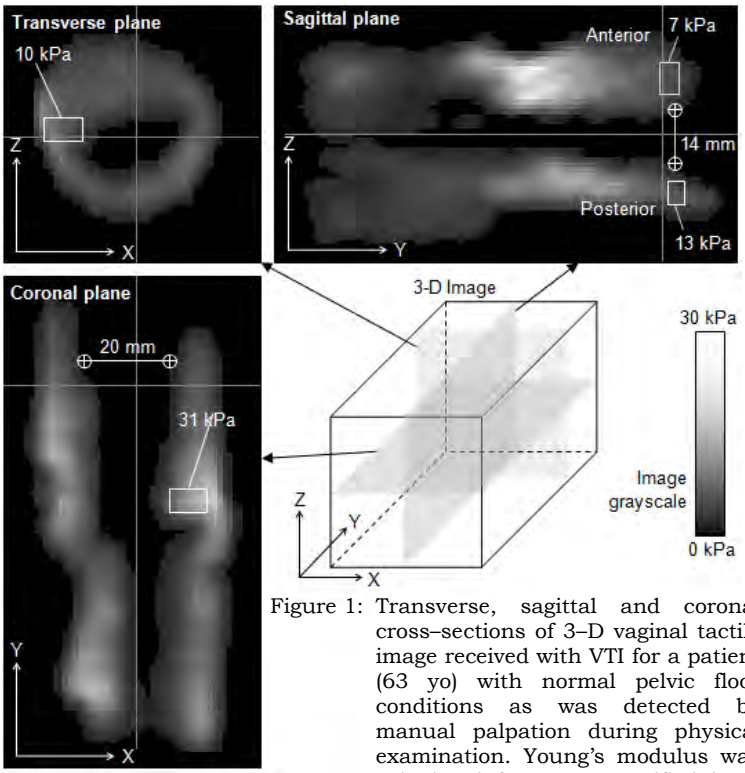

Figure 1: Transverse, sagittal and coronal cross–sections of 3–D vaginal tactile image received with VTI for a patient (63 yo) with normal pelvic floor conditions as was detected by manual palpation during physical examination. Young's modulus was calculated for areas specified by a rectangle.

Conclusions: Our findings suggest that VTI is suitable for 3–D imaging of the vagina and quantitative assessment of vaginal tissue elasticity.

Acknowledgements: The work was supported by the National Institute on Aging, USA, grant R43 AG034714.

References:

[1] Egorov V, van Raalte H, Sarvazyan AP: Vaginal Tactile Imager. IEEE Trans. Biomed. Eng., 57(7), pp. 1736–44, 2010.
[2] Sarvazyan AP: Mechanical Imaging: A New Technology for Medical Diagnostics. Int. J. Med. Inf., 49 pp. 195–216, 1998.

* *indicates Presenter*

076 **OBJECTIVE ASSESSMENT OF CERVICAL SOFTENING DURING PREGNANCY.**

Sabrina Badir[1], Edoardo Mazza[1], Michael Bajka[2].*
[1]Swiss Federal Institute of Technology, 8092 Zurich, SWITZERLAND; [2]University Hospital Zurich, 8091 Zurich, SWITZERLAND.

Background: Preterm cervical ripening is a leading cause of fetal death worldwide. It is still an unsolved important clinical problem. In daily practice, digital palpation is used to determine consistence, effacement, dilatation and position of the cervix (Bishop–Score) in a purely qualitative manner and may be complemented by transvaginal ultrasound to describe cervical total length.

Aims: We report on an ongoing longitudinal clinical study (Ethical approval by KEK Zurich StV02/2007) aiming at quantifying the well known progressive softening of the human uterine cervix during pregnancy. Written informed consent is obtained from any participant. So far 48 pregnant women have been followed during pregnancy. 300 measurements were performed on the regular pregnancy controls at five week intervals ranging from week 5 to week 35.

Methods: Measurements are based on the aspiration method (e.g. M. Hollenstein, ETH PhD thesis Nr 19587). A dedicated instrument has been developed for the present application in pregnancy. It consists of a tube with a circular opening, a pressure sensor, a camera, an aspiration tube and a peristaltic pump, Figure 1. Measurements are performed by the gynecologist during standard gynecological inspections. After speculum application, the tube is inserted in the vagina. Visual monitoring from the camera allows placing the circular opening on the anterior lip of the cervix, at 12 o'clock position, not overlying columnar epithelium (to minimize the risk of bleeding). The tip of the device is positioned vertically on the epithelium and put in contact as gently as possible. Pressure in the cylinder is reduced by extraction of the air through a thin aspiration pipe. Cervical tissue is sucked into the cylinder through the circular opening until it reaches and closes the aspiration pipe. The (negative) pressure value, p_{cl}, at which tissue deformation caused the pipe to close, is recorded, the pressure quickly completely reversed and the tip of the device is disconnected. Two or three complete aspiration cycles are performed at the same location for each measurement session.

Results: Figure 2 shows all p_{cl} values obtained thus far (first measurement). There is a general trend of softening (lower values of p_{cl}) for increasing gestational age. The scatter is larger in the early stages of pregnancy. Three representative individual histories are highlighted, indicating in some cases a continuous decrease, in other cases a fluctuation of the measured resistance to deformation.

Conclusions: The displacement field generated using the aspiration device leads to deformations of cervical tissue up to 3–4 mm below the squamous epithelium. The present study will evaluate whether the structural changes occurring in the cervix to inform delivery decisions might be objectively detected using the aspiration technique. Our measurement results currently support the potential use of this method for monitoring the compliance of the cervix. As expected, there is a general trend towards increasing compliance throughout gestation. Furthermore, evaluation of repeatability and influence of device placement have shown a level of uncertainty in the range of ±10% for the measured closure pressure, p_{cl}, thus a much lower value compared to the observed stiffness change in the course of pregnancy.

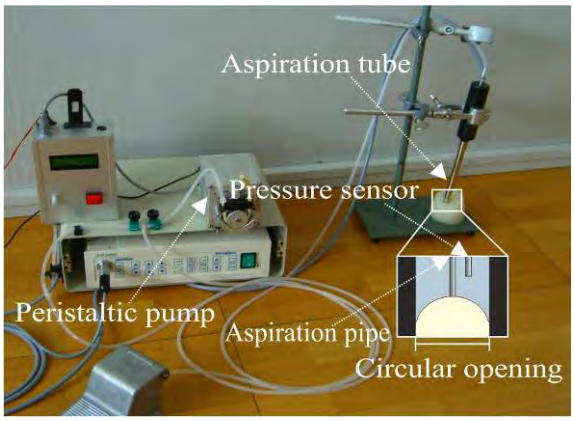

Figure 1: Aspiration experiment, main components

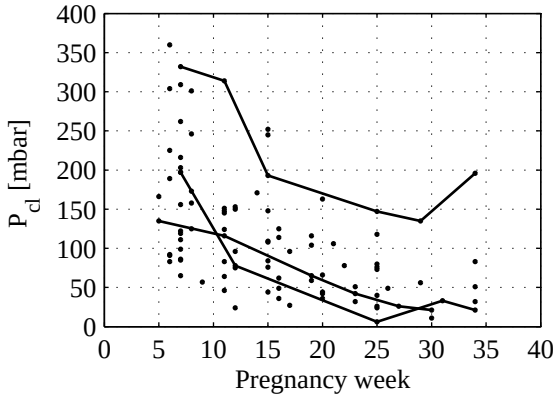

Figure 2: Aspiration pressure during gestation

006 **TRANSRECTAL SHEAR WAVE ELASTOGRAPHY OF THE PROSTATE: INITIAL RESULTS AND POTENTIAL IMPLICATIONS.**

Richard G. Barr[1], Joseph R. Grajo[2].*
[1]Southwoods Radiology Consultants, 250 DeBartolo Place, Youngstown, OH, USA; [2]University of South Florida, 12901 Bruce B Downs Blvd, MDC 41, Tampa, FL, USA.

Background: Prostate cancer is the second–leading cause of cancer mortality in men in the United States. Current diagnosis relies on digital rectal exam (DRE), prostate specific antigen level (PSA), transrectal ultrasound (TRUS) and magnetic resonance imaging (MRI). These techniques have limitations, and PSA levels have a low positive predictive value for cancer. Shear wave elastography (SWE) has the potential to address these limitations and add to the current diagnostic workup [1,2].

Aims: To determine if SWE of the prostate can lead to higher sensitivity and specificity in detecting cancer; To determine if SWE can increase the negative predictive value for prostate cancer screening and better direct image-guided biopsy.

Methods: Patients scheduled for TRUS biopsy with an elevated PSA and/or abnormal DRE were asked to participate in the IRB approved study. A total of 32 patients participated in the study, providing 192 sextants. Average patient age was 64.2 years (range 53–79). Average PSA was 5.05 (range 0.21–18.6). TRUS was performed with B–mode and color Doppler imaging. Nodules and other suspicious areas were noted by the radiologist. SWE was then performed using a SE12–3 probe on a SuperSonic Imagine (SSI, France) system. Afterwards, the urologist performed a DRE, scanned with B–mode ultrasound and performed sextant biopsy based on standard clinical practice without knowledge of the SWE findings. Any abnormalities on B–mode alone were also biopsied per standard protocol. If abnormalities on SWE were not included in the original biopsy, additional samples of these areas were obtained after the completion of standard biopsy. The prostate was divided into sextants for analysis. SWE was deemed positive if the area was greater than 35 kPa, negative if less than 20 kPa and borderline if 20–35 kPa. B–mode nodules were documented and correlated with SWE values. SWE, and biopsy results were compared for each sextant. Biopsies were staged based on the Gleason score (scale of 2–10).

Results: A total of 14 foci of cancer were detected in 7 of the 32 patients (22%). Based on the SWE findings, 173/178 sextants were true negatives. 14/14 sextants were true positives. There were 5 false positives and 0 false negatives. This produced a sensitivity of 100%, specificity of 97%, positive predictive value of 74% and negative predictive value of 100%.

Conclusions: Transrectal shear wave elastography of the prostate has the potential to become the primary imaging modality for detection of prostate cancer. With a high negative predictive value, this technique could eliminate a significant number of biopsies.

Acknowledgements: Dr. Barr receives equipment support from SuperSonic Imagine.

References:

[1] Bercoff J.: ShearWave Elastography. Supersonic Imagine White Paper. October, 2008.
[2] Correas JM, Khairoune A, Tissier AM, et al.: Trans–Rectal Quantitative Shear Wave Elastography: Application to Prostate Cancer – A Feasibility Study. Proceedings of the European Congress of Radiology, 2011.

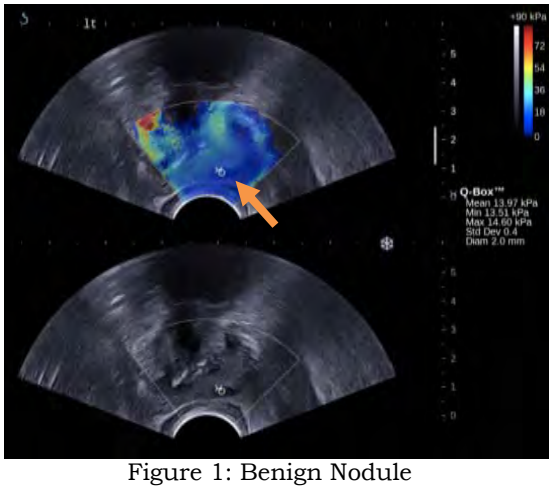

Figure 1: Benign Nodule


Figure 2: Adenocarcinoma (Gleason 6)

* *indicates Presenter*

081 **ELASTOGRAPHY MAY PLAY AN IMPORTANT ROLE IN DIAGNOSIS OF PROSTATE CANCER: INITIAL RESULTS.**

Rafal Z. Slapa[1], Wieslaw S. Jakubowski[1], Artur Przewor[2], Tadeusz Dmowski[2].*
[1]Diagnostic Imaging Department, Medical University of Warsaw, Faculty of Medicine II with the English Division and the Physiotherapy Division, Warsaw, POLAND; [2]Urology Department, Mazovia Specialist Hospital, Siedlce, POLAND.

Background: The prostate specific antigen (PSA) and digital rectal examination are not accurate enough diagnostic tools in the diagnosing prostate cancer. The introduction of B–mode ultrasound and color Doppler has not significantly improved diagnosis. Investigations of new diagnostic methods, such as elastography, aim at pointing out biopsy sites to reduce the number of cores and to improve the accuracy of diagnosis and quality of life of patients [1]. The current diagnostic gold standard for the diagnosis of prostate carcinoma in our Department is eight core systematic biopsies of prostate.

Aims: The purpose of the study was to compare the usefulness of strain elastography for biopsy guidance in relation to eight core systematic biopsies of the prostate in diagnosis of prostate cancer.

Methods: We evaluated 14 patients with suspicion of prostate adenocarcinoma (elevated PSA levels > 6 ng/mL and/or positive digital rectal examination). Ultrasound examination was performed with Aplio XG (Toshiba, Japan) and endorectal 6 MHz transducer. The stiffness of the prostate tissue was evaluated with strain elastography qualitatively and with symmetric sites strain ratio with elasto Q (Toshiba). The strain was produced by manual compression of the prostate with the endorectal probe at 3 levels from base to apex of the prostate.

Results: Final diagnoses were 7 adenocarcinomas of prostate. Eight core systematic prostate biopsies revealed 5 adenocarcinomas. Elastography revealed 2 additional adenocarcinomas, however did not reveal 1 advanced multifocal tumor. Elastography also revealed prostatic intraepithelial neoplasia (PIN), high grade that was not revealed by systematic biopsy.

Conclusions: (1) Preliminary results indicate that elastography maybe a valuable tool in diagnosis of prostate carcinoma. (2) Elastography may outperform the eight core systematic prostate biopsy due to: (a) improvement of sensitivity in low–grade or uni–focal cancers, (b) decrease of side effects (infections, bleeding) and (c) improvement of quality of life of patients (decrease of pain and side effects). (3) Further multicenter large scale studies evaluating the usefulness of elastography in diagnostics of prostate cancer are warranted.

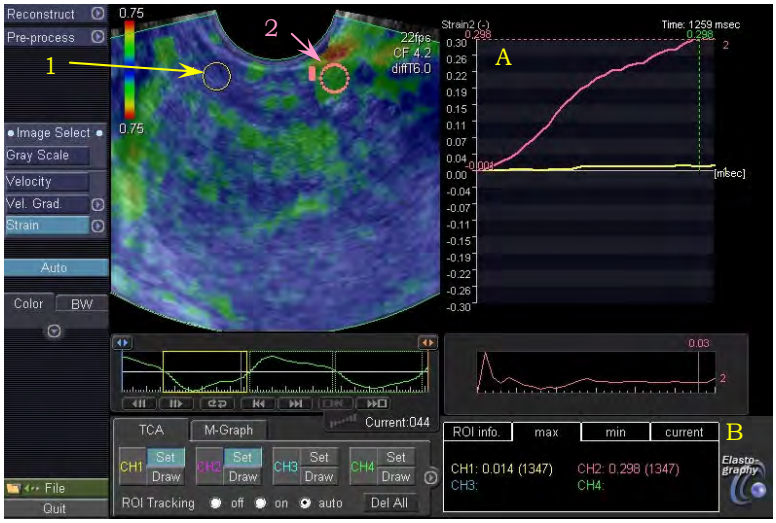

Figure 1: Strain elastography of a patient with Gleason 7 adenocarcinoma in the right side of the prostate [circle 1 (yellow)]. The deeply blue color of the lesion indicates low strain, e.g. high stiffness of the lesion that was revealed only by elastography but not revealed by systematic eight core prostate biopsy. The graph (A) and measurements of the maximal strain (B) of the lesion [yellow (1)] and symmetric prostatic tissue [pink (2)] shows that the cancer is over 20 times stiffer than normal prostatic tissue.

References:

[1] Ginat DT, Destounis SV, Barr RG, Castaneda B, Strang JG, Rubens DJ: US Elastography of Breast and Prostate Lesions. RadioGraphics, 29, pp. 2007–2016, 2009.

Invited Presentation:

100 **MAINSTREAM SIGNAL PROCESSING METHODS FOR STRAIN IMAGING.**

Richard G.P. Lopata[1,2].*
[1]Cardiovascular BioMechanics, Biomedical Engineering Department, Eindhoven University of Technology, Eindhoven, THE NETHERLANDS; [2]Biomedical Engineering Department, Maastricht University Medical Center, Maastricht, THE NETHERLANDS.

Aims: This presentation will provide an overview of the developments of cross–correlation based signal techniques strain imaging using RF data.

The Early, One–Dimensional Days: From the beginning of elastography in 1991 [1], strong emphasize has been on estimating the displacement of tissue to calculate the strain. Initially, the displacement along the ultrasound beam was calculated from 1D cross–correlation analysis. The peak of the cross–correlation function determines what the shift between the two ultrasound signals is. To increase resolution, different interpolation methods were investigated [2]. Soon, fast implementation for time delay estimation was investigated [3] as well as adaptive strain imaging techniques [4]. Furthermore, theoretical studies were performed to determine the best window size and transmitted frequency for a given strain level and signal to noise ratio [5,6].

Multi–Dimensional Strain Imaging: After a decade, strain estimation in the direction perpendicular to the ultrasound beam also became an issue. Initially, displacements in this direction were determined with computationally intensive algorithms [7]. Later, fast implementations for 2D and 3D strain imaging were developed [8,9]. Especially in cardiology, 3D speckle tracking is now widely used [10]. Recently, coarse–to–fine algorithms for this application were developed with increased sensitivity and resolution with respect to speckle tracking methods [11–13]. The problem with strain estimation perpendicular to the ultrasound beam is the lack of phase information in this direction. Dedicated imaging schemes using data acquired at large beam steered angles were developed to circumvent this problem. Initially this technique was used for improving the axial strain estimate [14], but this technique has demonstrated to be very beneficial for lateral and elevational strain estimation [15].

References:

[1] J. Ophir, et al.: Elastography: A Quantitative Method for Imaging the Elasticity of Biological Tissues. Ultrason.Imaging, Vol. 13, pp. 111–134, 1991.
[2] E.I. Céspedes, et al.: Methods for Estimation of Subsample Time Delays of Digitized Echo Signals. Ultrasonic Imaging, Vol. 17, pp. 142–171, 1995.
[3] A. Pesavento, et al.: New Real–Time Strain Imaging Concepts using Diagnostic Ultrasound. Phys Med Biol, Vol. 45, pp. 1423–35, 2000.
[4] S.K. Alam, et al.: An Adaptive Strain Estimator for Elastography. IEEE Trans. on Ultras., Ferro., and Freq. Cntrl., Vol 45(2), pp. 461–472, 1998.
[5] T. Varghese and J. Ophir: A Theoretical Framework for Performance Characterization of Elastography: The Strain Filter. IEEE Trans. on Ultras., Ferro., and Freq. Cntrl., Vol. 44, pp. 164–172, 1997.
[6] T. Varghese, et al.: Tradeoffs in Elastographic Imaging. Ultrasonic Imaging, Vol. 23, pp. 216–248, 2001.
[7] E. Konofagou and J. Ophir: A New Elastographic Method for Estimation and Imaging of Lateral Displacements, Lateral Strains, Corrected Axial Strains and Poisson's Ratios in Tissues. Ultras. in Med. and Biol., Vol. 24, pp. 1183–1199, 1998.
[8] X. Chen, et al.: Lateral Speckle Tracking using Synthetic Lateral Phase. IEEE Trans. on Ultras., Ferro., and Freq. Cntrl., Vol. 51(5), pp. 540–550, 2004.
[9] X. Chen, et al.: 3–D Correlation–Based Speckle Tracking. Ultrason.Imaging, Vol. 27, pp. 21–36, 2005.
[10] L.P. Koopman, et al.: Comparison between Different Speckle Tracking and Color Tissue Doppler Techniques to Measure Global and Regional Myocardial Deformation in Children. J.Am.Soc.Echocardiogr., 2010.
[11] R.G. Lopata, et al.: Three–Dimensional Cardiac Strain Imaging in Healthy Children using RF–Data. Ultrasound Med. Biol., Vol. 37, pp. 1399–1408, 2011.
[12] R.G.P. Lopata, et al.: Performance Evaluation of Methods for Two–Dimensional Displacement and Strain Estimation using Ultrasound Radio Frequency Data. Ultrasound Med.Biol., Vol. 35, pp. 796–812, 2009.
[13] R.G.P. Lopata, et al.: Cardiac Biplane Strain Imaging: Initial *In Vivo* Experience. Phys.Med.Biol., Vol. 55, pp. 963–979, 2010.
[14] M. Rao, et al.: Spatial-Angular Compounding for Elastography using Beam Steering on Linear Array Transducers. Med. Phys., –ol. 33, pp. 618–626, 2006.
[15] H.H.G. Hansen, et al.: Full 2D Displacement Vector and Strain Tensor Estimation for Superficial Tissue using Beam Steered Ultrasound Imaging, Physics in Medicine and Biology, Vol. 5, pp. 3201–3218, 2010.
[16] And many, many others …

021 **RETAINING AXIAL-LATERAL ORTHOGONALITY IN STEERED ULTRASOUND DATA FOR IMPROVED IMAGE QUALITY IN RECONSTRUCTED LATERAL DISPLACEMENT DATA.**

Leo Garcia[1], Jérémie Fromageau[1], Richard J. Housden[2], Graham M. Treece[2], Christopher Uff[1], Jeffrey C. Bamber[1].*

[1]Institute of Cancer Research, Joint Department of Physics, 15 Cotswold Rd, Sutton, Surrey SM2 5NG, England, UK; [2]University of Cambridge, Engineering Department, Trumpington Street, Cambridge, CB2 1PZ, England, UK.

Background: In quasi–static ultrasound (US) elastography, only tissue displacements in the direction of beam propagation, referred to as 'axial', are measured to high quality, although an ability to measure other components of displacement is desired to more fully characterize the mechanical behavior of tissue. This has prompted a number of studies that use displacements measured from multiple US beams at different angles, to reconstruct the full displacement vector. Most previous such studies (except [1]) implemented this method using one–dimensional (1D) US tracking only, despite the fact that 2D tracking helps to retain echo correlation and hence improves tracking precision. The need for 2D tracking is expected to be particularly important when tissue is displaced across steered US beams, by pressing with the US probe.

Aims: We show that 2D displacement tracking with unmodified electronically–steered echo data results in tracking errors due to loss of point spread function (PSF) separability and present a method of scan converting RF data to retain axial–lateral orthogonality (Figure 1, Equation 1). This permits 2D displacement tracking, improves the angled axial displacement estimates and allows angled lateral displacements to be used in displacement vector reconstruction. Changes in image quality of lateral displacements reconstructed using 1D and 2D tracked steered axial and steered lateral data are compared.

Methods: Simulated and experimental ultrasound data from the compression of a homogeneous elastic medium are used in this study.

Figure 1: RF A–lines are rearranged, using Equation 1, according to the known steering angle α_i and image dimensions. Where Δh_j is the axial displacement applied to the jth A–line, S is the total number of RF samples in the scan plane, j is the A–line number where the zeroth is the furthest left (for $\alpha_i < 0°$) or furthest right (for $\alpha_i > 0°$), w is the width of the scan plane and N is the total number of A–lines. PSFs, measured by scanning a wire target in water, are shown as the inserted images.

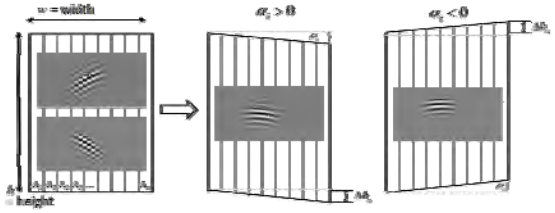

$$\Delta h_j = \frac{S}{h}\left(j\frac{w}{N}\tan\alpha_i \right) \qquad \text{Equation 1}$$

Results: 2D displacement tracking of reshaped data increases the lateral coherence of the PSF (Figure 1) and the mean correlation coefficient across the image plane for all steering angles, compared to a 1D track alone (Figure 2). However, the root mean square error (RMSE) for lateral displacements reconstructed from 2D tracked displacements was slightly poorer than for those obtained by 1D tracking at low levels of compression. This may be due to an interpolation error during the reshaping process, which we will endeavor to eliminate in future work. Residual standard deviation and RMSE (Figure 3) improves at high strains, where 2D tracking is most needed. Displacements reconstructed using angled lateral inputs are of better quality than unsteered lateral displacements, but worse than axial–only reconstructed data.

Figure 2: Difference in mean image correlation coefficient between 2D and 1D tracked simulated data.

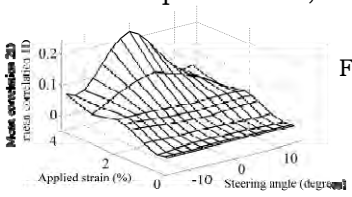

Figure 3: Difference in mean image residual RMSE between 2D and 1D tracked simulated data.

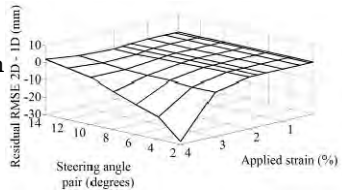

Conclusions: The technique of RF echo image reshaping according to the steering angle permits 2D displacement tracking of steered ultrasound data, improving the steered axial displacement estimates and allowing steered axial and lateral displacement data to be used in displacement vector reconstruction, at the cost of additional computation time. Our future interests include accounting for variations between the input steering angle and the actual direction of beam propagation, and investigating corresponding potential improvements *in vivo*.

Acknowledgements: This work was funded by the EPSRC.

References:

[1] Hansen et al.: IEEE Trans Med Imaging. 28(6), pp. 872–80, 2009.

053 **PHYSICAL BOUNDARY RECONSTRUCTION: A NOVEL METHOD TO DETERMINE VISCOELASTIC PARAMETERS FROM MAGNETIC RESONANCE ELASTOGRAPHY DATA.**

Philippe Garteiser[1], Sabrina Doblas[1], Valerie Vilgrain[2], Bernard Van Beers[1,2], Ralph Sinkus[1].*
[1]IPMA (Physiologic and Molecular MRI of the Abdomen), INSERM UMR773, Bichat–Beaujon Biomedical Research Center, 100, Bd. Du General Leclerc, 92110 Clichy, FRANCE, [2]Radiology Department, Beaujon Hospital, 100, Bd. Du General Leclerc, 92110 Clichy, FRANCE.

Background: The direct reconstruction of viscoelastic parameters in MR–Elastography (MRE [1]) is based on measured displacement data and the subsequent estimation of their spatial derivatives to solve the underlying wave equation. When operating in 3D, inversion of each spatial component of the wave equation leads different estimates for the viscoelastic parameters [2]. Here, we are proposing a new approach for estimating the viscoelastic parameters from 3D displacement data; this novel algorithm is designed to better reflect the underlying physics by including physical boundary conditions (PBC) as constraints to the partial differential equation governing the reconstruction process (Figure 1).

Aims: To introduce physical constraints into the fit to stabilize the MRE wave equation inversion problem in the presence of experimental noise.

Methods: For many *in–vivo* applications, we assume that tissue is mechanically isotropic. Hence, the estimates for the complex shear modulus G^* obtained from the different displacement directions are simply averaged. With PBC (Figure1b) the constraints of incompressibility and isotropy were included in the reconstruction process, thereby introducing mechanical parameter terms into the inversion matrix. Consequently, the polynomial fit procedure was carried out over a range of reasonable G^* values, and the combination of $G^*=Gd+iGl$ yielding the lowest x^2 for the fit was taken as solution for that location in space. Validity of the method was demonstrated on analytical solutions of propagating noisy plane waves and on experimental data acquired with conventional MRE techniques [3,4] from patients with liver disease.

Results: PBC reconstruction estimates stayed within 10% of the true value for noise levels sufficient to fail the conventional method (Figure 2a). Consequently, noise sensitivity, as seen from a gradual decrease of viscoelastic estimates along an arbitrary attenuation direction (Figure 2b), was less pronounced in maps calculated with the PBC method. This result remained valid over noise levels spanning typical experimental noise. PBC reconstruction was applied to clinical datasets from a cohort of patients with varying degrees of liver fibrosis or steatosis (Figure 2c and d). In addition to qualitatively better maps (Figure 1c and d), PBC reconstruction detected differences between normal and cirrhotic parenchyma or between normal and fibrotic components with higher statistical power than the conventional reconstruction.

Conclusions: The PBC reconstruction algorithm described herein shows promise as a robust, noise–insensitive method with direct applicability to clinically relevant magnetic resonance elastography data.

References:

[1] Muthupillai & al.: Nat. Med., 1996.
[2] Sinkus & al.: Phys. Med. Biol., 2000.
[3] Huwart & al.: Eur. Radiol., 2008.
[4] Huwart & al.: Radiol., 2007.

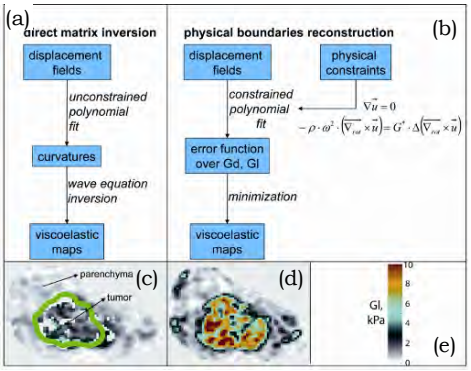

Figure 1: Presentation of the conventional (a) and PBC; (b) reconstruction methods. U=displacement, G^*=complex shear modulus, ρ=density, ω=acoustic frequency, Gd=storage modulus, Gl=loss modulus; (c) conventional method; (d) PBC reconstruction of a liver cancer patient dataset, green outline=tumor; (e) colour scale in kPa.

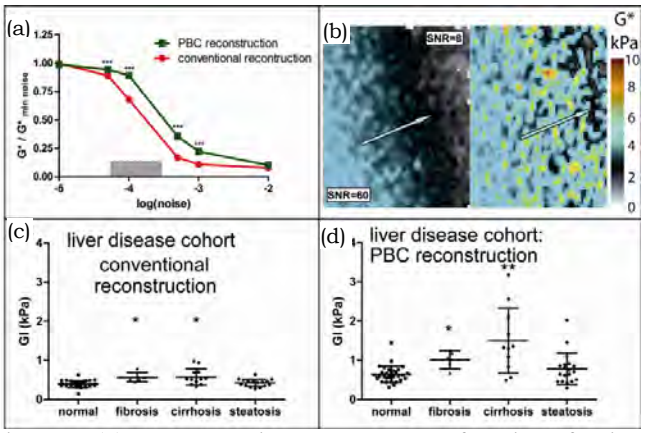

Figure 2: (a) Reconstruction accuracy as a function of noise levels; (b) Units=kPa, arrows=attenuation direction, insets=local signal to noise ratios in the displacement maps simulated with G^*=6.0kPa; (c, d) Evaluation of viscosity in diffuse liver disease patients with conventional or PBC reconstruction.

* *indicates Presenter*

064 **LATERAL MODULATION IMAGING USING SIMPLE NON–STEERING BEAMFORMING.**

Chikayoshi Sumi[1], Yuuki Takanashi[1], Yousuke Ishii[1], Naoto Yamazaki[1].*
[1]Sophia University, 7–1, Kioi-cho, Chiyoda–ku, Tokyo 102–8554, JAPAN.

Background: A number of ultrasonic (US) displacement/velocity measurement methods have been extensively developed for measurements of blood flow, tissue motion (breast, liver, heart) and strain [1]. Lateral modulation (LM) methods have also been reported using steered crossed beams, and these methods permit measurement of a displacement vector [1]. LM echo imaging has almost the same lateral resolution as the axial resolution [2]. Another new beamforming using only a steering angle (ASTA) or an echo rotation [3,4] has also been proposed.

Aims: Even when using a simple beamforming, i.e., a non–steering, a higher lateral modulation frequency is generated after the beamforming which allows high quality LM imaging and more accurate displacement vector/strain tensor and shear modulus measurements. This can be achieved by disregarding laterally, low frequency spectra as an application of the spectra frequency division method [SFDM, i.e., the original multidimensional autocorrelation method (MAM)] [1–4]. Lateral cosine and sine modulations can also be interchangeable in a frequency domain, i.e., by changing the sign of spectra. For the echo imaging, a lateral cosine modulation should be used.

Methods: The same laterally compressed agar phantom data previously obtained [1,2] were used (a stiff cylindrical inclusion with dia=10mm; a relative shear modulus, 3.29). For the apodization, parabolic (PA) and rectangular (RECT) functions were used. For comparison, LM using steered crossed beams was also performed. The lateral resolution is evaluated using an autocorrelation function at respective depths. For comparison, over–determined systems for axial as well as lateral and vector measurements were also realized by SFDM or generating more beams than theoretically required beams. Incoherent superposition of echo images obtained by SFDM and the original image was also performed for speckle reduction.

Results: Figure 1 shows (a) the lateral cosine and sine modulation imaging, (b) autocorrelation functions and (c) measured displacement vectors and elasticity. Cutoff frequencies used are indicated. Interestingly, LM using RECTs yielded a lower accuracy than that using Pas ((c) middle vs upper). As shown, LM with RECTs yielded fewer oscillations than that using PAs due to the large wideband generated ((b) middle). In such a case, the sine modulation yields a higher frequency than the cosine modulation. However, disregarding of the low frequency spectra improved the oscillations (b) and measurement accuracy (c), although the bandwidth decreased. Similarly to LM using Pas (upper), the cosine and sine modulations yielded almost the same accuracy. The effectiveness was also confirmed for the non–modulation case, particularly, using RECT (lower). However, LM with PAs yielded the best LM imaging and measurements. Moreover, even an over–determined system generated from non-steering echo data yielded a higher accuracy than the corresponding normal system (omitted). With a high echo SNR, the least squares measurement was more accurate than the superposition of measurements and vice versa. Multiple steered beams were effective particularly for a low echo SNR case (e.g., steered plane wave transmissions). We also succeeded in the speckle reduction (e.g., horizontal divisions for the non–steering, (d)).

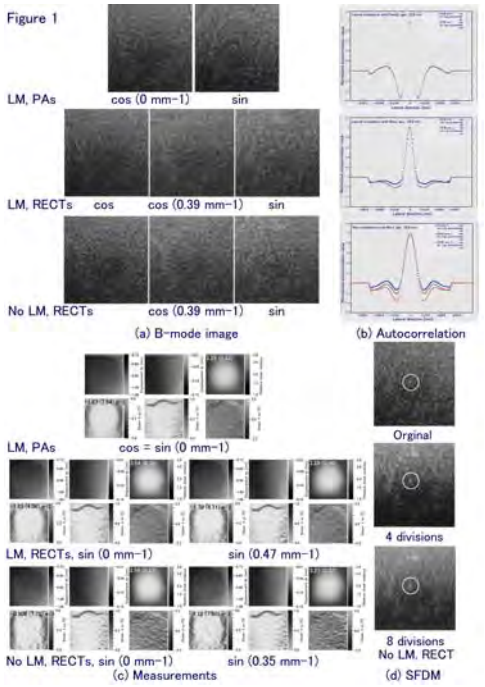

Conclusions: New imaging and measurements were effective for a simple non–steering beamforming and LM. In terms of accuracy, an over–determined system was also effective. Properly, these will be used for US microscope, acoustic radiation force imaging and high intensity focus ultrasound treatment as well.

References:

[1] C. Sumi: IEEE Trans. UFFC, 55, pp. 24–43, 2008.
[2] C. Sumi et al.: IEEE Trans. UFFC, 55, pp. 2607–2625, 2008.
[3] C. Sumi: Rep Med Imag, Vol. 3, pp. 61–81, 2010.
[4] C. Sumi: Proc. 9th Int Tissue Elasticity Conf, p. 72, 2010.

068 **A COMBINED REGION–EDGE–BASED APPROACH TO SEGMENTATION OF THE PROSTATE IN MAGNETIC RESONANCE ELASTOGRAPHY.**

Guy Nir[1], Ali Baghani[1], Ramin S. Sahebjavaher[1], Ralph Sinkus[2], Septimiu E. Salcudean[1].*
[1]University of British Columbia, Vancouver, BC, CANADA; [2]Centre de Recherche Biomédicale Bichat–Beaujon (CRB3), Paris, FRANCE.

Background: Accurate localization of the prostate gland is critical in the planning and delivery of prostate cancer treatment. Automatic segmentation methods improve speed, consistency and reproducibility of the localization process. MRI is currently the gold standard for imaging of the prostate. While high resolution T2–weighted images are very detailed, the global intensity statistics are not sufficiently descriptive, requiring most segmentation approaches to employ prior information and initialization. MR elastography (MRE) [1] is a non–invasive imaging technique that characterizes the mechanical properties of tissues. In order to speed up the acquisition process, the produced elastograms typically have low resolution. However, in our experience, elastograms have superior prostate–to–background contrast compared to T2–weighted images, although the prostate edges may appear blurred. While the phase component of the acquired MRE signal is used to obtain the elastograms, the magnitude component produces images that provide similar edge continuity as in normal T2–weighted images. Thus, fusion of an elastogram and its corresponding magnitude image may improve segmentation accuracy without operator intervention.

Aims: To develop a method for an automatic prostate segmentation in MRE images that does not require prior shape information by utilizing the complementary property of the elastogram and magnitude image.

Methods: Five volunteers underwent a T2–weighted MRI scan followed by MRE. Each MRE dataset comprises seven 64x64 mid–gland transverse slices with 1.5mm^3 voxels. For each slice, an elastogram and a magnitude image were extracted. We use an active contour model that evolves an (arbitrary) initial segmentation curve until convergence. The model is a linear combination of the region–based model in [2] and the edge–based model in [3]. The region–based model is global and relies on image statistics to partition the image into two homogeneous regions. The edge–based model drives the curve to lock onto local maxima of image gradient values. Due to the nature of MRE images, we employ the region–based term on the elastogram and the edge–based term on the corresponding magnitude image.

Results: We applied the proposed algorithm to each of the 35 pairs of images and compared the automatic contours to manual segmentations of the T2–weighted images. The resulted mean absolute distance between the contours was 1.8±0.6mm with a maximum distance of 5.6±1.9mm. The relative area error was 7.6±2.4%, and the duration of the segmentation process was 2s per slice.

Conclusions: We outlined a method for the automatic segmentation of the prostate in MRE images without prior shape information or operator intervention. To the best of our knowledge, this is the first method for automatic prostate segmentation in MRE. The method combines region information from the elastogram and edge information from the magnitude image. It is fast, robust and achieves good results.

Acknowledgements: This project was funded by NSERC and CIHR.

References:

[1] Muthupillai R, Lomas D, Rossman P, Greenleaf J, Manduca A, Ehman R: Magnetic Resonance Elastography by Direct Visualization of Propagating Acoustic Strain Waves. Science, 269, pp. 1854–1857, 1995.
[2] Chan T, Vese L: Active Contours without Edges. IEEE Trans. on Image Processing, 10, pp. 266–277, 2001.
[3] Caselles V, Kimmel R, Sapiro G: Geodesic Active Contours. Int. J. Computer Vision, 22, pp. 61–79, 1997.

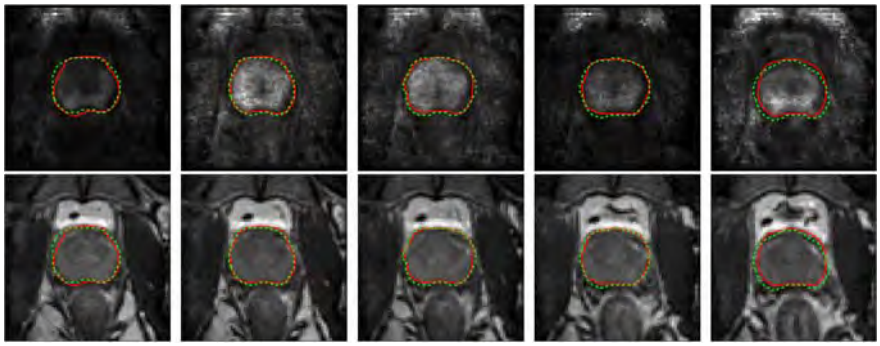

Figure 1: Segmentation results of five slices from one dataset. The automatic (solid red) and the manual (dashed green) contours are overlaid on the elastograms (top row) and corresponding magnitude images (bottom row).

* *indicates Presenter*

091 **GRATING LOBES AND STRAIN IMAGING AT LARGE BEAM STEERING ANGLES.**

HHG Hansen[1], CL de Korte[1].*
[1]Radboud University Nijmegen Medical Centre, Nijmegen, THE NETHERLANDS.

Background: Compounding or projection of axial displacement data obtained with a beam steered linear array transducer is often used to improve the accuracy of displacement and strain estimation [1,2]. For estimation of the displacement component perpendicular to the transducer footplate, projection of axial data obtained at the largest possible beam steering angles is preferred [1]. However, with increasing angle, the distortion caused by grating lobes increases which might reduce displacement estimation precision.

Aims: To determine the effect of grating lobes on displacement estimation precision.

Methods: A Medison Accuvix V10 ultrasound system equipped with a linear array transducer L5–13 (pitch 200μm, 3–13MHz, 20dB bandwidth) was used to acquire RF data of a homogeneous block phantom before and after ~2mm vertical displacement of the phantom. The phantom was created by freeze thawing a solution of 1% of scatterers, 10% of polyvinyl alcohol, 20% cooling liquid and water. RF data were acquired at beam steering angles of –30° to +30° in steps of 15°. Because grating lobes are frequency dependent and dominate most at higher frequencies, pre– and post–displacement datasets were created after band–pass filtering with upper frequency cut–off points varying between 5 and 11MHz in steps of 1MHz. The lower frequency cut–off was kept fixed at 3MHz. Axial displacements for each dataset were determined using a coarse–to–fine 2D cross–correlation based algorithm. The angular axial displacement fields were projected vertically and mean and standard deviations were determined.

Results: The graph below shows the standard deviations of the displacement estimates for the various steering angles, and cut–off frequencies. For the transducer used, theoretically no grating lobe signal is present below 5.1MHz and 6.1MHz at beam steering angles of 30° and 15°, respectively [3]. However, the standard deviations are much larger at these cut–off frequencies than for higher frequency cut–off points. For ±30°, an optimum is observed at a cut–off frequency of 7MHz, and for ±15°, it is most optimal to use the highest possible cut–off. An explanation for this might be that the grating lobe signal is still weak compared to the main lobe signal at relatively low frequencies and does not disturb the displacement estimation, whereas the higher frequency information in the main lobe is necessary for accurate displacement estimation. Furthermore, the grating lobe motion is frequency dependent whereas the signal of the main lobe displaces similar for the entire frequency range.

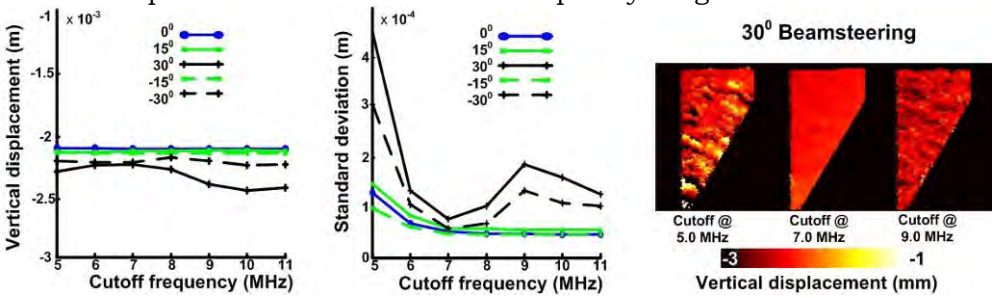

Conclusions: Grating lobes do disturb displacement estimation at high frequencies at large angles. However, for optimal displacement estimation it can be better not to remove the grating lobe signal entirely by low pass filtering, because it also removes part of the main lobe which can be vital for accurate displacement estimation.

Acknowledgements: The support of the Dutch Technology Foundation (STW) is acknowledged, and the authors would like to thank Medison for the development of the automatic multi–angle scanning mode.

References:

[1] H.H.G. Hansen, R.G.P. Lopata and C.L. de Korte: Full 2D Displacement Vector and Strain Tensor Estimation for Superficial Tissue Using Beam Steered Ultrasound Imaging. Phys. Med. Biol., (55), pp. 3201–3218, 2010.
[2] M. Rao, Q. Chen, H. Shi, T. Varghese, E.L. Madsen, J.A. Zagzebski and T.A. Wilson: Normal and Shear Strain Estimation using Beam Steering on Linear-Array Transducers. Ultras. Med. Biol., (33), pp. 57–66, 2007.
[3] H.H.G. Hansen, R.G.P. Lopata and C.L. de Korte: Noninvasive Carotid Strain Imaging using Angular Compounding at Large Beam Steered Angles: Validation in Vessel Phantoms. IEEE Trans. Med. Imaging., 28, pp. 872–880, 2009.

Invited Presentation:

098 **SOFT TISSUE MECHANICAL PROPERTIES AND OPPORTUNITIES TO MEASURE THEM.**

Armen P. Sarvazyan[1].*
[1]Artann Laboratories, 1753 Linvale-Harbourton Rd, Lambertville, NJ, 08530, USA.

Background: In the past 10 years the body of data that describes the elastic properties of soft biological tissues *in vivo* and *in vitro* has grown immensely. It is shown that measuring and imaging tissue elasticity may not only provide means for detecting abnormalities but can also allow differential diagnostics. Sensitivity and specificity of cancer detection and benign/malignant tumor differentiation achieved with the use of elasticity data are comparable to and may exceed that of conventional imaging techniques. Areas of applications of elasticity imaging (EI) in medical diagnostics and treatment monitoring are steadily expanding. The success of EI is a result of the fact that shear mechanical properties are the most variable and structure–sensitive physical characteristics of soft tissues. The range of variation of the Young's modulus, E, of different soft tissues is over three orders of magnitude: from less than 1kPa to more than 1MPa. Ideally, multiple parameters need to be introduced for accurate representation of tissue mechanics, such as viscosity, nonlinearity, hysteresis in the stress–strain curve, anisotropy of elasticity moduli, etc.; although in most applications, it may be sufficient to assess shear (or Young's) elasticity modulus. However, despite great progress in elasticity imaging, there is a widespread lack of understanding of different kind of mechanical properties and what opportunities there are to measure and/or image them.

What Kind of Database of Tissue Mechanical Properties Is Needed? It is believed that the scarcity of reliable accurate experimental data on tissue elasticity is the main limiting factor in fully realizing the potential of EI in differential diagnostics. However, despite the increasing number of publications presenting seemingly accurate experimental data on elasticity of different tissues *in vivo* and *in vitro*, we hardly see any direct impact of these data on clinical efficacy of EI. Indeed, it is hard to make use of tissue elasticity modulus measured with high accuracy, while even within the same tissue, the modulus may vary by hundreds of percent due to normal tissue structural heterogeneity or variations in blood supply. Large variations of tissue elasticity may occur also due to various physiological processes. Systolic elasticity of artery may be twice as that for diastolic artery and systolic versus diastolic elasticity of heart muscle may differ by an order of magnitude. There is not much use of available *in vitro* data because there could be hundreds percent differences between *in vivo* and *in vitro* elasticity values for the same tissue. The bottom line is that much more extensive systematic studies on tissue elasticity are needed than is currently available to fully realize the diagnostic potential of EI. Specifically, the range of variation of tissue mechanical properties as a function of numerous factors including various physiological and pathological processes need to be explored and the correlation between tissue elasticity and histology should be investigated for quantitative differentiation of normal and diseased tissues.

Methods of Tissue Elasticity Measurements: Technologies for assessing mechanical properties of soft tissues are advancing at a rapid pace. Numerous methods and devices based on the use of MRI and ultrasound to track internal deformations induced by external or internal stress were introduced in the last two decades and are being developed currently. There are numerous techniques for *in vivo* assessment of elasticity of directly accessible tissues, e.g., techniques based on the use of surface acoustic waves and on measurement of tissue impedance. These techniques are mainly used for assessment of skin and underlying tissues. A well known aspiration–based method is widely used for measurements of elasticity of biological objects *in vivo* and *in vitro* at micro and macro levels. A new promising technique of testing elasticity of hollow organs such as urethra, cervix, esophagus, intestines and blood vessels is balloon elastography. Indentation method of elasticity measurements widely used in *in vitro* studies is hardly applicable for *in vivo* tests.

Other Uses of Tissue Elasticity Data: Tissue mechanical property data are also necessary for the development of realistic surgical simulators with force feedback. Surgeons have limited tools for safe practicing new or challenging procedures or refreshing their existing skills. One explanation for this shortcoming is that current surgical simulation systems lack data on *in vivo* tissue elasticity. The diseased tissue elasticity differences are of primary interest during an operation. Despite much publicity, telesurgical robotics and virtual reality based surgical simulators, particularly training simulators for minimally invasive surgery, did not live up to their perceived potential. One of the key limiting factors is the absence of life–like phantoms built using realistic tissue elasticity data.

013 **ON THE COMPARISON BETWEEN MRI AND US IMAGING FOR HUMAN HEEL PAD THICKNESS MEASUREMENTS.**

Sara Matteoli[1], Nadège Corbin[1], Jens E. Wilhjelm[1], Søren T. Torp–Pedersen[2].*
[1]DTU Elektro, Biomedical Engineering, Technical University of Denmark, Ørsteds Plads, Bldg. 348, DK–2800, Kgs. Lyngby, DENMARK; [2]The Parker Institute, Frederiksberg Hospital, University of Copenhagen, Nordre Fasanvej 57, DK–2000 Frederiksberg, DENMARK.

Background: The human heel pad thickness, defined as the shortest distance between the calcaneus and heel skin, is one of the intrinsic factors which must be taken into account when investigating the biomechanics of the heel pad [1,2]. In fact, heel pad thickness has been reported to be an important factor in determining stresses observed in healthy as well as pathological feet [1,2]. US, MRI, CT and X–ray can be used to measure the heel pad thickness. Among those, US (portable, fast scanning time, ionizing–free radiation, low expense) and MRI (ionizing–free radiation) are preferable choices. For US however, measurement errors may occur due to the operator–dependability, the uncertainty of the speed of sound in heel pad tissues as well as the presence of artifacts and angle–dependence. It is thus, necessary to verify the reliability of the imaging techniques by comparing results with a gold reference. PVA–cryogel, being a suitable material for mimicking the human soft tissues and compatible to both MRI and US imaging [3], was chosen to build artificial heel pad phantoms in order to investigate the reliability of the measurements.

Aims: The present study concentrates on measuring the bone to skin distance of nine heel pad phantoms from MRI and US images. The comparison with a gold reference allows finding the error.

Methods: Nine heel pad phantoms were created by embedding the lowest part of an artificial calcaneus in PVA–cryogel by use of a mould [4]. The models had three different elasticities (E_1=64kPa, E_2=127kPa, E_3=161kPa) combined with 9 different known skin–to–bone distances. All heel pad phantoms underwent both 3D MRI (3T–VIBE isotropic sequence) and 3D US (12MHz transducer LOQICE9–GE Healthcare). For each modality, the thickness was taken as the average between two measurements done by the same operator. Furthermore, for US measurements, the thickness was also calculated by using a speed of sound of 1530ms^{-1}; for PVA–cryogel phantoms, it ranges from 1520ms^{-1} to 1540 ms^{-1} [3].

Results: Paired sample t–test was used to compare the thickness measured by MRI or US images with the gold reference (GR). A P–value less than 0.05 was accepted as significant. Results showed a statistically significant difference between MRI and US_{1530} (P–value=0.024), whereas there was not a significant difference between GR and US_{1530} or GR and MRI (P–value=0.438 and P–value=0.480, respectively). Figure1 shows the errors made by US and MRI measurements when compared with GR.

Conclusions: Since the errors (Figure 1) for US are essentially positive, the assumed speed of sound (1540ms^{-1}) is too high. Results thus indicate that the main uncertainty concerning US is the average speed of sound assumed by the scanner. This confirms the necessity to investigate on the real speed of sound for the heel pad tissues, in order to have realistic measurements when dealing with humans.

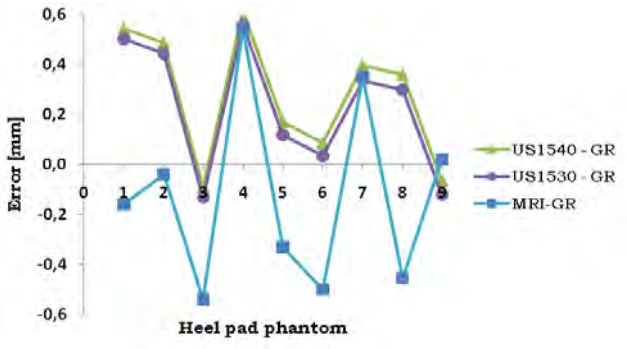

Figure 1: Difference between US or MRI measurements and the gold reference (GR).

References:

[1] Uzel M., et al.: Comparison of Ultrasonography and Radiography in Assessment of the Heel Pad Compressibility Index of Patients with Plantar Heel Pain Syndrome. Joint Bone Spine, 73, pp.196–199, 2006.
[2] Rome K., Campbell R., Flint A., Haslock I.: Ultrasonic Heel Pad Thickness Measurements: A Preliminary Study. Br J Radiology, 71, pp. 1149–1152, 1998.
[3] Surry KJM., Austin HJB., Fenster A., Peters TM.: Poly(Vinyl Alcohol) Cryogel Phantoms for Use in Ultrasound and MR Imaging. Phys. Med. Biol. 49, pp.5529–5546, 2004.
[4] Torp–Pedersen S., et al.: Diagnostic Accuracy of Heel Pad Palpation–A Phantom Study. Journal of Forensic and Legal Medicine, 15, pp.437–442, 2008.

* *indicates Presenter*

022 **CAN ULTRASOUND ELASTOGRAPHY DIFFERENTIATE BETWEEN A THIN LAYER OF SOFT TISSUE AND A SLIPPERY BOUNDARY?**

Leo Garcia[1], Jeffrey C. Bamber[1], Jérémie Fromageau[1], Christopher Uff[1].*
[1]Institute of Cancer Research, Joint Department of Physics, 15 Cotswold Rd, Sutton, Surrey, England, SM2 5NG, UK.

Background: Previous studies such as [1,2] have shown that image features may be extracted from axial shear strain elastograms for use in the assessment of tumor mobility. It was previously noted that in axial strain elastograms, mobile tumors are surrounded by a high strain 'halo', which we showed [3] was due to a displacement discontinuity across the tumor boundary but is visually similar to a thin layer of soft tissue surrounding the tumor; a phenomenon which may manifest if the tumor forms within, or adjacent to, soft fatty tissue, e.g., [4]. Hence, there is motivation to study the extent to which this situation may confound mobility assessment, such that clinical elastograms may be more accurately interpreted.

Aims: To answer the following questions: firstly, are axial shear strain elastogram (ASSE) normalized image feature measurements proposed by [1] significantly different between a mobile inclusion and a soft layer model, and secondly, what elastographic characteristics, if any, can aid differentiation of the two cases?

Methods: Two 2D plane–strain models were generated in Comsol 3.5a (Comsol Inc., USA): a stiff (20kPa) circular inclusion which was free to slip against a homogeneous (10kPa) background, and a circular inclusion adhered to an annulus which was, in turn, adhered to a homogeneous background (Figure 1a). The annulus width was set equal to the length of the strain estimator window such that strain generated within it was similar in elastographic appearance to the strain estimator response to the displacement step across the mobile inclusion boundary. The effects of variation of the Young's modulus of the annulus and the applied axial strain were studied. Axial shear strain image features were measured as in [1].

Results: Visual inspection of Figure 1b and c indicates similarity in both axial and axial shear strain images between the two cases, including the orientation and sign of strain concentrations surrounding the inclusion, as well as heterogeneous strain distributions within the inclusion. Measurement of image feature values (Table 1) produced values (<1) for both models that are typical of mobile tumors. However, axial strain and axial shear strain magnitude within the inclusion are less (-0.14% and -0.15%, respectively, for a 1kPa annulus at 1% applied strain) for the soft halo model, indicating that more strain is transmitted to the inclusion through the slip boundary than the soft layer.

Conclusions: This simulation study presents the case of an inclusion surrounded by a thin layer of soft material, the axial and axial shear strain elastograms of which are strikingly similar to those of a mobile inclusion. Differentiation of the two cases is difficult as image feature measurements yield similar results. One solution may be found through dynamic elastographic assessment, to attempt to deliberately induce slip/stick motion at the tumor to background interface (Figure 2), as suggested in [5].

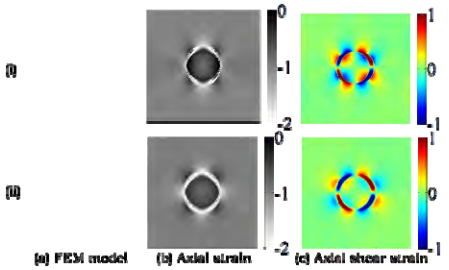

Figure 1: Simulated images from (i) mobile inclusion and (ii) soft halo model.

Normalized ASSE image feature	Mobile inclusion model	Soft halo adhered model
+ve area	0.6682	0.6821
-ve area	0.6546	0.3920
+ve/-ve area difference	0.0136	0.2901
+ve/-ve	0.14	0.20

Table 1: Normalized image feature values for a mobile inclusion model compared to those from the soft halo model.

Figure 2: Sequence of experimental axial strain images from the compression of a phantom containing a stiff mobile inclusion. Contact at the inclusion/background interface is gradually induced.

Acknowledgements: This work was funded by the EPSRC.

References:

[1] Thitaikumar et al.: Phys Med Biol, 52, pp. 2615–2633, 2007.
[2] Thittai et al.: Ultrasound Med Biol, 36(5), pp. 814–820, 2010.
[3] Garcia et al.: IEEE Ultrason Symp, pp. 2426–2428, 2009.
[4] Lorenz et al.: IEEE Ultrason Symp, pp. 1761–1764, 1998.
[5] Uff et al.: Proc of 9th ITEC, p. 115, 2010.

* *indicates Presenter*

029 **SHEAR WAVE ELASTOGRAPHY ON *IN VIVO* PIG KIDNEY: IMPACT OF URINARY AND VASCULAR PRESSURE ON VISCOELASTIC MEASUREMENTS.**

Jean–Luc Gennisson[1], Nicolas Grenier[2], Mickaël Tanter[1].*
[1]Institut Langevin–Ondes et Images, ESPCI ParisTech, CNRS UMR7587, INSERM U979, Paris, FRANCE; [2]Service de Radiologie, Hôpital Pellegrin, Bordeaux, FRANCE.

Background: Chronic kidney disease is a major source of mortality due to an increase of risk factors. Sequential measurement of renal elasticity could help in following the progression of intrarenal fibrosis. However, we know that increased elasticity values can be related to increased fibrotic processes, inflammatory changes or application of an external pressure. Moreover, the kidney is a highly compartmentalized organ with a high level of perfusion.

Aims: The purpose of this study is to evaluate on *in vivo* pig kidneys how renal anisotropy, perfusion and urinary pressure changes have an impact on measured elasticity values in each renal compartment using the Supersonic Shear Imaging (SSI) technique.

Methods: The SSI technique is based on the combination of the radiation force induced by a linear ultrasonic probe (8 MHz) to generate shear waves deep into tissues and ultrafast ultrasound imaging to catch their propagation throughout the medium (5000 frames/s) in real time. Shear wave spectroscopy and time of flight algorithms were applied to recover quantitative tissue viscosity and elasticity respectively. Viscoelastic anisotropy was also studied regarding the axis of kidney pyramids. Investigation of the relationship between viscoelasticity and urinary or vascular pressure was obtained by filling the kidney with saline solution through the ureter or clamping artery or vein respectively. Measurements were controlled with a pressure sensor through a catheter in the ureter.

Results: Six (6) *in vivo* pig kidneys were investigated, with the ultrasound axis perpendicular to the pyramid axis showing strong elasticity differences between outer cortex (OC: 23±7 kPa), inner cortex (IC: 31±6 kPa) and medulla (26±7 kPa), whereas viscosity does not change within the cortex (OC and IC: ~1 Pa.s). The anisotropy ratio was also quantified when the ultrasound axis was perpendicular versus parallel to the pyramids axis (~1.5 for each anatomical zone). Elasticity rose with urinary pressure by a factor of 4 when 40 mmHg of saline solution were injected. Finally, clamping the renal artery or vein drastically changed elasticity values within the cortex by a factor of 5 (OC: ~100 kPa) or 0.5 (OC: ~10kPa), respectively.

Conclusions: Viscoelastic and anisotropic properties of the kidney were quantified. Separation of outer and inner cortex could be due to a difference in perfusion. By artificially increasing the urinary pressure, we have observed a strong increase of elasticity due to hydrostatic pressure. This suggests that using the acoustoelasticity theory, it could be possible to recover pressure quantification within the organs through elasticity measurements. Influence of vascular pressure or anisotropy is also extremely important to provide a realistic diagnosis. Finally, by taking carefully into account these parameters, non–invasive identification and follow–up of these processes could improve renal prognosis and help define adapted targeted therapies.

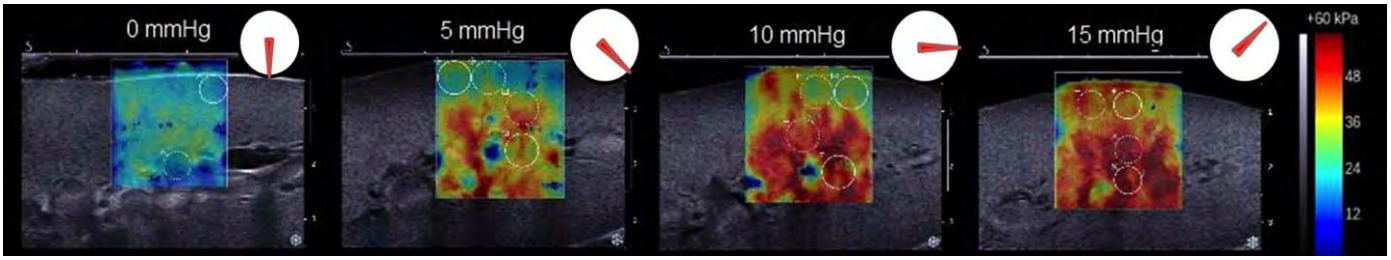

Figure1: Color–coded elasticity maps (25x25 mm²) in kPa of *in vivo* pig kidney for different pressure applied in the urinary cavity (from 0 to 15 mmHg). We notice the clear difference of elasticity between the inner and outer cortex. (Images acquired with Aixplorer™ system and linear probe SL15–4, Supersonic Imagine, Aix en Provence, France).

030 **SHEAR VISCOELASTICITY QUANTIFICATION OF BREAST CANCER TUMOURS IMPLANTED IN MICE BEFORE AND AFTER CHEMOTHERAPY TREATMENT.**

Heldmuth Latorre–Ossa[1], Foucauld Chamming's[2], Jean–Luc Gennisson[1], Laure Fournier[2], Olivier Clément[2], Mickaël Tanter[1].*

[1]Institut Langevin–Ondes et Images, ESPCI ParisTech, CNRS UMR7587, INSERM U979, Paris, FRANCE; [2]Service de Radiologie, Hôpital Européen George Pompidou, Paris, FRANCE.

Background: It is believed that tumour development and its response to chemotherapy are highly linked to variations in the tissue elasticity and viscosity. The monitoring through ultrasound elastography imaging of the tumour's early response to neo–adjuvant chemotherapy would be fundamental to avoid unwanted effects caused by the prolongation of ineffective treatments intended to preserve the breast and proceed directly to surgery.

Aims: The aim of this work is to perform a quantitative analysis of the behaviour of a human model of breast cancer implanted on mice, before and after neo–adjuvant chemotherapy treatment using the Supersonic Shear Imaging (SSI) technique [1].

Methods: The SSI technique is based on the combination of radiation force induced by an ultrasonic beam (15MHz) and an ultrafast imaging sequence (5000 frames/s) capable of catching the propagation of the resulting shear waves in real time. A time of flight algorithm is employed to retrieve the elasticity maps. The large bandwidth of the shear waves (150–1000 Hz) also allows the retrieval of viscous properties [2]. A xenograft of a human breast cancer was implanted on the 26 Swiss–nude mice aged 4–6 weeks. The mice were monitored every 7 days from the day the tumors were measurable. The neo–adjuvant chemotherapy treatment began when tumours reached a diameter of at least 10mm. Elasticity and the viscosity measurements were performed longitudinally for each mouse every week and correlated with histopathological results (two mice were sacrificed each week). Moreover magnetic resonance imaging (4.7T) was also used in order to get apparent diffusion coefficient (ADC) linked to cellularity.

Results: B–mode images and their corresponding elasticity maps were obtained for each mouse with a good reproducibility and accuracy (as an example, over 5 measurements, the elasticity was 7.6±0.8kPa for mouse #2 with a tumour diameter of 3.5mm). The average tumour diameters 2 and 5 weeks after being implanted were about 6mm and 10mm respectively. The mean elasticity values after the same number of weeks increased significantly (as an example, from 15.6±3.9kPa to 46.9±4.7kPa respectively for mouse #7). Viscosity did not change significantly and ADC decreased during tumour growth. Chemotherapy is currently under investigation and elasticity values seem to show a progressive decrement.

Conclusions: This study shows that the tumour increment in size is directly proportional to its elasticity values. The progressive decrease in elasticity allows consideration of the effectiveness of the neo–adjuvant chemotherapy treatment. Correlation of these results and histopathological measurement will explain the link between mechanical properties and tumour physiology. Moreover, the results of this work will open the way for future studies to evaluate the contribution of transient elastography in the detection of tumoral residues in patients suffering from locally advanced breast cancer treated by chemotherapy.

References:

[1] J. Bercoff, M. Tanter, M. Fink: Supersonic Shear Imaging: A New Technique for Soft Tissue Elasticity Mapping. IEEE Trans. Ultra., Ferro. Freq. Ctrl., 51(4), pp. 396–409, 2004.

[2] T. Deffieux, G. Montaldo, M. Tanter and M. Fink: Shear Wave Spectroscopy for *In Vivo* Quantification of Human Soft Tissues Visco–Elasticity. IEEE Trans. on Medical Imaging, Vol. 28, No. 3, pp. 313–322, March 2009.

* *indicates Presenter*

085 **LIVER FIBROSIS ASSESSMENT USING TRANSIENT ELASTOGRAPHY GUIDED WITH REAL–TIME B–MODE ULTRASOUND IMAGING: INVESTIGATION OF FOOD INTAKE EFFECT.**

TM Mak[1], X Yu[1], YP Zheng[1].*
[1]Health Technology and Informatics Department, The Hong Kong Polytechnic University, Hong Kong, CHINA.

Background: Liver fibrosis is a kind of chronic damage of the liver that may lead to cirrhosis and affects many people. The demand for a noninvasive diagnostic method for liver fibrosis is high. Recently, transient ultrasound (US) elastography has shown promising results for noninvasive assessment of liver elasticity [1,2]. We have earlier developed a transient elastography system based on a B–mode ultrasound scanner, which can provide real–time imaging of liver during elasticity measurement. There is lack of studies on the effect of food intake on liver elasticity [3].

Aims: The aim of this study was to use our image–guided transient elastography measurement system to systematically investigate the effect of food intake on liver elasticity.

Methods: The measurement probe was designed with a B–mode US probe fixed along the axis of a mechanical vibrator. It was integrated with the transient elastography system to measure liver stiffness based on the shear wave propagation in liver tissue. The system was tested using a series of custom-made phantoms with different stiffnesses and results were compared with a conventional mechanical test. For the *in vivo* measurement, an area close to the projection of the rib cage was identified, the intercostal space between the 7th and 8th ribs. It was possible to identify the location of the area to be measured, about 5cm in length from the intercostal space, under the guidance of real–time B–mode US imaging. A total of 26 subjects (age 22±2), including male and female, were tested. All subjects fasted for about 8 hours prior to measurement to ensure a resting state of liver stiffness. The inter– and intra–observer tests were conducted. In the food intake study, 9 subjects were tested before and after a meal at a constant time interval. The testing time points included 30min before meal (–30 min), immediately after meal (0 min) and 30, 60, 90 and 120 min. after meal. A control group of 6 subjects were also tested with the same testing time interval within 120 min after about 8 hours fasting, but without any food intake.

Results: Using the established protocol, the inter– and intra–observer tests indicated the measurements were repeatable with interclass correlation of 0.85 for 10 subjects and intraclass correlation of 0.97 for 14 subjects. For the control group, there was no significant change of liver elasticity along the time (p=0.72), showing the liver stiffness remained unchanged within 2–hour testing period. Repeated measure one–way ANOVA showed liver stiffness had a trend of increase at 30 min (p=0.018), 60 min (p=0.036), for 90 min (p=0.006) and for 120 min (p=0.038) after food intake (Figure 1). There was no significant change of the liver stiffness immediately after a meal (p=0.346). In this study, we further confirmed that the real–time B–mode image can help the operator to easily identify blood vessels in the liver and select a suitable region for the measurement (Figure 2).

Conclusions: Using the transient elastography measurement guided with B–mode image, we found that the liver stiffness significantly increased after a meal intake. This result suggests that subjects need to fast for a certain period of time before assessment; otherwise, the liver elasticity can be over-estimated.

Acknowledgements: This study was partially supported by Hong Kong Innovative Technology Fund (GHP/047/09).

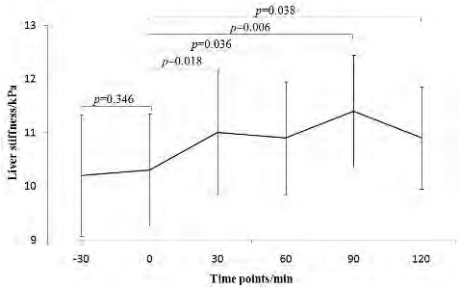

Figure 1: Change of liver stiffness (Mean±SD) after the meal

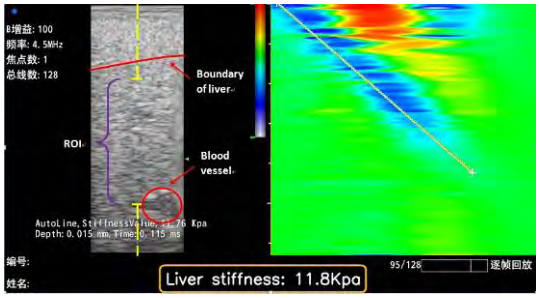

Figure 2: Typical result of liver stiffness (11.8kPa) of a healthy young man

References:

[1] Sandrin L, et al.: Ultrasound in Medicine and Biology, 29, pp. 1705–13, 2003.
[2] Ganne–Carrie N, et al.: Hepatology, 44, pp. 1511–7, 2006.
[3] Mederacke I, et al.: Liver International, 29, pp. 1500–6, 2009.

* *indicates Presenter*

028 **INITIAL CLINICAL RESULTS OF SHEAR WAVE SPECTROSCOPY IN CHRONIC LIVER DISEASE PATIENTS.**

Thomas Deffieux[1], Jean–Luc Gennisson[1], Mathieu Couade[12], Jeremy Bercoff[2], Laurence Bousquet[3], Simona Cosconea[3], Vincent Mallet[3], Stanislas Pol[3], Mickael Tanter[1].*
[1]Institut Langevin–Ondes et Images, ESPCI ParisTech, CNRS UMR 7587, INSERM U979, Paris, FRANCE; [2]Supersonic Imagine, Aix en Provence, FRANCE; [3]Service Hépatologie, Hôpital Cochin, Paris, FRANCE.

Background: Shear Wave Spectroscopy (SWS) is a method to obtain *in vivo* shear wave dispersion curves. Based on Supersonic Shear Imaging, a planar shear wave is generated by acoustic radiation force and tracked during its propagation using an ultrafast ultrasound scanner. The shear wave propagation movie is then processed to estimate the shear wave dispersion curve and the rheological properties of the tissue *in vivo* and in real time.

Aims: The goal of the study is to test the feasibility in clinical conditions of the SWS technique on chronic liver disease patients and to discuss the methodology and associated results.

Methods: 10 shear wave propagation movies are acquired using an ultrafast scanner (Aixplorer, Supersonic Imagine, France) with a 3MHz curved probe (SC6–1), for each patient (n>30) diagnosed with hepatitis C and low fibrosis stage (F0–F1 assessed by liver biopsy). For each acquisition, an algorithm for motion correction and vein removal is first applied. Then the shear wave dispersion curve is estimated by different methods: Firstly, by retrieving, for each frequency, the phase velocity in a region of interest; secondly, using the k–space energy distribution of the shear wave ($c=\omega/k$); lastly using a Voigt's model *a priori* to estimate the dispersion curve from all frequencies. For all methods, shear modulus and viscosity are then assessed from the different dispersion curves using the Voigt's model.

Results: The presence of veins and respiration movements (up to 10µm) are successfully removed by the algorithms. As expected, the algorithm taking advantage of the Voigt's model *a priori* performs the best and significantly improves the stability of the viscoelastic measurements in clinical conditions. A good reproducibility of Voigt parameters assessment (μ_0=1.6±0.7kPa, η=1.3±0.6Pa•s) is shown in clinical conditions.

Conclusions: The shear wave spectroscopy can be used to estimate the liver viscosity in clinical conditions. This new parameter, together with the stiffness estimation, could be helpful in providing a more complete equivalence to the Metavir scoring system (fibrosis and activity levels) which is currently only fully assessed by liver biopsies. However, more clinical data are required to assess its true clinical relevancy.

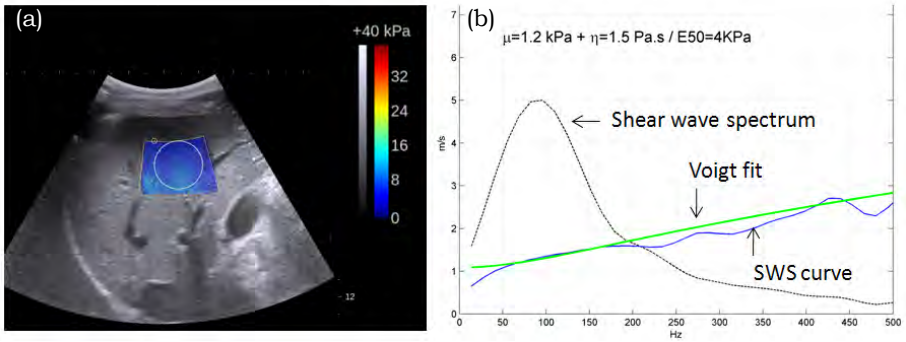

Figure1: (a) A patient liver echography and quantitative stiffness map. (b) For each patient, Shear Wave Spectroscopy enables estimation locally of the dispersion curve of the shear wave from 50–500Hz. The shear modulus and viscosity can then be estimated reliably under a Voigt model assumption.

* *indicates Presenter*

034 **COMPARING THE PERFORMANCE OF PLANE WAVE AND SPARSE ARRAY ELASTOGRAPHY IMAGING SYSTEMS.**

Sanghamithra Korukonda[1], Marvin M. Doyley[1].*

[1]Electrical and Computer Engineering Department, University of Rochester, Rochester, NY, 14627 USA.

Background and Aims: Non–invasive vascular elastography (NIVE) imaging of the carotid artery provides quantitative information on vessel morphology and its mechanical properties. This information may be used to characterize plaque vulnerability. In this work, we compare sparse array [1] and plane wave imaging [2] to perform ultrafast elastographic imaging of the carotid artery.

Methods: A SONIX RP commercial ultrasound scanner (Ultrasonix Corp., Vancouver, Canada) equipped with an L14–5/38 linear array probe was configured to acquire (1) sparse array data with only 7 active transmit elements and 128 receive elements and (2) plane wave data by transmitting simultaneously with all 128 elements and receiving in parallel with all elements. Elastographic imaging was performed on vessel phantoms at intra–luminal pressures differences ranging from 4–20mmHg. Three–dimensional data sets were acquired by translating the transducer along the long axis of the phantoms in increments of 2mm. Axial and lateral displacement images were computed by applying 2D cross–correlation to the beam–formed radio–frequency (RF) echo frames obtained at different pressures. Radial and circumferential elastograms were obtained from the gradients of the displacement estimates.

Results: Strain elastograms were obtained with both plane wave and sparse array imaging methods over the range of pressures employed in this study. Figure 1 shows representative examples of elastograms obtained from a cross–section of a phantom containing a soft plaque (4 o'clock). The plaque appears as a localized region of high strain, which is clearly demarcated in the radial (a) and circumferential (b) strain elastograms obtained with the sparse array. The plaque is also seen in both sets of the plane wave elastograms (c, d), albeit it is less discernable. In the case of the homogeneous elastograms, higher variance was observed in the plane wave elastograms as compared to the sparse array elastograms, particularly in the lateral sectors.

Conclusions: Sparse array imaging is a promising elastography technique that can image the carotid artery in real time at ultrafast frame rates. While plane wave imaging has greater speed and higher signal power, sparse array imaging has greater sensitivity to tissue motion, particularly in the lateral direction. In addition, with the high acquisition speeds, 3D data can be acquired to improve the diagnostic value of this technique.

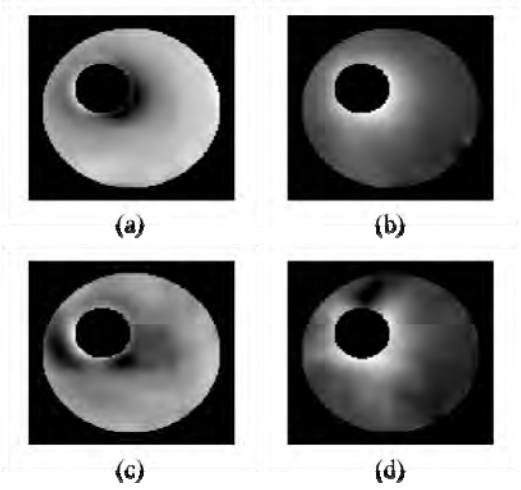

Figure 1: Sparse Array Strain Elastograms (a,b); Plane Wave Strain Elastograms (c, d)

Acknowledgements: This work was supported by startup funds from the University of Rochester.

References:

[1] Chiao RY, Thomas LJ: Aperture Formation on Reduced-Channel Arrays using the Transmit–Receive Apodization Matrix. IEEE Ultrasonics Symposium, pp. 1567–71, 1996.

[2] Shattuck DP, Weinshenker MD, Smith SW, and von Ramm OT: Explososcan: A Parallel Processing Technique for High Speed Ultrasound Imaging with Linear Phased Arrays. J. Acoust. Soc. Am., Vol. 75, Is. 4, pp. 1273–1282, 1984.

037 **IMAGING OF THE 4D STRAIN DISTRIBUTION IN POROELASTIC MEDIA UNDER SUSTAINED UNIFORM AND LOCALISED COMPRESSIVE LOADING.**

Jérémie Fromageau[1], Leo Garcia[1], Nigel Bush[1], Gearoid Berry[1], Jeffrey Bamber[1].*
[1]Joint Department of Physics, Institute of Cancer Research and Royal Marsden NHS Trust, Cotswold Road Sutton, Surrey, England, UK.

Background: It is known that the response of a poroelastic material to a sustained applied unidirectional strain is an internal strain that varies with position and time in a manner that is characteristic of the capacity of the fluid to diffuse through the elastic porous structure. We have shown previously, with finite element analysis (FEA), that knowledge of the volume change, or equivalently the time–varying 3D deformation, is necessary to estimate poroelastic parameters of the medium. In addition, when compression is applied with the ultrasound transducer, as is typical in clinical quasi–static elastography, strain in a homogeneous poroelastic medium will mainly occur in the directions orthogonal to the load. This is not optimal for ultrasound strain measurement. Ultimately, clinical interest would be earlier scoring and detecting the development of lymphedema.

Aims: In the current work, the final goal was to verify experimentally the capacity to observe 3D poroelastic strain relaxation during compression with a 3D ultrasound probe.

Methods: FEA software (MARC Mentat, MSC Software) was used to model a cylinder with homogeneous poroelastic material constants. Two different loads and boundary conditions (BC) were simulated: 1) a uniform constant displacement was applied to the whole top surface, and only the circumferential boundary was permeable; 2) a constant displacement was applied to a limited region of surface (i.e. indentation), and the sample was impermeable on all boundaries, simulating the clinical pitting test. Experiments with similar geometry and BC were performed using a poroelastic matrix consisting of a mixture of agarose and cellulose, and water as the fluid. The phantom was observed with an ultrasound scanner (DIASUS, Dynamic Imaging), using a 7MHz 3D probe, which was also used to apply the compression. The probe was connected to a mechanical test instrument (Instron, Inspec 2200), to record the applied force. The strain in the phantom was estimated from the RF echo signals using cross–correlation speckle tracking methods. To improve lateral and elevation strain estimations, both RF interpolation and beam steering were used.

Results: Experiments were in a good broad agreement with the FEA, showing a shrinking of the sample volume during the sustained compression. For the indention case, this time–dependent reduction in volume strain was concentrated beneath the indentor. For both cases, the combined temporal and spatial variation of volumetric strain indicated the direction of fluid flow.

Conclusion: It is the first time to our knowledge that the complete time–varying 3D deformation has been experimentally measured to characterise a relaxing poroelastic medium, demonstrating that, unlike the elastic case, the response to a sustained axial compression is a temporally and spatially varying volumetric strain.

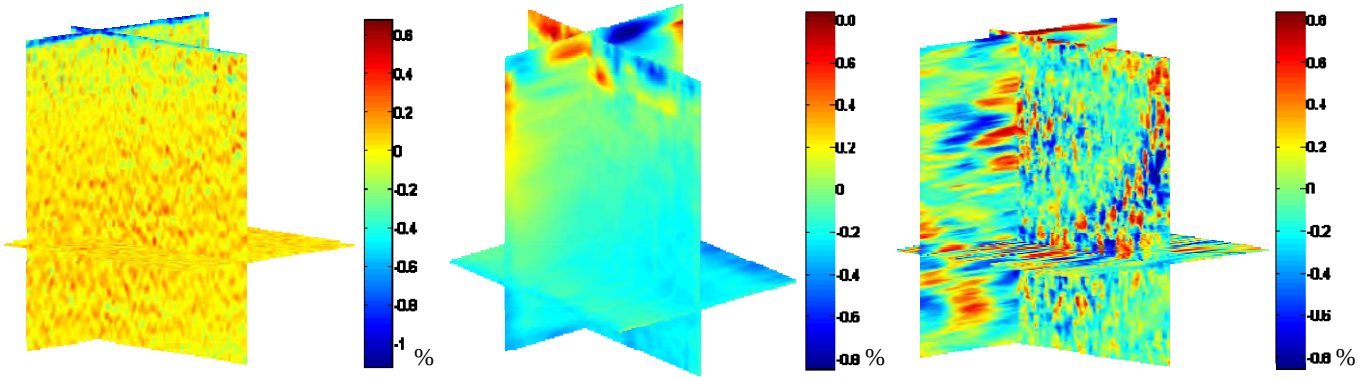

Figure 1: Axial, lateral and elevational strains at a fixed time t=300s. Axial strain appears spatially constant whereas lateral and elevational strains show a spatial strain pattern converging to the centre of the volume.

* *indicates Presenter*

038 **COMBINED ARFI AND SHEAR WAVE SPEED IMAGING FOR QUANTITATIVE, HIGH RESOLUTION ELASTICITY IMAGING.**

Stephen J. Rosenzweig[1], Ned C. Rouze[1], Michael H. Wang[1], Mark L. Palmeri[1], and Kathy R. Nightingale[1].*
[1]Duke University, Durham, NC, USA.

Background: Acoustic radiation force impulse (ARFI) imaging provides high resolution, qualitative images of tissue stiffness. However, due to inertial and structural effects, the contrast transfer efficiency [1] is less than unity in ARFI images [2]. ARFI excitations can also be used to generate quantitative shear wave speed (SWS) images which more accurately reflect the mechanical contrast of the underlying tissue; however, these images have poorer spatial resolution due to the size of the reconstruction kernel.

Aims: The aim of this work is to investigate methods to combine ARFI and SWS imaging to generate quantitative elasticity images of tissue which combine the high resolution of ARFI images and the high contrast of SWS images.

Methods: ARFI and SWS data were acquired from a commercial (CIRS, Norfolk, VA) phantom with stiff inclusions using acquisition sequences implemented on modified Siemens Antares and SC2000 systems, and a Verasonics imaging system. ARFI images were reconstructed using depth–dependent normalization of ARFI displacements [2]. SWS images were reconstructed by determining the wave arrival time at positions laterally offset from the excitation axis and calculating the SWS from the slope of arrival time vs. position data in overlapping kernels [3]. In order to generate combined, quantitative images, signals from regions with uniform ARFI and SWS signals were identified, and a relation between ARFI displacement and SWS was obtained using a nonlinear empirically derived model of the form $1/SWS^2 = A\,(displacement)^p$. Images were evaluated by comparing image contrast, calculated from regions inside and outside the inclusion, and resolution, calculated from parameters estimated in the fit of a double sigmoid function to a signal profile through the center of the inclusion.

Results: Figure 1 shows ARFI (left), SWS (center), and combined (right) images reconstructed from acquisitions in a phantom with a 20mm diameter (top row) and concentric (bottom row) inclusions. The resolution of the edges is 0.4mm in (a,d), 4.2mm in (b,e), and 0.5mm in (c,f). For images (a–c), the contrast of the lesion relative to the background is 0.4, 0.7 and 0.6 respectively. For images (d–f), the contrast of the annulus and center relative to background are (d) 0.4, 0.6, (e) 0.5, 0.7 and (f) 0.5, 0.7, respectively.

Conclusions: The combined ARFI/SWS images provide spatial resolution comparable to that of the ARFI images and quantitative results with the high contrast characteristics of the SWS images.

Acknowledgements: This work was supported by NIH grants R01 EB002132 and R01 142824. We thank Siemens Healthcare, Ultrasound Business Unit, Mountain View, CA for their system support.

References:

[1] Ponnekanti H, Ophir J, Huang Y, and Céspedes I: Fundamental Mechanical Limitations on the Visualization of Elasticity Contrast in Elastography. Ultrasound Med. Biol., 21(4), pp. 533–543, 1995.
[2] Nightingale K, Palmeri M, and Trahey G: Analysis of Contrast in Images Generated with Transient Acoustic Radiation Force. Ultrasound Med. Biol., 32(1) pp. 61–72, 2006.
[3] Palmeri ML, Wang MH, Dahl JJ, Frinkley KD, Nightingale KR: Quantifying Hepatic Shear Modulus *In Vivo* using Acoustic Radiation Force. Ultrasound Med. Biol., 34(4), pp. 546–558, 2008.

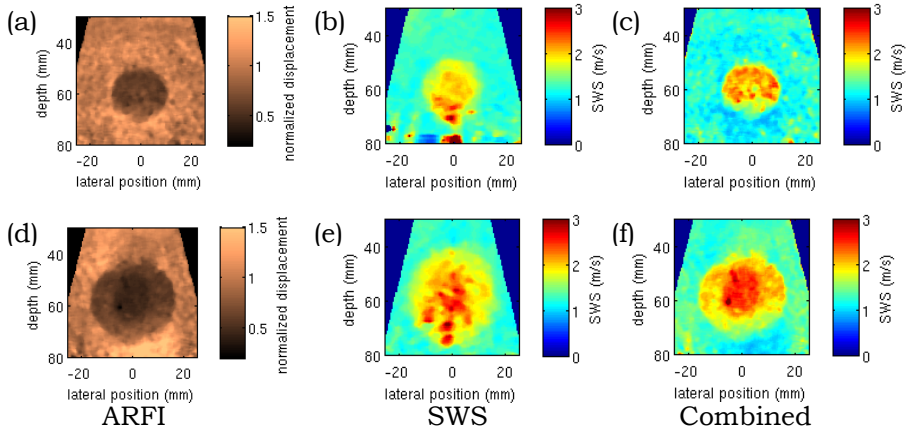

Figure 1: ARFI (a,d), SWS (b,e), and combined (c,f) images reconstructed from ARFI and SWS acquisitions in a phantom with a 20mm diameter (top row) and concentric (bottom row) inclusions in a softer background. The ARFI images were reconstructed from data acquired 0.8ms after excitation. A 6mm kernel was used to reconstruct the SWS images.

* *indicates Presenter*

039 **NONINVASIVE ASSESSMENT OF MECHANICAL PROPERTIES OF THE CRYSTALLINE LENS.**

SR Aglyamov[1], S Yoon[1], AB Karpiouk[1], RK Manapuram[2], KV Larin[2], SY Emelianov[1].*
[1]University of Texas at Austin, Austin, TX, USA; [2]University of Houston, Houston, TX, USA.

Background: According to the most widely accepted theory, presbyopia is due to a gradual age–related loss of flexibility of the crystalline lens of the eye [1,2]. A better understanding of how the lens' biomechanical properties change with age and its relation with the loss of accommodation is a fundamental requirement for the development of better models of accommodation, presbyopia and effective correction techniques [3]. The success of the clinical outcome of vision–restoring procedures such as lens ablation, cataract surgery and lens–refilling treatment is greatly dependent on knowledge of the lens' biomechanical properties. Therefore, there is a great need for a technique that can be used for nondestructive quantification of the lens' biomechanical properties. The availability of a clinical method capable of assessing biomechanical properties of the crystalline lens *in situ* and noninvasively would significantly enhance our fundamental understanding of the causes of presbyopia. A major challenge in the development of such procedures is that the location of the lens inside the eye makes it inaccessible to direct mechanical probing.

Aims: The aim of this work is to develop noninvasive methods for the topographical assessment of crystalline lens' elastic properties based on analysis of ultrasound–induced mechanical wave propagation in the lens.

Methods: The major challenge of noninvasive estimation of the lens' elasticity is that the lens motion can be measured only on the lens surface. The lens is transparent for both ultrasound and optical methods. The technique proposed in this application overcomes these limitations of standard elastography and provides lateral spatial distribution of the lens' mechanical properties by analyzing both shear waves and mechanical longitudinal waves on both surfaces of the lens. Usually, shear waves are used in the acoustic radiation force approach to evaluate tissue mechanical properties. However, longitudinal elastic waves also carry information about tissue properties and can be used to evaluate tissue elasticity and viscosity. Specifically, for application to the lens, speed and attenuation of the longitudinal waves travelling from the anterior to the posterior lens surface is used to estimate the distribution of lens' mechanical properties. Experiments on gelatin–based phantoms with known elastic properties and animal crystalline lenses were performed to measure velocity and attenuation of the mechanical wave propagation. A 3.5MHz focused single element transducer was used to generate a wave in the lens and a high frequency (25MHz) transducer tracked displacements on the lens surface. A low frequency single element transducer (F/#=4, center frequency 3.5MHz) was used to generate waves at the surface of the lens and a high frequency tracking transducer (F/#=4 and center frequency 25MHz) captured the shear or longitudinal wave propagations on the surface of the phantom and lens.

Results: Results demonstrate that there is a strong correlation between parameters of the mechanical wave propagation measured on the surface of tissue and elastic properties. Also, there is good agreement between experimental results and theoretical predictions of wave propagation in homogeneous medium. Phantom measurements show that velocity of the longitudinal elastic wave increases with increased elasticity of the medium. For inhomogeneous phantoms, the velocity is higher in the area of hard inclusion. Central zones of the 20–30 month old bovine lenses demonstrate higher longitudinal velocity in comparison with peripheral zones. That is in agreement with the results of the independent mechanical tests which showed that there is a stiffness gradient within the lens, i.e., nucleus demonstrates higher elasticity than cortex.

Conclusions: An approach based on mechanical wave propagation in crystalline lens can be used to assess elastic properties of the lens.

Acknowledgements: Support in part by the National Institutes of Health under grants EY018081 and EB008821 is acknowledged.

References:

[1] A. Glasser and M.C. Campbell: Presbyopia and the Optical Changes in the Human Crystalline Lens with Age. Vision Research, Vol. 38, pp. 209–229, 1998.
[2] K.R. Heys, S.L. Cram and R.J. Truscott: Massive Increase in the Stiffness of the Human Lens Nucleus with Age: The Basis for Presbyopia? Mol Vis, Vol. 10, pp. 956–63, 2004.
[3] A. Glasser: Restoration of Accommodation: Surgical Options for Correction of Presbyopia. Clin Exp Optom, Vol. 91, pp. 279–95, 2008.

* *indicates Presenter*

001 **ABSCESS INDURATION VISUALIZED WITH SONOGRAPHIC ELASTOGRAPHY PREDICTS FAILURE OF THERAPY.**

Romolo J. Gaspari[1], David Blehar[1], Matthew Dayno[1].*
[1]Emergency Medicine Department, University of Massachusetts Memorial Hospital, 55 Lake Avenue North, Worcester, MA, 01655 USA.

Background: Ultrasound can visualize components of skin and soft tissue abscesses including the abscess cavity and abscess cavity debris, but sonographic elastography is unique in that it provides information related to tissue stiffness and can visualize induration. The primary therapy for treating skin abscesses involves incision and drainage (I&D), but failure rates following I&D have increased over the last decade. The surrounding tissue induration represents the host response to the infection, and it is possible that characteristics of the induration surrounding an abscess may predict which abscesses will eventually fail therapy.

Aims: The aim of this research was to determine if sonographic elastography findings are associated with failure of therapy following treatment for skin and soft tissue abscesses.

Methods: A prospective trial of patients with a suspected skin abscess requiring surgical drainage in the emergency department of an urban tertiary care center. All patients received an I&D for the suspected abscesses, and those with no purulence following drainage were excluded from the study. Abscesses (n=45) were imaged prior to I&D using B–mode and elastography (Zonare Medical Systems, Mountain View, CA) in orthogonal planes. Telephone follow–up using a standardized questionnaire was performed 10 days after the initial presentation to determine failure of therapy. Physicians blinded to patient outcome analyzed the ultrasound images for predetermined image characteristics of the abscess induration including 1) asymmetry of induration surrounding abscess cavity, 2) ratio of volume of induration to abscess cavity volume and 3) ratio of depth of abscess cavity to depth of induration.

Results: The average volume of the abscess cavity and induration were 1.8cc's ($\pm$1.2) and 20.8 ($\pm$11.4) respectively. 33% of patients demonstrated asymmetry of the surrounding induration (Figures 1 & 2). The average ratio of volume of induration to abscess cavity volume was 38.8 (95% CI – 20.3–57.3). The average ratio of abscess cavity depth to depth of induration was 0.50 (95% CI – 0.44–0.56). 22.7% of patients failed therapy. The association between failure of therapy and ratio of volumes was not statistically significant. Asymmetry of induration surrounding abscess cavity demonstrated a PPV of 46.7 (30.7–52.1) and a NPV of 95.0 (83.0–99.1) for failure of therapy (p=0.01). ROC analysis determined an optimal cut–off for ratio of depth of abscess cavity to induration of 0.5, which demonstrated a PPV of 68.0 (57.1–71.3) and a NPV of 93.3 (75.2–98.8) for failure of therapy (p=0.04). Both findings together demonstrated a PPV of 75.0 (47.3–90.0) and a NPV of 92.9 (84.9–97.1) for failure of therapy (p=0.008).

Conclusions: Measurements of abscess induration with sonographic elastography are associated with failure of therapy. Imaging an abscess with sonographic elastography may predict which abscess cavities will fail therapy. Sonographic elastography has the potential to impact the treatment of skin abscesses by identifying individuals requiring more aggressive therapy.

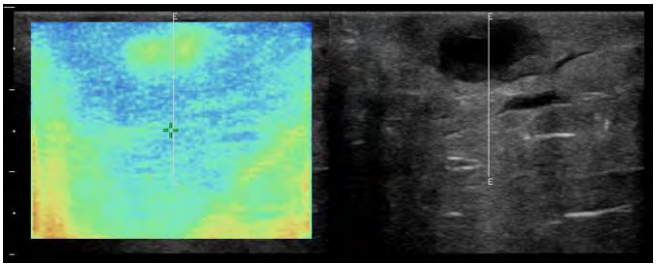

Figure 1: Symmetrical abscess induration.

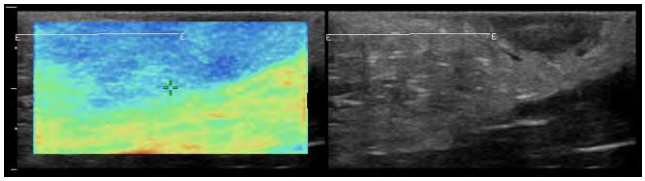

Figure 2: Asymmetrical abscess induration.

055 **HIGH RESOLUTION MAGNETIC RESONANCE ELASTOGRAPHY OF ORTHOTOPIC MURINE GLIOMA *IN VIVO*.**

Yann Jamin[1], Jessica K.R. Boult[1], Jeffrey C. Bamber[1,2], Ralph Sinkus[3], Simon P. Robinson[1].*
[1]CRUK and EPSRC Cancer Imaging Centre, The Institute of Cancer Research and Royal Marsden NHS Trust, Sutton, Surrey SM2 5PT, England, UK; [2]Joint Department of Physics, Institute of Cancer Research and Royal Marsden NHS Trust, UK; [3]INSERM U773, CRB3, Centre de Recherches Biomédicales Bichat–Beaujon, Paris, FRANCE.

Background: Noninvasive *in vivo* imaging biomarkers of tumor phenotype and response are needed to improve the diagnosis and staging of malignancies and to facilitate and accelerate the further development of cancer therapeutics. Oncogenesis, tumour progression and treatment cause dramatic changes in the architecture and mechanical properties of both tumor and host tissue [1,2]. Elastography may therefore provide useful biomarkers. Indeed, magnetic resonance elastography (MRE) has been shown to afford accurate biomarkers of disease progression [3].

Aims: This preliminary study assessed the ability of high resolution MRE to measure the visco–elastic properties *in vivo* and display the pattern of growth of orthotopically propagated RG2 gliomas in mouse brain, a tumor model that faithfully represents the most common primary brain tumour, astrocytoma [4].

Methods: RG2 rat glioma cells engineered to express luciferase were implanted in the brains of NCr nude mice. Tumor establishment was monitored by bioluminescence imaging (Xenogen IVIS® 200). MRE was performed on a 7T Bruker Microimaging system using a 3cm birdcage coil. The tumor was localized using high resolution (150 µm x 150 µm in–plane) axial T_2–weighted RARE images, and 3D steady–state MRE data were acquired, as previously described [5], using a 1kHz continuous vibration of the skull. Maps of complex shear modulus, elasticity and viscosity were reconstructed with an isotropic pixel size of 300µm. Tumor extent was confirmed histologically.

Results: RG2 gliomas were found to be softer and less viscous than the surrounding brain. Such soft consistency has been previously reported for this model [4] and for astrocytomas in the clinic [6]. The visco–elastic properties of the brain were in good agreement with previous measurements of healthy mouse brain [5]. Maps of the magnitude of the complex shear modulus (combining elasticity and viscosity) corresponded well with histology which revealed relatively well–encapsulated tumors, albeit with some areas of localized invasion into the brain parenchyma (Figure 1).

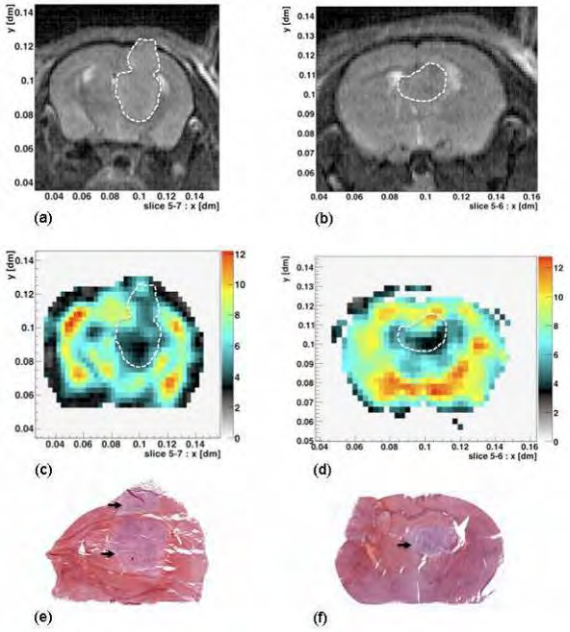

Figure 1: Outlines (---) of orthotopic RG2 gliomas in two mice, defined by high resolution T2–weighted MRI (a and b), the corresponding maps of the magnitude of the complex shear modulus (c and d), and corresponding whole brain haematoxylin and eosin stained sections, with the tumor location indicated (e and f).

Conclusions: This proof–of–principle study demonstrated that MRE provides a powerful platform to interrogate the utility of elasticity and viscosity as emerging non–invasive imaging biomarkers for monitoring tumor behavior and response to treatment. As both MRE and quantitative ultrasound elastography have been performed in man, these biomarkers should readily translate to the clinic.

Acknowledgements: Support was received from the CRUK and EPSRC Cancer Imaging Centre, with the MRC and Department of Health (England) grant C1060/A10334, NHS funding to the NIHR Biomedical Research Centre.

References:

[1] Butcher et al.: Nat Rev Cancer, 9, pp. 108–122, 2009.
[2] Paszek et al.: Cancer Cell, 8, pp. 241–254, 2005.
[3] Huwart et al.: Gastroenterol 1:32–40, 2005.
[4] Aas et al.: J Neurooncol 23:175–183, 2005.
[5] Diguet et al.: Proc ISMRM 714, 2009.
[6] Hedges: Tumors of Neuroectodermal Origin. Clinical Neuro–Opthalmology, pp. 1413–1483, 2004.

* *indicates Presenter*

003 **SHEAR WAVE ELASTOGRAPHY MAY OUTPERFORM STRAIN ELASTOGRAPHY AND MAY ADD A NEW DIMENSION TO THYROID ULTRASOUND.**

RZ Slapa[1], WS Jakubowski[1], J Slowinska–Srzednicka[2] A Piwowonski[3], J Bierca[4], KT Szopinski[1].*
[1]Diagnostic Imaging Department, Medical University of Warsaw, Warsaw, POLAND; [2]Endocrinology Department, Center for Postgraduate Medical Education, Warsaw, POLAND; [3]Diagnostic and Research Medical Centre, Walbrzych, POLAND; [4]Surgery Department, Solec Hospital, Warsaw; POLAND.

Background: From a clinical background, hard nodules on palpation are more suspicious for thyroid cancer. Although elastography can assist in the differential diagnosis of thyroid nodules, its diagnostic performance is not ideal at present. Further improvements in the technique and the diagnostic criteria are necessary for this examination to provide a useful contribution to diagnosis [1].

Aims: The purpose of the study was to compare the usefulness of strain elastography and a new generation of elasticity imaging called supersonic shear wave elastography (SSWE) for differential evaluation of thyroid nodules.

Methods: We evaluated with B–mode and power Doppler ultrasound of the whole thyroid and neck lymph nodes in 4 consecutive patients (one patient with single thyroid nodule and three patients with nodular goiter). Six dominant nodules (in regard to ultrasound features) were evaluated with strain elastography and with SSWE qualitatively and quantitatively and with an ultrasound contrast agent, Sonovue (Bracco), with following scanners: Aixplorer™ (Supersonic Imagine, Inc. France) – SSWE, Aplio XG (Toshiba, Japan) – strain elastography, Logiq E9 (GE, USA) – strain elastography, Technos (Esaote, Italy) – contrast enhanced ultrasound with linear high resolution transducers. The final diagnosis was based on clinical evaluation, multiple FNA (1 of 6 nodules) or surgery (5 out of 6 nodules).

Results: Final diagnosis established 1 papillary carcinoma, 4 colloid nodules and a benign nodule with degeneration. SSWE revealed 1 true–positive, 5 true–negative. Strain elastography revealed 5 false–positive and 1 false–negative diagnoses. False–positives on strain ultrasound could be due to liquid (not evident on B–mode ultrasound) or degenerative content of the nodules. A novel finding was the punctate increased stiffness in microcalcifications in 4 nodules, some not visible on B–mode ultrasound as opposed to soft inspissated colloid visible on B–mode ultrasound in 2 nodules.

Conclusions: (1) This preliminary report based on small number of cases indicates that SSWE may outperform strain elastography in differentiation of thyroid nodules with regard to their stiffness. (2) SSWE showed the possibility of differentiation of high echogenic foci into microcalcifications and inspissated colloid adding a new dimension to thyroid elastography. (3) Further multicenter large scale studies of thyroid nodules evaluating different elastographic methods are warranted, including: (a) Investigation of developmental models of diseases that link biomechanical properties (elastography findings) with genetic, cellular, biochemical and gross pathological changes [2]; (b) Comparison of accuracy of different elastographic methods, (c) Establishment of optimal diagnostic elastographic criteria, (d) Establishment of limitations of different elastographic methods in relation to evaluation of thyroid pathology.

Acknowledgements: Supported by the Ministry of Science and Higher Education of Poland grant Nr N N402 476437 in years 2009–2011.

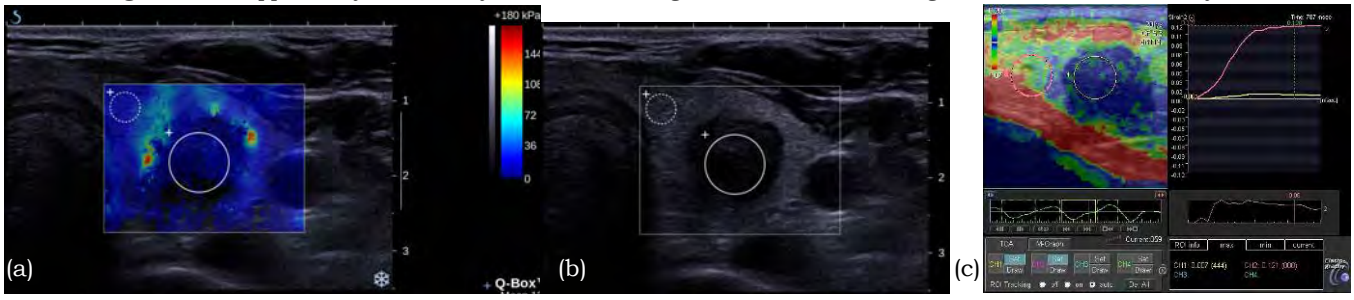

Figure 1: Benign dominant nodule of the left thyroid lobe filled with degenerative changes on pathology examination, in a pt with multinodular goiter, evaluated (a) with SSWE where the nodule is very soft that indicating benign lesion, (b) on B–mode ultrasound where the nodule is deeply hypoechoic, taller than wide, with micro–calcifications indicating a suspicious lesion and (c) evaluated with strain elastography qualitatively and quantitatively where the lesion presents as very hard – more than 17 times harder than surrounding thyroid tissue (strain ratio = 17.28) that strongly indicates malignant lesion.

References:

[1] Kagoya R, et al.: Utility of Elastography for Differential Diagnosis of Benign and Malignant Thyroid Nodules. Otolaryngology–Head and Neck Surgery, 143, pp. 230–234, 2010.
[2] Parker KJ, et al.: Imaging the Elastic Properties of Tissue: The 20 Year Perspective. Phys. Med. Biol., 56, pp. R1–R29, 2011.

082 **DIAGNOSTIC PERFORMANCE OF STRAIN ELASTOSONOGRAPHY IN MULTINODULAR THYROID GOITER IS UNSATISFACTORY.**

Rafal Z. Slapa[1], Wieslaw S. Jakubowski[1], Jacek Bierca[2], Bartosz Migda[1], Jadwiga Slowinska-Srzednicka[3].*

[1]Diagnostic Imaging Department, Medical University of Warsaw, Faculty of Medicine II with English and Physiotherapy Divisions, Warsaw, POLAND; [2]Surgery Department, Solec Hospital, Warsaw; POLAND; [3]Endocrinology Department, Center for Postgraduate Medical Education, Warsaw, POLAND.

Background: Although elastography can assist in the differential diagnosis of thyroid nodules, its diagnostic performance is not ideal at present [1]. Patients with a nontoxic multinodular goiter are a relatively common clinical problem. Thyroid cancer is present in approximately 5% of multinodular goiter patients, which is comparable to the risk in solitary thyroid nodules [2].

Aims: The purpose of the study was to assess the usefulness of strain elastosonography for differential evaluation of thyroid nodules in patients with multinodular goiter.

Methods: During years 2009–2010, a single observer (a radiologist with 18 years of experience in thyroid ultrasound, instructed how to perform and evaluate the strain elastography) evaluated the whole thyroid and neck lymph nodes 56 patients (51 with multinodular goiter and 5 with single thyroid nodule) using B–mode and power Doppler ultrasound. After this examination, the patients underwent thyroidectomy. During ultrasound examination, 79 dominant nodules were examined with strain elastosonography with Aplio XG (Toshiba) with linear 5–17 MHz transducer. The stiffness of each thyroid nodule was evaluated on the pair of images with strain elastosonography qualitatively (with elasticity scores, threshold 2/3) [3] and with thyroid tissue/nodule strain ratios with elasto Q (Toshiba) (threshold 2) [4]. The final diagnosis was based on pathology examination after surgery.

Results: Final diagnosis established 7 papillary carcinomas (6 in multinodular goiter), 4 follicular adenomas and 68 benign nodular goiter nodules. On elastosonography, images 51 nodules (64.6%) could be visualized completely and 28 nodules (35.4%) partially together with surrounding thyroid tissue. Sensitivity and specificity for diagnosis of carcinoma with strain elastosonography including evaluation of elasticity score, single strain ratio or mean of two strain ratios were respectively 35.7%, 35.7%, 28.6% and 35.4%, 51.4%, 52.8%.

Conclusions: (1) The incidence of thyroid cancer, that was not known before our ultrasound examination (5 nodules) in our study shows that cancer is present in 9% of the 54 patients and is comparable to the incidence of cancer in the general population of multinodular goiter patients [2], however, the number of cancers in the study is small. (2) Diagnostic performance of strain elastosonography in multinodular thyroid goiter is unsatisfactory. (3) Further improvements in the elastographic techniques and the diagnostic criteria are necessary for this examination to provide a useful contribution to diagnosis [1].

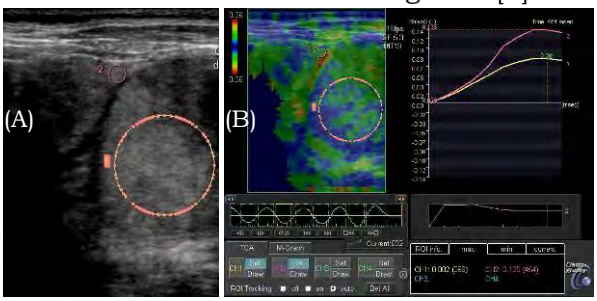

Figure 1: Papillary carcinoma of thyroid follicular variant (ROI1) in patient with multinodular goiter. (A) On B–mode, part of the neoplasm is seen. The ROI for elastography measurement is placed in the solid part of the carcinoma. ROI2 is placed in the surrounding thyroid parenchyma. (B) False negative qualitatively and quantitatively strain elastosonography image presents an elastic nodule (elastography score = 2 [4]) with thyroid tissue/lesion strain ratio = 1.65 – within range for benign lesions [5].

Acknowledgements: Supported by the Ministry of Science and Higher Education of Poland grant Nr N N402 476437, 2009–11.

References:

[1] Kagoya R, Monobe H, Tojima H: Utility of Elastography for Differential Diagnosis of Benign and Malignant Thyroid Nodules. Otolaryngology–Head and Neck Surgery, 143, pp. 230–234, 2010.

[2] Bonnema SJ, Bennedbaek FN, Ladenson W, Hegedüs L: Management of the Nontoxic Multinodular Goiter: A North American Survey. J Clin Endocrinol Metab., 87, pp. 112–117, 2002.

[3] Rubaltelli L, Corradin S, Dorigo A, Stabilito M, Tregnaghi A, Borsato S, Stramare R: Differential Diagnosis of Benign and Malignant Thyroid Nodules at Elastosonography. Ultraschall Med, 30, pp. 175–179, 2009.

[4] Cantisani V, Ricci P, Medvedeieva M, Olive M, Segni MDi, Mancuso E, Maggini E, Passariello R: Prospective Evaluation of Multiparametric Ultrasound and Quantitative Elastosonography in the Differential Diagnosis of Benign and Malignant Thyroid Nodules. Insights into Imaging, 2, Supp. 1, p. 180, 2011.

* *indicates Presenter*

Invited Presentation:

097 **MEASUREMENT METHODS FOR THE MECHANICAL CHARACTERIZATION OF SOFT BIOLOGICAL TISSUE.**

Edoardo Mazza[1]*.
[1]Institute of Mechanical Systems, Swiss Federal Institute of Technology, 8092 Zurich, SWITZERLAND.

Introduction: Mechanical characterization of soft human tissue provides valuable information for diagnosis. Experimental observations of the mechanical behavior of soft tissue are also essential for determining model parameters of constitutive equations for biomechanical models. These equations aim at describing the *in vivo* mechanical behavior of tissues and organs when subjected to physiological conditions of loading and deformation. Recent developments in experimental biomechanics contribute to the attainment of corresponding experimental data. Three aspects will be considered in this presentation: (I) the characterization of biological membranes subjected to uniaxial and biaxial stress states, (II) the *in vivo* measurement of the mechanical response of soft human organs with quasi static experiments and (III) whole organ experiments.

I Multi–axial Characterization of Biological Membranes:
Methods were developed to extend the use of conventional mechanical testing procedures for the characterization of biological materials. Examples will be given of multi–axial characterization of the mechanical response of biological membranes, such as fetal membranes (amnio–chorion) and Glisson's capsule. Different configurations are combined for this purpose: uniaxial stress tests, pure shear (using test pieces with large ratio of width to length) and so called "inflation experiments". Quantitative assessment of elastin and total collagen content in the membranes allows evaluating correlations between mechanical parameters and tissue microstructure.

II *In Vivo* Quasi Static Measurement of the Mechanical Response of Soft Human Organs:
Indentation, aspiration and grasper devices were proposed to evaluate the *in vivo* mechanical behavior of soft tissue. The different techniques and the corresponding data analysis procedures will be outlined. Experiences from clinical studies with aspiration experiments on the liver during open abdominal surgery and intra–vaginal on the uterine cervix in the course of gestation will be summarized. Histopathological characterization with biopsies taken at the measurement location allows analyzing the correlation between mechanical response and local tissue microstructure.

III Whole Organ Experiments:
Whole organ experiments provide information for a mechanical characterization of the tissues involved and represent a benchmark for a quantitative verification of the predictive capabilities of corresponding numerical models. Examples will be presented for the validation of a detailed finite element model of the face. Medical imaging techniques as well as dedicated mechanical devices were used to quantitatively evaluate modeling assumptions.

Interdisciplinary research has enabled significant progress in the past ten years towards quantitative assessment and interpretation of soft tissues' mechanical properties. Enhancing the clinical significance of biomechanical investigations represents the main objective of current and future studies.

Figure I: Tests on fetal membranes

Figure II: Liver aspiration

Figure III: Whole organ experiments on face and spine.

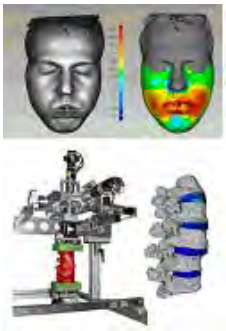

079 **MULTI–PUSH (MP) ARF ASSESSMENT OF VISCOELASTIC PROPERTIES IN A TISSUE MIMICKING PHANTOM.**

Mallory R. Scola[1], Caterina M. Gallippi[1].*
[1]Joint Department of Biomedical Engineering, The University of North Carolina at Chapel Hill, Chapel Hill, NC, USA.

Background: Noninvasively discriminating viscoelastic properties of tissue has a multitude of diagnostic purposes. Acoustic radiation force (ARF) based imaging methods have been used successfully over the past 15 years in several medical applications, but these approaches have primarily focused on only the elastic properties of tissue. Multi–Push (MP) ARF, a novel ARF method, exploits both the elastic and viscous tissue properties. MP ARF interrogates multiple points along the viscoelastic displacement curve. The relative shape of the displacement curve is then estimated by comparing the displacements at successive points. For two successive pushes, we calculate the marginal peak displacement (MPD) achieved by the second push relative to the first as:

$$MPD = 1 - \frac{PD_1 - (PD_2 - D)}{PD_1}$$

where PD_1 is the peak displacement (PD) achieved by the first push, PD_2 is the PD achieved by the second push and D is the displacement remaining at the time of the second push. We hypothesized that MPD would decrease with increased stiffness and viscosity.

Aims: This work investigates the use of MP ARF for delineating differences in viscoelastic properties of tissue mimicking phantoms.

Methods: Three homogenous, gelatin–based phantoms sets (A, B and C) were prepared with different concentrations of corn syrup to alter the viscosity; each set consisted of three phantoms prepared with different concentrations of gelatin to vary stiffness. Imaging was performed using a Siemens SONOLINE Antares™ imaging system specially equipped for research purposes and a VF7–3 linear array transducer. MP ARF was implemented using two 300–cycle ARF excitations administered to the same region of excitation and separated by 1.0ms in time. For each phantom, the MPD was calculated, and a Monitored Steady–State Excitation Recovery (MSSER) sequence consisting of thirty 10–cycle ARF excitations was used to estimate the spring constant (μ) and the coefficient of viscosity (η) in terms of the applied force magnitude (A) [1]. Phantoms were also characterized using a compressional mechanical testing device.

Results: Measurements of μ, η estimated by MSSER and MPD are summarized in Table 1. Phantom A3 which was stiffer (larger μ) and more viscous (larger η) than phantoms A1 and A2, experienced smaller MPD values than A1 and A2. Similarly, phantoms B3 and C3 had the largest μ and η and smallest MPD values in the B and C phantom sets, respectively.

Phantom	μ [μm^{-1}]	η [ms/μm]	MPD
A1	0.240 ± 0.014 × A	0.198 ± 0.026 × A	0.877 ± 0.095
A2	0.254 ± 0.025 × A	0.205 ± 0.022 × A	0.804 ± 0.144
A3	0.443 ± 0.044 × A	0.252 ± 0.027 × A	0.694 ± 0.193
B1	0.173 ± 0.021 × A	0.169 ± 0.022 × A	0.867 ± 0.103
B2	0.236 ± 0.028 × A	0.178 ± 0.026 × A	0.743 ± 0.177
B3	0.399 ± 0.046 × A	0.302 ± 0.040 × A	0.682 ± 0.227
C1	0.205 ± 0.016 × A	0.230 ± 0.023 × A	0.908 ± 0.076
C2	0.261 ± 0.030 × A	0.235 ± 0.025 × A	0.858 ± 0.107
C3	0.428 ± 0.064 × A	0.267 ± 0.040 × A	0.781 ± 0.149

Table 1: Summary of measurements (mean ± std), where A indicates the applied force magnitude

Conclusions: Preliminary results indicate that MPD was smaller in phantoms with higher stiffness and viscosity.

Acknowledgements: This work was supported the Integrated Biomedical Research Training Program

References:

[1] F.W. Mauldin, et al.: Monitored Steady–State Excitation and Recovery (MSSER) Radiation Force Imaging using Viscoelastic Models. IEEE Trans. on Ultras. Ferr. and Freq. Cntrl., Vol. 55, pp. 1597–1610, Jul, 2008.

** indicates Presenter*

083 **DEVELOPMENT OF A MINIATURIZED WATER–JET ULTRASOUND INDENTATION PROBE FOR DETECTION OF ARTICULAR CARTILAGE DEGENERATION.**

Yan–Ping Huang[1], Yong–Ping Zheng[1].*
[1]Health Technology and Informatics Department, Hong Kong Polytechnic University, Hong Kong, CHINA.

Background: Osteoarthritis (OA) is a common joint disease, especially for the elderly. Cartilage is significantly degenerated in OA. Current diagnostic methods can only detect degeneration at a very late stage through examination of clinical symptoms or plain radiography; however, no cure exists for this late stage of cartilage degeneration. Therefore, new tools for quantitative assessment of early cartilage degeneration are needed. We have previously developed a water–jet ultrasound indentation method for evaluating the mechanical properties of soft tissues [1]. It cannot be directly used for the assessment of articular cartilage i*n vivo* due to its large size originally designed for workbench operation.

Aims: The aim of this study is to develop a miniaturized water–jet ultrasound indentation probe that can be potentially incorporated for arthroscopic assessment of articular cartilage degeneration or repair.

Methods: A water–jet ultrasound indentation probe was fabricated in a small rod (Ø = 12 mm). It comprised of a 10MHz ultrasound transducer for collecting ultrasound signals and a channel for generating the pressurized water–jet (Figure 1). To demonstrate the performance of the probe, we used it to collect data from *in vitro* bovine osteochondral cartilage samples using ultrasound measurement and indentation tests. The parameters being measured were cartilage thickness, surface integrated reflection coefficient (IRC, dB), stiffness (MPa) and energy dissipation ratio (EDR, %). Stiffness was defined as the indention pressure over the percentage deformation of cartilage, and EDR was defined as the energy loss over the total energy applied in loading in one cycle of indentation. Ten samples were used for the measurement reproducibility test in terms of the standardized coefficient of variation (SCV). Another 40 were divided into two groups (20 each) with trypsin and collagenase digestion, respectively, to simulate the degeneration of articular cartilage.

Results: The SCV was 2.6%, 10.2%, 11.5% and 12.8% for thickness, IRC, stiffness and EDR, respectively. No significant difference of cartilage thickness was detected after collagenase (1.73±0.37mm vs 1.73±0.37mm, p=0.70, t–test) or trypsin (1.97±0.54mm vs. 1.96±0.52mm, p=0.70) treatment. IRC significantly decreased in the collagenase digestion group (-31.5±4.2dB vs. -24.8±1.9dB, p<0.001) but not in the trypsin digestion group (-23.3±2.2dB vs. -23.1±1.8dB, p=–0.56). Stiffness significantly decreased (4.68±1.52MPa vs. 11.70±6.43MPa for collagenase, p<0.001; 3.12±1.37MPa vs. 10.73±5.15MPa for trypsin, p<0.001) and EDR significantly increased (55.5±7.5% vs. 22.7±5.5% for collagenase, p<0.001; 63.2±4.5% vs. 22.7±6.9% for trypsin, p<0.001) after both enzymatic digestions. A 3D plot of the experimental data is shown in Figure 2. The change of mechanical parameters was also verified using the traditional indentation technique (mechanical testing machine, Instron). Histological analysis showed proteoglycan loss in both enzymatic digestions.

Conclusions: The miniaturized probe was developed and tested with an experimental model of cartilage degeneration. With this probe, the measured morphological, mechanical and acoustic parameters have a potential to be used in differentiation of degeneration induced by collagen network from proteoglycan destruction.

Acknowledgements: This project was partially supported by the Research Grant Council of Hong Kong (PolyU5354/08E) and The Hong Kong Polytechnic University (J–BB69).

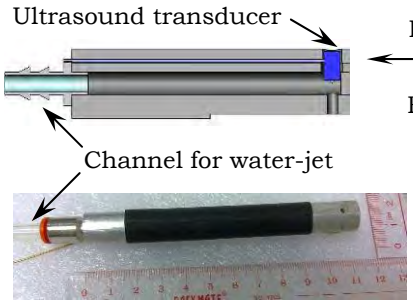

Figure 1: A schematic diagram of the probe (a) and its realization (b).

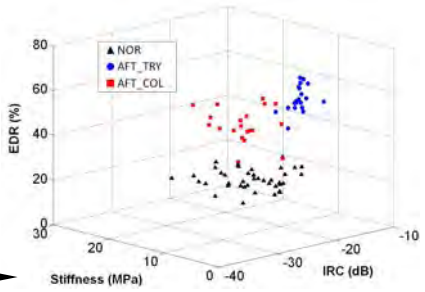

Figure 2: A 3D scatter plot of the measured parameters: Energy dissipation ratio (EDR, %), effective stiffness (MPa) and integrated reflection coefficient (dB) in three groups: NOR (normal); AFT_TRY (after trypsin treatment); AFT_COL (after collagenase treatment).

References:

[1] Lu MH et al.: A Novel Noncontact Ultrasound Indentation System for Measurement of Tissue Material Properties Using Water Jet Compression. Ultrasound Med. Biol., 31, pp. 817–826 2005.

* *indicates Presenter*

084 **A MINIATURIZED AIR JET INDENTATION PROBE BASED ON OPTICAL COHERENCE TOMOGRAPHY (OCT) FOR MECHANICAL ASSESSMENT OF SOFT TISSUE.**

Li–Ke Wang[1], Yan–Ping Huang[1], Yong–Ping Zheng[1].*
[1]Health Technology and Informatics Department, Hong Kong Polytechnic University, Hong Kong, CHINA.

Background: Indentation has become one of the widely used methods to quantitatively assess tissue mechanical properties which have a close relationship with their physiological functions. However, most of them measure the tissue elasticity through contact. We have previously developed an OCT–based air jet indentation system to measure tissue elasticity with a non–contact way [1]. It has been used for characterizing the biomechanical properties of normal plantar tissue and wound tissue [2]. However, the large size of the detection probe limits its application for various body regions *in vivo*.

Aims: This study aims to develop a miniaturized OCT–based air jet indentation probe which can be suitable for assessing the biomechanical properties of tissues at various regions, even endoscopically.

Methods: A miniaturized probe, of which the diameter was approximately 4.5 mm, was developed in our study (Figure 1). This probe consisted of a single–mode optical fiber, a gradient index (GRIN) lens and an airway bubbler, which allowed passing of the optical beam and the pressured air together. The GRIN lens was mounted on a fixed base of the bubbler with through holes, and also made the light beam focus on the detection point with small light loss. Using the current design, the probe size was significantly reduced to meet the miniaturization requirement for assessing tissues in various regions. In this study, a cyclic triangular wave of air jet pressure was used for the indentation. During the indentation, air jet force calibrated from the air jet pressure and OCT signal from the tissue surface were recorded synchronously for off–line processing. A cross–correlation method was adopted to track the tissue layer displacement under the corresponding air jet force. The elasticity of tissue was calculated from the regressed line of air jet force and tissue deformation. In order to validate its feasibility, 17 tissue–mimicking silicone phantoms with different elasticity were measured using indentation by the current system and a standard mechanical test system, Instron. Furthermore, 10 subjects were recruited to measure the change of mechanical properties of skin and soft tissue of the hand, with underlying muscles in relaxed and contracted states.

Results: Three repeated tests of one phantom indicated a stiffness coefficient of 81.8±1.1 mN/mm (1.3% variation). Correlation between the air jet indentation and the Instron test showed that the results of the two tests were highly comparable ($r=0.955$, $p<0.001$) (Figure 2). A paired sample *t*–test was used to compare the difference between the stiffness of hand tissue for contracted and relaxed muscles. The stiffness' of the two states were 28.1±7.2 and 67.5±27.9 mN/mm (Figure 3, $p<0.001$) showing that the current system could distinguish the difference of muscle contraction status.

Conclusions: Preliminary results of phantom tests and *in vivo* tissue tests showed that this miniaturized probe was useful for measuring the mechanical properties of tissue. It offers potential for non–contact tissue assessment using micro–indentation. In minimally invasive surgery, this novel miniaturized probe could reach the inside body using a working channel of an endoscope. Therefore, it has potential for elasticity measurement of internal organs such as the gastrointestinal tract.

Acknowledgements: This work was partially supported by the Research Grant Council of Hong Kong (PolyU5354/08E) and The Hong Kong Polytechnic University (J-BB69).

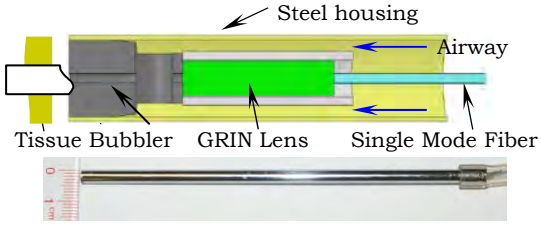

Figure 1: A schematic of the miniaturized OCT–based air jet indentation probe and its structural design.

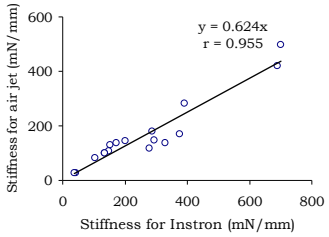

Figure 2: Correlation of elasticity coefficients obtained from our system and Instron.

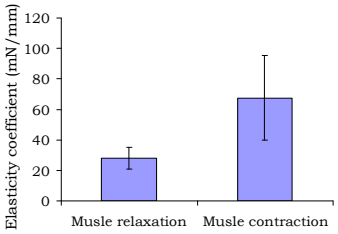

Figure 3: Comparison of tissue elasticity measured *in vivo* with underlying muscle relaxed and contracted.

References:

[1] Huang YP, et al.: An Optical Coherence Tomography (OCT)–Based Air Jet Indentation System for Measuring the Mechanical Properties of Soft Tissues. Meas. Sci. Technol., Vol. 20, 015805, Jan. 2009.
[2] Chao CYL, et al.: Biomechanical Properties of the Forefoot Plantar Soft Tissue as Measured by an Optical Coherence Tomography–Based Air–Jet Indentation System and Tissue Ultrasound Palpation System. Clin. Biomech., Vol. 25, pp. 594–600, 2010.

* *indicates Presenter*

086 DEVELOPMENT OF A VIBRO-ULTRASOUND METHOD FOR SKELETAL MUSCLE STIFFNESS ASSESSMENT UNDER HIGH LEVELS OF ISOMETRIC CONTRACTION.

Cong–Zhi Wang[1], Yong–Ping Zheng[1].*
[1]Health Technology and Informatics Department, The Hong Kong Polytechnic University, Hong Kong, CHINA.

Background: A number of methods have been developed to quantify muscle stiffness along its action direction, and each has unique features and limitations. One major limitation is that the measurement ranges cannot exceed 50% maximum voluntary contraction (MVC) level [1–3]. However, the information at high contraction levels is considered more important for muscle functional assessment. Stiffness of skeletal muscle has been reported to be correlated to its non–fatiguing contraction intensity. However, this conclusion has not been verified over the entire step isometric contraction range, i.e. from 0–100% MVC level. Furthermore, the dependences of joint angle, gender and age on the relationship between muscle stiffness and contraction intensity has seldom been studied systematically.

Aims: We developed a vibro–ultrasound system based on the measurement of shear wave velocity which was suitable for the assessment of elasticity along the muscle longitudinal direction. It was used to assess the shear modulus of *vastus intermedius* (VI) of the thigh along the muscle action direction. The relationship between the muscle stiffness and the step isometric contraction level was studied under two different knee joint angles, 90° and 60° (0° for full extension). The gender and age dependences of this relationship were also studied.

Methods: A vibrator was used to disturb the thigh muscle and the induced shear wave inside the muscle with a frequency of 100Hz was monitored using two A–lines of a linear probe with a distance of 15mm. The frame rate for each A–line was 4600 frames/s. Forty healthy subjects volunteered to participate in the experiment and were divided into four groups: young males (n=10, 29.4±4.8 yr), young females (n=10, 27.6±5.0 yr), elder males (n=10, 60.6±7.6 yr) and elder females (n=10, 56.7±4.9 yr). Measurements were first performed under the relaxed condition with 3 trials. Then the subjects were asked to maintain isometric contraction at 10 different percentages of MVC levels, from 10–100%, for approximately 4 seconds in 3 trials for each level. One minute of rest was allowed between any two measurements to avoid muscle fatigue.

Results: The results showed that VI stiffness along the muscle action direction was positively correlated to the step isometric contraction level over the entire range at both knee joint angles ($p<0.001$). The relationship was close to a quadratic polynomial curve ($p<0.001$). It was also found that under both the relaxed condition and isometric contraction, VI shear modulus measured at a 90° knee joint angle was larger than that measured at 60° ($p<0.001$). There was no significant difference in the relaxed VI shear modulus between different genders ($p=0.156$) and age ranges ($p=0.221$). However, when performing isometric contraction, the VI shear modulus of the male subjects was found to be larger than that of the females ($p<0.001$), and the shear modulus of the young subjects was larger than that of the elderly ($p<0.001$), at the same contraction level and knee joint angle. There was up to 100 times increase of the stiffness from relaxed to 100% MVC (Figure 1).

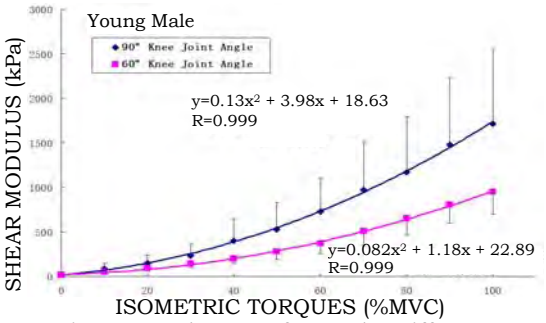

Figure 1: Change of muscle stiffness under contraction

Conclusions: We have successfully demonstrated that the vibro–ultrasound method can provide a tool for muscle stiffness assessment over the entire range of step isometric contraction. We also investigated the relationship between muscle stiffness and muscle contraction intensity, considering the effects of gender, age and joint angle. The change of muscle elasticity along the action direction is up to 100 times, from relaxed state to 100% MVC.

Acknowledgements: This study was partially supported by Hong Kong Innovative Technology Fund (GHP/047/09).

References:

[1] Chen SG, et al.: Shearwave Dispersion Ultrasound Vibrometry (SDUV) for Measuring Tissue Elasticity and Viscosity. IEEE Trans Ultrason Ferroelectr Freq Control, 56, pp. 55–62, 2009.
[2] Shinohara M, et al.: Real–Time Visualization of Muscle Stiffness Distribution with Ultrasound Shear Wave Imaging During Muscle Contraction. Muscle Nerve, 42, pp. 438–441, 2010.
[3] Bensamoun SF, et al.: Determination of Thigh Muscle Stiffness using Magnetic Resonance Elastography. J Magn Reson Imaging, 23, pp. 242–247, 2006.

Invited Presentation:

093 **BIOMECHANICAL IMAGING: ELASTOGRAPHY BEYOND YOUNG'S MODULUS.**

Paul E. Barbone[1]*.
[1]Mechanical Engineering, Boston University, Boston, MA 02215, USA.

Background: Elastography is often described as a technique to image tissue structures on the basis of contrast in elastic modulus. In this context, attempts to quantify tissue properties typically focus on linear shear modulus or Young's modulus, assuming isotropic, incompressible, linear elastic behavior of the tissue.

As both experience and ability with elastography grows, so is the recognition growing that soft tissues display biomechanical behaviors well beyond those characterized by the single number, E, Young's Modulus. When such behaviors are present to a significant degree, they can act as confounding effects in the attempt to characterize tissue elastic modulus. To the extent that such behaviors are observed, however, they are measurable and hence present opportunities for further tissue characterization and discrimination.

Aims: This presentation will give a brief overview of the mechanical behavior of soft tissues beyond the isotropic linear elastic incompressible tissue model.

Approach: Selected examples illustrating novel and observable anisotropic [1–4], nonlinear [5–12], inelastic [1,2,13–16], and compressible (multiphase) [17–24] tissue behavior will be presented from the literature. Any one of these phenomena violates the assumptions inherent in the isotropic linear elastic incompressible tissue model. For each of the phenomena surveyed, an explanation of the phenomenon will be presented, an illustrating example from the literature will be shown, and the potential to extract quantitative diagnostic value will be discussed.

Conclusions: Our optimistic assessment is that the techniques developed within the elastography community can be applied to assess a large number of biomechanical processes *in vivo*. Some of these are accessible with minor alterations of current protocols; others require further development, but are within practical reach. In summary, the community is poised to take elastography beyond Young's Modulus.

Acknowledgements: R21CA133488, R01CA140271.

References:

[1] Gao L., et al.: Ultras. in Med. & Bio., 22(8), pp. 959–977, 1996.
[2] Sinkus R., et al.: Mag. Res.e in Med., 53(2), pp. 372–387, 2005.
[3] Gennisson, J.L., et al.: J. of the Ac. Soc. of Am., 114, pp. 536–541, 2003.
[4] Spencer W., et al.: J. of Biomech. Eng., 133(6), 2011, DOI: 10.1115/1.4004231.
[5] Skovoroda, A.R., et al.: IEEE Trans. on Ultras., Ferr. and Freq. Cntrl., 46(3), pp. 523–535, 1999.
[6] Varghese, T., et al.: Ultras. in Med. & Biol., 26(5), pp. 839–851, 2000.
[7] Erkamp, R.Q., et al.: IEEE Trans on Ultras., Ferr. and Freq. Cntrl., 51(5), pp. 532–539, 2004.
[8] Oberai, A.A., et al.: Phys. in Med. & Biol., 54, p. 1191, 2009.
[9] Timothy J. Hall, et al.: Current Medical Imaging Reviews, 2011, in press.
[10] Catheline, S., et al.: J. of the Acous. Soc. of Am., 114, pp. 3087–3091, 2003.
[11] Sack, I., et al.: Mag. Res. in Med., 52(4), pp. 842–850, 2004.
[12] Samani, A., Plewes, D.: Phys. in Med. & Biol., 49, p. 4395, 2004.
[13] Insana, M.F., et al.: J. of Mamm. Gland Biol. & Neopl., 9(4), pp. 393–404, 2004.
[14] Sridhar, M., et al.: Phys. in Med. & Biol., 52, p. 2425, 2007.
[15] Sridhar, M., Insana, M.F.: Med. Phys., 34, p. 4757, 2007.
[16] Qiu, Y., et al.: Academic Radiology, 15(12), pp. 1526–1533, 2008.
[17] Konofagou, E.E., et al.: Ultras. in Med. & Biol., 27(10), pp. 1387–1397, 2001.
[18] Righetti R, et al.: Ultras. in Med. & Biol., 30(2), pp. 215–228, 2004.
[19] GP Berry, et al.: Ultras. in Med. & Biol., 32(4), pp. 547–567, 2006.
[20] GP Berry, et al.: Ultras. in Med. & Biol., 32(12), pp. 1869–1885, 2006.
[21] R Leiderman, et al.: Phys. in Med. & Biol., 51 (24), pp. 6291–6313, 2006.
[22] Righetti, R., et al.: Phys. in Med. & Biol., 52, p. 6525, 2007.
[23] GP Berry, et al.: Ultras. in Med. & Biol., Vol. 34, Is. 4, pp. 617–629, 2008.
[24] R Leiderman, et al.: Comptes Rendus Mecanique, 338, pp. 412–423, 2010.

004 **A NOVEL FRACTIONAL ORDER VISCOELASTIC MATERIAL MODEL FOR SOFT BIOLOGICAL TISSUES AND ITS FINITE ELEMENT APPLICATION.**

Nagehan Demirci[1], Ergin Tönük[1].*
[1]Middle East Technical University, Ankara, TR–06800, TURKEY.

Background: *In–vivo* experimental studies of bulk soft tissue indicate that the mechanical response of soft tissues is non–linear and viscoelastic. Fractional order models involving derivatives and integrals of none–integer order have proven to be very useful for studying viscoelastic materials and material parameter identification. As fractional differential equations obey the "fading memory principle", they are suitable for representing viscoelastic behavior. It has been shown that fractional order material models give better results compared to integer order models with fewer parameters in experimental data fit. Several fractional order linear viscoelastic material models are present in the literature, where those models include a "spring–pot" element instead of a "dashpot" which is regularly seen in integer order (Kelvin–Voigt, Maxwell, Zener) models. The order of the spring–pot element defines the "material memory" parameter and gives an insight to fractal–like behavior of the tissue. In addition, the solution of fractional order viscoelastic constitutive relations involve a generalized exponential function, called the Mittag–Leffler function, where a fast computation scheme for the Mittag–Leffler function is offered specifically for finite element analysis applications [1]. The implementation of the 3D fractional order viscoelastic material model into a finite element analysis package program yields future better success of analyzing soft tissues in interaction with their mechanical environments.

Aims: The aim of this study is to develop a 3D viscoelastic material model for soft biological tissues involving fractional operators and to implement the developed material model into the finite element analysis package program Msc.Marc 2010®.

Methods: The time–dependent, viscoelastic, dissipative part of extended James–Green–Simpson material model including the two–term Prony series [2] is further modified to a less parameter fractional order nonlinear viscoelastic material model including the Mittag–Leffler function. The novel material model developed is implemented into the Msc.Marc 2010® software via the user–subroutine "uelastomer". The verification of the user–subroutine developed is performed via Matlab R2009b® by employing the same parameters under the same loading condition. Two set of "normalized reaction force vs. time" data are obtained for verification under constant displacement (unit–step input, relaxation response), small strain loading condition, one from 3D finite element analysis result on Msc.Marc 2010® and the other from 1D analytical result on Matlab R2009b® (Figure 1). Further, the viscoelastic material mechanical responses which are creep, relaxation and hysteresis are simulated via finite element analysis (FEA) using the novel material model user–subroutine identified to the program.

Results: Two sets of relaxation response data obtained are shown to be perfectly fitted, therefore verifying the user–subroutine developed. Fractional order viscoelastic material models provide better fit capabilities to experimental creep, relaxation and hysteresis data compared to integer order one–term and two–term Prony series representation with fewer number of parameters (Figure 2).

Conclusions: Fractional order viscoelasticity (FOV) provides valuable understanding of tissue viscoelastic behavior. With the aid of implementing the fractional order viscoelastic material model into finite element analysis will lead to more realistic simulation and problem solving of soft tissue–mechanical environment interactions.

References:

[1] A. Freed, K. Diethelm, Y. Luchko: Fractional–Order Viscoelasticity (FOV): Constitutive Development Using the Fractional Calculus: First Annual Report. NASA/TM–2002–211914.
[2] E. Tönük, M.B. Silver–Thorn: Nonlinear Viscoelastic Material Property Estimation of Lower Extremity Residual Limb Tissues. Journal of Biomech. Eng., 126, pp. 289–299, 2004.

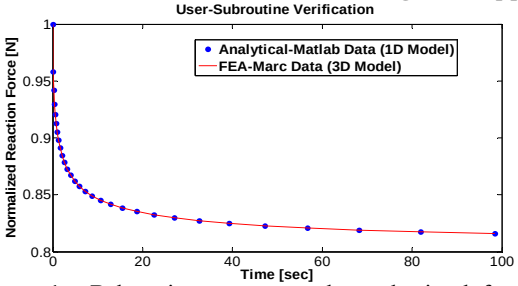

Figure 1: Relaxation response data obtained from (3D) FEA and (1D) analytical model.

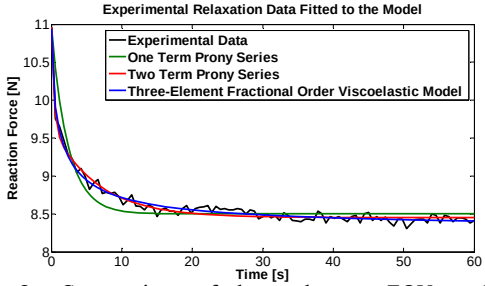

Figure 2: Comparison of three–element FOV model to integer order one and two term Prony series.

* *indicates Presenter*

036 **DISPERSION AND DISTORTION OF SHEAR WAVE PULSES.**

Kevin J. Parker[1], Zaegyoo Hah[1].*
[1]University of Rochester, Hopeman Engineering Building 203, P.O. Box 270126, Rochester, NY, 14627, USA.

Background: In a variety of applications and techniques, a shear wave is created by an impulsive radiation force, and the wave propagates away from the source. The influence of dispersion, that is, frequency dependent phase velocity and attenuation, is particularly strong for shear wave pulses formed by conventional focused ultrasound beams. Dispersion effects begin to distort the shear wave pulse within millimeters of travel, and these effects can confound some tracking estimators. A number of models have been proposed for shear waves in tissues (Oestreicher 1951, Sarvazyan 1998, Palmieri 2004), however a closed form analytical solution with explicit dispersion terms is still desired.

Aims: Develop closed–form solutions for the effects of dispersion on propagating shear wave pulses, assess the impact of these dispersion effects and develop estimators for characterizing the dispersion.

Methods: A model of shear wave propagation is developed for the Gaussian beam shape, first in a one dimensional solution and then in cylindrical coordinates. Analytical expressions are derived for the propagating beam under realistic values of shear wave speed and shear wave attenuation that are frequency dependent. The solutions are compared with experimental results.

Results: It is shown that the shear wave pulse from a Gaussian impulsive beam propagates with two distinct distortion functions. The first is a broadening function due to progressive attenuation of the higher spatial and temporal frequencies. The second is an asymmetric distortion due to a quadratic phase term. These progressively distort the propagating beam and shift the peak value of the pulse with respect to the expected location using simpler models.

Conclusions: The effects of dispersion can be quite significant within a few millimeters or milliseconds of propagation. The progressive distortion of the pulse from frequency–dependent propagation will complicate peak tracking. The estimation of phase velocities over the bandwidth can be assessed using alternate means.

Acknowledgements: This work was supported by NIH Grant 5R01AG29804.

References:

[1] Oestreicher HL.: Field and Impedance of an Oscillating Sphere in a Viscoelastic Medium with an Application to Biophysics. J Acout Soc Am., 23(6), pp. 707–14,1951.
[2] Palmeri ML and Nightingale KR: On the Thermal Effects Associated with Radiation Force Imaging of Soft Tissue. IEEE Trans Ultrason Ferroelectr Freq Control. 51(4), pp. 551–65, 2004.
[3] Sarvazyan AP, Rudenko OV, Swanson SD, Fowlkes JB and Emelianov SY: Shear Wave Elasticity Imaging: A New Ultrasonic Technology of Medical Diagnostics. Ultrasound Med Biol, 24(9), pp. 1419–35, 1998.

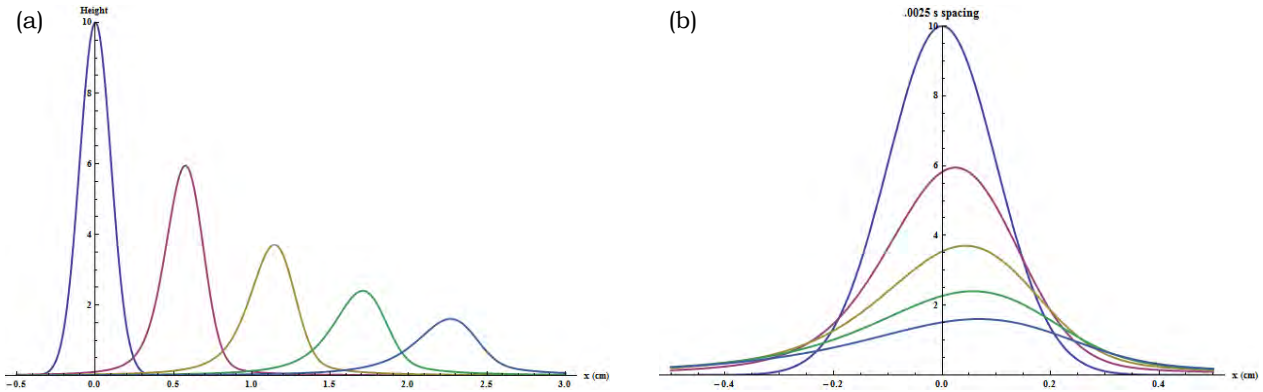

Figure 1: Theoretical shear waves from an initially Gaussian beam propagating in a dispersive and attenuating homogenous medium. Vertical axes: z–displacement in microns. Horizontal axis: distance in cm. (a) Propagating pulses at regular intervals. (b) Re–centered pulses from different times to show progression of asymmetry.

* *indicates Presenter*

041 **SHEAR WAVE SPEED (SWS)-BASED ASSESSMENT OF NONLINEAR MATERIAL PROPERTIES.**

Veronica M. Rotemberg[1], Mark L. Palmeri[1,2], Kathryn R. Nightingale[1].*
[1]Biomedical Engineering Department, Duke University, Durham, NC, USA; [2]Anesthesiology Department, Duke Medical Center, Durham, NC, USA.

Background: Increased hepatic interstitial pressure can be observed in patients with advanced liver disease and congestive heart failure. Previous studies have linked advanced stages of liver fibrosis and elevated hepatic pressures to increases in liver shear wave speed (SWS) derived stiffness estimates [1–4]. While the SWS increase with fibrosis is attributed to increases in extracellular collagen, the underlying mechanism for the observed stiffening behavior with pressurization is not well understood and cannot be explained with classical linear elastic or linear poroelastic models. Compression in hyperelastic phantoms has been investigated [5,6] in the context of compression and shear wave speed estimates. We are developing finite element method (FEM) modeling tools to simulate hyperelastic material models in the context of radiation force based excitation. In order to interrogate this behavior, analyses were performed on the impact of tissue mechanical nonlinearity on estimates of shear wave speed. Two simple nonlinear materials were chosen to model the liver tissue type: Neo–Hookean and Mooney–Rivlin. These models rely on one or two parameters of nonlinearity respectively and have been extensively studied analytically, so they provide the ideal basis for beginning to study nonlinear behavior with SWS assessment [7].

Aims: Neo–Hookean and Mooney–Rivlin nonlinear hyperelastic models were investigated and compared to classical linear elastic materials using analytic and finite element method approaches to test the hypothesis that tissue nonlinear models could predict observed increases in SWS with hepatic pressurization.

Methods: The relationship between SWS and applied uniaxial tension was derived analytically for Neo–Hookean and Mooney–Rivlin material models. These models were selected because they are consistent with previous reports from tissue and tissue–mimicking materials [4]. Both models predict increases in SWS with material compression. Finite element simulations in compressed hyperelastic materials were performed as follows to verify these relationships. A solid, three–dimensional, quarter–symmetric mesh was constructed using HyperMesh™ (HyperMesh™, Altair Computing, Inc., Troy, MI). The elements were cubic in the range of the ARFI excitation (node spacing .1mm), and the element properties were applied using the *MAT_MOONEY_RIVLIN card in LS–PREPOSTTM (Livermore Software Technology Corp., Livermore, CA). The acoustic intensity field of the ARFI excitation was calculated in FIELD II and converted to nodal point loads using the volume of each element in Matlab (MathWorks™, Natick, MA) [8]. Shear waves were propagated in the model at various stages of uniaxial compression between 0–20% strain.

Results: Shear wave speed estimates were observed to increase with compression for a Mooney–Rivlin and Neo–Hookean materials. The Mooney–Rivlin model is higher order and supports a broader range of stiffening behavior with material compression than the Neo–Hookean model. There were no sound speed differences between the models.

Conclusions: Increases in SWS with compression in Mooney–Rivlin and Neo–Hookean materials suggest that hyperelastic models may be useful for describing hepatic SWS increases with pressurization.

Acknowledgements: This work was supported by NIH grants R01 EB002132, R01 CA142824 and T32 GM007171. Special thanks to Siemens Healthcare, Ultrasound Business Unit, Mountain View, for their technical assistance.

References:

[1] G. Millonig, S. Friedrich, et al.: Liver Stiffness is Directly Influenced by Central Venous Pressure. Journal of Hepatology, 52, pp. 206–210, 2010.
[2] B. Schlosser, M. Biermer, et al.: Evaluation of Magnetic Resonance Elastography (MRE) as a Non–Invasive Method to Assess the Stage of Liver fibrosis in Patients with Chronic Liver Diseases. Hepatology, 50(4), p. 919, 2009.
[3] M. Wang, M. Palmeri, et al.: Non–Invasive Assessment of Liver Fibrosis with Quantitative Acoustic Radiation Force Methods. Hepatology, 50(4), p. 932, 2009.
[4] M. Palmeri, M. Wang, et al.: Noninvasive Evaluation of Hepatic Fibrosis using Acoustic Radiation Force-Based Shear Stiffness in Patients with Nonalcoholic Fatty Liver Disease. Journal of Hepatology, 2011.
[5] J–L Gennisson, M. Rénier, et al.: Acoustoelasticity in Soft Solids: Assessment of the Nonlinear Shear Modulus with the Acoustic Radiation Force. Journal of the Acoustical Society of America, 122(6), pp. 3211–3219, 2007.
[6] R. Erkamp, A. Skovoroda, et al.: Measuring the Nonlinear Elastic Properties of Tissue–Like Phantoms. IEEE Trans. on UFFC, 51(4), pp. 410–418, 2004.
[7] R. Ogden: Non-Linear Elastic Deformations. Mineola, New York, Dover, 1984.
[8] M. Palmeri, A. Sharma, et al.: A Finite Element Model of Soft Tissue Response to Impulsive Acoustic Radiation Force. IEEE Transactions on UFFC, 52(10), pp. 1699–1712, 2005.

062 **DEVELOPMENT OF A NEW MICROSTRUCTURE–BASED CONSTITUTIVE MODEL FOR HEALTHY AND CANCEROUS TISSUE.**

Elizabete Rodrigues Ferreira[1,2], Sevan Goenezen[1], Paul E. Barbone[3], Assad A. Oberai[1].*
[1]Mechanical Aerospace and Nuclear Engineering Department, Rensselaer Polytechnic Institute, Troy, NY 12180, USA; [2]Département de Mathématique, Université Libre de Bruxelles, Campus Plaine C.P. 218/1, 1050 Bruxelles, BELGIUM; [3]Mechanical Engineering Department, Boston University, Boston, MA 02215, USA.

Background: In second harmonic generation (SHG) images of breast tissue, it has been observed [1] that the tissue microstructure changes during tumorigenesis. In particular, the collagen fiber bundles in healthy glandular tissue are significantly coiled, in benign tumors, they are less coiled and in malignant tumors they are almost straight and rod–like.

Aims: The aim is to develop a new microstructure–based, macroscopic hyperelastic model for tissue by taking into account the presence of collagen fiber bundles, their curvature and their density. This model may then be used in conjunction with finite–strain, nonlinear elasticity imaging to infer the microstructural properties of tissue.

Methods: We consider a unit cell with a single fiber bundle and apply periodic boundary conditions. The Neo–Hookean material model is used for both the unit cell and the fiber. This incompressible material model is characterized by one constitutive constant, the shear modulus. A different shear modulus value is chosen for the background and for the fiber bundle. A prescribed macroscopic deformation is applied to this unit cell, and two–dimensional plane stress or two–dimensional plane strain is assumed. Then, a homogenization procedure [2] is used to determine the macroscopic strain energy density function for a given microstructural configuration. Different curvatures of the fiber bundles representing the collagen fiber bundles encountered in normal, benign and malignant tissue, along with various densities of fibers are considered. In each case, the macroscopic strain energy function is plotted as a function of the first invariant of the Cauchy–Green strain tensor. A new strain energy density function is thus constructed with material parameters that directly relate to the curvature and density of fiber bundles.

Results: We have demonstrated that the crimpled collagen fiber bundles observed in healthy tissue have a different macroscopic response when compared to the straight rod-like bundles observed in cancerous tissue. As shown in Figure 1, where the strain energy density is plotted as a function of I1–3, a measure of stretch, the variation of the curvature of the fibers leads to a different response when the tissue is strained. This also holds for stress. Indeed, when the curvature of the fiber is high as observed in normal tissue, the fiber bundles tend to uncoil and straighten with little resistance until the strain is sufficient so as to stretch the fibers. At this stage, they offer significant resistance to any further stretch. When the curvature is small as observed in cancerous tissue, this state is attained at smaller overall strains than in healthy tissues. This causes the cancerous tissue to exhibit increased stiffness at lower strain when compared with healthy tissue. These results confirm the observations made in [1], i.e. the difference in the curvature between fiber bundles in the benign and malignant tissue is statistically significant.

Figure 1

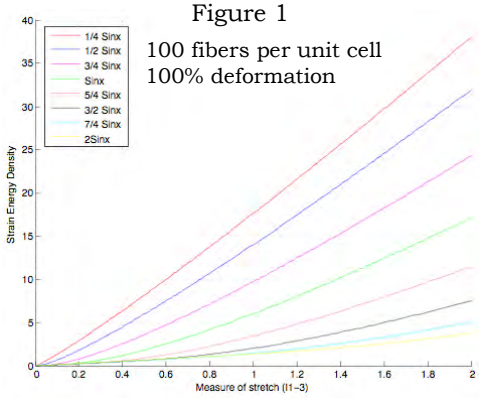

100 fibers per unit cell
100% deformation

Conclusions: In this study, a new constitutive model for collagenous tissue is developed in which accounts for the density and curvature of collagen fibers. The influence of fiber density and curvature on the strain energy density function is also analyzed. Future work will consist of the implementation of this new constitutive model in an inverse framework developed by the group. By solving this inverse problem, it will be possible to determine the distribution of the macroscopic parameters within the tissue, which will be directly linked to the average microstructural properties.

Acknowledgements: The first author acknowledges the Fulbright Foundation and the Université Libre de Bruxelles.

References:

[1] G. Falzon, S. Pearson, R. Murison: Analysis of Collagen Fiber Shape Changes in Breast Cancer. Physics in Medicine and Biology, 53, pp. 6641–6652, 2008.
[2] C. Miehe, J. Schröder, M. Becker: Computational Homogenization Analysis in Finite Elasticity: Material and Structural Instabilities on the Micro– and Macro–Scales of Periodic Composites and Their Interaction. Computer Methods in Applied Mechanics and Engineering, 191, pp. 4971–5005, 2002.

* *indicates Presenter*

066 **MECHANICAL MODEL ANALYSIS FOR QUANTITATIVE EVALUATION OF LIVER FIBROSIS BASED ON REAL–TIME TISSUE ELASTOGRAPHY.**

Tsuyoshi Shiina[1], Makoto Yamakawa[2], Masashi Kudo[3], Akiko Tonomura[4], Tsuyoshi Mitake[4].*
[1]Graduate School of Medicine, [2]Advanced Biomedical Engineering Research Unit, Kyoto University, Kyoto, JAPAN; [3]Gastroenterology and Hepatology Department, Kinki University School of Medicine, Osaka–Sayama, JAPAN; [4]Hitachi Aloka Medical, Ltd., Chiba, JAPAN.

Background: Chronic liver damage attributable to hepatitis C virus (HCV) infection results in hepatic fibrosis, which progresses towards cirrhosis, leading to hepatic carcinoma. Thus, precise evaluation of the stage of chronic hepatitis C with respect to fibrosis has become an important issue in preventing the occurrence of cirrhosis and in initiating the appropriate therapeutic intervention. Tissue elasticity imaging is expected to provide a noninvasive approach for staging disease progression. We have developed commercial–based equipment for tissue elasticity imaging (Real–time Tissue Elastography, Hitachi) for detecting tumors in the breast, prostate, etc. Considering the process of fibrosis, it is expected that fibrosis causes the inhomogeneous distribution of tissue hardness, which produces the non–uniform texture pattern in strain images. We recently reported that the texture of an elasticity image is based on strain changes as cirrhosis progresses [1,2].

Aims: The goal of this study is to clarify how fibrosis progression is reflected in the elasticity image by using mechanical models of hepatic fibrosis and to evaluate fibrosis progression quantitatively based on tissue elasticity imaging.

Methods: Progression of hepatic fibrosis causes the fine liver lobule structure to change to a coarse nodular structure stage by stage [3]. The fibrous progression model was constituted to simulate the process of lobule conjugation to nodules. Young's modulus at the lobule and nodule is set to values determined by considering the experimentally measured data. Next, the tissue deformation model was constituted to calculate the tissue deformation caused by compression using the finite–element method (FEM). Finally, the strain was calculated by comparing two frames of data acquired before and after compression. The obtained strain distribution is color–coded and displayed as elastography. Simulation was performed to verify the feasibility of the proposed model. For the model of normal liver, 2538 central points of liver lobules were distributed within a 40x40mm area; the distance between lobules was about 1mm. Conjugation is repeated until a specified limit of nodule size.

Results: Figure1a depicts the fibrous structure for stage 1 and stage 3 chronic hepatitis obtained based on the fibrous progression model. Figure 1b presents the Young's modulus distribution assigned based on the tissue–deformation model. The strain distribution obtained by FEM analysis for each fibrous stage is shown in Figure 1c. Results of this simulation validate the assumption that fibrosis causes a non–uniform texture pattern in strain images. The mean values of strain within ROI decreases as fibrosis progresses as shown in Figure 2.

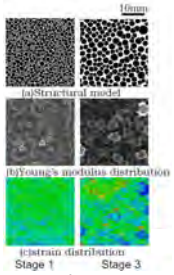

Figure 1: Examples of images obtained by using models of fibrous progression and tissue deformation.

Figure 2: Relation between the mean values of strain and fibrous stage derived from simulation analysis.

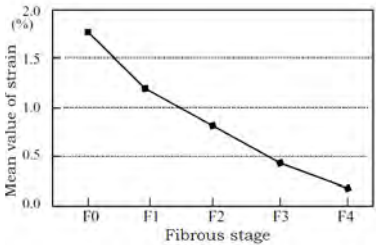

Conclusions: As a result of the simulation of fibrosis progression using mechanical model of hepatic tissue, we confirmed that the strain image pattern is related to the change of fibrous structure and elastic modulus distribution caused by hepatic disease. For further investigation, it is necessary to quantitatively examine the relation and develop CAD system for chronic hepatitis based on ultrasound tissue elasticity imaging.

Acknowledgements: This work was supported by Grant–in–Aid for Science Research [22103507], Mext, Japan.

References:

[1] M. Yamazaki, H. Takizawa, T. Shiina: Computer–Aided Diagnosis of Diffuse Disease Based on Ultrasound Elasticity Images. Proc. of 2008 IEEE Int. Ultrasonics Symp., pp. 2033–2035, 2008.
[2] Chie Tatumi, Masatoshi Kudo, et al.: Noninvasive Evaluation of Hepatic Fibrosis for Type C Chronic Hepatitis. Intervirology, Vol. 53, pp.76–81, 2010.
[3] T. Yamaguchi, K. Hirai, et al.: Evaluation of Ultrasonic Fiber Structure Extraction Technique using Autopsy Specimens of Liver. Jap. J. of App. Phys., Vol. 44, pp. 4615–4621, 2005.

* *indicates Presenter*

073 ***IN VIVO* MR RHEOLOGY OF LIVER AT MULTIPLE FREQUENCIES IN 3D: EFFECT OF DISPLACEMENT DATA DIMENSIONALITY ON SHEAR MODULUS**

Ramin S. Sahebjavaher[1,2], Philippe Garteiser[2], Bernard E. Van Beers[2], Septimiu Salcudean[1], Ralph Sinkus[2].*

[1]University of British Columbia, Vancouver, BC, CANADA; [2]Centre de Recherche Biomedicale Bichat–Beaujon (CERB3), Paris, FRANCE.

Background: In MRI, tissue motion is encoded in the phase images using motion sensitizing gradients that are synchronized to an externally applied excitation [1]. Conventional MR rheology experiments result in extended acquisition times which are impractical for full 3D acquisition even at single excitation frequency [2]. We use a novel pulse sequence to acquire 3D motion–encoded data in a volume for single and multiple excitation frequencies in a clinically feasible time frame. *In vivo* liver data from a healthy volunteer was acquired and processed with one (1D), two (2D) or all (3D) spatial components of the wave in an effort to evaluate the added value of this fully 3D acquisition scheme. Displacement maps, obtained using this pulse sequence, were used to study the frequency response of the mechanical parameters of the liver.

Aims: To study the frequency response of liver tissue using the new 3D motion–encoded MR technique. To evaluate the clinical feasibility of this technique in terms of acquisition time and data quality.

Methods: *In vivo* liver experiments were carried out on a Philips (Best, NL) 3T scanner. The acquisition (FOV 320x256x32, 4mm isotropic, TE/TR=6.8/147ms, 8 mech. phases) was performed within four ~15s breath holds. Excitation of 28, 56 and 84Hz were used for the mono– and multi–frequency experiments. From the resulting wave images (Figure 1), the wavelength was evaluated as the 1D, 2D or 3D Laplacian of one component of the curl in a region of liver. The dynamic shear modulus was manually calculated using $G_d=\rho(f\cdot\lambda)2$ (for ideal elastic material) and also calculated via software using the full 3D data [3].

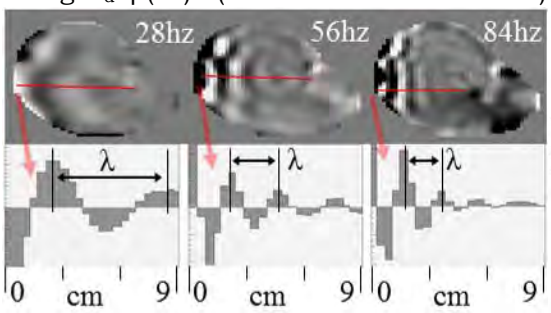

Figure 1: Wave images acquired using the new MR sequence at 28, 56 and 84Hz.

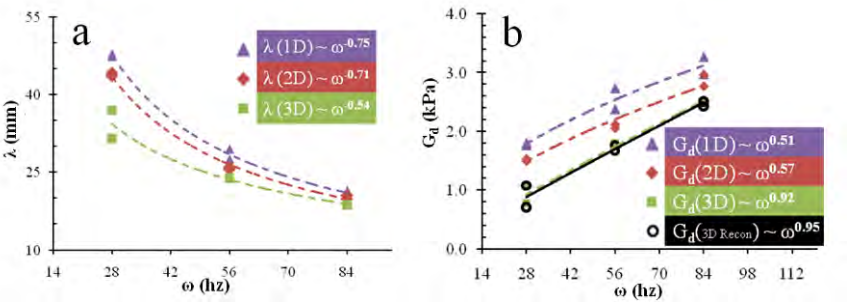

Figure 2: (a) Estimated wavelength λ and calculated shear modulus G_d at multiple frequencies using 1D, 2D or 3D displacement fields.

Results: The entire 3D motion–encoded acquisition for the FOV lasted 59s. The wavelength of the 1D was directly evaluated by a line profile perpendicular to the wave propagation (clearly observed in Figure 1); this matched with the 1D evaluation based on the region of interest (ROI) estimate. Figure 2 shows the wavelength (a) and the corresponding dynamic shear modulus (b) for a ROI considering 1D, 2D and 3D displacement data. A power–law fit was applied to the wavelength (exponents: -0.75, -0.71, -0.54) and Gd (exponents: 0.51, 0.57, 0.92) for 1D, 2D and 3D (respectively) cases. It was observed that the exponent changed significantly based on the available dimension of the displacement field.

Conclusions: A novel MR technique suitable for mono– and multi–frequency was experimentally validated as capable of acquiring 3D motion–data in a volume in less than a minute. The full 3D displacement field allows for correct estimation of mechanical parameters especially for low frequencies. Reducing the dimensionality of the Laplacian leads to significant underestimation of the according slopes of the frequency data. Further validation using simulations and larger patient studies will follow.

Acknowledgements: This work was supported by NSERC, CIHR and INSERM.

References:

[1] Muthupillai et al.: Nat Med, 2, pp. 601–603, 1996.
[2] Asbach et al.: Radiology, 257, pp. 80–86, 2010.
[3] Sinkus, R. et al.: MRI, 23, pp. 159–165, 2005.

* *indicates Presenter*

011 **RENAL ALLOGRAFT ELASTICITY ASSESSED BY SUPERSONIC AIXPLORER™ AND BY MAGNETIC RESONANCE ELASTOGRAPHY – PRELIMINARY RESULTS.**

R Souchon[1], S Lounis[2], G Pagnoux[3], JM Ménager[2], E Morelon[3], O Rouvière[3].*
[1]INSERM, Lyon, FRANCE; [2]SCM IRM Lyon–Villeurbanne, Lyon, FRANCE, [3]Hospices Civils de Lyon, Lyon, FRANCE.

Background: Renal allograft failure is associated with interstitial fibrosis, which is currently assessed by biopsies. This process is prone to sampling errors and to complications. We hypothesize that fibrosis stiffens the renal parenchyma, making it detectable and quantifiable by elasticity imaging. Our previous study showed the feasibility and reproducibility of MRE in healthy volunteers [1]. The present study reports measurements in patients.

Aims: To assess renal allograft elasticity with a Supersonic Aixplorer™ scanner and with Magnetic Resonance Elastography (MRE).

Methods: 18 patients were included in the study. MRE was performed 2.5 months after transplantation. Vibrations were produced by a loudspeaker mounted in a sealed enclosure. Vibration frequency was varied between 40–138 Hz to investigate viscoelastic behavior. All three directions of motion were acquired. The wave images were processed using the curl operator and the Local Frequency Estimator algorithm to estimate shear velocity. Supersonic Aixplorer™ examination was performed 3 months after transplantation. Elasticity images were acquired both in transverse and longitudinal orientations to investigate anisotropy. Young's moduli (E) were converted to group velocity using $c=(E/3\rho)^{1/2}$.

Results: MRE results (Figure 1) showed evidence of viscoelastic behavior. Fitting a Kelvin-Voigt model on this data set yields a dynamic modulus $G^*=\mu+i\eta\omega$ with μ=1 kPa and η=8 Pa.s/rad. Moreover, MRE measurements were fairly consistent among patients, as visible from the error bars (typ. ±0.2 m/s). Group velocities measured by Supersonic Aixplorer™ (Figure 2) were in the same range as MRE results. Comparison of longitudinal and transverse orientations showed no evidence of anisotropy. Comparison of parenchyma, cortex and medulla showed no significant difference. Intra– and inter–patient variability was larger than in MRE, as visible from the error bars (typ. ±0.7 m/s). We hypothesize that part of the variability is attributable to nonlinear elasticity (user–dependent pre–compression of the graft).

Conclusions: The current results show encouraging consistency among patients and between imaging modalities. However, these data only represent a snapshot of the ongoing study. Coherence among subjects was already observed in healthy volunteers [1]. In our patients, no severe dysfunction was observed so far. The same patients will have a follow–up examination 12 months after surgery. We expect that biopsies and elasticity imaging will reveal higher fibrosis at that stage.

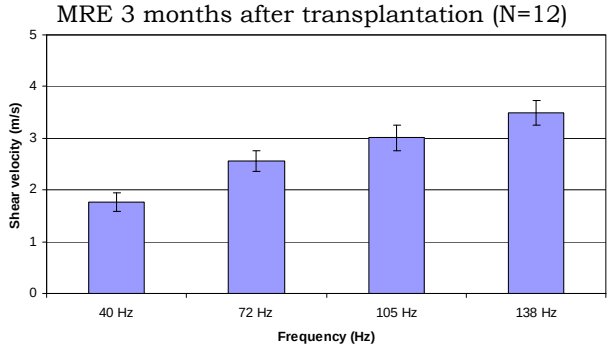

Figure 1: MRE results showing viscoelastic behavior.

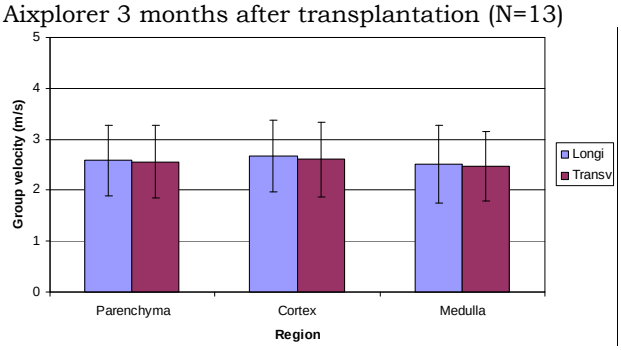

Figure 2: Supersonic Aixplorer™ results, showing group velocities in the same range as MRE.

Acknowledgements: The authors gratefully acknowledge Pr. RL Ehman, Dr. K Glaser and Dr. R Grimm (Mayo Clinic, Rochester, MN, USA) for providing the MRE pulse sequence and the MRELAB wave inversion software, General Electric Healthcare for technical support and Supersonic Imagine for providing the Aixplorer™ scanner. This study is funded by the "Actions Incitatives 2007" grant of Hospices Civils de Lyon.

References:

[1] Rouvière O et al.: Magnetic Resonance Elastography of the Kidneys: Feasibility and Reproducibility in Young Healthy Volunteers. J Magn Reson Imag, 2011 (in press).

012 **A NOVEL NONLINEAR ANALYSIS IN ULTRASOUND ELASTICITY IMAGING OF EDEMA AND FIBROSIS IN CROHN'S DISEASE.**

Jonathan M. Rubin[1], Jingping Xu[2], Sakya Tripathy[2], Ryan W. Stidham[1], Laura A. Johnson[1], Peter D. Higgins[1], Kang Kim[2].*

[1]University of Michigan, Ann Arbor, MI, USA; [2]University of Pittsburgh, Pittsburgh, PA, USA.

Background: Strain developed under quasi–static deformation has been mostly used in ultrasound elasticity imaging (UEI) to determine the stiffness change of tissues. However, the strain measure in UEI is often less sensitive to a subtle change of stiffness. This is particularly true for Crohn's disease where we have applied strain imaging to the differentiation of acutely inflamed bowel from chronically fibrotic bowel.

Aims: Given that the thickening in inflamed bowel is largely due to edema, while the thickening in fibrotic bowel is basically analogous to scar formation, we believed that we could exploit the non–linear mechanical properties of tissue to improve the differentiation between inflamed and fibrotic bowel. In this regard, we developed a new non–linear elastic parameter of the soft tissues and applied it to *in vivo* ultrasound elasticity imaging using an animal model of inflammatory bowel disease.

Methods: A non–linear characteristic of soft tissues over a relatively large dynamic range of strain was investigated. A simplified tissue model based on a finite element (FE) analysis using a commercially available software package (ABAQUS, Dessault Systems, RI, USA) was integrated with a laboratory developed ultrasound radio frequency (RF) signal synthesis program. Two dimensional speckle tracking was applied to this model to simulate the non–linear behavior of the strain developed in a target inclusion over the applied average strain to the surrounding tissues. A non–linear empirical Hill equation was formulated and optimized to best match to the developed strain–to–applied strain relation obtained from the FE simulation. The proposed non–linear equation was applied to *in vivo* measurements and non–linear parameters were further empirically optimized. For an animal model, acute and chronic inflammatory bowel disease was induced in 8 Lewis rats with trinitrobenzene sulfonic acid (TNBS)–ethanol treatments. After UEI using a linear ultrasound probe (L10–5, centered at 6.5 MHz, ZONARE Medical System, Mountain View, CA, USA), histopathology and direct mechanical measurements using a commercially available compression elasticity device (MicroElastometer, Model 0501, ARTANN Laboratories, Inc, West Trenton, NJ, USA) were performed on the excised tissues.

Results: The extracted non–linear parameter from developed strain–to–applied strain relation differentiated the three different tissue types with 1.96±0.12 for normal, 1.50±0.09 for the acutely inflamed and 1.03±0.08 for the chronically fibrotic tissue. T–tests determined that the non–linear parameters between normal, acutely inflamed and fibrotic tissue types were statistically significantly different (normal/fibrotic (P=0.0000185), normal/acutely inflamed (P=0.0013), and fibrotic/acutely inflamed (P=0.0029)). Typical quasi-static linear strain estimates could not distinguish between fibrotic/acutely inflamed bowel walls (P=0.744) in this small population. The simulation results closely correspond to the empirical results.

Conclusions: We present a new non–linear parameter to detect and characterize tissue mechanical property changes, especially subtle differences in stiffness such as those seen in acutely inflamed bowel and fibrotic bowel. The proposed non–linear fitting of the developed strain-to-applied strain relation was tested using a simple FE based non–linear soft tissue model. Using a rat TNBS treated model of inflammatory bowel disease, *in vivo* feasibility was successfully shown with some limitations, differentiating normal, acutely inflamed and chronically fibrotic bowel with no overlap. This method can be applied to other applications of ultrasound elasticity imaging with the proper adjustment of the involved non–linear parameters in the Hill equation depending on the stiffness contrast of the tissues of interest. A relatively easy adaptation to the human subject study is also expected. This technique may provide a sensitive and robust tool to assess subtle stiffness changes in tissues such as in acutely inflamed bowel wall.

Acknowledgements: This project was supported in part by Grant 1R21DK081123–01 from the National Center for Research Resources (NCRR), a component of the National Institutes of Health (NIH) and NIH Roadmap for Medical Research.

* *indicates Presenter*

052 **APPLICATION OF THE MEASUREMENT OF VISCOSITY BY MAGNETIC RESONANCE ELASTOGRAPHY TO THE CHARACTERIZATION OF HEPATIC TUMORS.**

Philippe Garteiser[1], Sabrina Doblas[1], Jean–Luc Daire[1,2], Mathilde Wagner[1], Helena Leitao[3], Valerie Vilgrain[2], Bernard Van Beers[1,2], Ralph Sinkus[1].*

[1]IPMA (Physiologic and Molecular MRI of the Abdomen), INSERM UMR773, Bichat–Beaujon Biomedical Research Center, 100, Bd. Du General Leclerc, 92110 Clichy, FRANCE; [2]Radiology Department, Beaujon Hospital, 100, Bd. Du General Leclerc, 92110 Clichy, FRANCE; [3]Radiology Department, Hospitais de Universidade de Coimbra, 3000–075, Coimbra, Portugal.

Background: Benign and malignant lesions are known to possess different microstructural properties which can affect their overall mechanical properties [1,2]. In the case of liver tumors, magnetic resonance elastography so far has only been assessed as a diagnostic tool for characterization through measurements of the magnitude of the shear modulus. The advantages of separately measuring the viscous and elastic components of shear have not been assessed to date in cohorts of liver cancer patients.

Aims: Evaluate the performance of MRE measurements of viscosity for the characterization of liver tumors.

Methods: MR imaging sessions were conducted at 1.5T. The study included seventy–six consenting patients with either benign (10 hemangiomas, 25 FNH and 7 adenomas) or malignant (14 metastases, 24 HCC and 5 hepatocholangiocarcinomas) histologically confirmed hepatic tumours. For MRR, acoustic waves (50Hz) were produced by a transducer located on the right flank of the patient, and motion–encoding gradients were added to a spin–echo sequence (TR/TE=560/40ms, field of view of 320×320mm^2 for an 80×80 matrix and 7 transverse slices of 4mm) to encode local displacements in phase images. G_d and G_l maps were reconstructed by fitting a polynomial function to the displacement values under physical constraints of local mechanical isotropy and tissue incompressibility. Average G_d and G_l values were obtained from regions of interest (ROIs) positioned over each lesion and compared with respect to tumour malignancy or tumour type.

Results: Malignant tumours were found to be more viscous than benign lesions (G_l=1.06±0.12kPa for benign tumors and 1.93±0.21 kPa for malignant tumors, p<0.001). The area under the receiver operating characteristic curve was 0.71, which was significantly larger than the theoretical value of 0.5. Optimal sensitivity (66%) and specificity (85%) with respect to the discrimination potential between benign and malignant lesions were obtained for a threshold value of 1.44kPa. Analysis of variance revealed significant differences between the viscosity values of HCC and FNH, hemangiomas and adenomas.

Conclusions: The distinction between elastic and viscous components of tissue stiffness enables a more correct characterization of hepatic tumours, as viscosity was an accurate marker of malignancy. The higher viscosity of malignant lesions, such as HCC, could be explained by their disorganized vasculature which may abnormally attenuate acoustic waves.

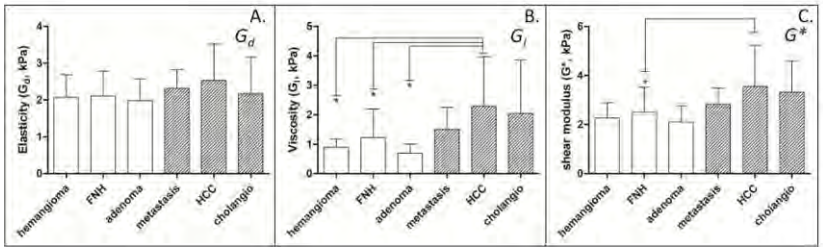

Figure 1: Mechanical parameters (A: elasticity, kPa, B: viscosity, kPa, C: shear modulus, kPa) found for the different tumor types (hemangioma: n=10, FNH: n=25, adenoma: n=7, metastasis: n=18, HCC: n=24, cholangiocarcinoma: n=5), as indicated below the bars. Tumors with a malignant phenotype are symbolized with hashed bars. Statistical significance of ANOVA post–test between individual tumor types to the 0.05 level are indicated with *.

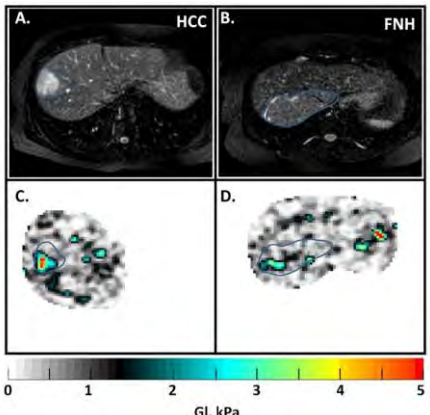

Figure 2: Viscosity maps of selected representative lesions of a malignant (hepatocellular carcinoma, HCC) and a benign lesion (focal nodular hyperplasia). The tumor localization, displayed as a blue outline, is represented on all images. A hyperviscous zone is visible in the central part of the HCC lesion.

References:

[1] Kumar, S. et al.: Cancer Metast. Rev., 28, p. 113, 2009.
[2] Venkatesh, S.K. et al.: AJR, 190, p. 1534, 2008.

* *indicates Presenter*

027 **NONINVASIVE EVALUATION OF HEPATIC FIBROSIS USING ACOUSTIC RADIATION FORCE–BASED SHEAR STIFFNESS IN PATIENTS WITH NONALCOHOLIC FATTY LIVER DISEASE.**

Mark L. Palmeri[1], Michael H. Wang[1], Ned C. Rouze[1], Manal F. Abdelmalek[2], Cynthia D. Guy[2], Barry Moser[2], Anna Mae Diehl[2], Kathryn R. Nightingale[1].*
[1]Duke University, Durham, NC, USA; [2]Duke University Medical Center, Durham, NC, USA.

Background: Nonalcoholic fatty liver disease (NAFLD), the most common form of chronic liver disease in developed countries, may progress to nonalcoholic steatohepatitis (NASH) in a minority of people. Those with NASH are at increased risk for cirrhosis and hepatocellular carcinoma [1]. The potential risk and economic burden of utilizing liver biopsy to stage NAFLD in an overwhelmingly large at–risk population are enormous; thus, the discovery of sensitive, inexpensive and reliable noninvasive diagnostic modalities is essential for population–based screening.

Aims: The purpose of this work was to evaluate the potential of radiation force based shear wave speed quantification to noninvasively assess the presence or absence of advanced fibrosis in patients with obesity–related liver disease.

Methods: Acoustic radiation force–based shear wave imaging [2], a noninvasive method of assessing tissue stiffness, was used to evaluate liver fibrosis in 172 patients diagnosed with NAFLD. Liver shear stiffness measures in three different imaging locations were reconstructed and compared to the histologic features of NAFLD and AST–to–platelet ratio indices (APRI).

Results: Reconstructed shear stiffnesses were not associated with ballooned hepatocytes (p=0.11), inflammation (p=0.69), nor imaging location (p=0.11). Using a predictive shear stiffness threshold of 4.24kPa, shear stiffness distinguished low (fibrosis stage 0–2) from high (fibrosis stage 3–4) fibrosis stages with a sensitivity of 90% and a specificity of 90% (AUC of 0.90) (Figure 1). Shear stiffness had a mild correlation with APRI (R^2=0.22). BMI>40kg/m^2 was not a limiting factor for ARFI imaging, and no correlation was noted between BMI and shear stiffness (R^2=0.05) [1].

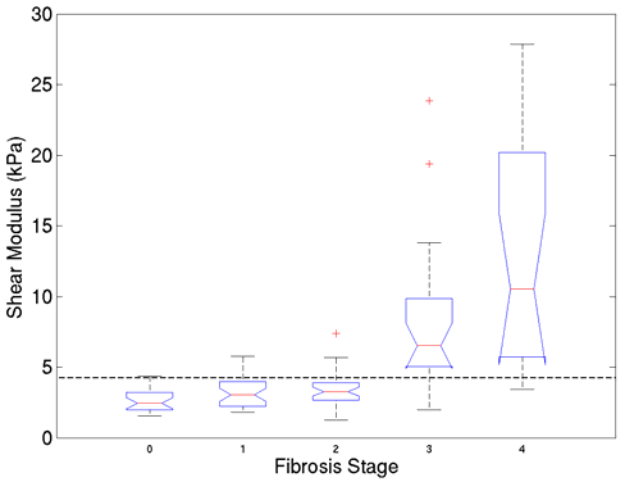

Figure 1: Reconstructed shear moduli in 135 patients being evaluated for NAFLD as a function of their biopsy–proven fibrosis stage. The boxes represent the interquartile range (IQR), while the whiskers represent 1.5 times the respective IQR level over the mean stiffnesses for each study subject (the mean of three replicate measures in the three imaging locations with an IQR/mean <0.3). The horizontal dashed line represents the threshold (4.24kPa) to distinguish fibrosis stages F0–2 from F3–4.

Conclusions: ARFI imaging is a promising imaging modality for assessing the presence or absence of advanced fibrosis in patients with obesity–related liver disease.

Acknowledgements: This work is supported by NIH Grants R01 EB002132 and K23-DK062116. The authors would like to thank Siemens Medical Solutions, USA for their technical support, and Veronica Rotemberg, Miriam Chitty, Samantha Kwan, Melissa Smith, Pamela Anderson and Nicole Rothfusz for their assistance in the hepatology clinic and with data collection.

References:

[1] Angulo P.: Nonalcoholic Fatty Liver Disease. N Engl J Med, 346, pp. 1221–1231, 2002.
[2] Palmeri et al.: Quantifying Hepatic Shear Modulus *In Vivo* Using Acoustic Radiation Force. Ultrasound Med Biol, 34, pp. 546–558, 2008.
[3] Palmeri, et al.: Noninvasive Evaluation of Hepatic Fibrosis using Acoustic Radiation Force–Based Shear Stiffness in Patients with Nonalcoholic Fatty Liver Disease. Journal of Hepatology, in press.

* *indicates Presenter*

077 **DIFFERENTIAL TISSUE STRAIN ESTIMATION ACROSS STRATA LUMBAR TISSUES UNDER INTRINSIC MOTION.**

J Triano[1], HM Langevin[2], EE Konofagou[3].*
[1]Canadian Memorial Chiropractic College, Toronto, Ontario, CANADA; [2]University of Vermont, Burlington, VT, USA; [3]Columbia University, New York, NY, USA.

Background: Muscle organs are critical actuators generating tension that may 1) initiate movement, 2) alter multi–joint segment rigidity or 3) attenuate external loads on the body. Pathways of force transmission include myotendinous and epimuscular myofascial networks [1]. Intramuscular transmission may be non–uniform, with motor units and connective tissue components contributing to tension gradients in different proportion when active or stretched. The question is: how significant these mechanical linkages are to health and disease [1]. Such information is necessary to measure and confirm the relative role of the different tissue strata in transmitting loads during injury, in manual therapy and exercise.

Aims: This study attempted to quantify the relative activity within and between soft tissue structures of the upper arm during intrinsic motions.

Methods: Ten healthy adult male subjects (age=26.7±1.8 years; Ht=178.6±5.4cm; Wt=76.8±8.9kg) were recruited. After informed consent, each was placed supine in the anatomical position. Each participant engaged in 5 tasks bending the elbow to approximately 20° while an ultrasound sensor was positioned over the midline biceps: unloaded, 20% maximum voluntary contraction (MVC) concentric no pressure, 20% MVC concentric 1cm indented, 20% MVC eccentric and 20% MVC concentric with the ultrasound moved distally to the myotendinous confluence. Ultrasound radiofrequency signals [2–5] (40MHz, 3cm depth, 70 fps) were post–processed using speckle tracking with displacement and strain estimation by cross–correlation techniques. The muscle mass was stratified into three bands: 1) skin and subcutaneous, 2) biceps, 3) brachialis. Maximal and cumulative displacement, lateral shear and lateral strain variables, normalized to the duration of movement expressed in fps, were compared across tasks and stratified bands by ANOVA.

Results: Differences between strata layers were highly significant across all tests ($0.0001<p<0.045$). Unloaded elbow flexion displacement (microns), normalized by frame rate (see Table), differed from all other test conditions ($p<0.057$) with an interaction effect between condition and strata ($p<0.0013$). Cumulative displacement of the strata was ordered from superficial to deep ($p<0.003$). Cumulative lateral strain was lowest in the biceps strata ($p<0.034$). Lateral shear values were similarly ordered.

	Unloaded Concentric	Loaded No Indent, Conc	Loaded, Indented Concentric	Loaded Eccentric	Loaded Distal Concentric
Skin	56.4 (71.7)	96.8 (55.1)	106.3 (68.5)	57.1 (110.4)	89.1 (73.3)
Biceps	81.3 (108.0)	72.2 (46.4)	87.3 (73.7)	48.5 (44.4)	84.1 (90.4)
Brachialis	370.8 (208.4)	520.9 (284.1)	402.3 (233.5)	292.9 (94.6)	408.1 (211.9)

Conclusions: This work sought characteristic differences in displacement and strain of layered tissue undergoing simple load conditions and test environments. The motor controlled action of the prime mover (biceps) showed the least variation in strain across all tasks. This would be consistent with the constant displacement under isoinertial load conditions. The subcutaneous tissue and brachialis muscle substance deform in response to lesser activation and, at least for subcutaneous strata, epimuscular force transmission. These differences represent local changes in tissue stiffness associated with select activation of the prime mover. Future work will correlate motions and strains to myoelectric measures.

Layer stratification for both internal tissue displacements and strains during activity can be quantified. Results suggest opportunities to test the way treatment and exercise loads applied to patients are distributed through the tissues. While the total force applied is known to dissipate, it may be that the force distribution itself is an important factor in driving clinically relevant change from treatment efforts. Only direct measurement will determine which tissues are affected.

Ultrasound elastography is capable of making these measures under controlled conditions.

References:

[1] Maas H, Sandercock T.G.: J Biomed Biotech. Article ID 575672, pp. 1–9, 2010.
[2] Luo J, Konofagou EE: Ultrasound Med Biol., 35(8), pp. 1352–66, 2009. Epub Jun 13, 2009.
[3] Luo J, Konofagou E: IEEE Trans Ultrason Ferroelectr Freq Control., 57(6), pp. 1347–57, 2010.
[4] Langevin HM, Konofagou EE, Badger GJ, Churchill DL, Fox JR, Ophir J, Garra BS: Ultrasound Med Biol., 30(9), pp. 1173–83, 2004.
[5] Varghese T, Konofagou EE, Ophir J, Alam SK, Bilgen M: Ultrasound Med Biol., 26(9), pp. 1525–37, 2000.

Invited Presentation:

096 **REVIEW ON STRAIN BASED CARDIOVASCULAR FUNCTIONAL IMAGING.**

Chris L. de Korte[1].*
[1]Clinical Physics Laboratory, Radboud University Nijmegen Medical Center, THE NETHERLANDS.

Background: Measurement of tissue deformation can be used to quantify the mechanical properties of tissue (elastography) [1] or assess functional information of structures (strain imaging) [2]. In the latter application, the strain is not directly representative for the mechanical properties but provides a direct measure of the contractility (muscles, myocard) or vulnerability (atherosclerotic plaque). The contractility of the heart muscle is of great diagnostic value since it directly reflects its function. Especially since strain can be quantified locally at high resolution, the severity and location of the disease can be determined as opposed to global functional parameters like cardiac output or shortening fraction. In arteries, the presence of vulnerable plaques may lead to acute events like stroke and myocardial infarction. Consequently, timely detection of these plaques is of great diagnostic value.

Cardiac Strain Imaging: The strain can be quantified using different methods. For myocardial strain estimation, initially Doppler based techniques were used. With Tissue Doppler Imaging (TDI), the strain and strain–rate could be quantified along the ultrasound beam. The disadvantage of this technique was the angle dependency and the relatively high frame rate required [2]. In the last decade, speckle tracking methods became commercially available. These methods are not angle dependent since strain can be quantified in two (conventional B–mode) or three (using 3D volume scanning) orthogonal directions. The advantage is that the technique can be applied to conventional B–mode images [3], although with the cost of reduced sensitivity with respect to Doppler based techniques. In research settings, RF–based techniques were developed. The latter techniques might be optimal since they combine high sensitivity with quantification of the multi–dimensional strain vector [4]. However, clinical studies that are currently performed have yet to demonstrate this.

Vascular Strain Imaging: Initially, vascular strain imaging was performed using intravascular catheters. The high resolution and co–alignment of the ultrasound beams and the radial strain resulted in high resolution strain images. Validation studies *in vitro* and *in vivo* revealed high sensitivity and specificity for identification of plaque components and vulnerability [5]. In the last decade, the technique has been translated into a non–invasive modality by different groups. Recently, vascular strain compounding of multiple beam steered angles was introduced [6]. *In vitro* and *in vivo* validations demonstrated the potential to perform functional vascular imaging and these techniques are currently being used in patient clinical evaluation.

Conclusions: Strain imaging will become one of the key ultrasound techniques for cardiovascular functional imaging. However, for cardiac strain imaging, the lack of sensitivity of speckle tracking methods requires more sensitive techniques like RF–based strain estimation methods. For vascular functional imaging, compounding of different beam steered angles will improve the strain images. In the next ten years, cardiovascular strain imaging will move to full 3D and combined with 3D flow imaging to further enhance the diagnostic capabilities of this technology.

Acknowledgements: This work is supported by the Dutch Technology Foundation, Philips Medical Systems, Andover MA, USA and Medison, Seoul, Korea.

References:

[1] J. Ophir, E.I. Céspedes, H. Ponnekanti, Y. Yazdi, and X. Li: Elastography: A Method for Imaging the Elasticity in Biological Tissues. Ultrason. Imaging, Vol. 13, pp. 111–134, 1991.
[2] J. D'hooge et al.: Echocardiographic Strain and Strain–Rate Imaging: A New Tool to Study Regional Myocardial Function. IEEE Trans Med Imaging, Vol. 21, No. 9, pp. 1022–30, 2002.
[3] M. Leitman et al.: Two–Dimensional Strain – A Novel Software for Real–Time Quantitative Echocardiographic Assessment of Myocardial Function. J. Am. Soc. Echocardiogr., Vol. 17, No. 10, pp. 1021–1029, Oct. 2004.
[4] R.G. Lopata, M.M. Nillesen, J.M. Thijssen, L. Kapusta, and C.L. de Korte: Three–Dimensional Cardiac Strain Imaging in Healthy Children using RF–Data. Ultrasound Med. Biol., Vol. 37, No. 9, pp. 1399–1408, Sept. 2011.
[5] C.L. de Korte, G. Pasterkamp, A.F.W. van der Steen, H.A. Woutman, and N. Bom: Characterization of Plaque Components using Intravascular Ultrasound Elastography in Human Femoral and Coronary Arteries *In Vitro*. Circulation, Vol. 102, No. 6, pp. 617–623, 2000.
[6] H.H.G. Hansen, R.G.P. Lopata, T. Idzenga, and C.L. de Korte: Full 2D Displacement Vector and Strain Tensor Estimation for Superficial Tissue using Beam Steered Ultrasound Imaging. Physics in Med. and Bio., Vol. 5, No. 11, pp. 3201–3218, 2010.

007 **NON–INVASIVE MECHANICAL CHARACTERIZATION OF CAROTID ATHEROSCLEROTIC PLAQUES WITH ULTRASOUND ELASTOGRAPHY AND CORRELATION WITH HIGH RESOLUTION MAGNETIC RESONANCE IMAGING: A CLINICAL REPORT.**

Cyrille Naim[1], Guy Cloutier[1,2], Elizabeth Mercure[1], François Destrempes[1], Marie–France Giroux[2,3], Gilles Soulez[2,3].*

[1]Laboratory of Biorheology and Medical Ultrasonics, University of Montréal Hospital Research Center (CRCHUM), Montréal, Québec, CANADA; [2]Radiology Department, Radio–Oncology and Nuclear Medicine, University of Montréal, Montréal, Québec, CANADA; [3]Radiology Department, University of Montréal Hospital (CHUM), Montréal, Québec, CANADA.

Background: Non–invasive vascular elastography (NIVE) is a new ultrasonic technique that maps carotid plaque strain (elasticity) characteristics to detect its vulnerability. Clinical validations of this imaging method are scarce, based on limited sample sizes, but more importantly no correlation has been proven between the elasticity of the plaque and its biological tissue content.

Aims: We demonstrate in this study the potential of NIVE for the diagnosis of human vulnerable carotid plaques by comparing plaque strains with plaque component measurements obtained by magnetic resonance imaging (MRI).

Methods: Thirty–one subjects with carotid stenosis of more than 50% in diameter reduction were recruited for ultrasound elastography (Sonix RP, Ultrasonix, Vancouver, Canada) and high resolution MRI (Avanto, Siemens, Erlangen, Germany) examinations of their internal carotid arteries. Time–varying axial strain images of pre–segmented plaques [1] were generated from ultrasonic radio–frequency (RF) sequences. Plaque elastograms were computed by applying the Lagrangian Speckle Model Estimator [2] for the near and far vessel walls, depending on the localization of the plaque. MR images of the corresponding carotid plaques were segmented, and plaque components were characterized and quantified using the QPlaque MR software (Medis, Netherlands).

Results: The subjects' mean age and percent stenosis at participation were 69.3 years and 72.7%. Nine subjects were symptomatic. Of the 31 subjects' plaques, 17 contained a lipid–rich necrotic core, 24 contained calcium, 19 showed post–gadolinium enhancements indicative of inflammation, and 7 plaques were deemed definitely vulnerable based on established vulnerability criteria. Mean strain at peak systolic plaque compression was not statistically different between symptomatic and asymptomatic patients (MR criteria of plaque vulnerability did not discriminate either both groups). However, a nonlinear quadratic relationship between mean strain at peak systolic compression and lipid content (joint p–value=0.039) was observed. A linear relationship between mean strain at peak systolic compression and calcium content was found and showed a trend towards significance (p=0.070).

Conclusions: This preliminary validation, still on a limited number of participants, suggests that NIVE is clinically feasible. Strain measurements correlate with the presence of a lipid core; however, this technique requires further development to discriminate vulnerable carotid plaques. NIVE determines time–varying atherosclerotic plaque strains; further optimization, likely including shear strain mapping, may warrant discriminating carotid plaque components and vulnerability.

Acknowledgements: This research was supported by a proof–of–principle research grant of the Canadian Institutes of Health Research (PPP–78763) and is now partially supported by a strategic grant of the Natural Sciences and Engineering Research Council of Canada (STPGP–381136–09).

References:

[1] Destrempes F., Meunier J., Giroux M.F., Soulez G., Cloutier G.: Segmentation of Plaques in Sequences of Ultrasonic B–Mode Images of Carotid Arteries Based on Motion Estimation and a Bayesian Model. IEEE Trans. Biomed. Eng., 58 (8): 2202-2211, 2011.

[2] Schmitt C., Soulez G., Maurice R.L., Giroux M.F., Cloutier G.: Non–Invasive Vascular Elastography: Toward a Complementary Characterization Tool of Atherosclerosis in Carotid Arteries. Ultrasound Med. Biol., 33 (12), pp. 1841–1858, 2007.

008 **REDUCING ARTIFACTS IN NON–INVASIVE VASCULAR ELASTOGRAPHY OF CAROTID ARTERIES.**

Elizabeth Mercure[1], François Destrempes[1], Younes Majdouline[1], Jacques Ohayon[2,3], Gilles Soulez[4,5], Guy Cloutier[1,5].*

[1]Laboratory of Biorheology and Medical Ultrasonics, University of Montréal Hospital Research Center (CRCHUM), Montréal, Québec, CANADA; [2]UJF–Grenoble 1, CNRS, Laboratory TIMC–IMAG UMR 5525, DyCTiM Research Team, Grenoble, F–38041, FRANCE; [3]University of Savoie, Polytech Savoie, Le Bourget du Lac, FRANCE; [4]Radiology Department, University of Montréal Hospital (CHUM), Montréal, Québec, CANADA; [5]Radiology Department, Radio–Oncology and Nuclear Medicine, and Institute of Biomedical Engineering, Montréal, Québec, CANADA.

Background: Characterization of vascular plaque components brings out information about its vulnerability to rupture. Non–invasive vascular elastography (NIVE) was developed for the assessment of mechanical properties of superficial arteries. However, NIVE motion estimates are affected by many artifacts, such as the underestimation of deformations due to projected movement angles with respect to the ultrasound beam, movements of the operator or of the patient during image acquisition.

Aims: The main objective of this work was to propose a compensation method for the strain parameters when tissue motion and the beam axis are not aligned and to introduce a filtering process on the time–varying strain curve to reduce motion artifacts as much as possible. We also wanted to evaluate the difference in the strain behavior of proximal and distal walls in longitudinal images (see Figure 1).

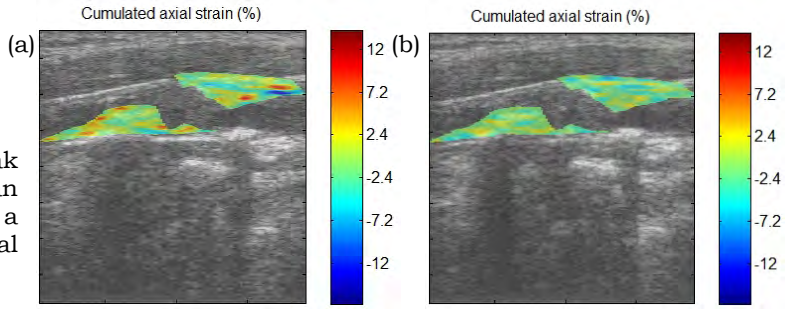

Figure 1: Cumulated axial elastogram, at peak systole (a) and at end diastole (b), of an internal carotid artery that exhibits a plaque on both proximal (near) and distal (far) walls of the vessel.

Methods: The NIVE technique is based on the Lagrangian speckle model estimator (LSME) [1] that computes the four components of the 2D deformation matrix. Compared to a previous implementation [2], we used three out of those four components for the angle compensation procedure of strain estimates. Also, the strain curve was band pass filtered to improve its systolic/diastolic profile and strain rate values were extracted from this smoothed curve. The database was composed of longitudinal images of internal carotid arteries of subjects without (30 sequences) and with (21 sequences) atherosclerosis.

Results: For the healthy group, statistically significant differences between proximal and distal walls were observed for axial strain measurements ($p \leq 0.02$). However, none of these differences were significant for the pathological group ($p \geq 0.44$). Without angle compensation and filtering, none of the strain parameters were able to dissociate healthy and pathological subjects. With the proposed pre–processing approaches, we found a significant difference between the two groups for the maximum ($p=0.001$) and minimum ($p=8\times10^{-4}$) strain rates calculated on the distal wall of internal carotid arteries.

Conclusions: The presence of artifacts in NIVE is almost unavoidable because the technique is not real–time; image acquisition is done blinded and processing is realized offline. An angle compensation method to locally assess the magnitude of motion within the vascular wall and a filtering process were proposed to remove some of these artifacts. The proposed techniques allowed differentiating healthy and pathological carotid arteries based on the strain rate and may help to diagnose vulnerable plaques.

Acknowledgements: This research was supported by a strategic grant of the Natural Sciences and Engineering Research Council of Canada (STPGP–381136–09).

References:

[1] Schmitt C., Soulez G., Maurice R.L., Giroux M.F., Cloutier G.: Non–Invasive Vascular Elastography: Toward a Complementary Characterization Tool of Atherosclerosis in Carotid Arteries. UMB, 33 (12), pp. 1841–1858, 2007.

[2] Mercure E., Deprez J.F., Fromageau J., Basset O., Soulez G., Cloutier G., Maurice R.L.: A Compensative Model for the Angle-Dependence of Motion Estimates in Noninvasive Vascular Elastography. Med. Phys., 38 (2), pp. 727–735, 2011.

* *indicates Presenter*

005 **PERFORMANCE OF NEW MECHANICAL CRITERIA USED TO EXTRACT *IN VIVO* VALID MODULOGRAMS FROM A CARDIAC CYCLE CORONARY IVUS STRAIN SEQUENCE.**

G. Cloutier[1], S. Le Floc'h[2], Y. Saijo[3], G. Finet[4], P. Tracqui[2], R.I. Pettigrew[5], J. Ohayon[2,6].*
[1]Laboratory of Biorheology and Medical Ultrasonics, University of Montréal Hospital Research Center (CRCHUM), Montréal, Québec, CANADA; [2]UJF–Grenoble 1, CNRS, Laboratory TIMC–IMAG UMR 5525, DyCTiM Research Team, Grenoble, F–38041, FRANCE; [3]Biomedical Engineering Department, Tohoku University, Sendai, JAPAN; [4]Hemodynamics and Interventional Cardiology Department, INSERM Unit 886, Lyon, FRANCE; [5]NIDDK, NIH, Bethesda, MD, USA. [6]University of Savoie, Polytech Savoie, Le Bourget du Lac, FRANCE.

Background: Vulnerable atherosclerotic plaque (VP) rupture is a recognized major cause of acute coronary syndrome [1]. Clinical and biomechanical studies have identified plaque composition and morphology as key predictors of vulnerability and likelihood of rupture [2]. Indeed, such knowledge can allow a precise quantification of the thin–cap fibro–atheroma (TCFA) peak cap stress (PCS), which is a good biomechanical predictor of VP rupture [3,4]. Several robust methods were proposed to compute modulograms of a plaque [5,6], i.e., an elasticity map, based on the estimation of the strain field inside the coronary atheroma plaque [7]. However, a major limitation of advancing intravascular (IVUS) modulography to cardiac *in vivo* applications is the motion of the heart and the acquisition of data in a pulsating artery.

Aims: In this work, we proposed and tested an original approach to extract valid modulograms from *a priori* elastograms, by excluding all modulograms affected by strain measurement artifacts.

Methods: Our numerical approach is based on the modulogram's reproducibility through the cardiac cycle and on the spatial distributions of the correlation coefficient between consecutive radio–frequency (RF) IVUS frames and the strain difference between measured and simulated strains. A finite element model and a segmentation–driven optimization procedure were used to estimate the plaque modulograms together with the criteria which were used to exclude the biased modulograms of our study. This algorithm was tested on IVUS sequences obtained in 12 patients referred for an atherectomy coronary intervention. The computed modulograms were compared to both the biological composition given by the histology analysis of the atherectomized plaque and to the quantitative echogenicity analysis of B–mode IVUS images.

Results: One patient was excluded from our study based on the weak RF correlation coefficients found over the sequence of one cardiac cycle. For all other patients, when the plaque histology showed lipid content, we found a large soft inclusion (i.e., a Young's modulus <10kPa in a region covering >10% of the plaque area). Moreover, the echogenicity of B–mode images was significantly lower in the region of the plaque with a low Young's modulus for 10/11 plaques compared to the surrounding tissue. However, no correlation was found between the presence of calcium and the presence of hard tissue (i.e., with a modulus >1000kPa).

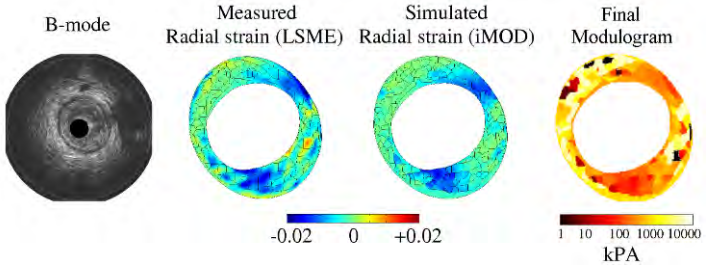

Figure 1: Modulogram of a human coronary plaque extracted from the IVUS investigation of Patient # 2. Column 1: IVUS B–mode image. Columns 2 and 3: measured and simulated radial strain (or elastogram). Column 4: Intraplaque Young's modulus distribution (or modulogram).

Conclusions: The proposed imaging method [8] and the new criteria proposed in this study to extract valid modulograms within a cardiac cycle, appears promising for the *in vivo* prediction of VP rupture.

References:

[1] Fuster, V., et al.: J Am Coll Cardiol, 46(6), pp. 937–54, 2005.
[2] Loree, H.M., et al.: Circ Res, 71(4), pp. 850–8, 1992.
[3] Finet, G. et al.: Coron Artery Dis, 15(1), pp. 13–20, 2004.
[4] Ohayon, J., et al.: Am J Physiol Heart Circ Physiol, 295(2), pp. H717–27, 2008.
[5] Baldewsing, R.A., et al.: IEEE Trans Med Imaging, 24(4), pp. 514–28, 2005.
[6] Le Floc'h, S., et al.: IEEE Trans Med Imaging, 28(7), pp. 1126–37, 2009.
[7] Maurice R.L. et al.: IEEE Trans Inf Tech Biomed, 12(3), pp. 290–298, 2008.
[8] Le Floc'h, S., et al.: Phys Med Biol, 55(19), pp. 5701–5721, 2010.

059 **SIMULATED PULSE WAVE IMAGING FOR LOCAL STIFFNESS ESTIMATION IN PATIENT–SPECIFIC AORTAS WITH PHANTOM VALIDATION**

Danial Shahmirzadi[1], Ronny X. Li[1], Jianwen Luo[1], Elisa E. Konofagou[1].*
[1]Columbia University, VC 12-232, 622 West 168th Street, New York, NY, 10032, USA

Background: The aortic stiffness has widely been reported as an independent indicator of all–cause mortality and cardiovascular diseases. Traditional methods for measuring arterial stiffness *in vivo* involve either invasive procedures or provide a global average estimate. An attractive alternative for noninvasive estimation of local arterial stiffness is based on pulse wave imaging (PWI), a method developed by our group [1–3] for regional pulse wave visualization and regional pulse wave velocity (PWV) measurement.

Aims: Examining the *in silico* performance assessment of PWI in the estimation of aortic stiffness.

Methods: A patient–specific geometry of a normal aorta was considered to construct both the simulation models and silicone aortic phantoms. The coupled Eulerian–Lagrangian (CEL) dynamic/explicit solver (Abaqus 6.10–1) was used to implement the finite–element simulation of the arterial wall deflection under fluid pulsation. The elastic material properties of the wall were selected based on the mechanical testing measurements of the Young's modulus and the Poisson's ratio using Instron and Digital Image Correlation (DIC) systems. Water material properties were used to model the non–viscous fluid flow. The wall velocity was plotted vs. time on spatiotemporal maps and the slope of the linear fit was equal to PWV. For verification purposes, a customized laboratory set up was used to perform PWI on a similar silicone phantom. An open–architecture ultrasound scanner (Sonix Touch, Ultrasonix, Canada) with a linear array transducer having a center frequency of 10 MHz was used to image the phantom wall with 16 beams at 950 fps. A 1D cross–correlation method was applied to estimate the wall displacement and the PWV. The Moens–Korteweg (MK) equation was finally used for modulus estimation.

Results: Figure 1 illustrates the simulation results of the radial wall displacement over time for three different values for the wall modulus and fluid initial velocity. When compared to the wave peak, it was found that the wave foot (defined here as the 50% of the peak) is a more robust measure for wave characterization and yields a higher linear correlation for PWV, particularly in cases such as in Figure 1.3.c. Regardless of the variation in the wall deflection magnitude due to the change in the fluid velocity or the stiffness (Figures 1.1.a–1.3.a), the PWV is found to be relatively independent of the fluid velocity magnitude (PWV of 12.96 m/s (Figure 1.1.c) vs. 14.86 m/s (Figure 1.3.c)). However, as suggested by the MK equation, the PWV is strongly dependent on the Young's modulus (e.g., from Figure 1.1.c – 1.2.c). The relationship between the PWV and the wall modulus is summarized in Table 1 for three different input Young's moduli. The simulation results were found to be consistent with experimental findings from the silicone phantoms.

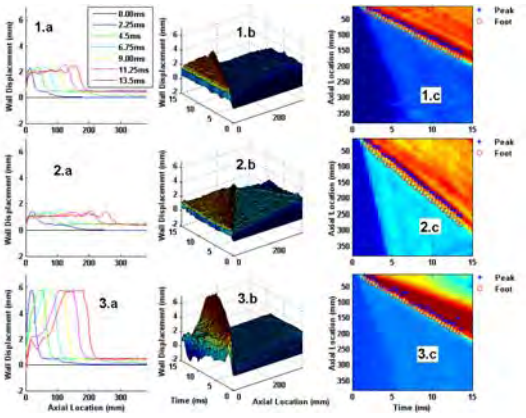

Figure 1:
(1)E=2.56 MPa, V_o=5m/s;
(2)E=7.68MPa, V_o=5m/s;
(3)E=2.56MPa, V_o=15m/s;
(a)Wall deflection profiles at different time points;
(b)3D illustration of pulse wave propagation;
(c)Spatiotemporal plot of pulse wave

Input E (MPa)	Theoretical M-K PWV (m/s)	Simulation PWV (m/s)		Silicone Phantom PWV (m/s)		Estimated E (MPa)	
		Wave Peak	Wave Foot	Wave Peak	Wave Foot	Simulation	Silicone Phantom
2.56	17.04	12.22 (r^2=0.996) error=-28.28%	12.97 (r^2=0.998) error=-23.88%	17.55 (r^2=0.856) error=2.99%	17.22 (r^2=0.971) error=1.06%	1.48	2.65
5.12	24.10	17.16 (r^2=0.997) error=-28.80%	17.15 (r^2=0.999) error=-28.84%	N/A	N/A	2.60	N/A
7.68	29.52	20.49 (r^2=0.998) error=-30.59%	20.67 (r^2=0.999) error=-29.98%	N/A	N/A	3.76	N/A

Table 1: PWV and stiffness estimates obtained from simulations and silicone phantom experiments.

Conclusions: Regional noninvasive measurements of the pulse wave velocity can play an important role in identifying the changes in arterial properties and enhancing the prognosis tools in the clinical practice. In this study, PWI in simulated and silicone aortic phantoms was shown to yield encouraging results on PWV and stiffness estimations, regionally and noninvasively. In this study, PWI in simulated and silicone aortic phantoms was shown to yield encouraging results on PWV and stiffness estimations, regionally and noninvasively.

References:

[1] Fujikura K, Luo J, Gamarnik V, Pernot M, Fukumoto R, Tilson MD, Konofagou EE: Ult Imag, 29(3), pp. 137–54, 2007.
[2] Luo J, Lee W-N, Wang S, Konofagou EE: Proc IEEE Ultrasonics Symp, pp. 859–62, 2008.
[3] Vappou J, Luo J, Konofagou EE: Am J Hypertension, 23(4), pp. 393–398, 2010.

* *indicates Presenter*

088 **MINIMALLY CONSTRAINED RECONSTRUCTIONS IN INTRAVASCULAR ULTRASOUND ELASTOGRAPHY: INITIAL CLINICAL INVESTIGATION.**

Michael S. Richards[1], Marvin M. Doyley[1].*
[1]Electrical and Computer Engineering Department, University of Rochester, Rochester, NY, USA.

Background: The study of arterial plaque mechanics, specifically the stresses within a plaque wall, is essential to the detection and monitoring of vulnerable plaque. Intravascular ultrasound (IVUS) elastography (IVUSe) is a method being developed for studying plaque mechanics, specifically strain levels during a cardiac cycle [1]. In addition to strains, a necessary step in calculating stress within a plaque is the material property recovery.

Aims: Our work aims to develop and characterize a minimally constrained, inverse reconstruction algorithm to quantify the shear modulus (μ) contrast of arterial tissue imaged with IVUS. Our algorithm uses a regularized solution, rather than geometric lumping or hard prior constraint to improve the ill–posedness of the inverse problem. Our method allows for the inclusion of geometric segmentation information, as a penalty or soft prior, to improve the contrast recovery where such information is known.

Methods: An initial clinical evaluation of our IVUSe method was tested on previously collected data taken from the abdominal aorta of an atherosclerotic rabbit model [2]. We obtained radial displacement estimates for various applied pressures at diastole that were used as input to the modulus reconstruction algorithm. This inversion scheme finds the shear modulus distribution that minimizes the error between the predicted and measured displacements. Results were repeated using segmentation information, found by manually segmenting the US B–mode image, and our soft prior algorithm (red dotted line, Figure 1a).

Results: Strain elastograms show a high strain region indicating a soft thrombus (Figure 1b). Reconstruction results show a similar region with a contrast recovery of approximately 0.6 (Figure 1c). Use of segmentation information improves the contrast recovery within the plaque region to 0.3 (Figure 1d). The shear modulus has been normalized such that the mean of the vessel region is unity.

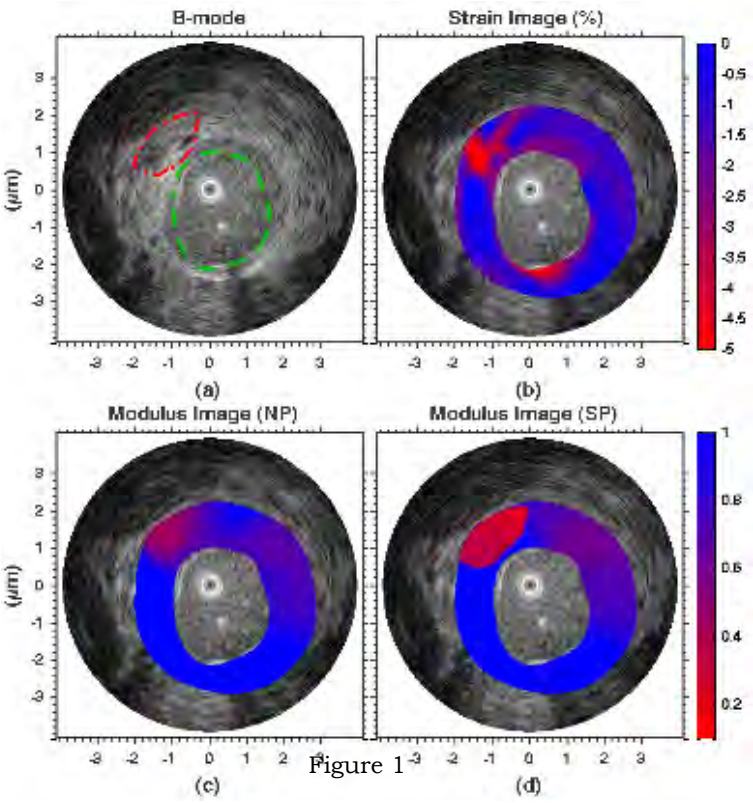

Figure 1

Conclusions: The feasibility of a minimally constrained reconstruction algorithm is shown using our regularized methods and soft prior methods. Results suggest that, if accurate, contrast recovery can be significantly improved with the inclusion, segmentation information specific to material regions.

Acknowledgements: This work is funded by the National Heart and Lungs Research grant R01 HL088523.

References:

[1] C.L. de Korte, and A.F. van der Steen: Intravascular Ultrasound Elastography: An Overview. Ultrasonics, Vol. 40, No. 1–8, pp. 859–65, May, 2002.
[2] R.L. Maurice, J. Fromageau, M.R. Cardinal M.M. Doyley, E. de Muinck, J. Robb, and G. Cloutier: Characterization of Atherosclerotic Plaques and Mural Thrombi with Intravascular Ultrasound Elastography: A Potential Method Evaluated in an Aortic Rabbit Model and Human Coronary Artery. IEEE Trans. on Inf. Tech. in Biomed., Vol. 12, No. 3, pp. 290–298, May 2008.

* *indicates Presenter*

072 **NUMERICAL EVALUATION OF ARTERIAL PRESSURE EQUALIZATION TECHNIQUES FOR ENHANCED VASCULAR STRAIN IMAGING.**

D. Dutta[1,2], P. Gottschalk[4], J. Hamilton[4], K. Kim[1,2,3].*
[1]The Center for Ultrasound Molecular Imaging and Therapeutics, [2]Cardiovascular Institute, [3]Bioengineering Department, University of Pittsburgh, Pittsburgh, PA, USA; [4]Epsilon Imaging, Inc, Ann Arbor, MI, USA.

Background: A significant challenge in vascular strain imaging is that the arterial deformations under physiologic conditions only result in small strain changes in the arterial wall. It was previously demonstrated [1] that large strain changes can be induced non–invasively by equalizing the internal arterial baseline pressure (~80mmHg in a healthy human). The equalization procedure involves the application of an external pressure equal to the internal baseline pressure, and the resultant strain changes can be subject to the boundary conditions.

Aims: To estimate true strains under the pressure equalization procedure and establish a nonlinear vascular strain analysis model under different boundary conditions.

Methods: A 9mm dia. (inner) and 0.75mm thick artery was modeled as a hyperelastic Rivlin solid with C11=50kPa, C10=10kPa, C01=7.5kPa, K (bulk modulus)=16.7MPa, ρ (density)=1050kg/m^3. Radial strains at different blood pressure levels were computed under quasi–static and axisymmetric assumptions (for both pressure equalized and non–equalized cases) using commercial finite element (FE) software, COMSOL. A non–axisymmetric plane–strain model, where the equalization pressure is applied via an ultrasound (US) probe, was also solved. This latter model includes the effects of bone and muscle.

Results: The nonlinear variation of radial compressive strain with luminal pressure is evident from Figure 1. Under physiologic conditions (80<P<120) the artery is already distended (stiff), and the strain change is only 2%. A pre–load free (not distended and softer) artery would have resulted in higher strain change (12%) for the same change in luminal pressure of 40mmHg (0<P<40). The fundamental idea of pressure equalization is to bring the distended artery back to the not distended condition by applying external compression which nullifies the inflating effect of the internal arterial baseline pressure. A uniform axisymmetric equalization pressure of 80mmHg successfully increases the strain range from 2% to 10% (Figure 2), although the absolute strain condition in such a case is different than that of a free, undistended artery (Figure 3). In practice, uniform axisymmetric compression is very difficult to implement and uniaxial compression using an US probe might be the most viable option (Figure 4). The deviation from uniform axisymmetric compression needs to be considered in practice (Figure 5).

Conclusions: Numerical solutions for a hyperelastic artery confirm that pressure equalization leads to a larger strain range than under normal physiologic conditions. US elasticity imaging techniques that distinguish normal and diseased arteries through strain measurement can be optimized using this nonlinear vascular model. US speckle tracking results also compare well with the numerical solutions.

Acknowledgements: The project was partly funded by NIH–5R44EB007842.

References: [1] K. Kim et al.: UMB, 30(6), pp. 761–771, 2004.

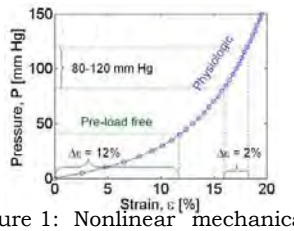

Figure 1: Nonlinear mechanical response of arterial wall subjected to luminal (blood) pressure.

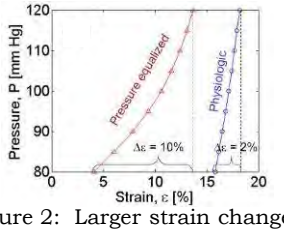

Figure 2: Larger strain change in a pressure equalized artery for the same change in pressure.

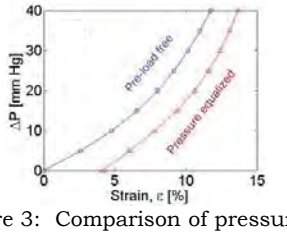

Figure 3: Comparison of pressure equalized vs. pre–load free artery.

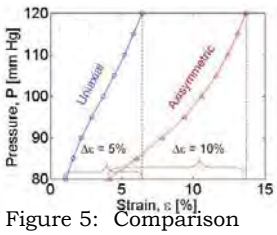

Figure 5: Comparison of uniaxial vs. axisymmetric pressure equalization.

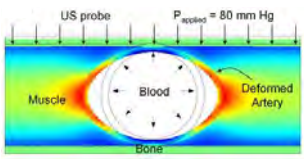

Figure 4: Axial strain due to uniaxial pressure equalization (FE simulation result).

042 **3D VECTOR FIELD MAGNETIC RESONANCE ELASTOGRAPHY FOR DETECTING TISSUE PRESSURE CHANGES IN HUMAN BRAIN.**

Dieter Klatt[1], Sebastian Hirsch[1], Jürgen Braun[1], Florian Baptist Freimann[1], Ingolf Sack[1].*
[1]Charité – University Medicine Berlin, GERMANY.

Background: Magnetic Resonance Elastography (MRE) [1] is a phase contrast–based MRI technique for assessing the mechanical properties of *in vivo* tissue. MRE has already shown its diagnostic potential for hepatic fibrosis [2], neurological disorders [3,4] and breast tumor classification [5]. While in these studies the shear modulus was measured, mechanical properties related to the inherent tissue pressure were not assessed. Assuming a variable tissue pressure implies consideration of the compressible properties of tissue associated with poroelastic constants [6].

Aims: The purpose of the presented work is the measurement of pressure changes by MRE induced to *in vivo* human brain using a loading paradigm to abdominal muscle.

Methods: Cerebral MRE was performed on 7 healthy volunteers in a 1.5T MRI scanner (Siemens Sonata) using a single–shot spin–echo EPI sequence. Mechanical waves of 25 Hz were introduced into the brain by a head–cradle. The full 3D displacement field was acquired in 30 adjacent transverse slices with a temporal resolution of 10 ms and 2 mm isovoxels. For each volunteer, cerebral MRE was performed in the relaxed state and with contracted abdominal muscle induced by a 20kg–weight placed on top of the abdomen. For viscoelastic parameter evaluation, the Navier equation (assuming local homogeneity)

$$\rho\ddot{u}=(\lambda+\mu)\nabla(\nabla\cdot u)+\mu\Delta u$$

was transformed into the frequency domain and solved for the complex Lamé parameters, λ^* and μ^*, by multiplying the wave field, u, with the pseudo–inverse of the derivative matrix. Finally, λ^* and μ^* were averaged over the brain parenchyma.

Results: The cerebral complex moduli of both Lamé parameters are shown in Figure 1. Abdominal muscle contraction is associated with a decrease of λ^* in the brain of all volunteers, whereas $\mu^*$is not sensitive to the abdominal muscle condition.

Conclusions: We observed the first Lamé parameter to be much lower than expected for a nearly incompressible medium. This indicates enhanced poroelastic properties of brain tissue that are associated with two compressional wave modes. Since the fast mode with modulus values on the order of GPa cannot be measured using the MRE technique. The first Lamé parameter given here is apparently on the order of kPa and might therefore correspond to the slow compressional mode. Furthermore, the compressibility of the brain is apparently changed by loading the abdominal muscle, which is known to alter the cerebrospinal fluid (CSF) pressure. The decrease of λ^* upon muscle load is associated with an increase in CSF pressure. This may be explained by an increased interaction of pore fluid with the solid matrix of the brain. Thereby, the interaction term reduces the compression modulus of the solid matrix [7]. In summary, our results suggest that CSF pressure changes can be detected by 3D vector field MRE.

References:

[1] Muthupillai et al.: Science, 269, pp. 1854–7, 1995.
[2] Asbach et al.: Radiology, 257, pp. 80–6, 2010.
[3] Würfel et al.: Neuroimage, 49, pp. 2520–5, 2010.
[4] Freimann et al.: Neuroradiology, (in press).
[5] Sinkus et al.: MRM, 58, pp. 1135–44, 2007.
[6] Leiderman et al.: Phys Med Biol, 51, pp. 6291–313, 2006.
[7] Biot: JASA, 28, pp. 168–78, 1956.

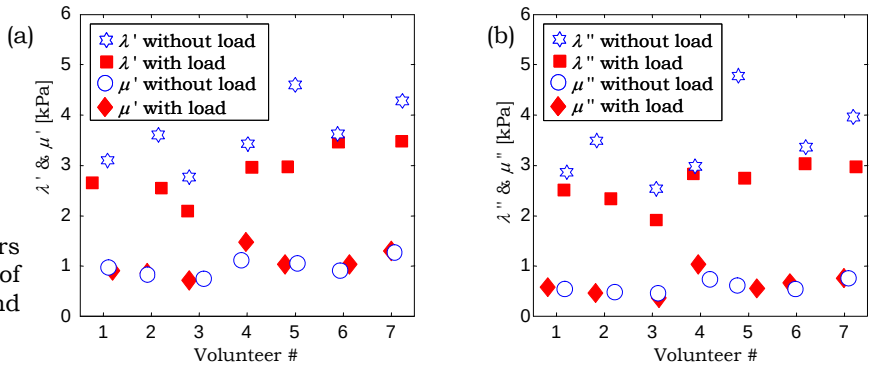

Figure 1:
Cerebral complex Lamé parameters ((a)storage moduli; (b) loss moduli) of all volunteers with relaxed and contracted abdominal muscle.

043 **LOCAL SHEAR SPEED ESTIMATION OF *EX–VIVO* PROSTATE USING ACOUSTIC CRAWLING WAVES (ARC) GENERATED FROM RADIATION FORCES.**

Zaegyoo Hah[1], Chris Hazard[2], Bradley N. Mills[1], Jorge Yao[3], Deborah J. Rubens[4], Kevin J. Parker[1].*
[1]ECE Department, University of Rochester, Rochester, NY, 14627, USA; [2]GE Global Research, One Research Circle, Niskayuna, NY, 12309, USA; [3]Dept. of Pathology, University of Rochester, Rochester; [4]Imaging Science Department, University of Rochester, Rochester, NY, 14627, USA.

Background: Crawling Waves can be created in a number of geometries using mechanical vibration sources and can be analyzed to provide accurate quantitative estimates of the local shear wave speed. This technique has been applied to homogeneous and inhomogeneous phantoms of known Young's modulus and to liver tissue, whole prostates and muscles *in–vivo* [1]. On the other hand, Crawling Waves generated from acoustic radiation force can overcome the limitations of mechanical vibration sources including the restraint of accessible surfaces, while improving system integration.

Aims: Previous reports describe the system modification for ARC (Acoustic Radiation force Crawling wave) signal processing to generate crawling wave movies and the estimation results for phantoms with an embedded inclusion [2]. This presentation extends the ARC for the estimation of shear wave speed and local elastic properties to *ex–vivo* prostates. Also ROI is extended to cover a wider area.

Methods: A Logiq 9 ultrasound system (GE), custom modified for this experiment, pushes and scans the phantom over the region of interest (ROI) with depth of 4cm and width of 3.89cm. The ROI consists of three overlapping scanning area (Fig. 1). The data set is in a pair: one from a push on the far left of a ROI and the other from the right push. The radiation force is generated by axicon focusing [3] to keep the intensity and the thermal dose level below FDA guidelines. The data set is processed to remove background noise, boundary reflections and high frequency noise. Processed displacement data are then used to synthesize a Crawling Wave for several frequencies. Many tractable estimation algorithms developed for mechanical crawling waves can be applied for the final estimation. The system and the procedure were tested first for a gelatin phantom with an inclusion (Figure 2). Also a human prostate specimen, embedded in a gelatin–based background within two hours after surgery, was scanned and the data was processed for a shear velocity map.

Results: The results of some ARC wave prostate experimental data are compared to the results obtained by mechanical vibration sources. The frequency of crawling wave synthesis is about 100–450Hz. The estimated shear speed of the tumor is about 3–5m/s while that of the background is 2–4.5m/s. Both the estimation results (one from ARC and the other from mechanical vibration sources) are verified against pathological slides pinpointing the location of tumors.

Conclusions: It is shown that the crawling waves generated from the radiation force can be used to estimate the local tissue elasticity. *Ex–vivo* prostates are studied as an example.

Acknowledgements: This study was partly supported by NIH grant 5RO1AG29804.

References:

[1] M. Zhang et al.: Congruence of Imaging Estimators and Mechanical Measurements of Viscoelastic Properties of Soft Tissues. Ultrasound Med Biol, Vol. 33, pp.1671–1631, 2007.
[2] Z Hah et al.: Synthesis and Analysis of Crawling Waves Generated from Radiation Force. Proc. 9th ITEC, Snowbird, Utah, p.119, 2010.
[3] C. Buckhardt et al.: Ultrasound Axicon: A Device for Focusing over a Large Depth. J Acoust Soc Am, Vol. 54, pp. 1628–1630, 1973.

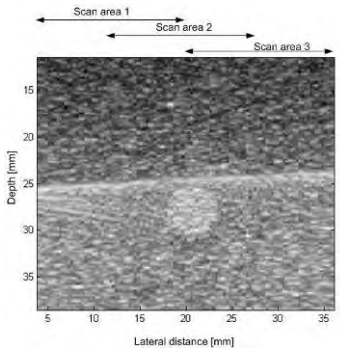

Figure 1: A B–mode image of a phantom with an inclusion. Scanning is done to cover a wide region of interest.

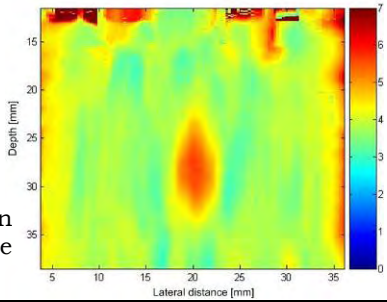

Figure 2: Shear speed estimation result from three overlapping scans.

* *indicates Presenter*

048 **REAL–TIME TRANSIENT ELASTOGRAPHY ON STANDARD ULTRASOUND USING MECHANICALLY INDUCED VIBRATION.**

Reza Zahiri Azar[1], Kris Dickie[1], Benjamin Kerby[1], Sergio Bernardo[1], Chris Cheung[1], Laurent Pelissier[1].*

[1]Ultrasonix Medical Corporation, Richmond, BC, CANADA.

Background: Transient elastography by means of mechanical vibration has been well established in the literature as a mean of assessing the elasticity of the liver which correlates with fibrosis stages. Previous studies have focused mainly on single element transducers [1] and ultrafast scanners [2].

Aim: In this presentation, we report implementation of a transient elastography system on a standard ultrasound scanner that enables quantitative assessment of tissue elasticity in real–time.

Method: To induce vibration, a linear actuator has been designed and mounted on an ultrasound transducer. To drive the actuator, a programmable signal generator and an amplifier has also been integrated into the mount. Two custom imaging modes have been implemented on the ultrasound system to provide fast RF acquisition rate for elastography. In the first mode, a 1D window of the RF signal from a single scan line is acquired at a fast rate (5kHz for 100ms i.e., 500 acquisitions). In the second mode, by relaxing the requirement for high acquisition rate, a 2D window of RF signals that consists of a small group of scan lines is acquired (1kHz for 100ms i.e., 100 acquisitions per scan line). Both imaging modes were followed by standard B–mode imaging to provide real–time ultrasound guidance. To facilitate imaging of the transient waves, the start of acquisition for both imaging modes was synchronized with the start of vibration. Following data acquisition, axial wave images were estimated from the sequences of RF signals. 1D and 2D Algebraic Helmholtz Inversion of the wave equation were then applied in the frequency domain (at the excitation frequency) to estimate the Young's modulus from these 1D and 2D wave images, respectively. Finally, the estimated Young's modulus was displayed on the screen along with the wave and B–mode images in real–time. Experimental validations were performed on an elasticity phantom (CIRS, VA, USA). The vibration was programmed to be a Gaussian modulated sine wave with multiple excitation cycles (7 excitation cycles of 75Hz) to provide narrow band wave images.

Results: In both 1D and 2D modes, the reported Young's moduli of 25±4kPa were estimated to be 27±7kPa for 10 subsequent measurements. Current interface of the system on the SonixTouch ultrasound machine (Ultrasonix, BC, CA) is shown in Figure 1.

Conclusions: The proposed system can be implemented on most ultrasound systems with small overhead. It can also be combined with compression elastography to provide quantitative elastograms. Our ultimate goal is to study the performance of the system in a clinical setup for noninvasive staging of liver fibrosis. However, further investigations are required to study the effect of different boundary conditions and tissue structures on estimated Young's modulus. This will be the topic of our future work.

Acknowledgements: The authors would like to thank Drs. Salcudean, Sandrin and Miette for their valuable feedback on this work.

References:

[1] Sandrin L., Tanter M., Gennisson J., Catheline S., Fink M.: Shear Elasticity Probe for Soft Tissues with 1–D Transient Elastography. ", IEEE UFFC, 49(4), pp. 436-–446, 2002.

[2] Sandrin, L., Tanter, M., Catheline, S., Fink, M.: Shear Modulus Imaging with 2–D Transient Elastography. IEEE UFFC, 49(4), pp. 426–435, 2002.

(a) (b)

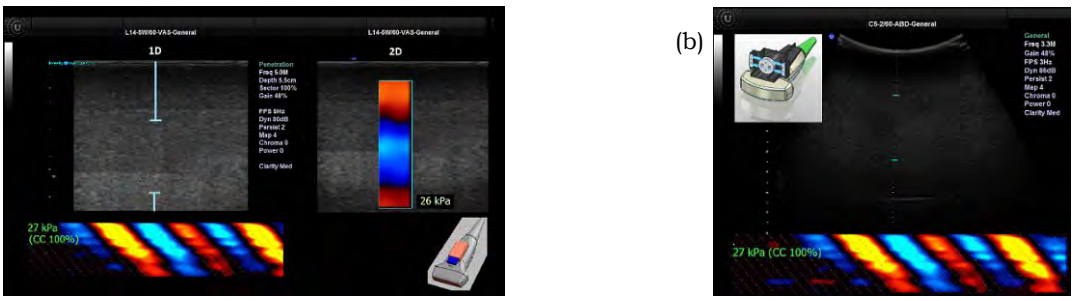

Figure 1: Current interface of the transient elastography on the SonixTouch ultrasound machine for both (a) linear transducer and (b) curvilinear transducer. The interface for both 1D and 2D modes for linear transducer are also displayed in (a).

050 **MULTI–PARAMETRIC MONITORING OF THERMAL LESIONS USING HARMONIC MOTION IMAGING FOR FOCUSED ULTRASOUND (HMIFU).**

Gary Y. Hou[1], Fabrice Marquet[1], Jianwen Luo[1], Elisa E. Konofagou[1,2].*
[1]Biomedical Engineering and [2]RadiologyDepartments, Columbia University, New York, NY, USA.

Background: HMIFU is a recently developed high–intensity focused ultrasound (HIFU) therapy monitoring method with feasibilities demonstrated *in vitro* and *in vivo* [1–3]. Its principle is based on Harmonic Motion Imaging (HMI) [3], an oscillatory radiation force technique for imaging tissue mechanical properties during HIFU application with an amplitude–modulated (AM) therapeutic beam. In this study, a multi–parametric study was performed to assess the performance of the use of the HMI strain and HMI displacement for HIFU treatment monitoring.

Aims: To assess the performance of HMI displacement and strain for HIFU treatment monitoring and post–ablation imaging.

Methods: *Ex vivo* fresh canine liver lobes (n=3) were excised immediately after animal sacrifice and immersed into a phosphate buffered saline (PBS) solution. A therapeutic transducer (f_{center}=4.755MHz, AM frequency=25Hz, Riverside Research Institute, NY, U.S.A) was used in conjunction with a confocal pulse–echo transducer (f_{center}=7.5MHz, Panametrics, MA, U.S.A.) for simultaneous acquisition of RF signals during the excitation (PRF of 4kHz). The extrapolated *in situ* acoustic intensities respectively were 363W/cm^2 and 1452W/cm^2 under imaging and ablation based on hydrophone calibration. The acquired RF signals were filtered through an analog band–pass filter (f_{c1}=5.84MHz, f_{c2}=8.66MHz at -60dB, Reactel Inc., MD, USA) and recorded at 80MHz using a high speed digitizer (Gage applied, IL, U.S.A.). A 1–D normalized cross–correlation (window size of 1mm, 85% overlap) was used to estimate the HMI displacement, and a least squares estimator was used to estimate the strain. HMI displacement maps were acquired in the transverse plane through raster scans before and after lesion formation. The same method was repeated in 10, 20 and 30–s HIFU treatment cases.

Results: Ten thermal lesions were formed and detected. During treatment planning, estimated focal displacement and compressive strain were 13.9±4.01μm and -0.62±0.03%, respectively. During treatment, displacement underwent a rise (from a baseline of 5.34±3.31μm) followed by a sharp drop stabilizing at (-14.41±9.09μm), indicating tissue softening and hardening under thermal treatment, which is consistent with results in previous studies [2,4]. The estimated displacement difference before and after lesion formation was -5.60±3.31μm. In addition, the same decrease was also detected in the estimated HMI compressive axial strain before (-1.28±0.34%, -1.48±0.56%) and after (-0.43±0.059%,-0.40±0.038%) lesion formation under 20– and 30–s HIFU treatments, respectively.

Conclusions: A multi–parametric analysis on HIFU treatment monitoring using HMIFU was hereby presented. First, local tissue properties were estimated using both displacement and strain before and after HIFU treatment. Secondly, changes in the slope of the displacement profile were observed, indicating the capability of HMIFU of monitoring the onset of tissue hardening after initial softening. Finally, transverse HMI maps confirmed the formation of thermal lesions. Monitoring with the use of phase shift and characterization of cavitation during HIFU treatment monitoring will also be shown.

Acknowledgements: Supported by the National Institutes of Health (NIH Grant R21EB008521). The authors wish to thank Riverside Research Institute (RRI) for providing the HIFU transducer.

References:

[1] Maleke C. and Konofagou E.E.: Phys. Med. Biol., Vol. 53, pp. 1773–1793, 2008.
[2] Maleke C. and Konofagou E.E.: IEEE Trans. Biomed. Eng., Vol. 57, pp. 7–11, 2010.
[3] Maleke C., Pernot, M. and Konofagou E.E.: Ultrasonic Imaging, 28, pp. 144–158, 2006.
[4] Sapin–de Brosses E., Gennisson J–L., Pernot M., Fink M., Tanter M.: Phys. Med. Biol., Vol. 55, pp.1701–1718. 2010.

* *indicates Presenter*

051 **FEASIBILITY OF ACQUIRING VOLUMETRIC B–MODE/ARFI/DOPPLER DATA BY SWEEPING.**

DM Dumont[1], JR Doherty[1], SY Lee[1],and GE Trahey[1].*
[1]Duke University, Durham, NC, USA.

Background: For many acoustic radiation force impulse (ARFI) imaging applications, the accurate identification of malignancy or treatment boundaries is essential for evaluating either the extent of disease or the efficacy of treatment. However, these problems are essentially three–dimensional in nature, and thus require three–dimensional imaging solutions if the entire region is to be characterized using ARFI–based methods. It would be useful if current 2D ARFI imaging methods could be adapted to permit volumetric scanning. This could be accomplished by using a dedicated 3D imaging probe or by sweeping a 2D probe across a region–of–interest (ROI).

Aims: To quantify volumetric ARFI imaging performance during stage–controlled sweeps.

Methods: ARFI sequences were developed to permit the rapid acquisition of approximately fifty frames of B–mode/ARFI/color–flow Doppler data at real–time frame rates (~20Hz). A VF–105 linear transducer was attached to a motion–controlled stage, and a 40x20x20–25mm volume of B–mode/ARFI/Doppler data were acquired from tissue mimicking phantoms of varying stiffness (5–68kPa) at different sweep rates (0–7.5mm/s). Jitter and SNR were quantified for each phantom and sweep rate case. Target imaging performance was quantified by acquiring volumetric datasets while sweeping across lesion and soft–plaque vascular phantoms and evaluating target CNR and area as a function of sweep rate.

Results: Jitter and SNR were found to vary with phantom stiffness, sweep rate and time following excitation. The results suggest that initial performance following the excitation is predominately a function of shearing, with degradation from motion becoming significant with increased time following excitation and for greater stiffness. For compliant phantoms (i.e., <10kPa), SNR was found to be robust to the effects of motion, with less than -2dB difference between stationary results and the fastest sweep velocity (~7.5mm/s) for up to 1ms following excitation. For the stiffest phantom (i.e., 67kPa), SNR was found to be degraded by approximately -8dB at 1ms at the fastest sweep rate, with noise overtaking the displacement signal for greater elapsed times. For all cases, a simple motion filter can improve performance such that SNR losses from motion degradation during typical ARFI tracking times (i.e., <1ms) is reduced to less than approximately -3dB for stiffness <24kPa and approximately -4dB for stiffness <67kPa.

Figure 1 shows sample B–mode/ARFI/Doppler orthogonal frames from the soft–plaque vascular phantom at the highest sweep rate, demonstrating that volumetric ARFI and B–mode/Doppler data can be acquired with a simple sweep in less than three seconds. Good agreement was observed between lesion areas determined by ARFI at all sweep rates, with no statistically significant difference between lesion area as a function of sweep rate.

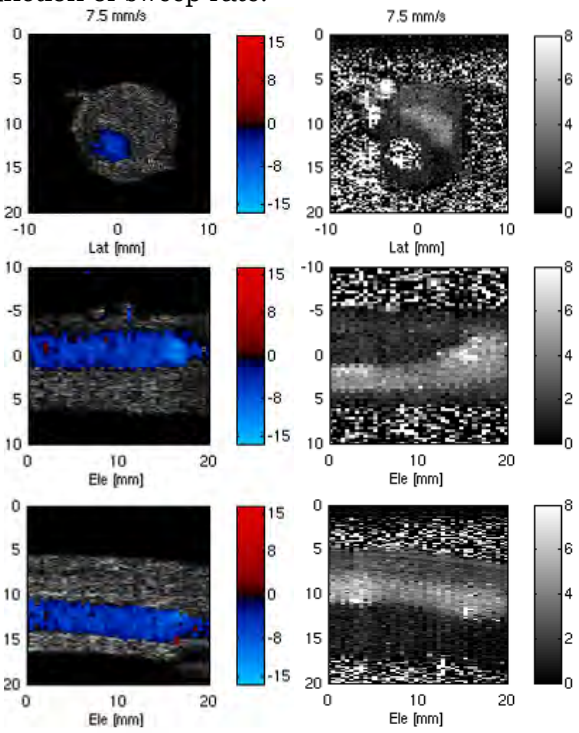

Figure 1: Orthogonal B–mode/Color–flow Doppler (left column) and ARFI (right column) images at the fastest sweep rate from a soft–plaque vascular phantom. Scales are in cm/s (left) and microns (right).

Conclusions: The results demonstrate the feasibility of acquiring volumetric B–mode/ARFI/Doppler data by sweeping a transducer. Performance is degraded for faster sweep rates and in stiffer materials, although the results do suggest that this degradation is not enough to significantly affect target identification.

Acknowledgements: This research was funded by NIH Grants: HL075485, HL096023 and T32EB001040.

* *indicates Presenter*

033 **COMPARISON OF ULTRASONIC MEASUREMENTS OF UNRIPENED AND RIPENED CERVICES.**

Lisa Reusch[1], Lindsey Carlson[1], Mark L. Palmeri[2], Jeremy J. Dahl[2], Helen Feltovich[1,3], Timothy J. Hall[1].*
[1]Medical Physics, University of Wisconsin–Madison, Madison, WI, USA; [2]Biomedical Engineering, Department, Duke University, Durham, NC, USA; [3]Maternal Fetal Medicine, Intermountain Healthcare, Park City, UT, USA.

Background: Spontaneous preterm birth has been and remains a problem in the US. Cervical dysfunction plays a large role in preterm birth [1], but a lack of noninvasive technology sophisticated enough to interrogate the microstructure of the cervix makes a quantitative assessment cervical function challenging. Collagen content and alignment gives the cervix its strength and undergoes rearrangement (ripening) long before gross changes (shortening, softening) can be seen, so early detection of these changes is important. A ripened cervix is much softer than a cervix that has not gone through this rearrangement, and these differences are reflected in their acoustical properties [2–4]. Additionally, after birth occurs for the first time, the cervix restructures itself but is very different from before this first pregnancy. Our initial results suggest that there are also differences in a cervix that has had a baby (multiparous) and one that has never had a baby (nulliparous).

Aims: We are developing a method, using quantitative ultrasound (QUS) techniques and acoustic radiation force impulse (ARFI) measurements, to assess the state of the cervix. We aim to be able to detect differences between ripened and unripened cervices, and between nulliparous and multiparous cervices.

Methods: Cervices from three groups were measured: nulliparous, multiparous and ripened nulliparous. The specimens were scanned with a Siemens Acuson S2000 ultrasound machine using a prototype catheter transducer (Siemens Medical Solutions USA, Malvern, PA, USA). Radiofrequency (RF) data were acquired with the transducer aperture aligned parallel to the endocervical canal. The angle between the acoustic beam and tissue was used to assess anisotropic acoustic propagation and was changed through electronic control of transmit and receive angles between ±40°. The integrated power was calculated for each angle and compared to normal incidence. Similar data were collected from a phantom with spherical scatterers for system calibration and removed from total integrated power. The shear sound speed of the tissue samples was then measured using ARFI measurements for angles of -20°, 0° and +20°. For comparison, we used second harmonic generation (SHG) optical microscopy to directly image the collagen fibers in a single sample from each group.

Results: The power loss compared to normal incidence for the three different groups is very different. The nulliparous group showed a loss that was nearly symmetric about normal incident and between 10–15dB. The multiparous group showed a similar loss at positive steering angles but showed a gain in power when the beam was steering to negative angles. The ripened nulliparous group had an asymmetric loss curve like the multiparous group, but instead of a gain in power, the loss was nearly zero for negative steering angles. The shear sound speed in the nulliparous is around 4.2m/s, and the multiparous group has a correspondingly lower shear sound speed of 3.0m/s. In corroboration with these results, a subjective analysis of the SHG images from each group indicates that the nulliparous cervix is much more organized than both the multiparous cervix and the ripened nulliparous cervix, and the ripened cervix is more disorganized than either the nulliparous or multiparous cervix.

Conclusions: We compared ultrasound measurements from multiparous, nulliparous and ripened nulliparous cervices. Results show a difference in the power loss among the three groups indicating a difference in structure. Further studies will aim to quantify this difference and measure the change throughout pregnancy. Early detection of changes in microstructure may open pathways to earlier, more specific interventions for preterm delivery.

Acknowledgements: This work is supported by National Institutes of Health grants R21HD061896 and R21HD063031.

References:

[1] C. Y. Spong: Obstetrics and Gynecology, Vol. 110, pp. 405–415, 2007.
[2] D. Parry: Biophys Chem, Vol. 29, pp. 195–209, 1988.
[3] M. Mahendroo, et al.: Mol Endocrinol, Vol. 13, pp. 981–992, 1999.
[4] Feltovich H et al.: Am J Obstet Gynecol, Vol. 92, pp. 753–760, 2005.

* *indicates Presenter*

056 **THE APPLICATION OF FREE–HAND TISSUE DEFORMATION AND SPATIO–TEMPORALLY REGULARISED SPECKLE TRACKING TO PHOTOACOUSTIC IMAGE CLUTTER REDUCTION: A FIRST CLINICAL DEMONSTRATION.**

Michael Jaeger[1,2], David Birtill[1], Andreas Gertsch[1], Elizabeth O'Flynn[2,3], Jeffrey C. Bamber[1,2].*
[1]Joint Department of Physics, Institute of Cancer Research and Royal Marsden NHS Foundation Trust, Sutton, Surrey, England, UK; [2]CRUK–EPSRC Cancer Imaging Centre, Institute of Cancer Research and Royal Marsden NHS Foundation Trust, Sutton, Surrey, England, UK; [3]Radiology Department, Royal Marsden NHS Foundation Trust, Sutton, Surrey, England, UK.

Background: Photoacoustic (PA) imaging is an emerging modality offering promise for cancer diagnosis, therapy planning and monitoring response. The images show optically absorbing tissue structures based on detection of ultrasound (US) signals after irradiation with short (ns) laser pulses. A multiple optical wavelength approach allows imaging of local blood oxygenation and optical contrast agent concentration, which may be molecularly targeted. Imaging with ultrasound resolution, to a depth of several centimeters, is expected. Unfortunately this considerable potential is currently not being realized, largely because strong clutter degrades PA contrast and typically limits the imaging depth to less than 1cm. A PA clutter reduction method that has previously been studied in simulation and phantom experiments involves (a) implementing PA imaging with freehand echography in a single device so that PA signals may be displayed in real time within the anatomical context, and (b) averaging a PA image sequence that has been compensated for tissue deformation induced by palpating with the ultrasound probe, where the deformation has been characterized from the echogram sequence using elastography. (Palpation produces clutter decorrelation while the true PA image remains correlated, deforming with the tissue.)

Aims: We see great potential in combining PA imaging with free-hand palpation elastography. As a first step, our goal was to demonstrate deformation-mediated PA clutter reduction in free-hand clinical PA scans.

Methods: Duplex PA and echo imaging was implemented on a commercial US scanner (Z.one™ Zonare, Mountain View, CA, USA) and a Q–switched Nd:YAG laser at 1064nm wavelength and 10Hz pulse rate. For accurate deformation compensation, real–time interleaved PA and echo image acquisition is crucial. Because technical limitations prevented this, a work–around was implemented: the scanner was operated in PA mode only, and a photoacoustically generated US transmit pulse was used to acquire low quality echograms simultaneously with PA data frames. A standoff gel pad was used for temporal separation of PA and echo signals, for their subsequent identification in sequences of 100 data frames that were acquired while palpating the tissue. Echographic speckle tracking provided the time–dependent local tissue displacement maps, which was then used for PA displacement compensation and averaging.

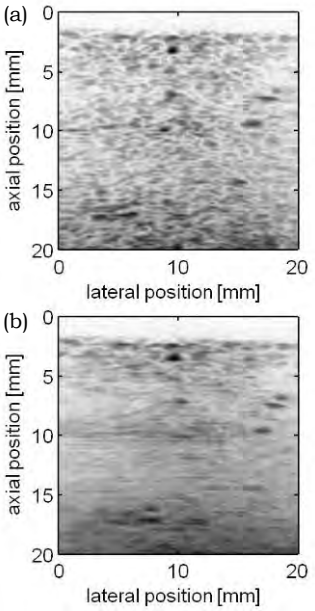

Figure 1: Example PA images from the human neck *in vivo*, before (a) and after (b) deformation–compensated averaging.

Results: Initial clinical scans of necks, forearms and breasts demonstrated loss of PA signal–to–noise ratio due to the existence of a PA–clutter background. Also the echograms (created photoacoustically) were found to suffer from strong echo clutter, which caused speckle to decorrelate rapidly with deformation. This necessitated the development of a novel spatially and temporally regularised speckle tracking technique, which will be described in the presentation. When used to produce deformation–compensated PA image sequences, this worked well enough for direct PA signals to show good temporal stability while the PA clutter decorrelated. Averaging of these sequences produced significant and useful PA clutter reduction in all cases.

Conclusions: It has been shown for the first time that deformation–compensated averaging leads to improved clinical PA imaging of human vasculature *in vivo*, providing significant reduction of PA clutter and allowing blood vessels to be seen at 2cm depth which were otherwise not reliably identifiable. The future application of the method, using conventional (transmit–focused) echo images to characterise the tissue deformation, should lead to improved performance.

Acknowledgements: Support was received from the CRUK and EPSRC Cancer Imaging Centre.

Champions Ballrooms Conference Center Floor Plan

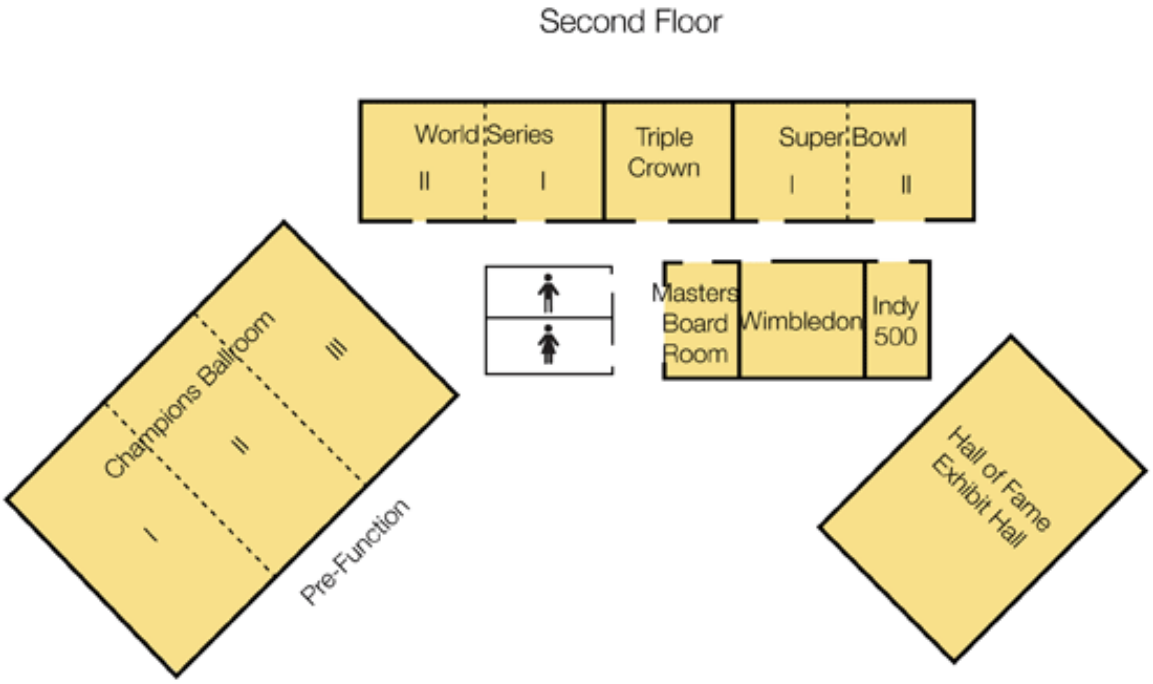

BACKWORD

Elasticity in Real Time (…this is not what you think it is…)

It is hard to believe that we have reached the 10th Anniversary of the Conference! These years have been profoundly joyous and inspirational and yet involved much effort for the organizers, our helpers and volunteers.

The joy was due to many things but was primarily due to the meeting of many new and old friends and colleagues. With every passing Conference, we were privileged to meet and get to know more and more young professors and students who were of keen mind and boundless enthusiasm and intensity; some of the students have graduated and moved on, and are now bringing their own students to the Conference – a great vote of confidence in the future of the field and the Conference. Many of these students have commented time and again on how easy and exciting it has been for them to be able to freely approach and discuss their work with many of the leaders in the field. The quality of the presentations has been steadily increasing, aided in part by the generous sponsorship of the Student Best Paper Award by Ultrasonix. The strong international participation has given the Conference a diverse yet intimate atmosphere. New collaborative research groups were constantly being formed on the sidelines of the Conference, consistent with our original goals.

The Conference has also been a source of inspiration for us. We have been watching the rapid and exciting development of the field unfold before us literally in real time. In the years that passed, several elasticity imaging technologies were discovered, researched and have made it all the way into the clinic; and they were all reported and discussed at this Conference. We would like to believe that the Conference was in some small way a catalyst for this remarkable progress, rather than being a mere organizational entity.

The organizational work in planning and hosting the Conference year after year proved to be an exciting yet arduous endeavor. Yet, this excitement transformed the work into a labor of love and its own reward for all concerned.

Please accept our sincere thanks for making this Conference an ongoing success!

Elastographic Encounters of the Best Kind

On my desk, in a place of honor, sit nine coffee mugs of different sizes and shapes, but all carrying the ITEC logo. Soon there will be ten, representing a decade of eventful Conferences. The First International Elasticity Conference was held in Niagara Falls, Canada, after some intensive deliberation and canvassing by Jon Ophir, me and some of our close colleagues and staff. The first Conference was an experiment, after all, but one designed to address the need to bring together the international community that was responsible for a rapidly evolving and exciting research frontier: to image the elastic properties of tissue. Part of the challenge of the "bootstrap operation" was that we had to gamble (somewhat) on the expected size, participation and cost of the new Conference series. Fortunately, it was a success and served as the launch pad for what is now a mature and superbly high quality Conference celebrating its 10th Anniversary. There are many people to thank, not the least being the great researchers and clinical experts who share their insights with other researchers every year. But just to single out one person, I'd like to publicly recognize Karen Ophir, who has been the "Chief Operating Officer" for the Conference, working largely as a "labor of love". Karen's diligent efforts have made this Conference series an enjoyable and productive success year after year. Please join me in thanking her when you have the opportunity.

I'm already looking forward to the breakthroughs in the next decade of research in "imaging the elastic properties of tissues" and seeing them presented at the future ITEC Conferences.

Editor's Notes: (Stretching the abstracts and straining over the results)

It has been a personal pleasure to facilitate this Conference. Originally, I only wanted to do the publications and pretty posters and badges. As a sonographer of almost 20 years and having worked before that in engineering support for over 25 years, reading every abstract has become enlightening and entertaining. Eventually, I took on more of the administrative work as well, which has provided me with yet another new career: Conference Organizer!

The best part of this Conference for me is the smile on each attendees face when he/she enjoys the effort we have put in, from the Proceedings Book and other materials to the venue, meals and entertainment. The year-long communications which intensify as the Conference grows closer has created an academic family for me as evidenced by the many personal photos you have shared with me over the last 10 years.

Kevin is correct in that we started on a shoestring and crossed our fingers. In 2001, Jonathan and I were visiting the University of Rochester. Jonathan mentioned to Kevin that S. Kaisar Alam (his former PhD student who did his Postdoctoral fellowship in Jonathan's lab) had suggested that they (JO & KJP) should start a conference on elasticity imaging. So, we attempted to get an R13 grant from NIH to start this Conference, an effort that predictably met with rather low reviewer enthusiasm. And that's how it all started. So, just like Mickey Rooney and Judy Garland, we put on a show!

Lest you think only the 3 of us are responsible for ITEC adminstration, be advised that the list is long: Manette Deranleau (Price), Pam Clark, Jeffrey Bamber, Lesley Brotherston, and their helpers in the UK, Tammy Keidel, Christina Andrews, Chris de Korte, Sonja van de Ven, and their helpers in the Netherlands, Charlene Waldron and all the volunteer attendees and guests who are willing to lend a hand at any time. Here's to the next 10! See you there!

Please Fill Out Both Sides

Conference Evaluation and Questionnaire

OVERALL CONFERENCE

	Poor		Mid		Excellent
Overall Conference Evaluation	1	2	3	4	5
General comments:					

SCIENTIFIC PROGRAM

	Poor		Mid		Excellent
Quality of the Presentations	1	2	3	4	5
Relevance of Presentations to the Conference's Theme	1	2	3	4	5
Time Allotted for Presentations	1	2	3	4	5
Time Allotted for Discussion	1	2	3	4	5
Poster Session	1	2	3	4	5
Tutorials	1	2	3	4	5
Equipment Exhibit	1	2	3	4	5
Student Participation	1	2	3	4	5
Additional comments:					

CONFERENCE MATERIALS

	Poor		Mid		Excellent
Printed Proceedings Book	1	2	3	4	5
CD Proceedings	1	2	3	4	5
Other Registration Materials	1	2	3	4	5
Additional comments:					

CONFERENCE FACILITIES & SOCIAL PROGRAM

	Poor		Mid		Excellent
Lecture Hall	1	2	3	4	5
Registration Desk	1	2	3	4	5
Meals: Dining facilities	1	2	3	4	5
Conference Breakfasts and Lunches	1	2	3	4	5
Conference Dinner and Concert	1	2	3	4	5
Coffee Breaks	1	2	3	4	5
Opening Dinner Reception	1	2	3	4	5
Closing Pizza Party	1	2	3	4	5
Audio–Visual: Screen Visibility	1	2	3	4	5
Sound Level	1	2	3	4	5
Presentation Transition	1	2	3	4	5
Internet Connectivity:	1	2	3	4	5
Additional comments:					

Please Fill Out Both Sides

Conference Evaluation and Questionnaire

VENUE AND HOTEL

	Poor		Mid		Excellent
Venue: Arlington, Dallas, Fort Worth, TX and Environs	1	2	3	4	5
Would you return to this city?	Yes		Perhaps		No
Area Attractions	1	2	3	4	5
Hotel: Overall	1	2	3	4	5
Reservations	1	2	3	4	5
Transportation and Accessibility	1	2	3	4	5
Reception and Check–In	1	2	3	4	5
Accommodations	1	2	3	4	5
Facilities	1	2	3	4	5
Parking	1	2	3	4	5
Would you return to this hotel?	Yes		Perhaps		No
Additional comments:					

CONFERENCE ADMINISTRATION

	Poor		Mid		Excellent
Website	1	2	3	4	5
Registration off–site	1	2	3	4	5
Registration on–site	1	2	3	4	5
Administrative staff	1	2	3	4	5
Correspondence	1	2	3	4	5
Additional comments:					

GENERAL INFORMATION

I am a Returning Delegate	Yes		No
I plan to attend the next conference	Yes	Perhaps	No
and present a paper(s) / poster(s)	Yes	Perhaps	No
Other(s) from my lab would attend the next conference	Yes	Perhaps	No
and he/she / they would present a paper(s) / poster(s)	Yes	Perhaps	No
How did you learn of this conference? (Check all that apply)	☐ Email Announcement		
☐ Internet	☐ Website		
☐ Other	☐ Colleague		
Tutorial Topic Suggestions for next year:			
Additional Comments:			

If you would be willing to host the Conference in your city, please give your name to the Conference Staff.

Questions or comments are welcome at any time at <secretariat@elasticityconference.org>

Thank You!